

3-10-2010

Time Dependent Channel Packet Calculation of Two Nucleon Scattering Matrix Elements

Brian S. Davis

Follow this and additional works at: <https://scholar.afit.edu/etd>

 Part of the [Nuclear Commons](#), and the [Numerical Analysis and Scientific Computing Commons](#)

Recommended Citation

Davis, Brian S., "Time Dependent Channel Packet Calculation of Two Nucleon Scattering Matrix Elements" (2010). *Theses and Dissertations*. 2159.

<https://scholar.afit.edu/etd/2159>

This Dissertation is brought to you for free and open access by the Student Graduate Works at AFIT Scholar. It has been accepted for inclusion in Theses and Dissertations by an authorized administrator of AFIT Scholar. For more information, please contact richard.mansfield@afit.edu.



TIME DEPENDENT CHANNEL PACKET CALCULATION OF TWO NUCLEON SCATTERING MATRIX ELEMENTS

DISSERTATION

Brian S. Davis, Major, USAF
AFIT/DS/ENP/10-M03

DEPARTMENT OF THE AIR FORCE
AIR UNIVERSITY

AIR FORCE INSTITUTE OF TECHNOLOGY

Wright-Patterson Air Force Base, Ohio

APPROVED FOR PUBLIC RELEASE; DISTRIBUTION UNLIMITED

The views expressed in this dissertation are those of the author and do not reflect the official policy or position of the United States Air Force, Department of Defense, or the United States Government.

AFIT/DS/ENP/10-M03

TIME DEPENDENT CHANNEL PACKET CALCULATION OF TWO NUCLEON SCATTERING MATRIX ELEMENTS

DISSERTATION

Presented to the Faculty

Graduate School of Engineering and Management

Air Force Institute of Technology

Air University

Air Education and Training Command

In Partial Fulfillment of the Requirements for the

Degree of Doctor of Philosophy

Brian S. Davis, BA, MS

Major, USAF

March 2010

APPROVED FOR PUBLIC RELEASE; DISTRIBUTION UNLIMITED

TIME DEPENDENT CHANNEL PACKET CALCULATION OF TWO NUCLEON SCATTERING MATRIX ELEMENTS

Brian S. Davis, BA, MS
Major, USAF

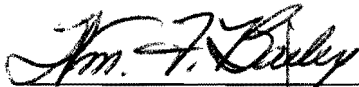
Approved:



David E. Weeks, PhD (Chairman)

2 Mar 10

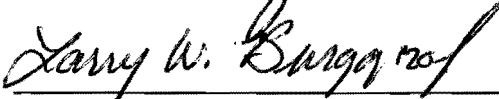
Date



William F. Bailey, PhD (member)

2 Mar 2010

Date



Larry W. Burggraf, PhD (member)

2 Mar 2010

Date



William P. Baker, PhD (member)

2 Mar 2010

Date

Accepted:



M. U. Thomas
Dean, Graduate School of
Engineering and Management

4 Mar 2010

Date

Abstract

A new approach to calculating nucleon-nucleon scattering matrix elements using a proven atomic time-dependent wave packet technique is investigated. Using this technique, reactant and product wave packets containing centripetal barrier information are prepared in close proximity to the nuclear potential energy well. This is accomplished by first using an analytic equation to determine the wave packets in a suitable intermediate asymptotic state where the centripetal barrier is negligible. Then, the split operator technique is used to propagate the wave packets back to their original positions under the full Hamiltonian. Here, the product wave packet is then held stationary while the reactant wave packet is allowed to evolve and explore the nuclear well. Scattering matrix elements are computed from the correlation function between the stationary wave packet and the evolving wave-packet after it has interacted with the nuclear potential. Determination of nucleon-nucleon phase shifts follows directly from computation of the scattering matrix elements. This technique is ideally suited for determining nuclear scattering matrix elements and phase shifts as it provides a high degree of energy resolution with lower computational effort than traditional time independent methods. These advantages will lead to a greater understanding of nuclear reaction dynamics.

To my family

Acknowledgments

As with any success story, there are a number of people working behind the scenes without whom this research would not have been accomplished. I would like to take the time to thank them for all their counsel and support over the past several years.

Several years or so ago when I was considering doing research in the quantum area, I sat down and talked with Dr. Weeks. At first, I was a little leery, as I had not studied quantum in some time. However, through his patience and constant tutelage, I was able to finally make some headway in the quantum area. In retrospect, one could not have asked for a better mentor, advisor, or friend. Thanks.

I should mention a few others. First, there is the weekly STOW crew, Dr. David Darkow and Dr. Vince Schmidt who listened to my frustrations over the years and kept me motivated to stay in the game. Second, there is Captain Louis Duncan, the other half of the “House of Pain.” Our punishment sets at the gym helped keep the stress level manageable. Then, there are my cohorts in crime, Lt Col Anthony Megofna and Lt Col Nick Prins, who helped me get up to speed on all those areas that I was either a little rusty on. I am forever in their debt. I would also like to thank the support from the folks of the MSRC, especially Mr. Rick Roberts who gave me the Marine training course on UNIX/Linux. Without his instruction, I would not have been able to complete the required calculations within a reasonable amount of time. To all of you a sincere thanks.

Finally, I need to thank my wife whose love, support and belief in me gave me the inspiration to come back and finish this research.

It is often said that behind every great man is a great woman. Well certainly, I have the greatest.

Brian S. Davis

Table of Contents

Abstract	iv
Acknowledgments	vi
List of Figures	x
List of Tables	xiii
1. Introduction	1
1.1. Motivation	1
1.2. Overview	5
2. Experimental Background	7
2.1. Electrostatic Accelerators	7
2.2. The Linear Accelerator	10
2.3. The Cyclotron	11
2.4. Production of Polarized Neutron Beams	12
2.5. Experimental S-Matrix Elements	14
3. The AV18 Potential	20
3.1. The AV18 Proton-Proton Model	20
3.1.1. The Proton-Proton EM Potential, $v_{EM}(pp)$	21
3.1.2. The Proton-Proton One Pion Exchange Potential, $v_{\pi}(pp)$	26
3.1.3. The Proton-Proton Short Range Potential $v_R(pp)$	31
3.2. The AV18 Neutron-Proton Model	37
3.2.1. The Neutron-Proton EM Potential, $v_{EM}(pn)$	37
3.2.2. The Neutron-Proton OPEP, $v_{\pi}(pn)$	39
3.2.3. The Neutron-Proton Short Range Potential $v_R(pn)$	39
3.3. The AV18 Neutron-Neutron Mode	40
3.3.1. The Neutron-Neutron EM Potential, $v_{EM}(nn)$	41
3.3.2. The Neutron-Neutron OPEP, $v_{\pi}(nn)$	41
3.3.3. The Neutron-Neutron Short Range Potential, $v_R(nn)$	41
3.4. The Numerov Method	42
4. Channel Packet Method Theoretical Background	48

5.	AV18 CPM Synthesis	55
5.1.	Coordinate System	55
5.2.	The Hamiltonian	57
5.3.	Basis	57
5.4.	Coupled Basis Digitalization	66
5.5.	Energy in the Center of Mass Frame and Lab Frame	68
5.6.	The 1/r Potential.....	69
5.6.1.	Asymptotic Free Motion	71
5.6.2.	The Method of Partial Waves	71
5.6.3.	The Coulomb Potential	74
5.6.4.	The Coulomb Plus Short Range Potential	77
5.7.	Nuclear Units	78
5.8.	S-Matrix Parameterizations	80
5.9.	1-D Sample Calculation – Square Well Potential.....	82
5.9.1.	Analytic Solution	83
5.9.2.	CPM Solution.....	86
5.9.3.	Analytic – Numerical Comparison	97
6.	Presentation of Results.....	100
6.1.	The 1S_0 Potential	100
6.1.1.	Selection of Initial Coordinate and Temporal Step Size.....	104
6.1.2.	Parameter Refinement and Convergence Tests	105
6.1.3.	Absorbing Boundary Conditions	107
6.1.4.	The 1S_0 Phase Shifts.....	109
6.1.5.	The 1S_0 pp Phase Shift Coulombic Correction	111
6.2.	Wave-Packets and the Asymptotic Limit	114
6.3.	An Intermediate State Calculation	119
6.3.1.	The Single Element Case	120
6.3.2.	The 2x2 calculation.....	130
6.3.3.	The Cross Section	142
7.	Conclusion and Recommendations for Future Work.....	145
7.1.	The Three-Body Problem	147
7.2.	Analytic Determination of the Møller State.....	151
	Appendix.....	154
	Bibliography	183
	Vita.....	191

List of Figures

Figure	Page
2.1. Schematic Diagram of Electrostatic Accelerator	9
2.2 Alvarez’s Basic Linac Concept.....	10
2.3. Basic Cyclotron Schematic	11
2.4. First Scattering Parameter – Differential Cross Section	15
2.5. Diagrammatic Representation of the Triple Scattering Parameter	17
2.6. Sample CNS Fit to Experimental 3P_0 Phase Shift Data	18
3.1. Vacuum Polarization Shielding Effect.....	23
3.2. Feynman Diagram of a Pi Meson Exchange.....	26
3.3. Centripetal Potential V_{cent} and Effective Potential V_{eff} Comparison.	45
3.4. ANL and AFIT Numerov 1S_0 Phase Shift Comparison.....	47
5.1 Space Fixed – Center of Mass Coordinates.	56
5.2. Evaluation of the Potential in the <i>LSTJR</i> Basis	64
5.2. Sample AV18 Potentials without Centrifugal Correction	65
5.4. Sample AV18 Potentials with Centrifugal Correction.....	65
5.5. Center of Mass vs Laboratory Frame.....	68
5.6. Impact Parameters and the Range of the Nuclear Force Range.....	73
5.7. Coulombic Phase Corrections at 140 fm, 1000 fm, 10000 fm, and 1m	76
5.8. Mixing Between 3S_1 and 3D_1 States	80
5.9. Square Well Approximation to 1S_0 Potential	83
5.10. 1-D Square Well Scematic Diagram.....	84
5.11. Scaled Wave Packets at t=0 in Coordinate Representation.	87

Figure	Page
5.12. The Coordinate and Momentum Representation Wave Packets.....	89
5.13. Scaled Evolving Wave Packet at $0.122 \tau_v$	92
5.14. Wave Packet Propagation at $0.244 \tau_v$	92
5.15. Wave Packet Propagation at $0.366 \tau_v$	93
5.16. Wave Packet Propagation at $0.977 \tau_v$	93
5.17. Scaled Overlap of equation (5.87) components	95
5.18. Analytic vs Numerical S-Matrix Amplitude.....	98
5.19. Analytic vs Numerical Phase Shift	99
6.1 . The 1S_0 AV18 potentials	101
6.2 . The 1S_0 potentials at cut-off	103
6.3 . Delta r Convergence for Fixed Delta t	106
6.4 . Dissipation of a Wave-Packet by an Absorbing Boundary	108
6.5 . 1S_0 CPM vs ANL neutron-neutron phase shift.....	110
6.6 . 1S_0 CPM vs ANL proton-neutron phase shift.....	110
6.7. 1S_0 CPM vs ANL proton-proton phase shift without correction.....	111
6.8. The Coulombic and Cut-off Corrections to the 1S_0 pp Phase Shift.....	113
6.9. Centrifugal Barrier Potentials for $L=1-3$	114
6.10. Decay of the Barrier Potential at Higher Values of r	115
6.11. 3P_1 pn Phase Shift Calculated at 800 fm	116
6.12. 1D_2 pn Phase Shift Calculated at 1600 fm	117
6.13. 3F_3 pn Phase Shift Calculated at 3200 fm.....	117
6.14. Crude 3F_3 Phase Shift Calculated at 12,800 fm.....	118
6.15. Absolute Value of Dispersed Initial Reactant Wave-Packet	121

Figure	Page
6.16. Initial Positions of the Three Wave-Packets.....	123
6.17. Initial Momentum Values of the Three Wave-Packets.....	123
6.18. Absolute Value of Wave Functions in the Asymptotic Limit.....	125
6.19. Composite CPM Calculation for the 3P_1 pn and 3P_1 pp Phase Shifts	127
6.20. Composite CPM Calculation for the 1D_2 pn and 1D_2 pp Phase Shift	128
6.21. Composite CPM Calculation for the 3F_3 pn and 3F_3 pp Phase Shift	129
6.22. Initial 2x2 Wave-Packet Positions	131
6.23. Evolving Packet Converges on Potential	132
6.24. Reactant Packet Couples to Mixing Channel.....	132
6.25. Mixed Packets Leave Interaction Region On Both Channels.....	133
6.26. Composite CPM Calculation for 3S_1 pn and ϵ_{bar_1} pn Phase Shifts	134
6.27. Composite CPM Calculation for 3D_1 pn phase shift.....	135
6.28. Composite CPM Calculation for the 3P_2 pn Phase Shift	136
6.29. Composite CPM Calculation for the ϵ_{bar_2} pn and the 3F_2 pn Phase Shift.....	137
6.30. Composite CPM Calculation for the 3P_2 pp and the ϵ_{bar_2} pp Phase Shift	138
6.31. Composite CPM Calculation for the 3F_2 pp Phase Shift	139
6.32. Comparison of the CPM 3F_2 Phase Shift to Other Published Results	141
6.33. Total np Scattering Cross Section Compared to the LANL ENDF Data.	143
6.34. Total pp and the Total nn Scattering Cross Sections	144
7.1. Jacobi Coordinates.....	148
7.2. AV18, AV18/IL2, and Experimental Binding Energy	150

List of Tables

Table	Page
1. Photon, Electron, Proton, and Neutron De Broglie Wavelengths.....	8
2. Neutron Beams Properties Produced from Different Productions Methods.....	14
3. Some Scattering Observables with 0,1, 2 and 3 Spin Indices.....	19
4. Constants used by the AV18 code.	25
5. Approximate Meson Masses, Lifetimes (Δt) and Ranges (Δx).....	27
6. $v_R(pp)$ Strong Component Constant Parameters	37
7. $v_R(pn)$ Strong Component Constant Parameters	40
8. $v_R(nn)$ Strong Component Constant Parameters.....	42
9. Selected Atomic Units	79
10. Nuclear Units	80
11. Nuclear Masses	80
12. 1-D Scattering Parameters	91
13. Initial Parameters used for nuclear CPM calculations.....	108
14. 1S_0 Coulombic and Cut-off Correction Parameters	112
15. Projected MSRC and PC Run-Times.....	119
16. Parameters used to calculate the Møller states for each wave-packet	124
17. Parameters Used to Calculate the Phase Shifts from Three Møller States.	126

TIME DEPENDENT CHANNEL PACKET CALCULATION OF TWO NUCLEON SCATTERING MATRIX ELEMENTS

1. Introduction

1.1. *Motivation*

In 1953, Hans Bethe published an article in Scientific American where he discussed the force that holds the nucleus together. In this article, he makes the following comment.

“In the past quarter century physicists have devoted a huge amount of experimentation and mental labor to this problem – probably more man-hours than have been given to any other scientific question in the history of mankind [1].”

Over the 50 years that have passed since Hans Bethe penned this article for Scientific American, not much has changed. Many of the world’s greatest minds are still engaged performing experiments, examining data, and developing models in an attempt to characterize the nuclear strong force that binds nuclei together. Currently, a first principles description of even the two-body nucleon interaction does not exist. Quantum chromodynamics, our closest first principles approach, performs well at high Giga-Electron Volt (GeV) energies but has not been extended to the lower energies for computational reasons [2,3].

In lieu of a first principles approach, the nuclear community has developed phenomenological nucleon – nucleon (NN) models to describe observed features of the strong force. Early attempts to describe the nuclear interaction phenomenologically, such as the one by Gammel and Thaller in 1957, were only able to recreate aspects of the experimental data set. The experimental data set consists primarily of scattering matrix elements derived from observables. Gammel and Thaller’s as well as all subsequent phenomenological model’s are all based on parameterized fits to experimental data [4-31]. Of the more recent models, three in particular, have been able to reproduce almost all of the features of the experimental two-nucleon data set: the high precision models of Nijmegen, Bonn, and Argonne National Labs (ANL) [2, 4, 32, 33].

A numerical technique is required to calculate scattering matrix elements from any modeled potential surface for comparison to experimental data. In order to compute scattering matrix elements, the nuclear community has traditionally relied on techniques based on solutions to the time-independent form of Schrödinger’s equation,

$$\psi'' = k^2\psi \tag{1.1}$$

where k is the wave vector. Indeed with the exception of some time-dependent momentum space calculations performed by Holz and Glöckle [12,34] and a couple of deuteron breakup calculations in the 80s’ [12], almost all nuclear scattering matrix elements have been computed via time independent means. In the time-independent approach, the coordinate or momentum space approximations to the wave function, ψ , provide s-matrix elements at a single energy for a variety of asymptotic quantum numbers. Although many techniques exist to solve a second order linear differential equation such as the Schrödinger equation, the one that is utilized typically by the nuclear

community is the Numerov method. In this approach, a Taylor series expansion of the wave function is used to develop a three-term recurrence relation. From this recurrence relation, scattering matrix elements are then computed by matching boundary conditions where solutions are assumed to be linear combinations of free space solutions.

While the nuclear community has focused primarily on computing scattering matrix elements via time-independent methods, the atomic and molecular community has researched, developed, and implemented time-dependent techniques as an alternative approach for calculating atomic reaction probability. References to time-dependent scattering theory first started to appear in the atomic and molecular literature as early as 1956 [35]. However, it was not until the early 80's that the computing power became available for effective employment of time-dependent algorithms. Since then, these techniques have made significant contributions to our understanding of few-body atomic interactions [36-50].

Time-dependent approaches rely on propagation of wave packets via approximations to the time evolution operator,

$$\hat{U}(t) = e^{-i\hat{H}t/\hbar} \quad (1.2)$$

where \hbar is the reduced Planck's constant (a.k.a. Dirac's constant) and \hat{H} is the Hamiltonian. In contrast to the previously mentioned time-independent methods, which provide s-matrix elements at a single energy for a variety of asymptotic quantum numbers, time dependent methods provide s-matrix elements for a single set of quantum numbers as a function of energy in a single calculation.

One time-dependent method that has been successfully applied to a variety of atomic and molecular problems is called the Channel Packet Method (CPM) [36-40, 52]. The CPM allows for calculation of a single scattering matrix element in contrast to time-independent techniques that compute the entire column of the scattering matrix. Since typically only one scattering matrix element for a range of energies is desired in a nuclear scattering calculation, the CPM is an ideal choice for nuclear scattering calculations.

CPM calculations begin by preparing two complex Gaussian wave packets over a range of energies for which we wish to determine s-matrix elements. One of these contains negative momentum and is designated as the reactant state. The other contains positive momentum and is designated as the product state. These two wave-packets are then typically propagated using the split-operator method first away from the interaction region under the asymptotic Hamiltonian then back to their original positions under the full Hamiltonian. At this point, the two wave-packets are handled differently. The product wave-packet is held stationary whereas its reactant state counterpart is allowed to continue to evolve and probe the characteristics of the nuclear potential. As the reactant wave packet leaves the interaction region, its correlation with the product wave-packet is assessed to determine the scattering matrix elements between the initial and final states.

In this dissertation, the CPM technique is used to compute nucleon-nucleon scattering matrix elements for proton-proton, proton-neutron, and neutron-neutron scattering events. Of course, for this application of the CPM technique to be successful, a complete understanding of the potential energy basis and form of the Hamiltonian is necessary. Since ANL's model has enough supporting documentation to give insight into a natural choice for potential energy basis and Hamiltonian, this research effort uses the

AV18 model to determine two-body nuclear scattering matrix elements. This novel approach to performing nuclear scattering calculations not only provides a significant improvement in computational efficiency over existing time independent techniques, it also provides the nuclear community with intuitive tool for visualizing nuclear reaction dynamics. These characteristics will be invaluable to future scattering research efforts in nucleon-deuteron scattering and muon catalyzed reactions.

1.2. Overview

This research effort examined the suitability of using the time-dependent channel packet method to calculate two nucleon scattering matrix elements. The effort was broken into two phases. Phase 1 evaluated the outputs and failure modes of the AV18 FORTRAN subroutine to gain insight into a suitable choice for the coordinate system, Hamiltonian and basis set. Phase 2 assessed how well the CPM technique could be adapted to the nuclear scattering problem. A FORTRAN CPM code was developed and validated against an analytic solution to a square well problem of similar dimensions as the nuclear well. Scattering matrix elements were then calculated from the AV18 potential surfaces.

The significant research accomplishments presented in this document are:

1. Establishment of new and more efficient, time-dependent nuclear technique, which is ideally suited for determining nuclear scattering matrix elements. (The numerical effort associated with the Time Dependent Channel Packet Method scales as N^2 or better whereas the time-independent methods currently employed by the nuclear community scale as N^3 .)¹ [50]

¹ Here, N refers to the number of grid points in the calculation.

2. Provides the nuclear community with a unique intuitive tool for visualizing scattering dynamics in both momentum and coordinate representations.
3. Provides a complete set of nuclear scattering information for a specified value of angular momentum with a significantly higher degree of energy resolution that is provided by the current time independent methods employed by the nuclear community.

This document is organized as follows. Chapter 2 outlines how scattering matrix elements are obtained from experimental observables. Chapter 3 focuses on the AV18 potential and the time-independent calculation of scattering matrix elements. A brief exploration into the physical basis behind the One Pion Exchange and the strong force parameterization is included. In Chapter 4, the theoretical background behind using the CPM to calculate S-Matrix elements is described. Later in Chapter 5, concerns pertaining to using the CPM technique to calculate scattering matrix elements from the AV18 potential surfaces are addressed. Topics reviewed here include reference frame, basis, Hamiltonian, $1/r$ cutoff correction, units, coupled basis diagonalization and s-matrix parameterizations. Also presented in this section is a comparison between a time-independent and a time dependent solution to a 1-D Square Well problem. Then in Chapter 6, the phase-shifts obtained from the nuclear CPM calculations are presented and compared to ANL's published results. Chapter 7 reviews the technical achievements of this research effort and presents possible avenues for future research. The appendices contain a complete set of CPM nuclear phase shifts through $J = 5$

2. Experimental Background

This chapter provides a heuristic discussion of how S-Matrix elements are calculated from experiment. It opens with a general discussion of why examining nuclear structure requires development of high-energy particle accelerators. The acceleration methods discussed here are limited to the basic theory of charged particle acceleration and the leading techniques of producing high-energy neutron beams. This section then concludes with a discussion of how scattering matrix elements are obtained from scattering high-energy polarized particle beams off target nuclei.

2.1. *Electrostatic Accelerators*

Based on Einstein's 1905 explanation of light's particle like behavior, De Broglie theorized that particles analogously might also exhibit a wave like behavior. His argument was simple. If photons have momentum like particles, should not particles have a wavelength, $\lambda_D = \frac{h}{p}$ similar to photons? His proof came in 1927 when Davisson and Germer observed an angle dependent interference pattern from the scatter of an electron beam off a Ni crystal target. It was learned that in order to obtain information about atomic structure, the De Broglie wavelength (λ_D) must be roughly on the same order or smaller than the dimensions of the target under study. As Table 2.1 indicates, obtaining information about underlying nuclear structure and the short-range nuclear force (range 1-2 *fm*) that binds nucleons together requires development of particle accelerators capable of accelerating particles to *MeV* energies.

Table 2.1. The De Broglie Wavelengths of the Photon, the Electron, the Proton, and the Neutron.

Energy	De Broglie Wavelength, λ_D <i>fm</i>			
	Photon	Electron	Proton	Neutron
0.1 <i>MeV</i>	1.2×10^4	3.7×10^3	9.1×10^2	9.0×10^2
1 <i>MeV</i>	1.2×10^3	8.7×10^2	2.9×10^2	2.9×10^2
10 <i>MeV</i>	1.2×10^2	1.2×10^2	9.0×10^1	9.0×10^1
100 <i>MeV</i>	1.2×10^1	1.2×10^1	2.8×10^1	2.8×10^1

Early accelerators such as the one used by Davisson and Germer to prove De Broglie's theory were quite simple (Figure 2.1). Electrons were accelerated from a grounded heated filament located at the cathode across a gap toward a positive anode. Instead of impinging upon the face of the anode, a small hole in the anode allows the particle beam to pass and interact with an intended target. Electrostatic generators, however, were unreliable and prone to electrostatic breakdown in the *KeV* energy range, well below the *MeV* energy range required to perform nuclear scattering experiments. The inability of electrostatic generators to provide suitable particle beams for nuclear scattering experiments spawned development of two new types of accelerators still used today, the linear accelerator and the cyclotron [53-56].

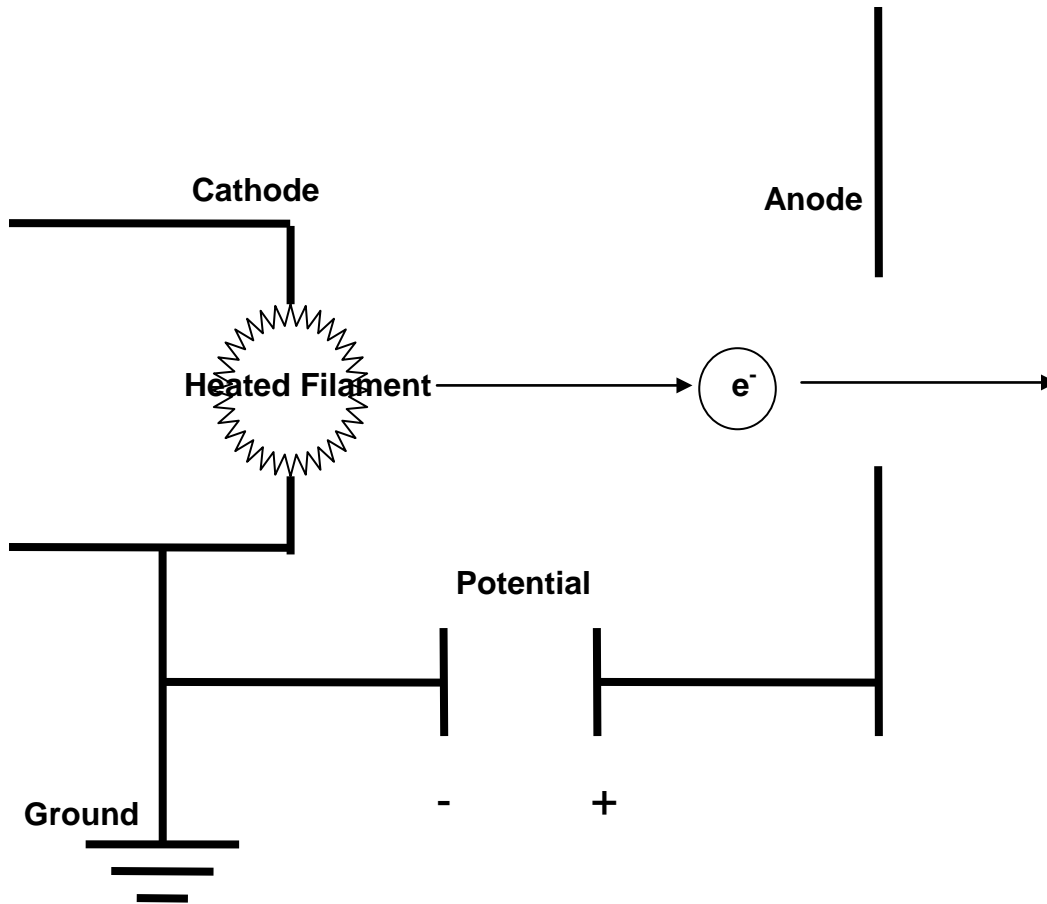


Figure 2.1. Schematic Diagram of Electrostatic Accelerator. A grounded heated filament accelerates electrons across a gap toward a positively charged anode. A gap in the anode allows the electron beam to pass on to an intended target

2.2. The Linear Accelerator

The basic concept of linear particle acceleration was developed by Ising and improved upon by Wideroe, Sloan, Lawrence, and Alvarez [57]. As previously mentioned, electrostatic accelerators have problems exceeding breakdown voltage. The linear accelerator, or linac, overcomes this by accelerating a particle in a series of stages (Figure 2.2).

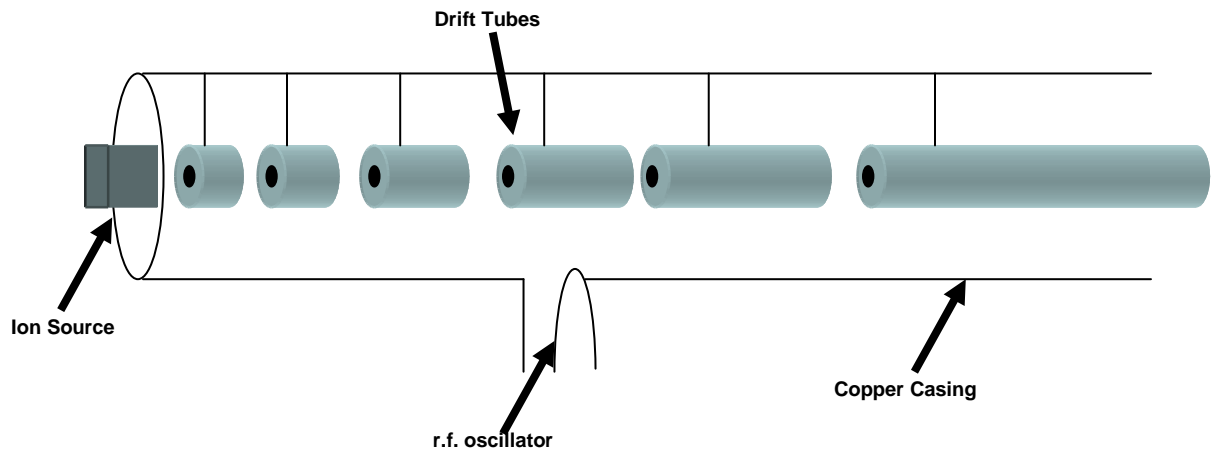


Figure 2.2. Alvarez's Basic Linac Concept. A pulsed waveform is applied to each cylinder (drift tube) to accelerate particles across each gap. The drift tubes also shield the particle beam from decelerating effects. [57]

Here, a charged particle emitted from an ion source passes through a series of hollow cylindrical electrodes called drift tubes. As the particle passes across each gap, it is accelerated by a pulsed waveform applied to each tube from a high power radio frequency oscillator. Each of the drift tubes also functions to shield the particle from a variety of decelerating effects. The beauty of this approach is that higher particle beam

energies can be achieved by simply adding more stages. Electron linacs such as the two-mile Stanford Linear Accelerator Center (SLAC) have been able to achieve electron energies in the 50 GeV range. Proton linacs have been able to achieve a maximum energy of about a GeV [57].

2.3. *The Cyclotron*

Extending the concept of the drift tube, Ernest Lawrence used a magnetic field to reduce the size of the accelerator. His idea was to manufacture a pair of drift tubes in the form of a bisected compressed hollow sphere (Figure 2.3).

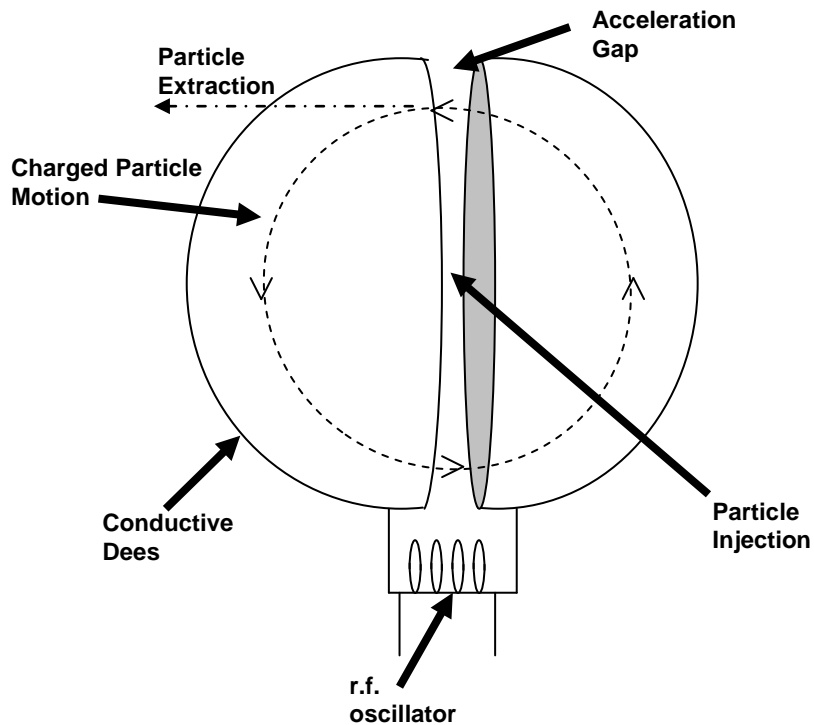


Figure 2.3. Basic Cyclotron Schematic. Particles injected between two strong magnets are forced to follow a circular path and are accelerated by an rf oscillator across the gap between the magnets. [57]

These “dee’s”, as he called them, were placed between two strong magnets which forces the particles to follow a circular path. An RF oscillator matched to the particles exact circulation frequency excites the cyclotron drift tubes and ensures the sign of acceleration is always in the same direction when the particles hit the gap. In this manner, cyclotrons have been able to produce proton beams up to 25 MeV . Above 25 MeV however, relativistic effects become significant. The relativistic mass increase requires more energy to maintain the specified velocity, which results in a drop in revolution frequency and a loss of synchronization with the accelerating potential. The synchrotron maintains synchronization by systematically varying the cyclotron RF frequency and magnetic field. Synchrotrons, such as CERN’s Super Proton Synchrotron have obtained energies in excess of 400 GeV [57].

2.4. Production of Polarized Neutron Beams

Having introduced basic accelerator theory for charged particles, the question remains how to produce a polarized neutron beam given that neutrons do not have charge and cannot be accelerated by any of the traditional means identified in the last section. A reasonable first choice as a source of neutrons is a nuclear reactor since copious free neutron production is a byproduct of the fission process. Reactors however can only produce neutrons with a maximum energy of about 1 MeV , far too low for nucleon-nucleon scattering experiments which typically require neutrons ranging from 1 MeV up to a GeV [57]. This section summarizes two of the leading techniques of producing a polarized neutron beam with a higher kinetic energy than a reactor can generate.

The first method of generating a high-energy neutron beam is through the breakup of polarized deuterons². In this technique, scatter of a polarized deuteron beam off a beryllium target induces dissociation and generates a polarized proton-neutron beam. Passing this beam through magnetic fields generated by spin rotating solenoids and precessing magnets not only strips away the residual charged particles but also provides a method of orienting the neutron beam along the vertical, horizontal, or longitudinal axis³. Since neutron beams generated by deuteron breakup have a high flux ($25 \times 10^5 \frac{n}{s \text{ cm}^2}$), polarization (60 %), and small energy spread (FWHM $\sim 50 \text{ MeV}$), this is considered the preferred method of neutron beam generation [58].

Few particle accelerators, however, are capable of accelerating deuterons, so proton – neutron exchange serves as an alternative method. In this technique, a stream of polarized neutrons is produced by scattering an incident polarized proton beam off a liquid deuterium target. Here, the polarization, flux, and energy spread of the neutrons depend on the scattering angle. If the proton beam has a 180-degree angle of incidence, the resultant neutron beam has optimal energy, intensity and minimal spread, but beam polarization is only $\sim 40\%$. Neutron beam polarizations upwards of 60% can be obtained if the incident proton beam has a 160-degree angle of incidence and a polarization normal to the scattering plane. If polarized neutron beam with energies greater than 800 MeV are

² A polarized deuteron has both the proton and neutron spin components aligned in the same direction.

³ Although the neutron is electrically neutral, it does have a magnetic moment of -1.913 magnetons. (The proton magnetic moment is 2.973 magnetons.) This is one of the leading indicators of underlying nuclear structure.

desired, the polarized proton beam is scattered off a light nuclei target such as Li, Be, B, or C instead of a liquid deuterium target. Scatter of protons beams off these targets can produce a 50%-60% polarized GeV beam with a peak neutron flux of approximately $50 \times 10^5 \frac{n}{s \text{ cm}^2}$. Table 2.2 summaries these methods of producing high-energy neutron beams [58].

Table 2.2. Properties of the Neutron Beams Produced by Different Neutron Beam Productions Methods [58]

Production Method	Liquid Deuterium	Deuteron Breakup	Carbon
Primary Beam Intensity	0.25-5.0 $\mu A (p \uparrow)$	$3 \times 10^{11} (d \uparrow / spill)$	2-10 $\mu A (p \uparrow)$
Neutron Flux $[10^5 n / (s \text{ cm}^2)]$	0.9-5.0	25	10-50
Neutron Energy MeV	180-788	300-1150	200-580
Neutron Polarization [%]	40-60	59	40-50
FWHM Resolution MeV	15-20	40-60	11-50

2.5. Experimental S-Matrix Elements

As we shall see in Section 5, it is rather easy to obtain cross sections or other observables given the S-matrix elements. The converse is not true as it is quite difficult to construct the S-matrix given observable information. Here, an outline of the process by which experimental S-matrix elements are determined from observables is summarized [58].

To determine nucleon-nucleon scattering matrix elements from observables single, double, and triple scattering parameters are required. The measurement of the single scattering parameter is illustrated in Figure 2.4.

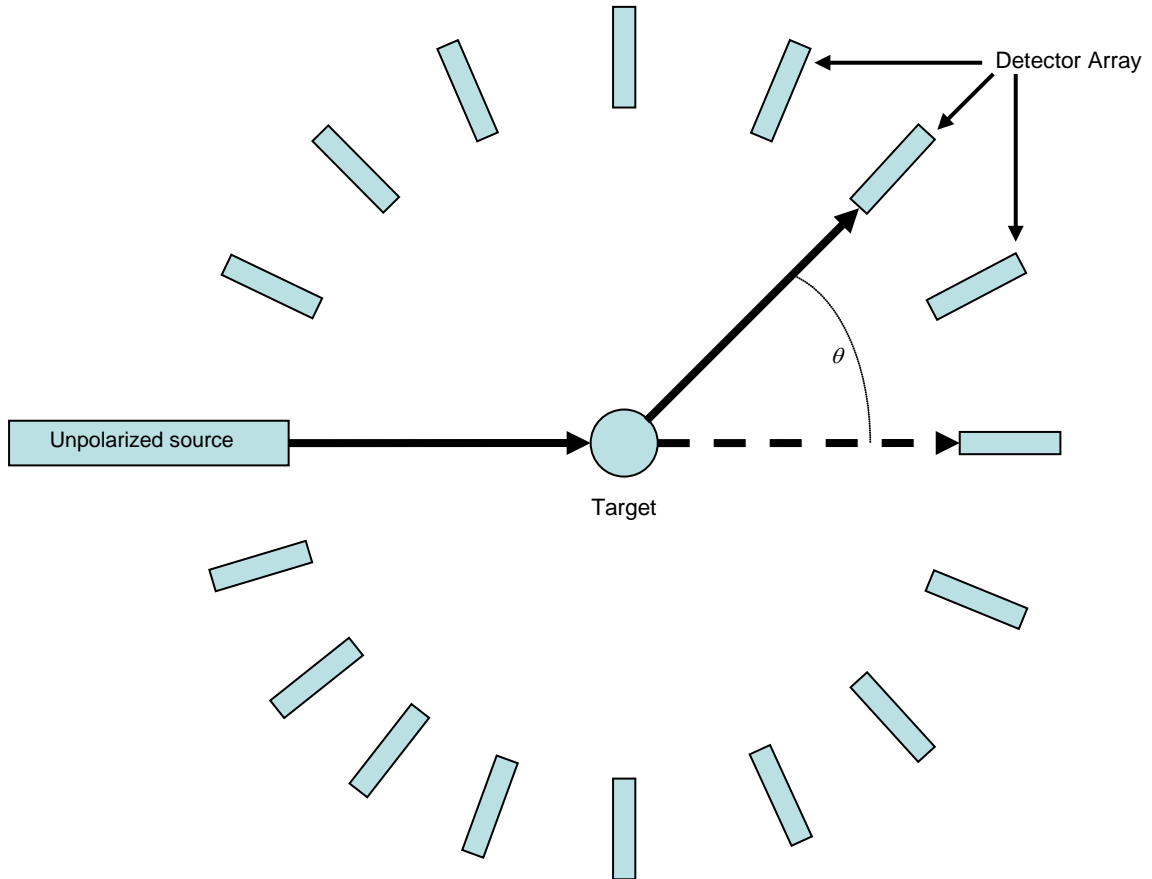


Figure 2.4. First Scattering Parameter – Differential Cross Section. A Circular Detector Array is Positioned Around a Target to Determine the Angular Distribution of Scattered Particles from an Unpolarized source.

Here, an incident unpolarized nucleon beam is scattered by a target located in the center of a nucleon detection ring. Detectors⁴ placed at discrete angles and fixed distance, r , record the scattered beam intensity S_r as a function of angle, θ , and in most cases as a

⁴ Physical limitations on detector size limit the amount of angular resolution.

function of azimuth, ϕ . The number of particles S_r , scattered into a solid angle $d\Omega$ at angle θ divided by the incident flux S_i is defined as the differential cross section $\frac{d\sigma}{d\Omega}$

[30],

$$\frac{d\sigma}{d\Omega} = \frac{S_r}{S_i} r^2 \quad (2.1)$$

In most cases, the first scatter also polarizes the randomly oriented spins of the incident nucleon beam. The amount of polarization of the nucleon beam resulting from the first scatter is the second scattering parameter. The Polarization observable, P , scattered at an angle θ is defined as,

$$P(\theta) = \frac{N_{\uparrow}(\theta) - N_{\downarrow}(\theta)}{N_{\uparrow}(\theta) + N_{\downarrow}(\theta)} \quad (2.2)$$

where N_{\uparrow} is the number of particles with spin up and N_{\downarrow} is the number of particles with spin down. The amount of polarization is scattering angle, energy, and particle dependent.

The triple scattering parameter characterizes how a second scatter alters the polarized beam's direction and magnitude [28]. The orientation of the incident beam polarization with respect to the secondary scattering plane determines the experimental quantity to be measured. For example, the depolarization observable, D , reflects the amount of polarization remaining in the beam perpendicular to the scattering plane after the second scatter. The depolarization triple scattering parameter measurement is represented diagrammatically in Figure 2.5 [28, 31].

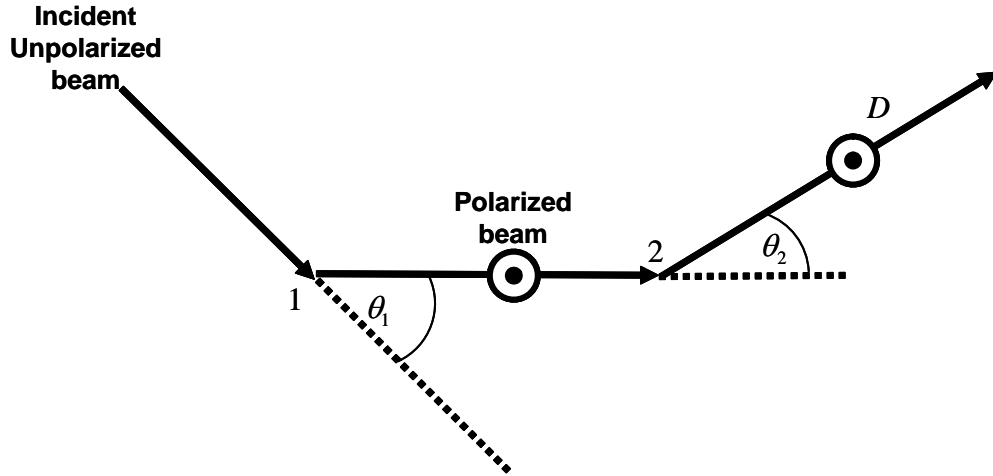


Figure 2.5. Diagrammatic Representation of the Triple Scattering Parameter – Depolarization, D . Angles 1 and 2 denote the first and second scatter. The arrows indicate the direction of beam travel and the circles indicate polarization normal to the page. [28, 31]

The triple scattering parameters (D, A, K, M, N), double scattering parameter (P), and single scattering parameter ($\frac{d\sigma}{d\Omega}$) can be expressed as combinations of five invariant amplitudes⁵ a, b, c, d , and e and the scattering angles from each stage θ_n . Here, A refers to the spin correlation, K refers to the polarization transfer, M refers to the scattered particle polarization, and N refers to the recoil particle polarization. Some of the equations used in the determination of the invariant amplitudes are presented in Table 2.3 [58]. In the table, subscripts on the observables label the polarization of the scattered (s), recoil (r), beam (b), and target (t) particles and the primes on the subscripts distinguish between initial (k), scattered (k'), and recoil (k'') basis. These equations and others

⁵ These five amplitudes are invariant with respect to parity conservation, time reversal invariance, the Pauli principle and isospin invariance [31]. Parity conservation, time reversal invariance and isospin invariance are discussed in Section 3.1.3

available in the literature may be combined to eliminate unknowns and solve for one of the five invariant amplitudes. It is these invariant amplitudes that define the experimental Scattering Matrix, S

$$S(k, k') = \frac{1}{2} [(a+b) + (a-b)(\sigma_1 \cdot \hat{n})(\sigma_2 \cdot \hat{n}) + (c+d)(\sigma_1 \cdot \hat{m})(\sigma_2 \cdot \hat{m}) + (c-d)(\sigma_1 \cdot \hat{l})(\sigma_2 \cdot \hat{l}) + e(\sigma_1 + \sigma_2) \cdot \hat{n}] \quad (2.3)$$

Here, $\sigma_1(\sigma_2)$ refer to the usual Pauli Spin Matrices and the center of mass basis vectors \hat{n} , \hat{m} , and \hat{l} reflect the orientation of scattered and incident particles [58]. Typically, results from nuclear scattering matrix calculations are presented in the form of a phase shift. How phase shifts are calculated from scattering matrix elements is discussed in Section 4. Here, a Center of Nuclear Studies (CNS) fit (solid line) to experimental data (error bars) is shown for the 3P_0 proton neutron scattering matrix element (Figure 2.6).

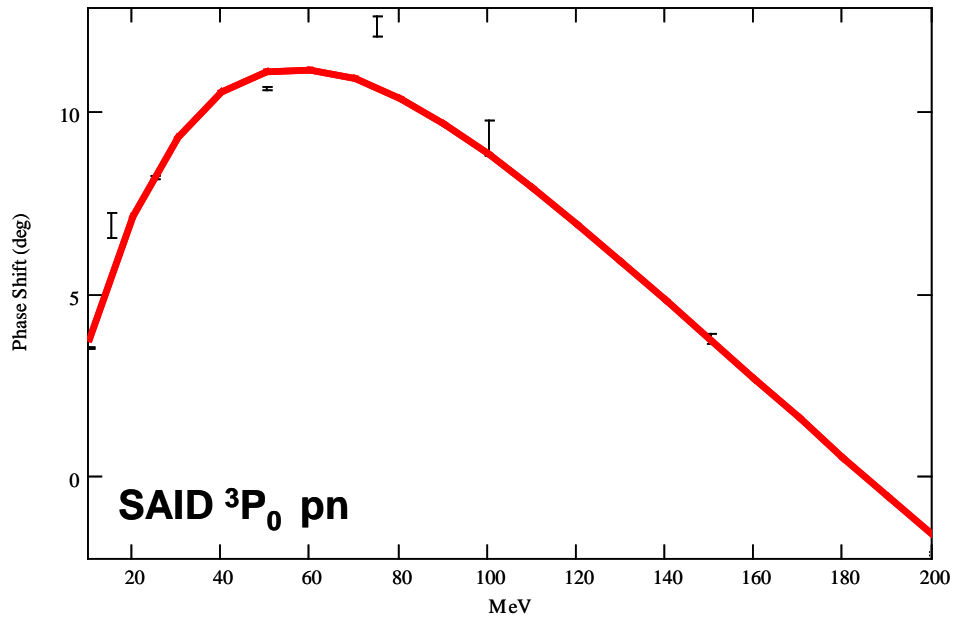


Figure 2.6. Sample CNS Fit to Experimental 3P_0 Phase Shift Data for a Proton-Neutron Scattering Event. The error bars are experimental results. The solid line is a fit to the observed data.

Table 2.3. Some Scattering Observables with 0,1, 2 and 3 Spin Indices. Here θ labels the center of mass scattering angle, θ_1 labels the laboratory angle of the scattered particle, and θ_2 labels the laboratory angle of the recoil particle. Observables may be combined to eliminate unknowns, solve for the invariant amplitudes ($a, b, c, d, \text{ or } e$) and construct the Scattering Matrix, S [58]

Designation	Definition
I	<i>Differential Cross Section</i>
	$\sigma = \frac{1}{2} \left\{ a ^2 + b ^2 + c ^2 + d ^2 + e ^2 \right\}$
P	<i>Polarization</i>
	$\sigma P_{nooo} = \text{Re}(a) \cdot e$
A	<i>Spin Correlation</i>
	$\sigma A_{nono} = \frac{1}{2} \left\{ a ^2 - b ^2 - c ^2 + d ^2 + e ^2 \right\}$
	$\sigma A_{ooss} = \text{Re}(a) \cdot d \cos(\theta) + \text{Re}(b) \cdot c - \text{Im}(d) \cdot e \sin(\theta)$
D	<i>Depolarization tensor</i>
	$\sigma D_{nono} = \frac{1}{2} \left\{ a ^2 + b ^2 - c ^2 - d ^2 + e ^2 \right\}$
	$\sigma D_{s'oso} = \text{Re}(a) \cdot b \cos(\theta - \theta_1) + \text{Re}(c) \cdot d \sin(\theta_1) - \text{Im}(b) \cdot e \cos(\theta - \theta_1)$
K	<i>Polarization Transfer</i>
	$\sigma K_{omno} = \frac{1}{2} \left\{ a ^2 - b ^2 + c ^2 - d ^2 + e ^2 \right\}$
	$\sigma K_{os''so} = -\text{Re}(a) \cdot c \cos(\theta + \theta_2) - \text{Re}(b) \cdot d \sin(\theta_2) + \text{Im}(c) \cdot e \cos(\theta + \theta_2)$
M	<i>Scattered Particle Polarization Contribution</i>
	$\sigma M_{noss} = \text{Re}(d) \cdot e \cos(\theta) + \text{Im}(a) \cdot d \sin(\theta)$
	$\sigma M_{nosk} = -\text{Re}(d) \cdot e \sin(\theta) + \text{Im}(a) \cdot d \cos(\theta) - \text{Im}(b) \cdot c$
N	<i>Recoil Particle Polarization Contribution</i>
	$\sigma N_{os''so} = -\text{Re}(c) \cdot e \cos(\theta + \theta_2) - \text{Im}(a) \cdot c \sin(\theta + \theta_2) - \text{Im}(b) \cdot d \sin(\theta_2)$
	$\sigma N_{os''kn} = \text{Re}(c) \cdot e \sin(\theta + \theta_2) - \text{Im}(a) \cdot c \cos(\theta + \theta_2) + \text{Im}(b) \cdot d \cos(\theta_2)$

3. The AV18 Potential

The Argonne National Labs (ANL) Theoretical Physics Division has been constructing nucleon-nucleon models for over three decades. ANL's latest eighteen operator model, known as the AV18, has been able to accurately describe the binding energy of light nuclei through the atomic number $A=12$ and faithfully reproduce the experimental phase shifts associated with nucleon-nucleon scattering. Embedded within the AV18 are actually three phenomenological models, one for each possible two-body interaction, pp , pn , and nn . Each of these models contains an electromagnetic (v_{EM}), one-pion exchange (v_{π}) and intermediate short-range (v_R) component [4]

$$\begin{aligned}v(pp) &= v_{EM}(pp) + v_{\pi}(pp) + v_R(pp) \\v(np) &= v_{EM}(pn) + v_{\pi}(pn) + v_R(pn) \\v(nn) &= v_{EM}(nn) + v_{\pi}(nn) + v_R(nn)\end{aligned}\tag{3.1}$$

The sum of the later two components of each model, v_{π} and v_R , constitutes the strong force contribution. The proton-proton model, proton-neutron model, and neutron-neutron model are summarized in Section 3.1, Section 3.2, and Section 3.3 respectively.

3.1. The AV18 Proton-Proton Model

The most complicated model within the AV18 is the pp as it deals with the interaction of two charged particles. Therefore, a majority of chapter 3 will deal with the development of this model. This chapter has three sub-sections, one for

$v_{EM}(pp)$, $v_{\pi}(pp)$, and $v_R(pp)$.

3.1.1. The Proton-Proton EM Potential, $v_{EM}(pp)$

The form of the electromagnetic portion of the potential utilized by the AV18 has the general structure,

$$v_{EM}(pp) = v_{C1}(pp) + v_{C2}(pp) + v_{DF}(pp) + v_{VP}(pp) + v_{MM}(pp) \quad (3.2)$$

where v_{C1} labels the one-photon exchange, v_{C2} labels the two-photon exchange, v_{DF} labels the Darwin-Foldy term, v_{VP} labels the vacuum polarization, and v_{MM} labels the magnetic moment contributions.

The Coulombic interaction is governed by the exchange of virtual photons, one for each charged particle involved in the interaction. Hence, a scattering event involving a single proton would undergo an exchange of a single virtual photon, v_{C1} , and a two proton event would undergo an exchange of two virtual photons, v_{C2} . The one and two photon exchange components for pp scattering are represented;

$$v_{C1}(pp) = \alpha' \frac{F_C^{pp}(r)}{r} \quad (3.3)$$

$$v_{C2}(pp) = \frac{-\alpha\alpha'}{2M_p^2} \left[\frac{F_C^{pp}(r)}{r} \right]^2 \quad (3.4)$$

where

$$\alpha' = \frac{k\alpha}{M_p v_{lab}} \quad (3.5)$$

includes an explicit energy dependence. Here, r is the separation between the nucleons, M_p is the mass of the proton, and α is the fine structure constant [4], a dimensionless fundamental physical quantity that characterizes the strength of the electromagnetic

interaction between the electron and the photon. The F function, $F_C^{pp}(x)$ first proposed by Auerbach [43] reflects the finite size of the nucleon charge distribution and compensates for the $\frac{1}{r}$ singularity in v_{EM} as r approaches zero [4]. It has functional form,

$$F_C^{pp}(x) = 1 - \left(1 + \frac{11}{16}x + \frac{3}{16}x^2 + \frac{1}{48}x^3 \right) e^{(-x)} \quad (3.6)$$

with $x = br$ and b referring to the exponential cutoff parameter 4.27 fm^{-1} . Auerbach F functions appear in all AV18 electro-magnetic components.

From special relativity, it is known that as a particle's velocity approaches the speed of light, the mass of the particle increases. Since the domain of the AV18 extends up to the pion production threshold of 350 MeV , (approximately 37 percent of a proton's rest mass) relativistic effects cannot be ignored. The Darwin-Foldy term,

$$v_{DF}(pp) = -\frac{\alpha}{4M_p^2} F_\delta(x), \quad (3.7)$$

is included to compensate for the relativistic effects of a finite sized charged spin $\frac{1}{2}$ particle interacting with an electromagnetic field. Here, M_p refers to the mass of the proton in MeV and $F_\delta(x)$ refers to another one of Auerbach's F functions,

$$F_\delta(x) = b^3 \left(\frac{1}{16} + \frac{1}{16}x + \frac{1}{48}x^2 \right) e^{(-x)}. \quad (3.8).$$

The vacuum polarization term (v_{VP}),

$$v_{VP}(pp) = \frac{2\alpha\alpha'}{3\pi} \frac{F_C^{pp}(r)}{r} \int_1^\infty e^{(-2m_e r x)} \left[1 + \frac{1}{2x^2} \right] \frac{(x^2 - 1)^{1/2}}{x^2} dx, \quad (3.9)$$

is a quantum correction to classical electrodynamics. As shown in Figure 3.1, virtual charged particle pairs form around the positively charged proton, which reduces the protons effective charge.

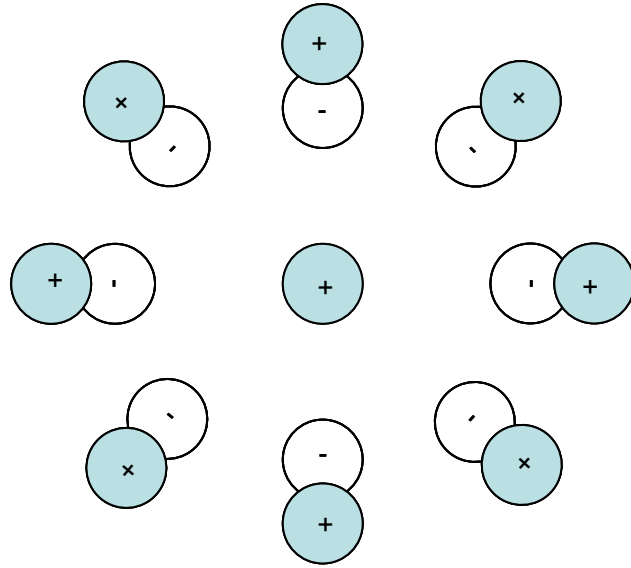


Figure 3.1. Vacuum Polarization Shielding Effect. Virtual charged particle pairs form around a proton in a vacuum. The formation of the virtual charged particle pairs reduces the protons effective charge.

The effective charge increases as distance to the charged particle decreases [59]. The vacuum polarization term is required to fit low energy scattering data [4]. Contributions from $v_{VP}(pp)$ cease to be important above about 30 MeV [27]. In the above equation for the vacuum polarization contribution, m_e is the mass of the electron in MeV and $F_C^{pp}(r)$ is the same F function used for v_{C1} back in the one photon exchange term.

The last term of equation (3.2) is the particles magnetic moment, $v_{MM}(pp)$. For the proton-proton interaction, the magnetic moment contribution takes the form,

$$v_{MM}(pp) = -\frac{\alpha}{4M_p^2} \mu_p^2 \left[\frac{2}{3} F_\delta(r) \vec{\sigma}_1 \cdot \vec{\sigma}_2 + \frac{F_T(r)}{r^3} S_{12} \right] - \frac{\alpha}{2M_p^2} (4\mu_p - 1) \frac{F_{LS}(r)}{r^3} \vec{L} \cdot \vec{S} \quad (3.10)$$

where μ labels the magnetic moment, $\vec{\sigma}_1 \cdot \vec{\sigma}_2$ labels the dot product of the Pauli spin matrices of the two protons, and $\vec{L} \cdot \vec{S}$ labels the dot product of the total orbital angular momentum and total spin angular momentum. In addition to $F_\delta(x)$ already introduced, this expression also contains two more of Auerbach's F functions,

$$\begin{aligned} F_T(x) &= 1 - \left(1 + x + \frac{1}{2}x^2 + \frac{1}{6}x^3 + \frac{1}{24}x^4 + \frac{1}{144}x^5 \right) \exp(-x) \\ F_{LS}(x) &= 1 - \left(1 + x + \frac{1}{2}x^2 + \frac{7}{48}x^3 + \frac{1}{48}x^4 \right) \exp(-x) \end{aligned} \quad (3.11)$$

and the tensor force, S_{12} .

$$S_{12} = 3(\sigma_1 \cdot \hat{r})(\sigma_2 \cdot \hat{r}) - \sigma_1 \cdot \sigma_2 \quad (3.12)$$

The tensor force term, S_{12} , stems from the slight asymmetry associated with the observed nature of the deuteron wave function. If the deuteron were comprised of merely two point particles, then the potential would be entirely symmetric (pure S state) and be completely described by spherical harmonics. This is not however, what is observed. The interacting bodies in a nucleon collision are not actually the nucleons but the constituents of the nucleons, the quarks. Protons contain two up and one down quark whereas neutrons contain two down and one up quark. It is the interaction between the quarks that gives rise to the slight 4 percent D state component of the deuteron wave function. [53]. A list of all AV18 constants is provided in Table 3.1.

Table 3.1. Constants used by the AV18 code.

AV 18 Constants	
$\hbar c$ (MeV fm)	197.32705
m_{π_0} (MeV/c ²)	134.9739
$m_{\pi_{\pm}}$ (MeV/c ²)	139.5675
M_p (MeV/c ²)	938.27231
M_n (MeV/c ²)	939.56563
α^{-1}	137.03599
μ_p	2.79285
μ_n	-1.91304
f^2	0.075
b (fm ⁻¹)	4.27
r_0 (fm)	0.5
a (fm)	0.2
c_{π} (fm ⁻²)	2.1

3.1.2. The Proton-Proton One Pion Exchange Potential, $v_{\pi}(pp)$

In quantum electrodynamics, the force between two particles can be described as being mediated by the exchange of virtual photons. Photons have no rest mass so the range of the electromagnetic interaction is infinite. It was Yukawa [26] that first suggested that the concept of virtual exchange could be extended to describe the strong force between two nucleons. In his theory, he proposed that since the strong force has a finite range, it could be described as being mediated by the exchange of virtual particles of non-zero mass called mesons [9, 60]. This simple extension of quantum electrodynamics is depicted as a Feynman diagram in Figure 3.2.

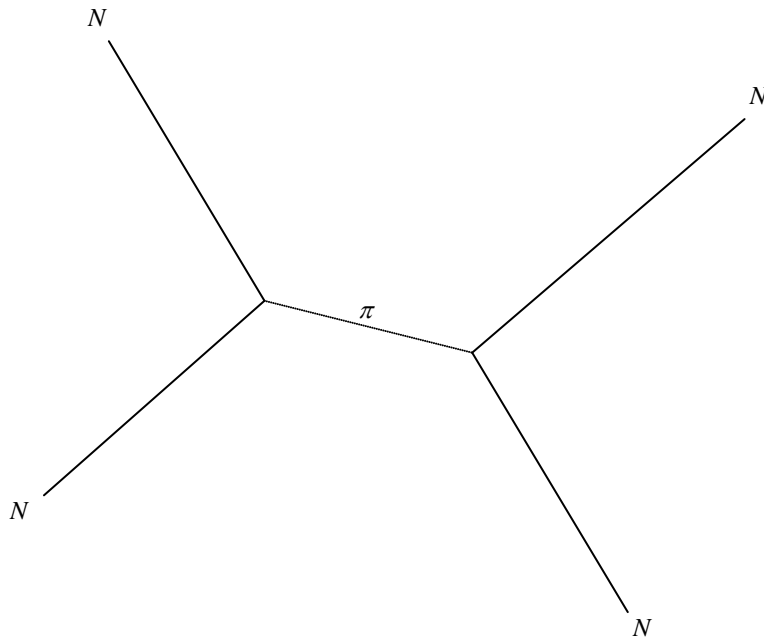


Figure 3.2. Feynman Diagram of a Pi Meson Exchange between Two Arbitrary Nucleons [9]

Here, a single meson π mediates the interaction between two arbitrary nucleons labeled by N . Since the virtual intermediate state shown here is at an energy $m_\pi c^2$ higher than the initial or final states, the Heisenberg uncertainty principle,

$$\Delta t \approx \frac{\hbar}{mc^2} \quad (3.13)$$

places a limit on how long the intermediate meson state may exist. This length of time depends inversely on the mass of the particle. Since a particle cannot travel farther than c times this lifetime, Δt , a limit is established on the range of the force component the particle can carry. Some calculated meson lifetimes (Δt) and force component ranges (Δx) based on the Standard Model of Fundamental Particles and Interactions are listed in Table 3.2.

Table 3.2 Approximate Meson Masses, Lifetimes (Δt) and Ranges (Δx) Calculated from the Standard Model of Fundamental Particles

Name	Mass (MeV)	Δt (s)	Δx (fm)
Pion	140	$4.70 \cdot 10^{-24}$	1.41
Kaon	494	$1.33 \cdot 10^{-24}$	0.40
Rho	770	$8.54 \cdot 10^{-25}$	0.26
D+	1869	$3.51 \cdot 10^{-25}$	0.11
Eta-c	2979	$2.2 \cdot 10^{-25}$	0.07

As shown in the table, the lightest meson, the pion, has a range roughly equivalent to the observed 1-2 femtometer range of the strong force. This is a reason why the strong force can be viewed as an exchange of virtual pions. In the laboratory, positive (π_+), negative (π_-), and neutral (π_0) pions have been observed. The negative pion (π_-)

is the anti-particle for the positive pion (π_+) and both have an approximate rest mass of 140 MeV . On the other hand, the neutral pion (π_0) has a slightly lower rest mass of 135 MeV and is its own anti-particle [60].

The charge independent Hamiltonian based on the exchange of virtual pions between two nucleons can be expressed as [9],

$$H' = f \mu^{-1} \sum_{i=1}^2 \int dr \delta(r - r_i) \vec{\tau}_i \cdot (\sigma_i \cdot \nabla \vec{\phi}(r)). \quad (3.14)$$

where $\vec{\phi}$ is a three component vector in isospin space which represents the three different pions,

$$\begin{aligned} |\pi_+\rangle &= |I=1, I_z = +1\rangle = \begin{pmatrix} 1 \\ 0 \\ 0 \end{pmatrix} \\ |\pi_0\rangle &= |I=1, I_z = 0\rangle = \begin{pmatrix} 0 \\ 1 \\ 0 \end{pmatrix} \\ |\pi_-\rangle &= |I=1, I_z = -1\rangle = \begin{pmatrix} 0 \\ 0 \\ 1 \end{pmatrix} \end{aligned} \quad (3.15)$$

r_i labels the location of the i^{th} nucleon, f labels an arbitrary coupling constant, σ_i labels the Pauli spin matrices, $\vec{\tau}_i$ labels the isospin matrices and μ labels the inverse scattering length/cutoff parameter,

$$\mu = \frac{mc}{h} \quad (3.16)$$

The isospin quantum number, τ , enables us to treat the proton and neutron as a different state of the same particle, the nucleon [7]. Possible values for the isospin

projection, τ_{nz} , in the uncoupled basis are $-\frac{1}{2}$ and $\frac{1}{2}$, with the neutron designated as $-\frac{1}{2}$ and the proton as $+\frac{1}{2}$. In the coupled basis, the total isospin T reflects the total isospin of the interaction pair analogous to the total spin quantum, S , either 0 or 1. In the triplet state, $T=1$, three possible combinations exist,

$$\begin{aligned} |\uparrow\uparrow\rangle &= |1\rangle \\ \frac{1}{\sqrt{2}}|\uparrow\downarrow\rangle + |\downarrow\uparrow\rangle &= |0\rangle \\ |\downarrow\downarrow\rangle &= |-1\rangle \end{aligned} \quad (3.17)$$

Here, a projection of $+1$ indicates a proton pair, -1 a neutron pair, and 0 a linear combination of proton and a neutron. The singlet state is also a linear combination of protons and neutrons,

$$\frac{1}{\sqrt{2}}|\uparrow\downarrow\rangle - |\downarrow\uparrow\rangle = |0\rangle \quad (3.18)$$

Since we are dealing with relativistic energies and spin 0 pions, the relativistic Klein-Gordon equation,

$$(\square^2 + \mu^2)\Psi = \text{source terms} \quad (3.19)$$

is used to construct the wave function. Taking the static limit, removes the time-dependence from the d'Alembertian such that,

$$\square^2 = -\nabla^2 \quad (3.20)$$

and we are left with,

$$(\nabla^2 - \mu^2)\vec{\phi}(r) = f\mu^{-1}\sum_{i=1}^2 \vec{\tau}_i (\sigma_i \cdot \nabla_i) \delta(r - r_i). \quad (3.21)$$

From equation(3.21), the pion field generated by nucleon 2 is determined to be,

$$\vec{\phi}(r) = -\frac{f}{4\pi\mu} \vec{\tau}_2 (\sigma_2 \cdot \nabla_2) \frac{e^{-\mu|r-r_2|}}{|r-r_2|}, \quad (3.22)$$

An assessment of the interaction energy of nucleon 1 with this pion field is obtained via substitution into the interaction Hamiltonian from equation (3.14),

$$H' = -\frac{f^2}{4\pi\mu^2} (\vec{\tau}_1 \cdot \vec{\tau}_2) (\sigma_1 \cdot \nabla_1) (\sigma_2 \cdot \nabla_2) \frac{e^{-\mu|r_1-r_2|}}{|r_1-r_2|} \quad (3.23)$$

Eisenberg [9] has reduced this equation by performing the specified derivatives to find,

$$v_\pi = \frac{1}{3} m_\pi c^2 \left(\frac{f^2}{4\pi\hbar c} \right) (\vec{\tau}_1 \cdot \vec{\tau}_2) \left\{ \sigma_1 \cdot \sigma_2 + S_{12} \left[1 + \frac{3}{\mu r} + \frac{3}{(\mu r)^2} \right] \right\} \frac{e^{-\mu r}}{\mu r} \quad (3.24)$$

$$v_\pi = \frac{1}{3} m_\pi c^2 \left(\frac{f^2}{4\pi\hbar c} \right) (\vec{\tau}_1 \cdot \vec{\tau}_2) \{ \sigma_1 \cdot \sigma_2 Y(r) + S_{12} T(r) Y(r) \} \quad (3.25)$$

where $T(r)$ and $Y(r)$ label the tensor and Yukawa terms in equation (3.24). As indicated by the isospin coupling term, $(\vec{\tau}_1 \cdot \vec{\tau}_2)$, a slightly different solution exists for each possible interaction combination (nn , pn , or pp).

The inclusion of a pion mass ratio $\frac{m_{\pi_0}}{m_s}$ and an exponential cutoff function,

$1 - \exp(-c_\pi r^2)$ are the only differences between the Eisenberg solution above and the documented form of the AV18 One Pion Exchange Potential [4],

$$v_\pi(pp) = \frac{1}{3} m_{\pi_0} c^2 \frac{f^2}{4\pi\hbar c} \left(\frac{m_{\pi_0}}{m_s} \right)^2 (\vec{\tau}_1 \cdot \vec{\tau}_2) \left[\sigma_1 \cdot \sigma_2 Y(r) (1 - \exp(-c_\pi r^2)) + S_{12} T(r) (1 - \exp(-c_\pi r^2))^2 \right] \quad (3.26)$$

The scaling mass, m_s non-dimensionalizes the coupling constant, $\frac{f^2}{4\pi\hbar c}$ and has an

experimentally determined value of 0.075 [4]. The exponential cutoff function,

$$1 - \exp(-c_\pi r^2) \quad (3.27)$$

ensures both the Yukawa ($Y_\mu(r)$) and Tensor ($T_\mu(r)$) components of the one pion exchange potential terminate smoothly as $r \rightarrow 0$ [4]. In the AV18, the cutoff parameter c_π is set at 2.1 fm^{-2} [4].

3.1.3. The Proton-Proton Short Range Potential $v_R(pp)$

Data obtained from low energy scattering events not only provides insight into the nuclear potential's physical characteristics but also aids in the development of a realistic parameterizations of v_R . Observations have shown that any constructed short-range nuclear potential must: decay rapidly around $1-2 \text{ fm}$, be strongly repulsive at distances less than 0.5 fm , be strongly attractive between 0.5 fm and 2 fm , have a depth on the order of 40 MeV , and depend on the each nucleon's intrinsic spin/isospin. With these ideas in mind, we begin our discussion of the theory behind phenomenological potentials [61].

Since any nucleon can be labeled by its position \vec{r} , momentum \vec{p} , spin $\vec{\sigma}$, and isospin $\vec{\tau}$, any realistic parameterization of the two nucleon nuclear potential must begin with the general functional form,

$$v(\vec{r}_1, \vec{r}_2, \vec{p}_1, \vec{p}_2, \vec{\sigma}_1, \vec{\sigma}_2, \vec{\tau}_1, \vec{\tau}_2) \quad (3.28)$$

Eisenbud/Wigner and later Okubo/Marshak proposed that this general form could be restricted since any potential should adhere to several invariance requirements [28, 61]:

1. Translational Invariance - The concept of translational invariance simply means that the potential should depend only on the relative separation between the two nucleons, $r = r_1 - r_2$, not where the two nucleons are in space.

The system is closed and no external forces act on the system other than those between the two particles so total linear momentum is conserved, $F = \frac{dp}{dt} = 0$.

2. Rotational Invariance - The potential should be constructed such that it is invariant under proper rotation. Since the system is again closed, there are no external torques acting in the system, $\tau = \frac{dL}{dt} = 0$ and the total angular momentum $L = r \times p$ is conserved.
3. Galilean Invariance – The concept of Galilean invariance implies that the potential should depend only on the relative momentum between the two nucleons, $p = p_1 - p_2$ and be independent of inertial reference frames. A change of coordinates involving a constant velocity does should not influence the potential. The same laws of physics apply to all inertial reference frames.
4. The potential should be Hermitian. This means that any potential matrix should be diagonalizable by a unitary transformations and that all the eigenvalues along the diagonal should be real (observable).

For the moment, we limit the discussion to \vec{r} , \vec{p} , $\vec{\sigma}_1$, and $\vec{\sigma}_2$.

Given the above invariance requirements, the functional form of the nucleon-nucleon potential can be restricted to [9],

$$v(\vec{r}, \vec{p}, \vec{\sigma}_1, \vec{\sigma}_2), \quad (3.29)$$

In addition to the four vectors \vec{r} , \vec{p} , $\vec{\sigma}_1$, and $\vec{\sigma}_2$, six other vectors may be constructed,

$$\vec{\sigma}_1 \times \vec{\sigma}_2, \quad \vec{\sigma}_1 \times \vec{r}, \quad \vec{\sigma}_1 \times \vec{p}, \quad \vec{\sigma}_2 \times \vec{r}, \quad \vec{\sigma}_2 \times \vec{p}, \quad \vec{r} \times \vec{p}. \quad (3.30)$$

Note that we do not need to consider other combinations of vectors or terms containing more than one σ_1 and/or σ_2 since the identities,

$$\begin{aligned}\vec{A} \times (\vec{B} \times \vec{C}) &= \vec{B}(\vec{A} \cdot \vec{C}) - \vec{C}(\vec{A} \cdot \vec{B}) \\ (\vec{A} \times \vec{B}) \cdot (\vec{C} \times \vec{D}) &= (\vec{A} \cdot \vec{C})(\vec{B} \cdot \vec{D}) - (\vec{A} \cdot \vec{D})(\vec{B} \cdot \vec{C})\end{aligned}\tag{3.31}$$

and the Pauli matrices property,

$$(\vec{\sigma}_1 \cdot \vec{A})(\vec{\sigma}_2 \cdot \vec{B}) = \vec{A} \cdot \vec{B} + i\vec{\sigma}_1 \cdot (\vec{A} \times \vec{B})\tag{3.32}$$

can be used to reduce them back to a lower form.

From these six vectors and \vec{r} , \vec{p} , $\vec{\sigma}_1$, and $\vec{\sigma}_2$, the following scalar combinations are possible for the nucleon-nucleon interaction [9]:

$$\begin{aligned}\vec{r} \cdot \vec{r} = r^2, \quad \vec{\sigma}_1 \cdot \vec{\sigma}_2, \quad \vec{\sigma}_1 \cdot \vec{r}, \quad \vec{\sigma}_2 \cdot \vec{r}, \quad \vec{\sigma}_1 \cdot \vec{p}, \quad \vec{\sigma}_2 \cdot \vec{p}, \quad \vec{r} \cdot \vec{p}, \\ \vec{r} \cdot (\sigma_1 \times \sigma_2), \quad \vec{p} \cdot (\sigma_1 \times \sigma_2), \quad \vec{\sigma}_1 \cdot (\vec{r} \times \vec{p}), \quad \vec{\sigma}_2 \cdot (\vec{r} \times \vec{p}), \\ (\vec{\sigma}_1 \cdot \vec{\sigma}_2)(\vec{r} \cdot \vec{p}), \quad (\vec{\sigma}_1 \cdot \vec{r})(\vec{\sigma}_2 \cdot \vec{r}), \quad (\vec{\sigma}_1 \cdot \vec{r})(\vec{\sigma}_2 \cdot \vec{p}), \quad (\vec{\sigma}_1 \cdot \vec{p})(\vec{\sigma}_2 \cdot \vec{r}) \\ (\vec{\sigma}_1 \cdot \vec{r})(\vec{r} \cdot \vec{p}), \quad (\vec{\sigma}_2 \cdot \vec{r})(\vec{r} \cdot \vec{p}), \quad (\vec{r} \cdot \vec{p})\vec{r} \cdot (\sigma_1 \times \sigma_2), \quad (\vec{r} \cdot \vec{p})(\vec{\sigma}_1 \cdot \vec{r})(\vec{\sigma}_2 \cdot \vec{r})\end{aligned}\tag{3.33}$$

As we are merely trying to garner an understanding of how nucleon-nucleon potentials are developed, we have limited this discussion to 1st order terms in momentum. In practice, higher order terms in momentum are often included in potentials like the AV18.

To these first four requirements, four more are typically added [9]:

5. The potential must commute with $(\vec{\tau}_1 + \vec{\tau}_2)$, which implies charge must be conserved. This requirement allows for five possible operators in isospin space,

$$1, \quad \tau_1 \cdot \tau_2, \quad \tau_1 + \tau_2, \quad \tau_1 - \tau_2, \quad \tau_1 \times \tau_2\tag{3.34}$$

In addition to charge conservation, charge independence is also typically imposed so that only the scalars, 1 and $\vec{\tau}_1 \cdot \vec{\tau}_2$, which are invariant under rotation in isospin space may appear in the nuclear potential [9].

6. Parity Invariance - The potential should be independent of reflection so only even powers of position and momentum may appear together in the potential expansion [62],

$$v(r, p, \sigma_1, \sigma_2, \tau_1, \tau_2) = v(-r, -p, \sigma_1, \sigma_2, \tau_1, \tau_2) \quad (3.35)$$

Of the scalars mentioned in (3.33) only

$$\begin{aligned} &1, \quad \vec{\sigma}_1 \cdot \vec{\sigma}_2, \quad \vec{r} \cdot \vec{p}, \\ &\vec{\sigma}_1 \cdot (\vec{r} \times \vec{p}), \quad \vec{\sigma}_2 \cdot (\vec{r} \times \vec{p}), \\ &(\vec{\sigma}_1 \cdot \vec{\sigma}_2)(\vec{r} \cdot \vec{p}), \quad (\vec{\sigma}_1 \cdot \vec{r})(\vec{\sigma}_2 \cdot \vec{r}), \\ &(\vec{\sigma}_1 \cdot \vec{r})(\vec{\sigma}_2 \cdot \vec{p}), \quad (\vec{\sigma}_1 \cdot \vec{p})(\vec{\sigma}_2 \cdot \vec{r}), \\ &(\vec{r} \cdot \vec{p})(\vec{\sigma}_1 \cdot \vec{r})(\vec{\sigma}_2 \cdot \vec{r}) \end{aligned} \quad (3.36)$$

are invariant under parity inversion in addition to the isospin scalars 1 and $\vec{\tau}_1 \cdot \vec{\tau}_2$.

7. Time Reversal Invariance - The potential should be invariant under time reversal operations which implies that spins and momentum can only couple only in even number combinations [62],

$$v(r, p, \sigma_1, \sigma_2, \tau_1, \tau_2) = v(r, -p, -\sigma_1, -\sigma_2, \tau_1, \tau_2) \quad (3.37)$$

Time reversal invariance then further restricts the allowable scalars from

(3.36) to

$$\begin{aligned} &1, \quad \vec{\sigma}_1 \cdot \vec{\sigma}_2, \quad (\vec{\sigma}_1 \cdot \vec{r})(\vec{\sigma}_2 \cdot \vec{r}) \\ &\vec{\sigma}_1 \cdot (\vec{r} \times \vec{p}), \quad \vec{\sigma}_2 \cdot (\vec{r} \times \vec{p}), \end{aligned} \quad (3.38)$$

Since the interaction always involves both particles, the last two terms of (3.38) can be expressed as the linear combination⁶ $(\vec{\sigma}_1 + \vec{\sigma}_2)(\vec{r} \times \vec{p})$. Typically this linear combination is written as $\vec{L} \cdot \vec{S}$ given the definitions for total orbital angular momentum, \vec{L} , and total spin, \vec{S} ,

$$\begin{aligned}\vec{L} &= \vec{r} \times \vec{p} \\ \vec{S} &= \vec{\sigma}_1 + \vec{\sigma}_2\end{aligned}\tag{3.39}$$

Protons and neutrons do not change their identity under time reversal so the isospin scalars 1 and $\vec{\tau}_1 \cdot \vec{\tau}_2$ remain.

Gammel and Thaler in 1957 utilized combinations of these scalars to create the first nucleon-nucleon phenomenological model [28],

$$v_{Gammel} = v_{central}(r) + v_{Tensor}(r)S_{12} + v_{LS}(r)L \cdot S.\tag{3.40}$$

by expressing $v_{central}(r)$, $v_{Tensor}(r)$ and $v_{LS}(r)$ in the Yukawa form $v(r) = \frac{e^{-r}}{r}$ and by

expressing the tensor force S_{12} (Section 3.1.1) as a combination of the scalars

$S_{12} = 3(\sigma_1 \cdot \hat{r})(\sigma_2 \cdot \hat{r}) - \sigma_1 \cdot \sigma_2$. Although the Gammel and Thaler model was unable to reproduce all observed nn and pp scattering data, it did serve as a basis for further short-range model development.

The AV18 short-range expression for v_R given by

$$v_R(pp) = v_{central}^{S,T}(r) + v_{L^2}^{S,T}(r)L^2 + v_{Tensor}^{S,T}(r)S_{12} + v_{L \cdot S}^{S,T}(r)L \cdot S + v_{(L \cdot S)^2}^{S,T}(r)(L \cdot S)^2\tag{3.41}$$

⁶ The linear combination $(\vec{\sigma}_1 - \vec{\sigma}_2)(\vec{r} \times \vec{p})$ vanishes, as it is odd under interchange of particle labels [21].

includes second order terms in momentum $(L \cdot S)^2$ and L^2 . Each of the five functions in equation (3.41) can be expressed as,

$$v_i^{S,T}(r) = I_i^{S,T} T_\mu^2(r) + \left[P_i^{S,T} + \mu r Q_i^{S,T} + (\mu r)^2 R_i^{S,T} \right] W(r) \quad (3.42)$$

Here, the i subscript labels the central, L^2 , *Tensor*, $L \cdot S$, and $(L \cdot S)^2$ potentials. The superscripts S/T label the total spin/isospin of the two-nucleon system and μ is the average of the charged and neutral pion masses. The constants I, P, Q , and R are obtained from curve fitting observed scattering data (Table 3.3).

Since $T=I$ for the pp interaction, only two possible potentials exist for $v_R(pp)$, one for the singlet state $S=0$, $v_R^{0,1}(pp)$

$$v_R^{0,1}(pp) = v_{central}^{0,1}(r) + v_{L^2}^{0,1}(r) L^2 \quad (3.43)$$

and another for triplet state $S=1$, $v_R^{1,1}(pp)$.

$$v_R^{1,1}(pp) = v_{central}^{1,1}(r) + v_{L^2}^{1,1}(r) L^2 + v_{Tensor}^{1,1}(r) S_{12} + v_{L \cdot S}^{1,1}(r) L \cdot S + v_{(L \cdot S)^2}^{1,1}(r) (L \cdot S)^2 \quad (3.44)$$

Equation (3.42) also includes a short-range repulsive core represented by the Wood-Saxon function, [4]

$$W(r) = \frac{1}{1 + \text{Exp}\left(\frac{r-r_0}{a}\right)} \quad (3.45)$$

and,

$$T_\mu^2(r) = \left(\left(1 + \frac{3}{\mu r} + \frac{3}{(\mu r)^2} \right) \frac{e^{(-\mu r)}}{\mu r} \left(1 - e^{-c_\pi r^2} \right)^2 \right)^2 \quad (3.46)$$

which has Yukawa form, $\frac{e^{(-\mu r)}}{\mu r}$. The parameters r_0 (core radius), a (surface thickness),

and c_π (cutoff) are given in Table 3.3[4].

Table 3.3. $v_R(pp)$ Strong Component Constant Parameters of the AV18 model

Channel	TYPE	I MeV	P MeV	Q MeV	R MeV
$S=0, T=1$	<i>Central</i>	-11.27028	3346.6878	1859.5627*	0
	L^2	0.12472	16.780	9.0972*	0
$S=1, T=1$	<i>Central</i>	-7.62701	1815.4920	969.3863*	1847.8059
	L^z	0.06709	342.0669	185.4713*	-615.2339
	<i>Tensor</i>	1.07985	0	-190.0949	-811.2040
	<i>LS</i>	-0.62697	-570.5571	-309.3605*	819.1222
	$(LS)^2$	0.74129	9.3418	5.0652*	-376.4384

3.2. The AV18 Neutron-Proton Model

Since the AV18 neutron-proton model is not as complicated as the AV18 proton-proton model, this section will be abbreviated. This section also has three sub-sections, one for each component.

3.2.1. The Neutron-Proton EM Potential, $v_{EM}(pn)$

The form of the electromagnetic portion of the AV18 pn model has the general structure,

$$v_{EM}(pn) = v_{C1}(pn) + v_{MM}(pn) \quad (3.47)$$

where again v_{c1} labels a one-photon exchange and v_{MM} labels a magnetic moment contribution. The two photon exchange, Darwin-Foldy, and vacuum polarization components are omitted since neutrons interact minimally with the electromagnetic field. The remaining two terms differ slightly from the proton-proton counterparts $v_{c1}(pp)$ and $v_{MM}(pp)$,

$$v_{c1}(pn) = \alpha\beta_n \frac{F_{np}^C(r)}{r}. \quad (3.48)$$

$$v_{MM}(pn) = -\frac{\alpha}{4M_n M_p} \mu_n \mu_p \left[\frac{2}{3} F_\delta(r) \vec{\sigma}_1 \cdot \vec{\sigma}_2 + \frac{F_T(r)}{r^3} S_{12} \right] - \frac{\alpha}{2M_n M_r} \mu_n \frac{F_{ls}(r)}{r^3} \left(\vec{L} \cdot \vec{S} + \vec{L} \cdot \left(\frac{1}{2} (\vec{\sigma}_1 - \vec{\sigma}_2) \right) \right) \quad (3.49)$$

In the above set of equations, β_n is the form factor associated with the electron-neutron interaction at the point of zero momentum [30, 63]. Since fixed neutron targets do not exist in nature, β_n at zero momentum is extrapolated from high-energy (GeV range) electron-deuteron scattering experiments [96]. In the AV18, $\beta_n = 0.0189 \text{ fm}^2$ [14]. The only other term not already introduced in Section 3.1.1. is another one of Auerbach F functions,

$$F_C^{pn}(x) = \frac{b^2}{384} (15x + 15x^2 + 6x^3 + x^4) \exp(-x) \quad (3.50)$$

Here, again $x = br$ and b refers to the exponential cutoff parameter of 4.27 fm^{-1} , M_r is the nucleon-proton reduced mass, and $\left(\frac{1}{2} (\vec{\sigma}_1 - \vec{\sigma}_2) \right)$ represents a mixing of spin singlet and triplet states. This mixing contributes minimally to the magnetic neutron-proton scattering amplitude [4].

3.2.2. The Neutron-Proton OPEP, $v_\pi(pn)$

Since the theory associated with $v_\pi(pn)$ has already been presented in Section 3.1.2, this discussion begins with the general expression for v_π presented in equation (3.25),

$$v_\pi = \frac{1}{3} m_\pi c^2 \left(\frac{f^2}{4\pi\hbar c} \right) (\vec{\tau}_1 \cdot \vec{\tau}_2) \{ \sigma_1 \cdot \sigma_2 Y(r) + S_{12} T(r) Y(r) \} \quad (3.51)$$

Here, a complex mixing of neutral pion (m_{π_0}) and charged pions (m_{π_\pm}) can transform the incident neutron into a proton and the incident proton into a neutron. In the AV18,

$$v_\pi(pn) = \frac{1}{3} \left(\frac{m_{\pi_0}^3}{m_s^2} \right) \frac{(cf)^2}{4\pi\hbar c} (1 - \exp(-c_\pi r^2)) (\sigma_1 \cdot \sigma_2 Y(r) + S_{12} T(r) Y(r)) + \\ (-1)^{T+1} \frac{2}{3} \left(\frac{m_{\pi_\pm}^3}{m_s^2} \right) \frac{(cf)^2}{4\pi\hbar c} (1 - \exp(-c_\pi r^2)) (\sigma_1 \cdot \sigma_2 Y(r) + S_{12} T(r) Y(r)) \quad (3.52)$$

represents the complex mixing of charged and neutral pions

3.2.3. The Neutron-Proton Short Range Potential $v_R(pn)$

The only real difference between the form of $v_R(pn)$ and $v_R(pp)$ rests in the constant parameters I , P , Q , and R that are fit to scattering data (Table 3.4),

$$v_R(pn) = v_{central}^{S,T}(r) + v_L^{S,T}(r) L^2 + v_{Tensor}^{S,T}(r) S_{12} + v_{L \cdot S}^{S,T}(r) L \cdot S + v_{(L \cdot S)^2}^{S,T}(r) (L \cdot S)^2 \quad (3.53)$$

$$v_i^{S,T}(r) = I_i^{S,T} T_\mu^2(r) + [P_i^{S,T} + \mu r Q_i^{S,T} + (\mu r)^2 R_i^{S,T}] W(r) \quad (3.54)$$

Since T can equal 0 or 1 for the pn interaction, there are four possible combinations, two for $S=0$

$$\begin{aligned}
v_R^{0,1}(pn) &= v_{central}^{0,1}(r) + v_{L^2}^{0,1}(r)L^2 \\
v_R^{0,0}(pn) &= v_{central}^{0,1}(r) + v_{L^2}^{0,0}(r)L^2
\end{aligned} \tag{3.55}$$

and two for $S=1$.

$$\begin{aligned}
v_R^{1,1}(pn) &= v_{central}^{1,1}(r) + v_{L^2}^{1,1}(r)L^2 + v_{Tensor}^{1,1}(r)S_{12} + v_{LS}^{1,1}(r)L \cdot S + v_{(LS)^2}^{1,1}(r)(L \cdot S)^2 \\
v_R^{1,0}(pn) &= v_{central}^{1,0}(r) + v_{L^2}^{1,0}(r)L^2 + v_{Tensor}^{1,0}(r)S_{12} + v_{LS}^{1,0}(r)L \cdot S + v_{(LS)^2}^{1,0}(r)(L \cdot S)^2
\end{aligned} \tag{3.56}$$

Table 3.4. $v_R(pn)$ Strong Component Constant Parameters of the AV18 Model

<i>Channel</i>	<i>TYPE</i>	<i>I MeV</i>	<i>P MeV</i>	<i>Q MeV</i>	<i>R MeV</i>
$S=0, T=1$	<i>Central</i>	-10.66788	3126.5542	1746.4298*	0
	L^2	0.12472	16.780	9.0972*	0
$S=0, T=1$	<i>Central</i>	-2.09971	1204.4301	511.9380*	0
	L^2	-0.31452	217.4559	117.9063*	0
$S=1, T=1$	<i>Central</i>	-7.62701	1815.5315	966.2483*	1847.8059
	L^2	0.06709	342.0669	185.4713*	-615.2339
	<i>Tensor</i>	1.07985	0	-190.0949	-811.2040
	<i>LS</i>	-0.62697	-570.5571	-309.3605*	819.1222
	$(LS)^2$	0.74129	9.3418	5.0652*	-376.4384
$S=1, T=0$	<i>Central</i>	-8.62770	2605.2682	1459.6345*	441.9733
	L^2	-0.13201	253.4350	137.4144*	-1.0076
	<i>Tensor</i>	1.485601	0	-1126.8359	370.1324
	<i>LS</i>	0.10180	86.0658	46.6655*	-356.5175
	$(LS)^2$	0.07357	-217.5791	-117.9731*	18.3935

3.3. The AV18 Neutron-Neutron Model

Since the neutron has an internal structure, it is still subject to electromagnetic, one pion exchange, and short-range effects. This section summarizes these components.

3.3.1. The Neutron-Neutron EM Potential, $v_{EM}(nn)$

The electromagnetic portion of the nn potential only has one component,

$$v_{EM}(nn) = v_{MM}(nn). \quad (3.57)$$

which results from the magnetic moment of the neutron. This single component of

$v_{EM}(nn)$ may be represented by,

$$v_{MM}(nn) = -\frac{\alpha}{4M_n^2} \mu_n^2 \left[\frac{2}{3} F_\delta(r) \sigma_1 \cdot \sigma_2 + \frac{F_t(r)}{r^3} S_{12} \right]. \quad (3.58)$$

As previously mentioned, the observed magnetic moment of the neutron was one of the first indications of an underlying particle structure.

3.3.2. The Neutron-Neutron OPEP, $v_\pi(nn)$

For the nn OPEP, the AV18 assumes this solution to be the same as $v_\pi(pp)$ as experimental data has shown little variation in the coupling constants below 350 MeV.

$$v_\pi(nn) = \frac{1}{3} m_{\pi_0} c^2 \frac{f^2}{4\pi\hbar c} \left\{ \left(\frac{m_{\pi_0}}{m_s} \right)^2 (1 - \exp(-c_\pi r^2)) \right\} [\sigma_1 \cdot \sigma_2 Y(r) + S_{12} T(r) Y(r)] \quad (3.59)$$

3.3.3. The Neutron-Neutron Short Range Potential, $v_R(nn)$

Analogous to $v_R(pp)$, $T=I$ for the nn interaction. Therefore, two potentials are possible, one for the $S=0$,

$$v_R^{0,1}(np) = v_{central}^{0,1}(r) + v_{L^2}^{0,1}(r)L^2 \quad (3.60)$$

and one for $S=I$.

$$v_R^{1,1}(np) = v_{central}^{1,1}(r) + v_{L^2}^{1,1}(r)L^2 + v_{Tensor}^{1,1}(r)S_{12} + v_{L \cdot S}^{1,1}(r)L \cdot S + v_{(L \cdot S)^2}^{1,1}(r)(L \cdot S)^2 \quad (3.61)$$

Here as before, each of the terms of equation (3.61) can be described by equation (3.42) with the constants parameters I , P , Q , and R provided in Table 3.5.

Table 3.5. $v_R(nn)$ Strong Component Constant Parameters of the AV18 model

<i>Channel</i>	<i>TYPE</i>	<i>I MeV</i>	<i>P MeV</i>	<i>Q MeV</i>	<i>R MeV</i>
$S=0, T=1$	<i>Central</i>	-11.27028	3342.7664	1857.4367*	0
	L^2	0.12472	16.780	9.0972*	0
$S=1, T=1$	<i>Central</i>	-7.62701	1811.5710	967.2603*	1847.8059
	L^2	0.06709	342.0669	185.4713*	-615.2339
	<i>Tensor</i>	1.07985	0	-190.0949	-811.2040
	LS	-0.62697	-570.5571	-309.3605*	819.1222
	$(LS)^2$	0.74129	9.3418	5.0652*	-376.4384

3.4. The Numerov Method

ANL typically utilizes the Numerov method to compute AV18 scattering phase shifts [5]. This time independent approach is ideally suited to linear second order differential equations like the Schrödinger equation,

$$\frac{\partial^2 \psi}{\partial r^2} = k^2 (E - V(r)) \psi(r) \quad (3.62)$$

$$k = \sqrt{\frac{2\mu}{\hbar^2}}$$

which have no first derivative. Here, V is the AV18 potential, μ is the reduced mass of the nucleon pair, and \hbar is Planck's constant divided by 2π

To use this technique, we first perform a Taylor series expansion of ψ at the point $(r+h)$

$$\psi(r+h) = \psi(r) + h\psi'(r) + \frac{h^2}{2}\psi''(r) + \frac{h^3}{6}\psi'''(r) + \frac{h^4}{24}\psi^{(4)}(r) + \dots \quad (3.63)$$

then perform a separate Taylor series expansion of ψ at the point $(r-h)$,

$$\psi(r-h) = \psi(r) - h\psi'(r) + \frac{h^2}{2}\psi''(r) - \frac{h^3}{6}\psi'''(r) + \frac{h^4}{24}\psi^{(4)}(r) + \dots \quad (3.64)$$

The sum of these two expansions eliminates odd powers of h and leaves an expression for $\psi''(r)$ which includes an undesirable fourth order derivative,

$$\psi''(r) = \frac{\psi(r+h) + \psi(r-h) - 2\psi(r)}{h^2} - \frac{h^4}{12}\psi^{(4)}(r) + O(h^6) \quad (3.65)$$

Here, h refers to the integration step size and should not be confused with the \hbar contained within k^2 in equation (3.62). In order to reduce this equation into something

more tractable, we operate on the Schrödinger equation (3.62) with $1 + \left(\frac{h^2}{12} \frac{\partial^2}{\partial r^2}\right)$ to

generate terms analogous to the Taylor Series Expansion,

$$\psi''(r) + \frac{h^4}{12}\psi^{(4)}(r) + k^2\psi(r) + \frac{h^2}{12} \frac{\partial^2}{\partial r^2} [k^2\psi(r)] = 0 \quad (3.66)$$

and then back substitute into equation (3.65) for $\psi''(r) + \frac{h^4}{12}\psi^{(4)}(r)$,

$$\psi(r+h) + \psi(r-h) - 2\psi(r) + h^2k^2\psi(r) + \frac{h^4}{12} \frac{\partial^2}{\partial r^2} [k^2\psi(r)] + O(h^6) = 0 \quad (3.67)$$

All that remains in equation (3.67) is one lone second derivative, $\frac{\partial^2}{\partial r^2} [k^2 \psi(r)]$

which is normally reduced to first order through an elementary difference formula approximation⁷,

$$\frac{\partial^2}{\partial r^2} [k^2 \psi(r)] \approx \frac{k^2 \psi(r+h) + k^2 \psi(r-h) - 2k^2 \psi(r)}{h^2} \quad (3.68)$$

After some algebra, we arrive at the general form for the Numerov method,

$$\psi(r+h) = \frac{2 \left(1 - \frac{5}{12} h^2 k^2\right) \psi(r) - \left(1 + \frac{1}{12} h^2 k^2\right) \psi(r-h)}{1 + \frac{1}{12} h^2 k^2} + O(h^6) \quad (3.69)$$

The Numerov method above is a three point difference formula that computes $\psi(r+h)$ based on the value of ψ at two previous points $\psi(r)$ and $\psi(r-h)$. Of course to start the iterative method, we must first seed a couple of values. The first point at $\psi(r-h)$ is given by the boundary condition at $r=0$, $\psi(0)=0$. The second point at a step h from the origin is considered to be sufficiently small so $\psi(r)$ is only slightly greater than zero. From these two points, $\psi(r+h)$ is determined. Then, $\psi(r) \rightarrow \psi(r-h)$ and $\psi(r+h) \rightarrow \psi(r)$ and a new $\psi(r+h)$ can be computed. The process is repeated until $\psi(r)$ is completely determined for a single energy value [64,65].

⁷ Although this difference approximation has an error of $O(h^2)$, it has minimal impact on the solution

since it is multiplied by the much smaller h^4 .

Thus far, we have shown how to obtain a solution to the Schrödinger equation via the Numerov method but not shown how a phase shift can be obtained from this solution.

To help motivate the phase shift discussion, consider Figure 3.3.

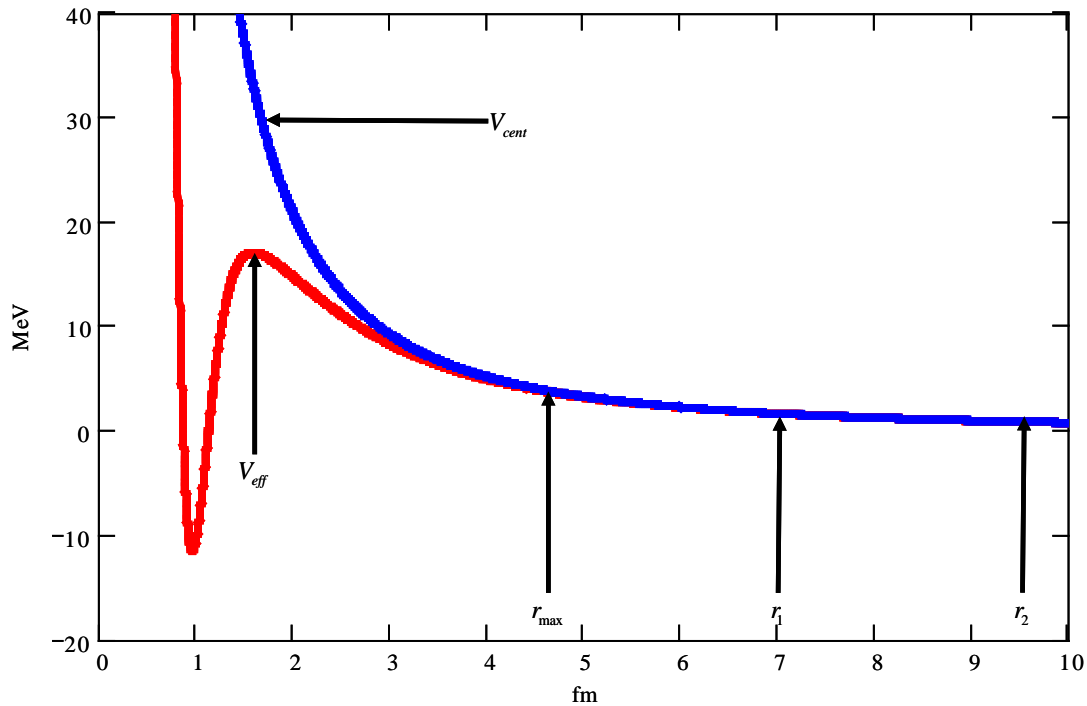


Figure 3.3. Centripetal Potential V_{cent} and Effective Potential V_{eff} Comparison. At some point r_{max} the centripetal barrier begins to dominate at arbitrary points r_2 and $r_1 > r_{max}$ the solutions the radial equation must be a linear combination of free solutions [64]

Here, a centripetal barrier potential V_{cent} and an effective potential V_{eff} including both the centripetal potential and one of the AV18 potentials are presented. Notice at a point roughly equal to r_{max} the centripetal potential begins to dominate. As r continues to increase past r_{max} , the solution to the radial equation at a point $r_1 > r_{max}$ must be a linear combination of free solutions,

$$\psi 1_L(r) = Akr_1 \left[j_L(kr_1) \cos \delta_L - \eta_L(kr_1) \sin \delta_L \right] \quad (3.70)$$

Here, A is an arbitrary constant, δ_L is the phase shift, and j_L and η_L the regular and irregular spherical Bessel functions of order L . We cannot calculate the phase shift from the solution at r_1 alone since the equation contains two unknowns. Calculation of the phase shift is facilitated by determining a second solution at a point $r_2 > r_1$ also given by the solution to the free radial equation,

$$\psi 2_L(r) = Akr_2 \left[j_L(kr_2) \cos \delta_L - \eta_L(kr_2) \sin \delta_L \right]. \quad (3.71)$$

Given the two solutions, $\psi 1_L(r)$ and $\psi 2_L(r)$, A can be eliminated through some more algebra to obtain an expression for the phase shift at a particular energy,

$$\tan \delta_L = \frac{r_1 \psi 2_L(r) j_L(kr_1) - j_L(kr_2)}{r_2 \psi 1_L(r) \eta_L(kr_1) - \eta_L(kr_2)}. \quad (3.72)$$

Note that the points r_1 and r_2 are typically chosen to be much farther away from the interaction potential than shown in the diagram. These positions are for illustrative purposes only [64, 65].

In order to get a better understanding of how phase shifts are currently obtained from the AV18, a separate time independent code was developed to recreate the published phase shifts at a 2 MeV energy resolution and coordinate step size, 0.00153 fm. A comparison between a phase shift obtained from this time independent code and a published phase shift for the $^1S_0 pn$ potential⁸ is presented in Figure 3.4.

⁸ Plots of this potential may be seen in Chapter 5.

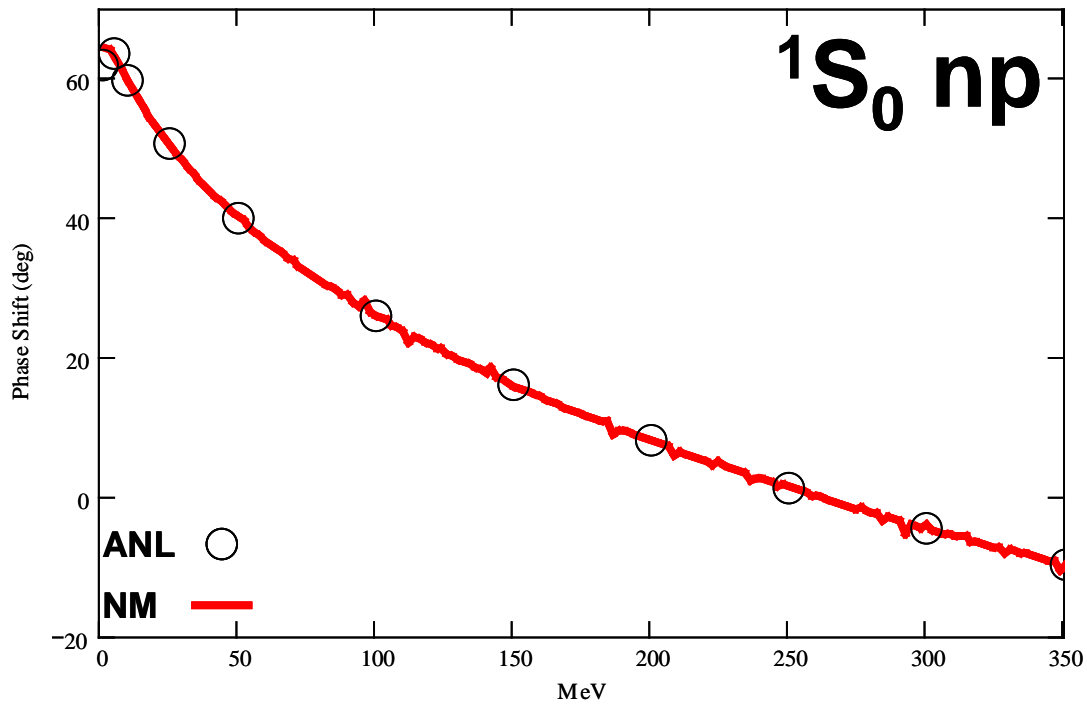


Figure 3.4. ANL and AFIT Numerov 1S_0 Phase Shift Comparison. ANL's published data is represented by circles and the Numerov calculation using the above method is represented by the solid line. The AFIT Numerov code exhibited sensitivity to coordinate step size and required twice as long as the CPM technique to complete the same calculation.

Throughout this exercise, it was observed that the fidelity of the phase shift produced by the Numerov method was inherently sensitive to coordinate step size. Step sizes greater than 0.00153 fm exhibited far greater noise than the present in the plot above. Plots of the same 1S_0 phase shift determined via the channel packet method (chapter 6) had a higher energy resolution (2 orders of magnitude lower) and were produced in half the time of the Numerov method. These CPM characteristics are well suited for examining phase shifts from many body potentials where sharp scattering resonances are likely to be encountered.

4. Channel Packet Method Theoretical Background

In quantum scattering theory, the scattering operator \hat{S} relates the incident reactant asymptotic state $|\psi_{in}\rangle$ to the resultant product asymptotic state $|\psi_{out}\rangle$,

$$|\psi_{out}\rangle = \hat{S}|\psi_{in}\rangle. \quad (4.1)$$

This unitary, time independent operator contains all information of experimental interest, since only asymptotic free motion is observed in the laboratory. Therefore given \hat{S} , physical insight into both reactive and non-reactive scattering events can be obtained for verification against experimental data [51].

The scattering operator, \hat{S} , is defined as the product of two isometric Møller operators [45, 51,],

$$\hat{S} \equiv \Omega_+^\dagger \Omega_+ \quad (4.2)$$

where,

$$\hat{\Omega}_\pm^\gamma = \lim_{t \rightarrow \mp\infty} \exp\left[\frac{i\hat{H}t}{\hbar}\right] \exp\left[\frac{-i\hat{H}_0 t}{\hbar}\right]. \quad (4.3)$$

Notice that the Møller operator above is essentially a product of time evolution operators; one corresponding to the asymptotic Hamiltonian, \hat{H}_0 and the other the full Hamiltonian, \hat{H} . When the Møller Operator Ω_+ is applied to some given reactant state $|\psi_{in}\rangle$, the wave packet is propagated backward in time under the asymptotic Hamiltonian, \hat{H}_0 , to an intermediate state at $t = -\infty$ then forward in time under the full Hamiltonian back to its initial position at $t = 0$. The other Møller Operator Ω_- has a

similar effect on the product state $|\psi_{out}\rangle$, first propagating the wave packet forward to time $t = +\infty$ then backwards in time back to $t = 0$. The action of propagating these wave packets to and from the asymptotic limit integrates information about how \hat{H}_0 is modified by \hat{H} into each wave packet prior to interaction. These new wave packets are designated as the reactant and product Møller states, $|\psi_+\rangle = \Omega_+ |\psi_{in}\rangle$ and $|\psi_-\rangle = \Omega_- |\psi_{out}\rangle$, respectively. Throughout the remainder of this section, + subscripts reference the reactant wave packet and – subscripts reference to the product wave packet.

In order to define these Møller states, it is necessary to first define a useful basis set in which to construct the initial reactant and product states $|\psi_{in}\rangle$ and $|\psi_{out}\rangle$. A convenient choice is the momentum basis, $|k\rangle$. The usefulness of this choice becomes apparent when we consider \hat{H}_0 in the momentum basis, $|k\rangle$

$$H_0 |k\rangle = \frac{\hbar^2 k^2}{2\mu} |k\rangle \quad (4.4)$$

Here we have expressed \hat{H}_0 in terms of the momentum eigenvalues $\frac{\hbar^2 k^2}{2\mu}$ where \hbar is

Plank's constant, k is the wave vector conjugate to r , and μ is the reduced mass. If we apply the Møller operator to these states

$$\begin{aligned} \Omega_+ H_0 |k\rangle &= \Omega_+ \frac{\hbar^2 k^2}{2\mu} |k\rangle = \frac{\hbar^2 k^2}{2\mu} \Omega_+ |k\rangle = \frac{\hbar^2 k^2}{2\mu} |k_+\rangle \\ \Omega_- H_0 |k\rangle &= \Omega_- \frac{\hbar^2 k^2}{2\mu} |k\rangle = \frac{\hbar^2 k^2}{2\mu} \Omega_- |k\rangle = \frac{\hbar^2 k^2}{2\mu} |k_-\rangle \end{aligned} \quad (4.5)$$

and use the intertwining relation $\Omega_{\pm} H_0 = H \Omega_{\pm}$ [51],

$$\begin{aligned}
H \Omega_+ |k\rangle &= \frac{\hbar^2 k^2}{2\mu} \Omega_+ |k\rangle = \frac{\hbar^2 k^2}{2\mu} |k_+\rangle \\
H \Omega_- |k\rangle &= \frac{\hbar^2 k^2}{2\mu} \Omega_- |k\rangle = \frac{\hbar^2 k^2}{2\mu} |k_-\rangle
\end{aligned} \tag{4.6}$$

we see that not only do we have a mapping between the eigenbasis $|k\rangle$ of \hat{H}_0 and the eigenbasis $|k_+\rangle$ and $|k_-\rangle$ of \hat{H} , but we also see that the eigenvalues between the basis are the same.

$$\begin{aligned}
H_0 |k\rangle &= \frac{\hbar^2 k^2}{2\mu} |k\rangle \\
H |k_+\rangle &= \frac{\hbar^2 k^2}{2\mu} |k_+\rangle \\
H |k_-\rangle &= \frac{\hbar^2 k^2}{2\mu} |k_-\rangle
\end{aligned} \tag{4.7}$$

The expansion of the reactant Møller state $|\psi_+\rangle$ and product Møller $|\psi_-\rangle$ state in the momentum basis set $|k_\pm\rangle$ have the form,

$$|\psi_+\rangle = \Omega_+ |\psi_{in}\rangle = \Omega_+ \int_{-\infty}^{\infty} \eta_+(k) |k\rangle dk = \int_{-\infty}^{\infty} \eta_+(k) |k_+\rangle dk . \tag{4.8}$$

$$|\psi_-\rangle = \Omega_- |\psi_{out}\rangle = \Omega_- \int_{-\infty}^{\infty} \eta_-(k) |k\rangle dk = \int_{-\infty}^{\infty} \eta_-(k) |k_-\rangle dk \tag{4.9}$$

where $\eta(k_+)$ and $\eta(k_-)$ represents the initial expansion coefficients of the product and reactant wave packets.

With the two Møller states now defined, we are now ready to determine the reaction probability S between these two states,

$$\langle \psi_- | \psi_+ \rangle = \langle \psi_{out} | \Omega_-^\dagger \Omega_+ | \psi_{in} \rangle = \langle \psi_{out} | \hat{S} | \psi_{in} \rangle = S . \tag{4.10}$$

To help further develop a usable expression for S in the standard momentum representation, consider now the arbitrary state $|A_+(E)\rangle$ represented by the Fourier transform of the time evolution of the Møller state,

$$|A_+(E)\rangle = \int dt \exp\left\{-\frac{i(E')t}{\hbar}\right\} \exp\left(\frac{-iHt}{\hbar}\right) |\psi_+\rangle \quad (4.11)$$

Since the Hamiltonian can be expressed as an energy, E , and both energies can be

expressed in wave vector form $E = \frac{\hbar^2 k^2}{2\mu}$ and $E' = \frac{\hbar^2 k'^2}{2\mu}$, we have

$$|A_+(E)\rangle = \int dt e^{i\left(\frac{\hbar k'^2}{2\mu} - \frac{\hbar k^2}{2\mu}\right)t} |\psi_+\rangle. \quad (4.12)$$

Here, the reactant Møller state $|\psi_+\rangle$ is independent of t , so the time integral has the delta function solution,

$$|A_+(E)\rangle = 2\pi \delta\left(\frac{\hbar k'^2}{2\mu} - \frac{\hbar k^2}{2\mu}\right) |\psi_+\rangle \quad (4.13)$$

If we substitute in the expansion for $|\psi_+\rangle$ from equation (4.8) and use two delta function identities,

$$\delta(bx) = \frac{1}{|b|} \delta(x) \quad (4.14)$$

$$\delta(x^2 - \alpha^2) = \frac{1}{2|\alpha|} [\delta(x + \alpha) + \delta(x - \alpha)] \quad (4.15)$$

we have,

$$|A_+(E)\rangle = \frac{2\pi\mu}{\hbar|k|} \int dk' \eta_+(k'_+) [\delta(k' - k) + \delta(k' + k)] |k'_+\rangle \quad (4.16)$$

Only two possible solutions for the integral above exist, one for $k' = +k$ and one for $k' = -k$. Therefore,

$$|A_+(E)\rangle = \frac{2\pi\mu}{\hbar|k|} [\eta_+(+k_+) |k_+\rangle + \eta_+(-k_+) |-k_+\rangle]. \quad (4.17)$$

Here, it is important to remember that the + subscript refers to the reactant state and the – subscript refers to the product state since the notation becomes more challenging as we proceed further. The reaction probability then is given by the overlap between the evolving reactant state and the stationary product Møller state,

$$\langle \psi_- | A_+(E) \rangle = \int dk' \eta(k') \langle k' | A_+(t) \rangle \quad (4.18)$$

$$\langle \psi_- | A_+(E) \rangle = \frac{2\pi\mu}{\hbar|k|} \int dk' \eta_-^*(k') \langle k'_- | [\eta_+(+k_+) |k_+\rangle + \eta_+(-k_+) |-k_+\rangle] \rangle \quad (4.19)$$

$$\langle \psi_- | A_+(E) \rangle = \frac{2\pi\mu}{\hbar|k|} \int dk' [\eta_-^*(k') \eta_+(+k_+) \langle k'_- | k_+\rangle + \eta_-^*(k') \eta_+(-k_+) \langle k'_- | -k_+\rangle] \quad (4.20)$$

Here there also exists degeneracy in k' analogous to (4.16) which enables (4.20) to be written as the sum of four similar integrals,

$$\begin{aligned} \langle \psi_- | A_+(E) \rangle = & \frac{2\pi\mu}{\hbar|k|} \int dk' \eta_-^*(+k_-) \eta_+(+k_+) \langle +k_- | +k_+\rangle + \\ & \frac{2\pi\mu}{\hbar|k|} \int dk' \eta_-^*(+k_-) \eta_+(-k_+) \langle +k_- | -k_+\rangle + \\ & \frac{2\pi\mu}{\hbar|k|} \int dk' \eta_-^*(-k_-) \eta_+(+k_+) \langle -k_- | +k_+\rangle + \\ & \frac{2\pi\mu}{\hbar|k|} \int dk' \eta_-^*(-k_-) \eta_+(-k_+) \langle -k_- | -k_+\rangle \end{aligned} \quad (4.21)$$

The integrals vanish provided the orthogonality relations from Taylor [51],

$$\langle k_- | k_+ \rangle = \langle k' | S | k \rangle = \langle k' | \Omega_-^\dagger \Omega_+ | k \rangle = \delta(k' - k) S_{k',k} \quad (4.22)$$

yielding an expression for the S matrix elements in the momentum representation

$$\begin{aligned} \langle \psi_- | A_+(E) \rangle = & \frac{2\pi\mu}{\hbar|k|} \eta_-^*(+k) \eta_+(+k) S_{+k,+k} + \\ & \frac{2\pi\mu}{\hbar|k|} \eta_-^*(+k) \eta_+(-k) S_{+k,-k} + \\ & \frac{2\pi\mu}{\hbar|k|} \eta_-^*(-k) \eta_+(+k) S_{-k,+k} + \\ & \frac{2\pi\mu}{\hbar|k|} \eta_-^*(-k) \eta_+(-k) S_{-k,-k} \end{aligned} \quad (4.23)$$

Here, the sign of the k subscript on S indicates the wave packets direction of travel, either toward or away from the interaction region. Therefore, in the case of the symmetric square well, the first two terms would represent the probability of transmission and reflection across the well from an incident wave packet from the left, whereas the last two terms would represent the probability of transmission and reflection from an incident wave packet from the right. Since only one particular set of matrix elements can be determined for each momentum pair, we can express (4.23) in the compact form,

$$S_{\pm k, \pm k}(E) = \frac{\hbar|k(E)|}{2\pi\mu \eta_-^*(\pm k(E)) \eta_+(\pm k(E))} \langle \psi_- | A_+(E) \rangle, \quad (4.24)$$

This is the CPM representation of the S-Matrix [36-38].

Solutions to equation (4.24) hinge on the numerical evaluation of the inner product $\langle \psi_- | A_+(E) \rangle$, which is given by the Fourier Transform of the correlation function, $C(t)$, between the time evolution of the reactant and stationary product Møller states,

$$\begin{aligned}
\langle \psi_- | A_+(E) \rangle &= \int_{-\tau}^{\tau} \exp\left[\frac{-i\hat{E}t}{\hbar}\right] \langle \psi(E)_- | \exp\left(\frac{-i\hat{H}t}{\hbar}\right) | \psi(E)_+ \rangle dt \\
&= \int_{-\tau}^{\tau} \text{Exp}\left[\frac{-i\hat{E}t}{\hbar}\right] C(t) dt
\end{aligned} \tag{4.25}$$

Scattering phase shifts $\delta(E)$ are obtained directly from $S_{\pm k, \pm k}(E)$ if we recall that solutions may be expressed in complex polar form⁹ as $\exp(i\delta)$ when the scattering matrix is diagonal (i.e. no coupling between states),

$$\delta(E) = \frac{a \tan\left(\frac{\text{Im}(S_{\pm k, \pm k})}{\text{Re}(S_{\pm k, \pm k})}\right)}{2} \tag{4.26}$$

Taylor mentions a few constraints to scattering calculations [51]. The first states the potential should be no more singular than r^{-2} at the origin, a criterion easily met by all existing nuclear models. The second, however, requires the potential decay faster than r^{-3} at infinity. This is a clear problem for the long-range Coulombic tail, which governs charged nucleon interaction at large r . Fortunately, a technique for handling the tail exists in the literature and an outline of the theory is provided in Section 5.6

⁹ The scattering matrix is unitary so the r associated with complex polar form is one.

5. AV18 CPM Synthesis

To couple the CPM methodology with the AV18 potential, an appropriate coordinate system, basis, Hamiltonian and units system, must be determined. These topics are the subjects of the first four sections of Chapter 5. Section 5.5 defines the relationship between the center-of-mass reference frame and laboratory frame from an energy standpoint. The standard methodology for handling calculation of s-matrix elements in the presence of a $1/r$ potential is reviewed in section 5.6. Section 5.7 develops a useful system of units for nuclear scattering. Section 5.8 gives an overview of the two leading parameterizations for the non-diagonal components of the nuclear S-Matrix. Finally, this section concludes with a sample problem designed to validate our time-dependent CPM technique against a time-independent analytic solution.

5.1. *Coordinate System*

Since we are considering two nucleons, there are six total degrees of freedom ($x_1, y_1, z_1, x_2, y_2, \text{ and } z_2$) which must be taken into account. However, if we move to the space fixed center of mass coordinate system (SF-CM) as illustrated in Figure 5.1, the problem becomes more tractable.

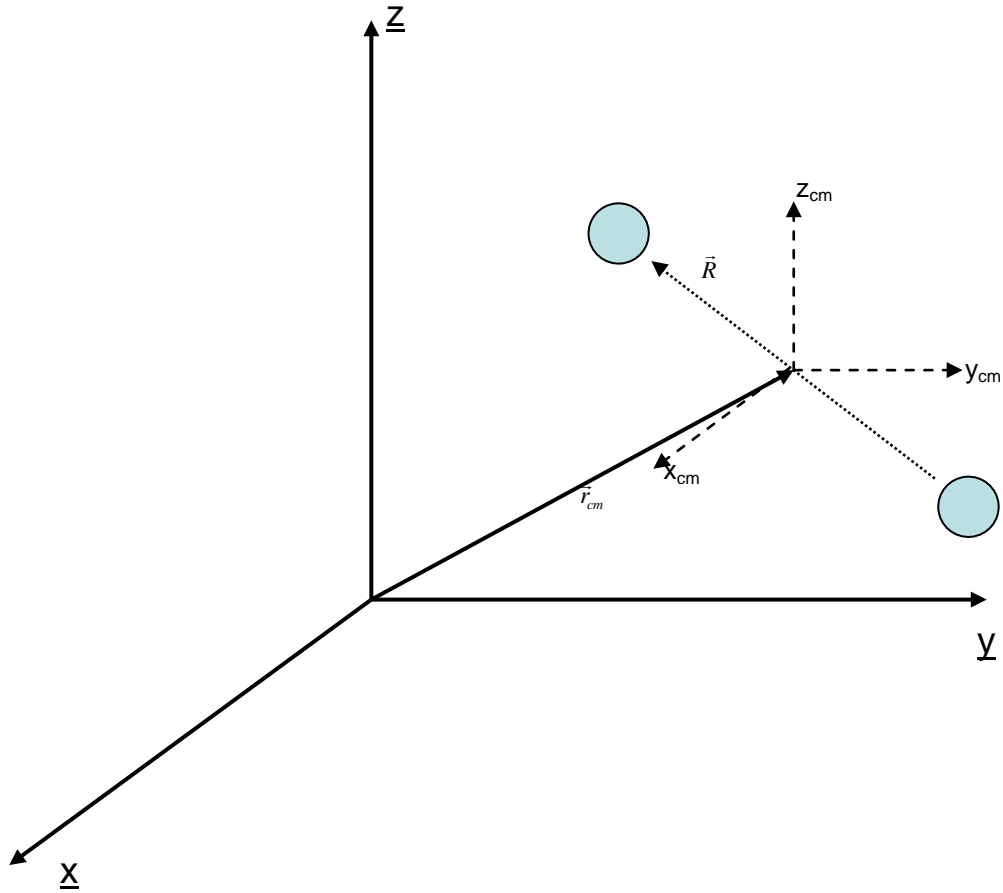


Figure 5.1. Space Fixed – Center of Mass Coordinates.

In this coordinate system, the aforementioned six degrees of freedom are exchanged for six others, three pertaining to the motion of the center of mass (x_{cm} , y_{cm} , z_{cm}) and three others that define the orientation of the two bodies around the center of mass (R, θ, ϕ). The resulting wave function can thus be treated as the product of two different wave functions,

$$\psi = \psi_R(R, \theta, \phi) \psi_{CM}(x_{cm}, y_{cm}, z_{cm}). \quad (5.1)$$

One which specifies the motion of the center of mass through space $\psi_{CM}(x_{cm}, y_{cm}, z_{cm})$ and another which specifies the dynamics of the particles about that center of mass $\psi_R(R, \theta, \phi)$. This construct provides an advantage. Since we are only interested in the physics associated with scattering dynamics between the nucleons not where in space the interaction takes place; ψ_{CM} can be effectively ignored. Only three coordinates therefore need to be considered, R which labels the separation between the nucleons and θ and ϕ which describe nucleons orientation about the center of mass.

5.2. The Hamiltonian

The Hamiltonian utilized by the CPM is expressed using SF-CM coordinates as [5],

$$\hat{H} = \frac{\hat{P}^2}{2\mu_{AB}} + \frac{\hat{L}^2}{2\mu_{AB}R^2} + \hat{V}_{AV18} = \frac{\hat{P}^2}{2\mu_{AB}} + \hat{V}_{eff} \quad (5.2)$$

Here, μ_{AB} represents the reduced mass of the two body system and V_{eff} is the effective potential that includes \hat{V}_{AV18} together with the kinetic energy tumbling term $\frac{\hat{L}^2}{2\mu_{AB}R^2}$.

The radial kinetic energy is given by $\frac{\hat{P}^2}{2\mu_{AB}}$.

5.3. Basis

A convenient basis well suited for representing this Hamiltonian in equation (5.2) is a mixed radial coordinate, angular momentum representation labeled with R , the distance between the nucleon pair, the total angular momentum J , the total orbital angular

momentum L , the total spin S , the total isospin T , the intrinsic spin σ , and isospin τ of each particle

$$|\psi\rangle = |J L S \sigma_1 \sigma_2 T \tau_1 \tau_2 R\rangle \quad (5.3)$$

Since we are dealing with two bodies in the SF-CM coordinate system, quantities are independent of M the projection of J onto the space-fixed axis [9]. In this section, we examine the \hat{V}_{AV18} scalar products $(\sigma_1 \cdot \sigma_2, \tau_1 \cdot \tau_2, L \cdot S, L^2, S_{12})$ introduced in Section 3.1.3 in the specified basis above

$$\langle R' \tau'_2 \tau'_1 T' \sigma'_2 \sigma'_1 S' L' J' | \hat{V} | J L S \sigma_1 \sigma_2 T \tau_1 \tau_2 R \rangle \quad (5.4)$$

to develop a useful abbreviated basis $|\psi\rangle = |J L S T R\rangle$. Matrix elements are then computed to determine the form of the potential in the abbreviated basis set. From this point forward, R 's presence throughout the remainder of this discussion is implied.

A convenient way to evaluate the spin scalar product $\sigma_1 \cdot \sigma_2$ is through the examination of the observable S^2 in the coupled basis,

$$S^2 = \left(\frac{\hbar}{2} (\sigma_1 + \sigma_2) \right)^2 = \frac{\hbar^2}{4} (\sigma_1^2 + \sigma_2^2 + 2\sigma_1 \cdot \sigma_2) \quad (5.5)$$

In this form, we can utilize the Pauli property,

$$\sigma^2 = \sigma_x^2 + \sigma_y^2 + \sigma_z^2 = 3 \begin{pmatrix} 1 & 0 \\ 0 & 1 \end{pmatrix} \quad (5.6)$$

and the requirement that S^2 must also satisfy

$$S^2 |s\rangle = S(S+1)\hbar^2 |s\rangle \quad (5.7)$$

to express the spin scalar product in a more convenient form,

$$\sigma_1 \cdot \sigma_2 = 2S(S+1) - 3. \quad (5.8)$$

Now as we have already seen in Section 3.1.2, the total spin S of the composite system is either 1 for the symmetric triplet state or 0 for the anti-symmetric singlet state. So, the spin scalar product $\sigma_1 \cdot \sigma_2$ in the coupled basis has two possible eigenvalues, [66, 67]

$$\begin{aligned} \sigma_1 \cdot \sigma_2 |\text{triplet}\rangle &= 1 |\text{triplet}\rangle \\ \sigma_1 \cdot \sigma_2 |\text{singlet}\rangle &= -3 |\text{singlet}\rangle \end{aligned} \quad (5.9)$$

The isospin scalar product $\tau_1 \cdot \tau_2$ has exactly the same eigenvalues for the coupled triplet and singlet states, since the isospin matrices

$$\tau_x = \begin{pmatrix} 0 & 1 \\ 1 & 0 \end{pmatrix} \quad \tau_y = \begin{pmatrix} 0 & -i \\ i & 0 \end{pmatrix} \quad \tau_z = \begin{pmatrix} 1 & 0 \\ 0 & -1 \end{pmatrix} \quad (5.10)$$

are analogous to the Pauli matrices [74]

$$\sigma_x = \begin{pmatrix} 0 & 1 \\ 1 & 0 \end{pmatrix} \quad \sigma_y = \begin{pmatrix} 0 & -i \\ i & 0 \end{pmatrix} \quad \sigma_z = \begin{pmatrix} 1 & 0 \\ 0 & -1 \end{pmatrix} \quad (5.11)$$

and the total isospin T for the two nucleon interaction is also 0 or 1 .

The total angular momentum J is a conserved quantity and is related to the total orbital angular momentum, L , and the total spin, S , via the relation,

$$J^2 = (\vec{L}^2 + \vec{S}^2) = L^2 + S^2 + 2L \cdot S \quad (5.12)$$

which may be manipulated to obtain an expression $L \cdot S$ as,

$$L \cdot S = \frac{J^2 - L^2 - S^2}{2} \quad (5.13)$$

Since the values for S are restricted to 0 and 1 and

$$\vec{J} = \vec{L} + \vec{S}, \quad (5.14)$$

L can only have possible values of $J+1$, J or, $J-1$ in the coupled basis. The evaluation of L^2 in the coupled basis follows directly from the eigenvalue equation,

$$L^2 |l\rangle = L(L+1)\hbar^2 |l\rangle \quad (5.15)$$

These limitations on L impose restrictions on the size of the potential matrix under consideration and are useful in the evaluation of the tensor component S_{12} .

The tensor piece S_{12} represents the only non-central, off diagonal component of the V_{AV18} potential. As discussed in Section 3.1.3, S_{12} is a combination of the scalar quantities $(\sigma_1 \cdot \hat{r})(\sigma_2 \cdot \hat{r})$ and $\sigma_1 \cdot \sigma_2$ which are utilized to help describe the observed asymmetry of the deuteron wave function. Wiringa [5] defines the S_{12} matrix to be,

$$\begin{aligned} \langle R' \tau'_2 \tau'_1 T' \sigma'_2 \sigma'_1 S' L' J' | S_{12} | J L S \sigma_1 \sigma_2 T \tau_1 \tau_2 R \rangle = \\ (-1)^{S'+J} [30(2L+1)(2S+1)(2L'+1)(2S'+1)]^{\frac{1}{2}} \\ X \left\{ \begin{matrix} J & S' & L' \\ 2 & L & S \end{matrix} \right\} \begin{pmatrix} L' & 2 & L \\ 0 & 0 & 0 \end{pmatrix} \begin{Bmatrix} s'_1 & s_1 & 1 \\ s'_2 & s_2 & 1 \\ S' & S & 2 \end{Bmatrix} \\ X (s'_1 \| \vec{\sigma}_1 \| s_1) (s'_2 \| \vec{\sigma}_2 \| s_2) \delta_{\tau_1 \tau_2} \end{aligned} \quad (5.16)$$

Here, 9-j Wigner symbol ensures that there is no off-diagonal contribution when $S = 0$, so

here we can focus our attention on the 3-J coefficient $\begin{pmatrix} L' & 2 & L \\ 0 & 0 & 0 \end{pmatrix}$ and 6-J symbol

$\left\{ \begin{matrix} J & S' & L' \\ 2 & L & S \end{matrix} \right\}$ when $S = 1$. The possible matrix elements for S_{12} are also limited when 3-J

coefficient is,

$$\begin{pmatrix} x_1 & x_2 & x_3 \\ 0 & 0 & 0 \end{pmatrix} = 0 \quad \text{if } x_1 + x_2 + x_3 \text{ is odd} \quad (5.17)$$

In this case, the non-repetitive combinations of L and L' are reduced to four,

$$\begin{aligned}
L &= J + 1, L' = J' + 1 \\
L &= J + 1, L' = J' - 1 \\
L &= J, L' = J' \\
L &= J - 1, L' = J' - 1
\end{aligned} \tag{5.18}$$

The 3-J coefficient for $L = J + 1, L' = J' + 1$ may be computed using the 3-J formula,

$$\begin{pmatrix} \mathcal{J} & \mathcal{J} & 2 \\ \mathcal{M} & -\mathcal{M} & 0 \end{pmatrix} = (-1)^{\mathcal{J}-\mathcal{M}} \frac{2[3\mathcal{M}^2 - \mathcal{J}(\mathcal{J}+1)]}{[(2\mathcal{J}-1)(2\mathcal{J})(2\mathcal{J}+1)(2\mathcal{J}+2)(2\mathcal{J}+3)]^{1/2}} \tag{5.19}$$

by making substitutions $\mathcal{J} = L = L', \mathcal{M} = 0, S = S' = 1$, and $L = L' = J + 1$. Similarly,

the 6-J symbol may be computed with the 6-J formula,

$$\begin{aligned}
\left\{ \begin{matrix} a & b & c \\ 2 & c & b \end{matrix} \right\} &= (-1)^{a+b+c} \\
& \times \frac{2[3(Y-1) - 4b(b+1)c(c+1)]}{[(2b-1)(2b)(2b+1)(2b+2)(2b+3)(2c-1)(2c)(2c+1)(2c+2)(2c+3)]^{1/2}}
\end{aligned} \tag{5.20}$$

$$Y = b(b+1) + c(c+1) - a(a+1)$$

by making the substitutions $a = J, b = S = S',$ and $c = L = L' = J + 1$. The remaining 3-J coefficients and 6-J symbols can be determined in a similar fashion by using these two formulas or others found in the appendices of Edmonds [68].

Now given,

$$\begin{aligned}
\left\{ \begin{matrix} 1/2 & 1/2 & 1 \\ 1/2 & 1/2 & 1 \\ 1 & 1 & 2 \end{matrix} \right\} &= 1/9 \\
(1/2 \|\vec{\sigma}_1\| 1/2) &= (1/2 \|\vec{\sigma}_2\| 1/2) = \sqrt{6}
\end{aligned} \tag{5.21}$$

and the formulas, the matrix elements for S_{12} are [9, 13],

$$\langle R' \tau'_2 \tau'_1 T' \sigma'_2 \sigma'_1 S' L' J' | S_{12} | J L S \sigma_1 \sigma_2 T \tau_1 \tau_2 R \rangle =$$

$$(5.22) \quad \begin{pmatrix} & L=J+1 & L=J & L=J-1 \\ L=J+1 & \frac{-2(J+2)}{2J+1} & 0 & \frac{6J^{1/2}(J+1)^{1/2}}{2J+1} \\ L=J & 0 & 2 & 0 \\ L=J-1 & \frac{6J^{1/2}(J+1)^{1/2}}{2J+1} & 0 & \frac{-2(J-1)}{2J+1} \end{pmatrix}$$

Since we are dealing with fermions, the wave function must be anti-symmetric under the exchange of like particles to satisfy the Pauli Exclusion Principle.

$$\psi(\textit{particle 1}, \textit{particle 2}) = -\psi(\textit{particle 2}, \textit{particle 1}) \quad (5.23)$$

In spherical polar coordinates, ψ is a function of r , θ , and ϕ where r reflects the relative separation between the two nucleons and θ and ϕ define the orientation of the two nucleons in space. Since the radial distance between the two particles is independent of particle exchange, the requirement that the wave function be anti-symmetric must be satisfied by θ and ϕ . Typically, the angular dependence is described by the spherical harmonics $Y_{L,M}(\theta, \phi)$, which have a parity of $(-1)^L$. So, even angular momentum eigenvalues will contribute to a symmetric wave function whereas odd angular momentum eigenvalues will contribute to an anti-symmetric wave function.

For nucleons and other particles with spin however, symmetry of the wave function is not completely determined by the orbital angular momentum alone, the

intrinsic spins of the particles also contribute. The $S = 1$ state where the nucleon intrinsic spins are aligned,

$$\begin{aligned} & \uparrow\uparrow \\ & \uparrow\downarrow + \downarrow\uparrow \\ & \downarrow\downarrow \end{aligned} \quad (5.24)$$

is a symmetric state whereas the $S = 0$ state where the nucleon spins are aligned

$$\uparrow\downarrow - \downarrow\uparrow \quad (5.25)$$

is an anti-symmetric state. This implies that in order to produce an anti-symmetric wave function either, an even L state must be paired with a $S = 0$ state or an odd L state must be paired with a $S = 1$ state. No such restrictions are imposed on the wave function if the interacting pair is a proton and a neutron.

Having evaluated all of the potential terms, we can now examine the full Hamiltonian in the abbreviated $|L S J T\rangle$ basis for a given value of J ,

$$\langle L' S' J' T' | \hat{H} | L S J T \rangle = \langle L' S' J' T' | \frac{\hat{P}^2}{2\mu} | L S J T \rangle + \langle L' S' J' T' | \hat{V}_{eff} | L S J T \rangle \quad (5.26)$$

The radial kinetic energy operator matrix elements are diagonal in all of the angular momentum quantum numbers but not R due to the derivative,

$$\langle L' S' J' T' | \frac{\hat{P}^2}{2\mu} | L S J T \rangle = \frac{-\hbar^2}{2\mu_{AB}} \frac{1}{R} \frac{\partial^2}{\partial R^2} R \delta(R - R') \delta_{L'L} \delta_{S'S} \delta_{T'T} \quad (5.27)$$

while the effective potential is diagonal except when $L = J \pm 1$ and $L' = J \mp 1$ as shown in Figure 5.2.

$\langle L,S,J,T V_{eff} L,S,J,T\rangle$	$ 0,0,0,1\rangle$	$ 1,1,0,1\rangle$	$ 1,0,1,0\rangle$	$ 1,1,1,1\rangle$	$ 0,1,1,0\rangle$	$ 2,1,1,0\rangle$	$ 2,0,2,1\rangle$	$ 2,1,2,0\rangle$	$ 1,1,2,1\rangle$	$ 3,1,2,1\rangle$	$\bullet \bullet \bullet$
$\langle 0,0,0,1 $	1S_0	0	0	0	0	0	0	0	0	0	
$\langle 1,1,0,1 $	0	3P_0	0	0	0	0	0	0	0	0	
$\langle 1,0,1,1 $	0	0	1P_1	0	0	0	0	0	0	0	
$\langle 1,1,1,1 $	0	0	0	3P_1	0	0	0	0	0	0	
$\langle 0,1,1,0 $	0	0	0	0	3S_1	ε_1	0	0	0	0	
$\langle 2,1,1,0 $	0	0	0	0	ε_1	3D_1	0	0	0	0	
$\langle 2,0,2,1 $	0	0	0	0	0	0	1D_2	0	0	0	
$\langle 2,1,2,0 $	0	0	0	0	0	0	0	3D_2	0	0	
$\langle 1,1,2,1 $	0	0	0	0	0	0	0	0	3P_2	ε_2	
$\langle 3,1,2,1 $	0	0	0	0	0	0	0	0	ε_2	3F_2	
\bullet											\bullet
\bullet											\bullet
\bullet											\bullet

Figure 5.2. Evaluation of the Potential in the $LSTJR$ Basis

Here, non-zero matrix elements on the diagonal are labeled using spectroscopic notation, where the elements have the form, ${}^{2S+1}L_J$. The off diagonal elements are labeled ε_j and refer to the mixing parameter that couples the $L=J-1$ and the $L=J+1$ states. The matrix is only fully populated as depicted above if the interacting pair is a proton and a neutron. If in the event the interacting pair is two protons or two neutrons, then only those elements highlighted in red will be allowed due to the Pauli Exclusion Principle.

Figure 5.3 and Figure 5.4 illustrate how some of the V_{AV18} potentials are modified with and without inclusion of a kinetic energy tumbling term $\frac{\hat{L}^2}{2\mu_{AB}R^2}$ in the selected basis.

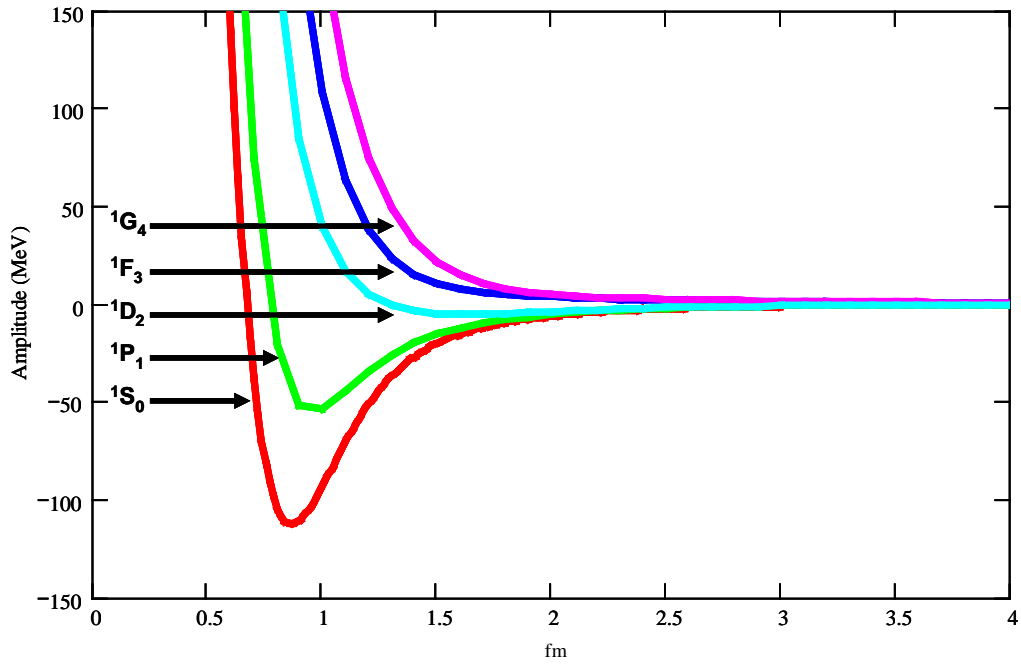


Figure 5.3. Sample AV18 Potentials without Centrifugal Correction

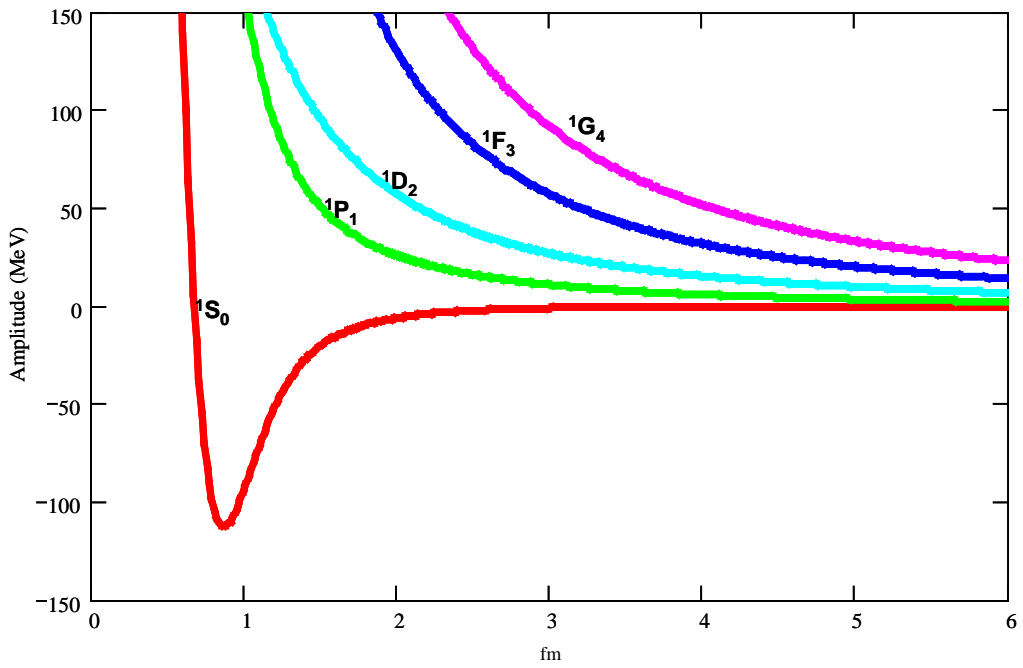


Figure 5.4. Sample AV18 Potentials with Centrifugal Correction

From a simple analysis of the potentials, we can gain some physical insight about the problem. As shown, the angular momentum component quickly dominates at small r . This implies three things. One, resonant features such as multiple peaks in the scattered wave packet should not be expected since there is little evidence of secondary wells in any of the plots. Two, phase shifts should have negative slopes at low L and become positive as L increases. A particle accelerates entering a well yielding a negative phase shift whereas a barrier retards it, producing a positive phase shift. Finally, since the ability to access regions defined by the potential diminishes as the angular momentum increases, values of $J \geq 5$ should contribute minimally to the over determination of the scattering cross section. As a result, values of $J > 5$ do not need to be calculated.

5.4. *Coupled Basis Digitalization*

As shown in the previous section, the Hamiltonian kinetic energy matrix is diagonal in the chosen $|L S J T\rangle$ basis whereas the AV18 potential is block diagonal (Figure 5.2). This mixing of states in the potential, such as between $|0,1,1,0\rangle$ and $|2,1,1,0\rangle$ couples the wave function from one surface to the other. However, it complicates the Fourier transform of the correlation function $C(t)$ from equation (4.25),

$$F(E) = \langle \psi_- | A_+(t) \rangle = \int_{-\tau}^{\tau} \text{Exp} \left[\frac{-i\hat{E}t}{\hbar} \right] C(t) dt \quad (5.28)$$

since exponentiation of a non-diagonal matrix requires additional computational effort.

A useful technique for dealing with an unwieldy adiabatic matrix is to perform a unitary

transformation to an appropriate diabatic¹⁰ basis where the potential is diagonal.

Although, this operation greatly simplifies the exponentiation, there is a problem. The diagonal representation of the potential operator is not the diagonal representation for the kinetic energy operator. So, the same unitary matrix must be applied to recover the original potential's adiabatic representation prior to performing the DFT and the kinetic energy operator, \hat{T} . Since, no coupling will occur between surfaces in the diabatic basis, we must transform back to the adiabatic basis and then repeat the process. Equation (5.29) summarizes the process and identifies when a unitary transformations, U , are required [36-40].

$$\begin{array}{|c|} \hline \text{Adiabatic Coordinate} \\ \text{Representation} \\ \hline \psi(x, t + \Delta t) = \exp \left[-\frac{iV\Delta t}{2\hbar} \right] U^\dagger \text{FFT}_{k \rightarrow x} \left[-\frac{iT\Delta t}{\hbar} \right] \text{FFT}_{x \rightarrow k} U \exp \left[-\frac{iV\Delta t}{2\hbar} \right] \psi(x, t) \\ \hline \end{array} \quad (5.29)$$

¹⁰ In quantum mechanics, “adiabatic” refers to a situation where a system undergoes a gradual change, which leaves the eigenstates unaffected. As an example, consider the simple harmonic oscillations of a pendulum. An “adiabatic” change to the oscillation would occur if the support is moved slowly enough to allow the system to adapt leaving the motion unperturbed [25].

5.5. Energy in the Center of Mass Frame and Lab Frame

Our phase shift calculations are performed in the SF-CM frame whereas published data are generally presented in the laboratory frame. In order to compare our phase shifts to published data, we need to understand how to convert from one frame to the other. This section investigates the relationship between the two reference frames.

Consider the following pictorial diagram of the center of mass and laboratory for a simple 1-D scattering experiment.

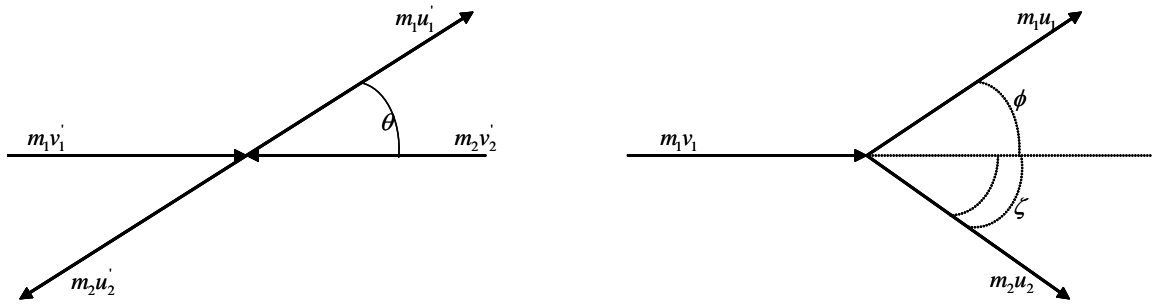


Figure 5.5. Center of Mass vs. Laboratory Frame

Here, primes label the center of mass frame, v label pre-collision velocities, and u labels post collision velocities. Vectors \vec{r}_1 and \vec{r}_2 (not shown) connect the positions of the particles to the origin whereas the vector,

$$\vec{R}_{CM} = \frac{1}{m_1 + m_2} (m_1 \vec{r}_1 + m_2 \vec{r}_2) \quad (5.30)$$

connects the origin to the center of mass of the system. Using definition (5.30) above, we can write the momentum between the two systems as,

$$M \vec{V}_{CM} = (m_1 \vec{v}_1 + m_2 \vec{v}_2) \quad (5.31)$$

where M has been used to label the total system mass $M = m_1 + m_2$. Since the velocity of m_2 in equation (5.31) prior to collision in the lab frame is zero, a relationship between \vec{V}_{CM} and \vec{v}_1 in terms of masses of the particles can be established

$$\vec{V}_{CM} = \frac{m_1}{M} \vec{v}_1. \quad (5.32)$$

Now if we consider the kinetic energy of each system prior to interaction,

$$\begin{aligned} E_{CM} &= \frac{1}{2} M V_{CM}^2 \\ E_{Lab} &= \frac{1}{2} m_1 v_1^2 \end{aligned} \quad (5.33)$$

we can substitute equation (5.32) into (5.33) for \vec{V}_{CM} and arrive at a relationship between the center of mass energy and laboratory frame energy given by,

$$E_{Lab} = \frac{m_1 + m_2}{m_2} E_{CM} \quad (5.34)$$

Since the mass of the proton is approximately the mass of the neutron, about a factor of two in energy exists between the two reference frames. As the mass of the target particle increases, E_{CM} approaches E_{Lab} [70].

5.6. The 1/r Potential

The Scattering Matrix developed in Section 4 was only defined for potentials, which decay at a rate of $\frac{1}{r^2}$ or better. This presents a problem for numerical calculations since a large number of scattering processes, including the pp interaction of interest

here¹¹, involve the Coulombic potential which decays at a rate of $\frac{1}{r}$. As r approaches infinity, the potential still influences particle motion violating the boundary condition that the wave function be stationary in the asymptotic limit. An outline of Taylor's [51] methodology for dealing with the Coulombic tail quandary is summarized here [30, 71-73].

The premise of the solution rests on the awareness that pure Coulombic potentials do not exist in nature. At some distance, other charged particles effectively “screen” the original Coulombic interaction between two particles, suggesting an appropriate way to handle the “well-behaved” potential is to impose some form of cutoff condition. For this discussion, we begin with the radial component of Schrödinger's equation,

$$\left(\frac{d^2}{dr^2} - \frac{L(L+1)}{r^2} - \frac{2\mu V(r)}{\hbar^2} + k^2 \right) u(r) = 0 \quad (5.35)$$

where we have used by using the standard convention $k^2 = \frac{2\mu E}{\hbar^2}$. Here, \hbar is Plank's constant, E is the total energy of the two-particle system, L refers to a particular value of angular momentum, and μ is the reduced mass. Before proceeding to discuss the specifics surrounding the phase shifts induced by the Coulombic or strong force, it is useful to consider asymptotic free motion.

¹¹ $v_{EM}(pp)$ of equation (2.4)

5.6.1. Asymptotic Free Motion

Under the asymptotic free motion assumption, $V(r)$ and $\frac{L(L+1)}{r^2}$ are both set to zero and the radial equation,

$$\left(\frac{d^2}{dr^2} + k^2 \right) u(r) = 0 \quad (5.36)$$

has a solution which is a linear combination of $\sin(kr)$ and $\cos(kr)$

$$u(r) = A \sin(kr) + B \cos(kr) \quad (5.37)$$

where A and B are arbitrary constants. Given that the boundary conditions at $r = 0$ requires $B = 0$, the free solution at large r must be proportional to,

$$u(r) \sim A \sin(kr) \quad (5.38)$$

5.6.2. The Method of Partial Waves

The potentials of interest here are all central in nature and depend on the relative distance r and the angular momentum L that is a constant of the motion. In these cases, it is useful to express the wave function as a product of radial and angular parts and then sum over the contributions of angular momentum L ,

$$\psi(r, \theta) = \sum_{L=0}^{\infty} a_L R_L(r) Y_{L,0}(\theta) \quad (5.39)$$

Here, coefficient a_L refers to the amplitude of each partial wave and $Y_{L,0}(\theta)$ refers to the spherical harmonics which are independent of azimuthal angle. To help understand why the use of partial waves is particularly useful to nuclear scattering, we will examine the impact parameter b .

From classical mechanics, we know that the impact parameter b is defined as the perpendicular distance from the center of force to the velocity vector of the incident particle. The impact parameter b can be expressed in terms of the incident particle's momentum μv and the classical angular momentum l through the relation,

$$b = \frac{l}{\mu v} \quad (5.40)$$

Scatter for higher values of angular momentum are only possible if the impact parameter is less than the range of the potential energy between the two particles [70].

This same concept can be made applicable to quantum mechanics by exchanging the angular momentum l with the eigenvalues of the momentum operator \hat{L} and expressing the momentum in wave vector form as $p = \hbar k$,

$$b = \frac{L(L+1)}{\sqrt{\frac{2\mu E}{\hbar^2}}} \quad (5.41)$$

Here we have chosen to express the wave vector k in terms of energy $k = \sqrt{\frac{2\mu E}{\hbar^2}}$ to make clear the relationship between impact parameter and the energy of the system. Since angular momentum in quantum mechanics can only assume discrete values, we can readily determine the number of partial waves, which may interact with a finite range potential. In Figure 5.6, the horizontal dotted line represents the range of nuclear potential and the curved lines represent the impact parameter $b(E)$ for the first five values of angular momentum. An angular momentum value of zero represents a head on collision between the two particles is not shown. From the diagram, it is clear that partial

waves of $L > 4$ contribute minimally to wave function in equation(5.39) and do not need to be calculated [30, 66, 74, 75].

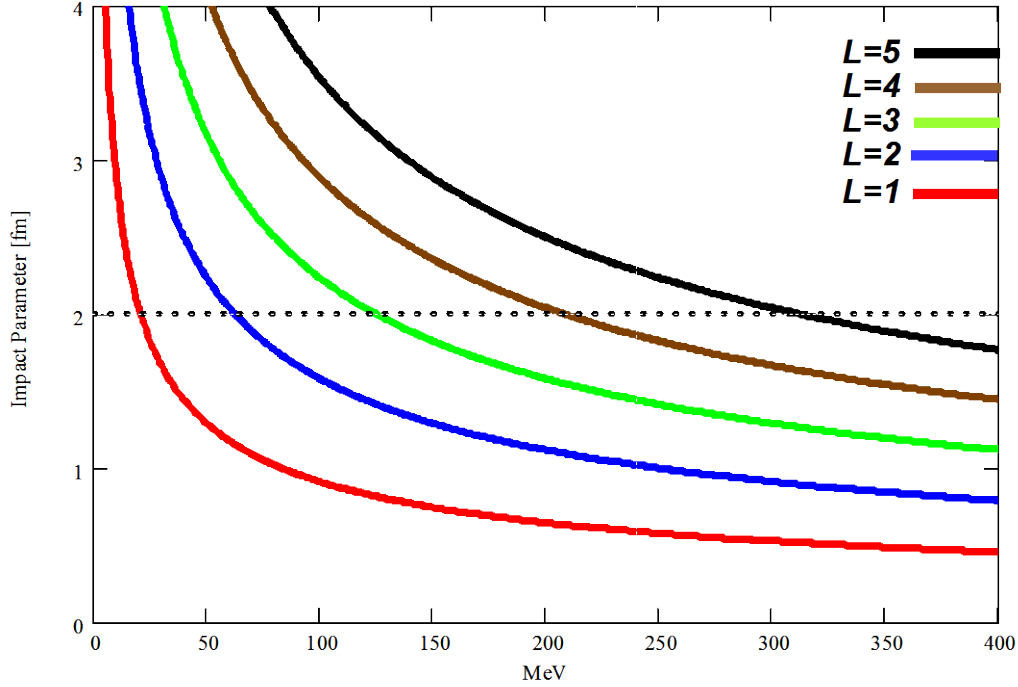


Figure 5.6. Impact Parameters and the Range of the Nuclear Force Range (dotted line)

So now, let us relax our initial asymptotic assumption and allow contributions

from $\frac{L(L+1)}{r^2}$ into the radial equation,

$$\left(\frac{d^2}{dr^2} - \frac{L(L+1)}{r^2} + k^2 \right) u_L(r) = 0 \quad (5.42)$$

If we non-dimensionalize the radial equation by performing a change of variables to $\rho = kr$, we obtain the familiar form of Bessel's differential equation,

$$\left(\rho^2 \frac{d^2}{d\rho^2} + \rho^2 - L(L+1) \right) u_L(\rho) = 0 \quad (5.43)$$

This solution is a linear combination of regular spherical $j_L(\rho)$ and irregular spherical functions $n_L(\rho)$.

$$u_L(\rho) = A_L j_L(\rho) + B_L n_L(\rho) \quad (5.44)$$

As in the asymptotic free case, the irregular solution $n_L(\rho)$ is eliminated through application of the boundary condition $u_L(0) = 0$ leaving,

$$u_L(\rho) = A_L j_L(\rho) \quad (5.45)$$

and an asymptotically form,

$$u_L(\rho) \sim \frac{1}{\rho} \sin\left(\rho - \frac{\pi L}{2}\right) \quad (5.46)$$

The inclusion of additional terms in the argument of the sine function suggests that the effect of introducing a potential into the radial equation is to induce a shift in phase in the solution for large r .

5.6.3. The Coulomb Potential

Having discussed the asymptotic free solution and the method of partial waves, we now consider inclusion of the Coulombic potential,

$$V(r) = \frac{e^2}{4\pi\epsilon_0 r}. \quad (5.47)$$

into the radial equation,

$$\left(\frac{d^2}{dr^2} - \frac{L(L+1)}{r^2} - \frac{2\mu}{\hbar} \frac{e^2}{4\pi\epsilon_0 r} + k^2 \right) u_L(r) = 0 \quad (5.48)$$

Here, ε_0 labels the permittivity of free space and e labels the fundamental charge of the electron. As we desire to present the Coulombic wave equation in a more compact form, it is useful to perform the same change of variables from the previous section $\rho = kr$ and make the substitution $\gamma = \frac{\mu e^2}{4\pi\varepsilon_0\hbar k}$,

$$\left(\frac{d^2}{d\rho^2} + 1 - \frac{2\gamma}{\rho} - \frac{L(L+1)}{\rho^2} \right) u_L(\rho) = 0 \quad (5.49)$$

Abramowitz and Stegun [76] give the solution to this equation for positive ρ , positive integer values of L , and $-\infty < \eta < \infty$ as a linear combination of the regular and irregular logarithmic hyper-geometric functions $F_L(\gamma, \rho)$ and $G_L(\gamma, \rho)$,

$$u_L(\rho) = A_L F_L(\gamma, \rho) + B_L G_L(\gamma, \rho) \quad (5.50)$$

which have the asymptotic property,

$$\begin{aligned} F_L(\gamma, \rho_{\rho \rightarrow \infty}) &\sim \sin\left(\rho - \frac{L\pi}{2} + \delta_L^C - \gamma \ln(2kp)\right) \\ G_L(\gamma, \rho_{\rho \rightarrow \infty}) &\sim \cos\left(\rho - \frac{L\pi}{2} + \delta_L^C - \gamma \ln(2kp)\right) \end{aligned} \quad (5.51)$$

For the pure Coulombic potential, the boundary condition at $r = 0$ requires $B_L = 0$. In equation (5.51) we see two new terms, δ_L^C and $\gamma \ln(2kp)$ as arguments of the sine and cosine functions. The first, δ_L^C is the actual Coulomb phase shift for the L^{th} partial wave,

$$\delta_L^C = \arg \Gamma(L+1+i\gamma) \quad (5.52)$$

and the other $\gamma \ln(2kp)$ is a Coulomb cutoff phase correction designed to compensate for the infinite range of the nuclear force where $p=r$ is the cutoff radius. The rationale

behind imposing a cutoff condition becomes clear when we consider that pure Coulombic potentials do not exist in nature. At some point, the Coulombic potential between two bodies is effectively screened by a Coulombic potential of another charged particle. For example in the classic Rutherford scattering experiment, the Coulomb field from gold nuclei was completely shielded by atomic electrons after a few angstroms [51]. Since now imposing a cutoff condition seems reasonable, the question remains at which point do we impose the cutoff. The answer is that the cutoff point is somewhat arbitrary as Figure 5.7 shows.

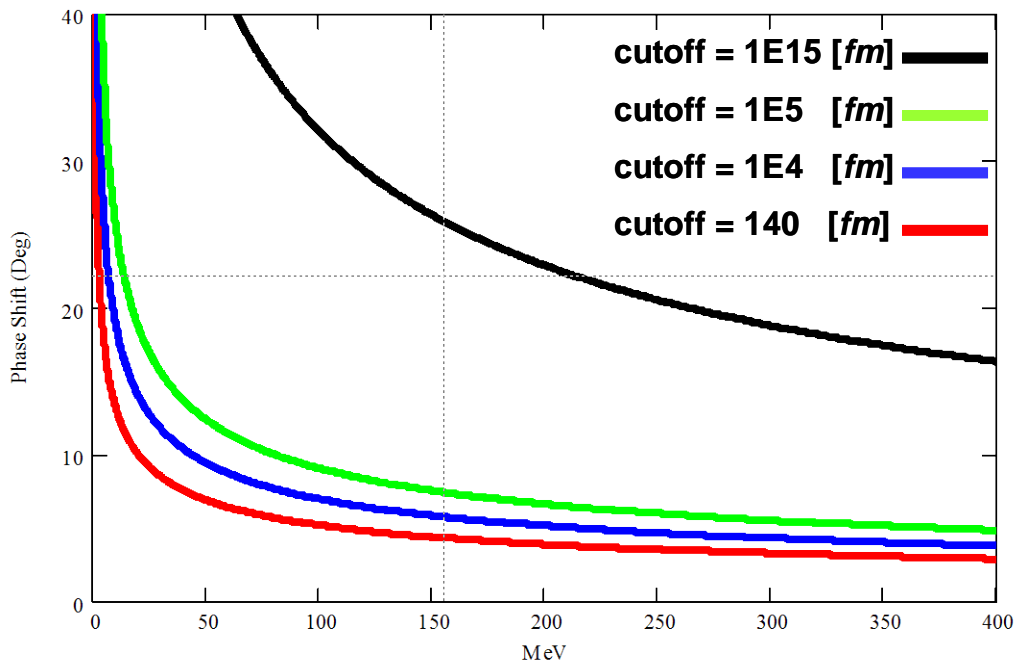


Figure 5.7. Coulombic Phase Corrections at 140 fm, 1000 fm, 10000 fm, and 1m. Coulombic corrections to the phase shifts do not vary greatly over small variations in r .

Coulombic phase corrections simply do not vary greatly with small variations in r . So here, we make the convenient choice of the V_{AV18} cutoff point of $p = 140$ fm.

5.6.4. The Coulomb Plus Short Range Potential

In the last section, we considered scattering from a pure Coulombic potential.

Now we wish to examine the implications of adding a short-range potential $V_{SR}(r)$ to the Coulombic term,

$$V(r) = \frac{e^2}{4\pi\epsilon_0 r} + V_{SR}(r). \quad (5.53)$$

Since we are adding a short-range potential to the Coulombic potential, we would expect the solution would appear as a small perturbation to the Coulombic solution. A useful way of representing this perturbation is to admit contributions from $G_L(\gamma, \rho_{\rho \rightarrow \infty})$ into the asymptotic solution,

$$u(\theta) \sim A \sin(\theta) + B \cos(\theta) \quad (5.54)$$

Here we have made the substitution $\theta = \rho - \frac{L\pi}{2} + \delta_L^C - \gamma \ln(2kp)$. Equation (5.54) can be

written in terms of exponentials

$$u(\theta) \sim \frac{(Ae^{i\theta} - Ae^{-i\theta})}{2i} + \frac{(Be^{i\theta} + Be^{-i\theta})}{2} \quad (5.55)$$

converted to polar form with magnitude $|A \pm iB|^{1/2}$ and phase $\nu = \tan^{-1}\left(\frac{B}{A}\right)$ to yield

$$u(\theta) \sim \frac{|A + iB|^{1/2} e^{i\nu} e^{i\theta}}{2i} + \frac{|A - iB|^{1/2} e^{-i\nu} e^{-i\theta}}{2i} \quad (5.56)$$

Since the scattering matrix is unitary, the magnitudes above are one and we have,

$$u(\theta) \sim \frac{e^{i(\theta+\nu)} - e^{-i(\theta+\nu)}}{2i} \sim \sin(\theta + \nu) \quad (5.57)$$

This implies that the asymptotic solution for a Coulombic potential modified by a short-range potential has the asymptotic form,

$$u_L(\gamma, \rho_{\rho \rightarrow \infty}) \sim \sin\left(\rho - \frac{L\pi}{2} + \delta_L^c - \gamma \ln(2kp) + \nu_L\right) \quad (5.58)$$

and overall phase shift δ_L is given by

$$\delta_L = \delta_L^c - \gamma \ln(2kp) + \nu_L \quad (5.59)$$

The term ν_L represents the additional phase shifts introduced by all short-range forces and should not be confused with the phase shift due to short-range forces alone [51]. For pp scattering, ν_L , the phase shift from the short range forces alone, is reported. In order to obtain the computed pp short-range phase shift, ν_L , for comparison to published data, a correction must be applied to the total phase shift δ_L obtained from our nuclear CPM pp calculations,

$$\nu_L = \delta_L - \delta_L^c + \gamma \ln(2kp) \quad (5.60)$$

5.7. Nuclear Units

In order to perform channel packet method calculations, a system of units must be defined. As all previous calculations utilizing the CPM have been performed on the Atomic Level, the traditional choice of units were the atomic units (See Table 5.1)

Table 5.1. Selected Atomic Units

	Designation	MKS Equivalent
Length	a_0	5.291772×10^{-11} [meters]
Mass	m_e	9.105953×10^{-31} [kg]
Angular Momentum	\hbar	1.054571×10^{-34} [J] [sec]
Energy	E_H	4.359744×10^{-18} [J]
Time	\hbar / E_H	2.418884×10^{-17} [sec]

where the unit of length is based on the Bohr Radius, the unit of mass on the rest mass of the electron, angular momenta are measured in units of \hbar and the unit of energy is the *hartree* (27.211 eV); twice the ionization energy of the hydrogen ground state electron. The atomic unit of time is a derived quantity based on \hbar and the *hartree*. These traditional units are ill suited for nuclear calculations since both the masses and energies involved are several orders of magnitude larger than those encountered in an atomic calculation.

In order to form a set of units, three base units must be considered, mass, length and time. The dimensions of the nuclear potential give insight to a natural unit selection. Width is measured in femtometers (*fm*) and the depth is measured in *MeV*. If we trade the mass for energy, we have only one more parameter to fix. Employing the useful atomic convention of setting \hbar to one, the nuclear unit of time may be derived from the uncertainty relation,

$$E\Delta t \leq \hbar = 1 \quad (5.61)$$

The nuclear unit of mass may then be obtained from our definition time, length and energy. Conversion factors between MKS and our derived units are included in Table 5.2 and values for nuclear masses are included in Table 5.3.

Table 5.2. Nuclear Units

	Designation	MKS Equivalent
Length	fm	1×10^{-15} [meter]
Mass	m_v	6.941×10^{-26} [kg]
Angular Momentum	\hbar	1.054571×10^{-34} [J][sec]
Energy	MeV	1.602×10^{-13} [J]
Time	$\tau_v = \hbar / MeV$	6.582×10^{-22} [sec]

Table 5.3. Nuclear Masses

	Designation	Value
Neutron Mass	m_n	$0.02412982 m_v$
Proton Mass	m_p	$0.02409661 m_v$
Neutron-Proton Reduced Mass	μ_{pn}	$0.01205660 m_v$
Neutron-Neutron Reduced Mass	μ_{nn}	$0.01206491 m_v$
Proton - Proton Reduced Mass	μ_{pp}	$0.01204830 m_v$

5.8. *S*-Matrix Parameterizations

As we saw in the matrix representation of V_{eff} back in Figure 5.2, a mixing between two states of different orbital angular momenta is possible in the $|L,S,J,T,R\rangle$ basis. The first mixing between the 3S_1 and 3D_1 states is shown in Figure 5.8.

$$\begin{array}{c}
 \langle L',S',J',T' | V_{eff} | L,S,J,T \rangle \quad |0,1,1,0\rangle \quad |2,1,1,0\rangle \\
 \begin{array}{c}
 \langle 0,1,1,0 | \\
 \langle 2,1,1,0 |
 \end{array}
 \begin{pmatrix}
 {}^3S_1 & \varepsilon_1 \\
 \varepsilon_1 & {}^3D_1
 \end{pmatrix}
 \end{array}$$

Figure 5.8. Mixing Between 3S_1 and 3D_1 States

The S-Matrix associated with this 2x2 block will also be a 2x2 since there is a possibility of transition from 3S_1 to 3D_1 and from 3D_1 to 3S_1 in addition to the possibility of reflection back into original states. Although many parameterizations of this 2x2 S-matrix block could exist, only two are repeatedly found in the literature; the Stapp, Ypsilatis, and Metropolis “bar” [18] and the Blatt/Biedenharn “eigen” [14] parameterizations.

Blatt and Biedenharn proposed viewing the symmetric 2x2 matrix in its most natural eigen-basis form,

$$S = \begin{pmatrix} \cos(\varepsilon_j) & -\sin(\varepsilon_j) \\ \sin(\varepsilon_j) & \cos(\varepsilon_j) \end{pmatrix} \begin{pmatrix} e^{2i\delta_{l=j+1}} & 0 \\ 0 & e^{2i\delta_{l=j-1}} \end{pmatrix} \begin{pmatrix} \cos(\varepsilon_j) & \sin(\varepsilon_j) \\ -\sin(\varepsilon_j) & \cos(\varepsilon_j) \end{pmatrix} \quad (5.62)$$

$$S = \begin{pmatrix} e^{2i\delta_{l=j+1}} \cos^2(\varepsilon_j) + e^{2i\delta_{l=j-1}} \sin^2(\varepsilon_j) & \cos(\varepsilon_j) \sin(\varepsilon_j) (e^{2i\delta_{l=j-1}} - e^{2i\delta_{l=j+1}}) \\ -\cos(\varepsilon_j) \sin(\varepsilon_j) (e^{2i\delta_{l=j-1}} - e^{2i\delta_{l=j+1}}) & e^{2i\delta_{l=j-1}} \cos^2(\varepsilon_j) + e^{2i\delta_{l=j+1}} \sin^2(\varepsilon_j) \end{pmatrix} \quad (5.63)$$

This unitary transformation can be thought of as a series of rotations where U is a function of the mixing parameter, ε_j and δ are the phase shifts of the eigen-state associated with a specific J state. Although on the surface it would seem to be the most natural basis for presenting the phase shift information, difficulties exist in separating the Coulombic and strong contributions for the pp triplet state. Thus, most phase-shift analyses are performed with the “barred” parameterization,

$$S = \begin{pmatrix} e^{i\bar{\delta}_{l=j-1}} & 0 \\ 0 & e^{i\bar{\delta}_{l=j+1}} \end{pmatrix} \begin{pmatrix} \cos(2\bar{\varepsilon}_j) & i \sin(2\bar{\varepsilon}_j) \\ -i \sin(2\bar{\varepsilon}_j) & \cos(2\bar{\varepsilon}_j) \end{pmatrix} \begin{pmatrix} e^{i\bar{\delta}_{l=j-1}} & 0 \\ 0 & e^{i\bar{\delta}_{l=j+1}} \end{pmatrix} \quad (5.64)$$

$$S = \begin{pmatrix} \cos(2\bar{\varepsilon}_j) e^{2i\bar{\delta}_{l=j-1}} & i \sin(2\bar{\varepsilon}_j) e^{i(\bar{\delta}_{l=j-1} + \bar{\delta}_{l=j+1})} \\ i \sin(2\bar{\varepsilon}_j) e^{i(\bar{\delta}_{l=j-1} + \bar{\delta}_{l=j+1})} & \cos(2\bar{\varepsilon}_j) e^{2i\bar{\delta}_{l=j+1}} \end{pmatrix}. \quad (5.65)$$

where the three parameters, $\bar{\delta}_{l=j-1}$, $\bar{\delta}_{l=j+1}$, and $\bar{\varepsilon}_j$, are the parameters that are generally reported. Since the unbarred phase shifts are required in the determination of the total cross section, the following transformations between representations are often useful,

$$\begin{aligned} \bar{\delta}_{l=j-1} + \bar{\delta}_{l=j+1} &= \delta_{l=j-1} + \delta_{l=j+1} \\ \sin(\bar{\delta}_{l=j-1} - \bar{\delta}_{l=j+1}) &= \frac{\tan(2\bar{\varepsilon}_j)}{\tan(2\varepsilon_j)} \\ \sin(\delta_{l=j-1} - \delta_{l=j+1}) &= \frac{\sin(2\bar{\varepsilon}_j)}{\sin(2\varepsilon_j)} \end{aligned} \quad (5.66)$$

5.9. 1-D Sample Calculation – Square Well Potential

It is often useful to first calculate and validate a new technique against a problem that has a known analytic solution. In this case we use an asymmetric square well of roughly the same dimensions as the actual nuclear potentials under investigation (Figure 5.9). This test verifies operation of all CPM modules except the 2x2 module. Section 5.9.1 will first develop the general form for an analytic solution for a square well of arbitrary dimensions then apply the formalism to the test case. Section 4.9.2 will develop the analogous CPM solution. Results are compared in section 4.9.3.

$$V(x) = \left\{ \begin{array}{ll} 3000 \text{ MeV} & \text{if } x \leq 0.65 \text{ fm} \\ 0 \text{ MeV} & \text{if } x > 1.65 \text{ fm} \\ -100 \text{ MeV} & \text{otherwise} \end{array} \right\} \quad (5.67)$$

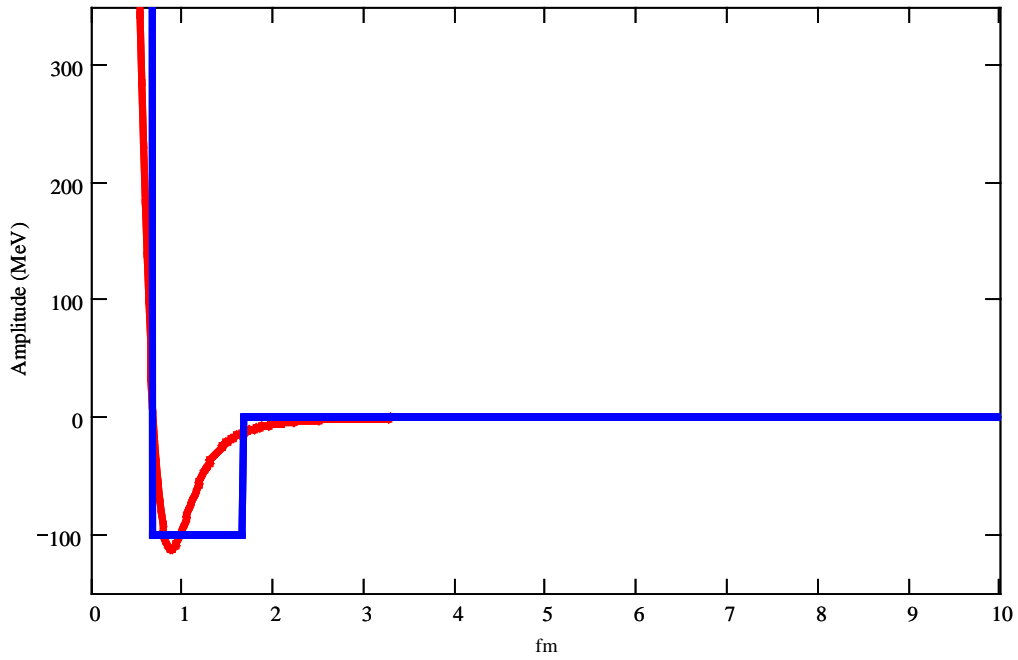


Figure 5.9. Square Well Approximation to 1S_0 Potential. The dimensions of the well were adjusted to the 1S_0 potential to provide a method of validating the Channel Packet Method algorithm against a known solution prior to propagating with actual AV18 model.

5.9.1. Analytic Solution

Consider the following generic square well problem,

$$V(x) = \begin{cases} V_I & \text{if } x < a \\ V_{II} & \text{if } a \leq x \leq b \\ V_{III} & \text{if } b < x \end{cases} \begin{matrix} \text{Region I} \\ \text{Region II} \\ \text{Region III} \end{matrix} \quad (5.68)$$

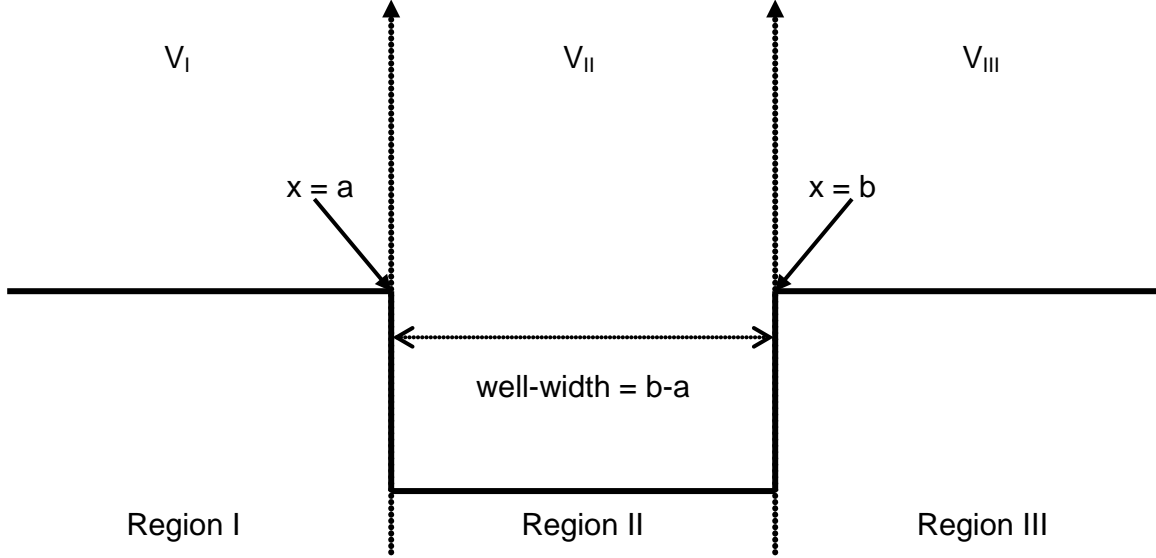


Figure 5.10. 1-D Square Well Schematic Diagram

Here, solutions to the time independent Schrödinger's equation, $\hat{H}\psi = (\hat{T} + \hat{V})\psi = \hat{E}\psi$, for each region are given by,

$$\langle x | \psi \rangle = \psi_R(x) = A_R \exp[ik_R x] + B_R \exp[-ik_R x], \quad (5.69)$$

where,

$$k_R = \frac{\sqrt{2\mu(E - V_R)}}{\hbar}, \quad (5.70)$$

and R refers to regions I , II , or III . Since the Schrödinger's equation is a second order differential equation, continuity must exist at the boundary between regions I/II and regions II/III for both ψ and its first derivative. Thus, we have the pair of transfer matrices.

$$\begin{bmatrix} A_I \\ B_I \end{bmatrix} = M_{I,II} \begin{bmatrix} A_{II} \\ B_{II} \end{bmatrix} = \begin{pmatrix} \alpha & \beta \\ \beta^* & \alpha^* \end{pmatrix} \begin{bmatrix} A_{II} \\ B_{II} \end{bmatrix} \quad (5.71)$$

$$\begin{bmatrix} A_{II} \\ B_{II} \end{bmatrix} = M_{II,III} \begin{bmatrix} A_{III} \\ B_{III} \end{bmatrix} = \begin{pmatrix} c & d \\ c^* & d^* \end{pmatrix} \begin{bmatrix} A_{III} \\ B_{III} \end{bmatrix} \quad (5.72)$$

where

$$\alpha = \frac{1}{2} \left(1 + \frac{k_2}{k_1} \right) \exp(i a (k_2 - k_1)) \quad (5.73)$$

$$\beta = \frac{1}{2} \left(1 - \frac{k_2}{k_1} \right) \exp(-i a (k_2 + k_1)) \quad (5.74)$$

$$c = \frac{1}{2} \left(1 + \frac{k_3}{k_2} \right) \exp(i b (k_3 - k_2)) \quad (5.75)$$

$$d = \frac{1}{2} \left(1 - \frac{k_3}{k_2} \right) \exp(-i b (k_3 + k_2)) \quad (5.76)$$

These matrices can be combined; eliminating two of the six unknown coefficients to create a scattering matrix between regions I/III,

$$\begin{pmatrix} B_I \\ A_{III} \end{pmatrix} = \begin{pmatrix} S_{11} & S_{12} \\ S_{21} & S_{22} \end{pmatrix} \begin{pmatrix} A_I \\ B_{III} \end{pmatrix} \quad (5.77)$$

where the components of S are expressed in terms of $\alpha, \beta, c,$ and d and A_I (B_{III}) refers to the incident amplitude from the left (right) and A_{III} (B_I) refers to the outgoing amplitude A_{III} to the left (right).

Now if we select our incident wave packet to be incident from the right, A_I is zero and only two scattering matrix elements must be considered; the transmitted amplitude to the left, S_{12} and reflected amplitude to the right S_{22} ,

$$S_{12} = \frac{(\alpha^* c^* + \beta^* d)(\alpha c + \beta d^*) - (\alpha^* d^* + \beta^* c)(\alpha d + \beta c^*)}{(\alpha c + \beta d^*)} \quad (5.78)$$

$$S_{22} = -\frac{(\alpha d + \beta c^*)}{(\alpha c + \beta d^*)}, \quad (5.79).$$

So far, the discussion has been limited to the generic square well. Our asymmetric square well approximation for the nuclear well from Figure 5.9, however, has a barrier. Here, the potential, V_1 , at $x = a$ is considered to be sufficiently large enough to minimize transmission. S_{12} is zero. With only one remaining element to consider, the determination of the reflected analytical phase shift is straightforward via application of equation (5.79),

$$\delta_{analytic_{22}} = \frac{\tan\left(\frac{im(S_{22})}{re(S_{22})}\right)}{2} \quad (5.80)$$

where,

$$S_{22} = \frac{(k_2 + k_1)(k_2 - k_3)e^{(ia(k_2 - k_1) - ib(k_3 + k_2))} + (k_1 - k_2)(k_2 + k_3)e^{(-ia(k_2 + k_1) - ib(k_3 - k_2))}}{(k_2 + k_1)(k_2 + k_3)e^{(ia(k_2 - k_1) - ib(k_2 - k_3))} + (k_2 - k_1)(k_3 - k_2)e^{(-ia(k_2 + k_1) + ib(k_3 + k_2))}} \quad (5.81)$$

5.9.2. CPM Solution

For CPM calculations, a useful choice is a complex Gaussian for $|\psi_{in(out)}\rangle$

$$\psi(x, t) = \left(\frac{\zeta^{-2}}{2\pi\Delta x_0^2}\right)^{1/4} \text{Exp}\left[\zeta^{-1}\left(\frac{-(x - x_0)^2}{4\Delta x_0^2} + ik_0(x - x_0) - i\omega t\right)\right] \quad (5.82)$$

$$\zeta = 1 + \frac{i\hbar t}{2\mu\Delta x_0^2}, \quad \omega = \frac{\hbar^2 k^2}{2\mu}$$

because it is simple in form and can be analytically propagated. Since CPM calculations involve both the coordinate and momentum spaces, choosing this form provides an analytic means of verifying numerical propagation techniques in the absence of an

interaction potential. In the above equation, t labels to time, \hbar labels Plank's constant, μ labels the reduced mass of the two nucleons, k labels the wave vector, x_0 labels the initial packet position, k_0 labels the initial momentum, and Δx_0^2 labels the wave-packet spread.

Although any position on the coordinate grid may be chosen for the initial complex Gaussian product (reactant) wave-packets, we choose to center both wave-packets peaks, designated $x1_0$ and $x2_0$ respectively, at 30 fm as shown in Figure 5.11 and proceed to find optimal values for the wave-packets propagation.

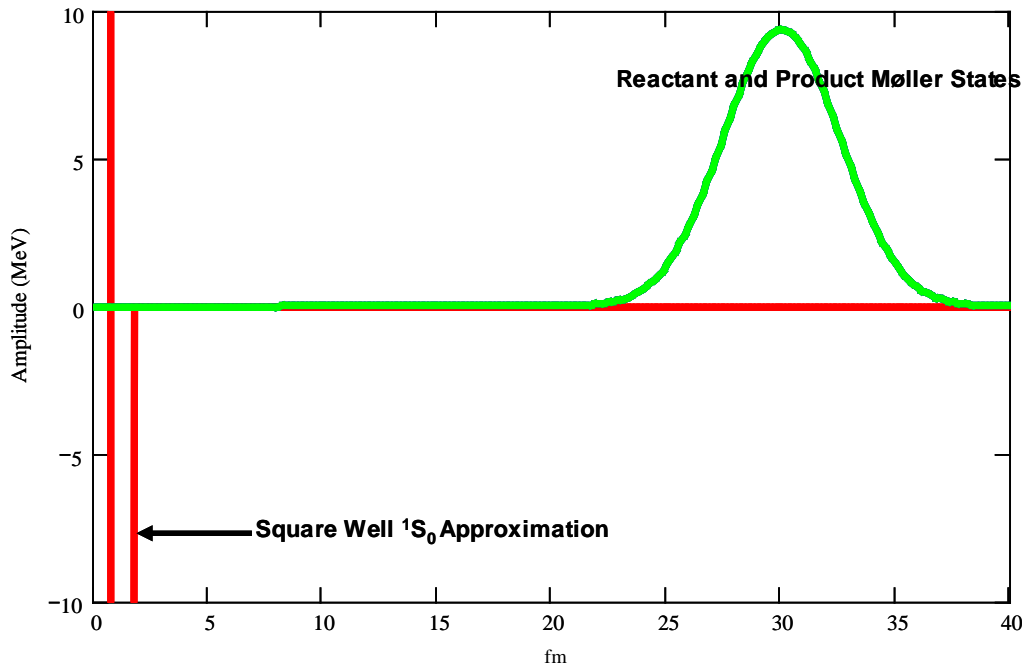


Figure 5.11. Scaled Wave Packets at $t=0$ in Coordinate Representation.

If we consider the time-independent form of equation (5.82),

$$\psi(x, 0) = \left(\frac{1}{2\pi\Delta x_0^2} \right)^{1/4} \text{Exp} \left[\left(\frac{-(x-x_0)^2}{4\Delta x_0^2} + ik_0(x-x_0) \right) \right] \quad (5.83)$$

and its momentum space complement,

$$\varphi(k, 0) = \left(\frac{2\Delta x_0^2}{\pi} \right)^{1/4} \text{Exp} \left[\left(-\Delta x_0^2(k-k_0)^2 + ikx_0 \right) \right] \quad (5.84)$$

it is evident that a decrease in coordinate space wave-packet's spread, Δx , corresponds to an increase in momentum space wave-packets spread. Equations (5.83) and (5.84) were plotted using Δx values of 2.474 fm , 1.814 fm , and 1.154 fm to help identify an appropriate choice for Δx given our chosen 1600 fm coordinate space and our desired $0\text{-}400 \text{ MeV}$ energy range. These are shown in Figure 5.12.

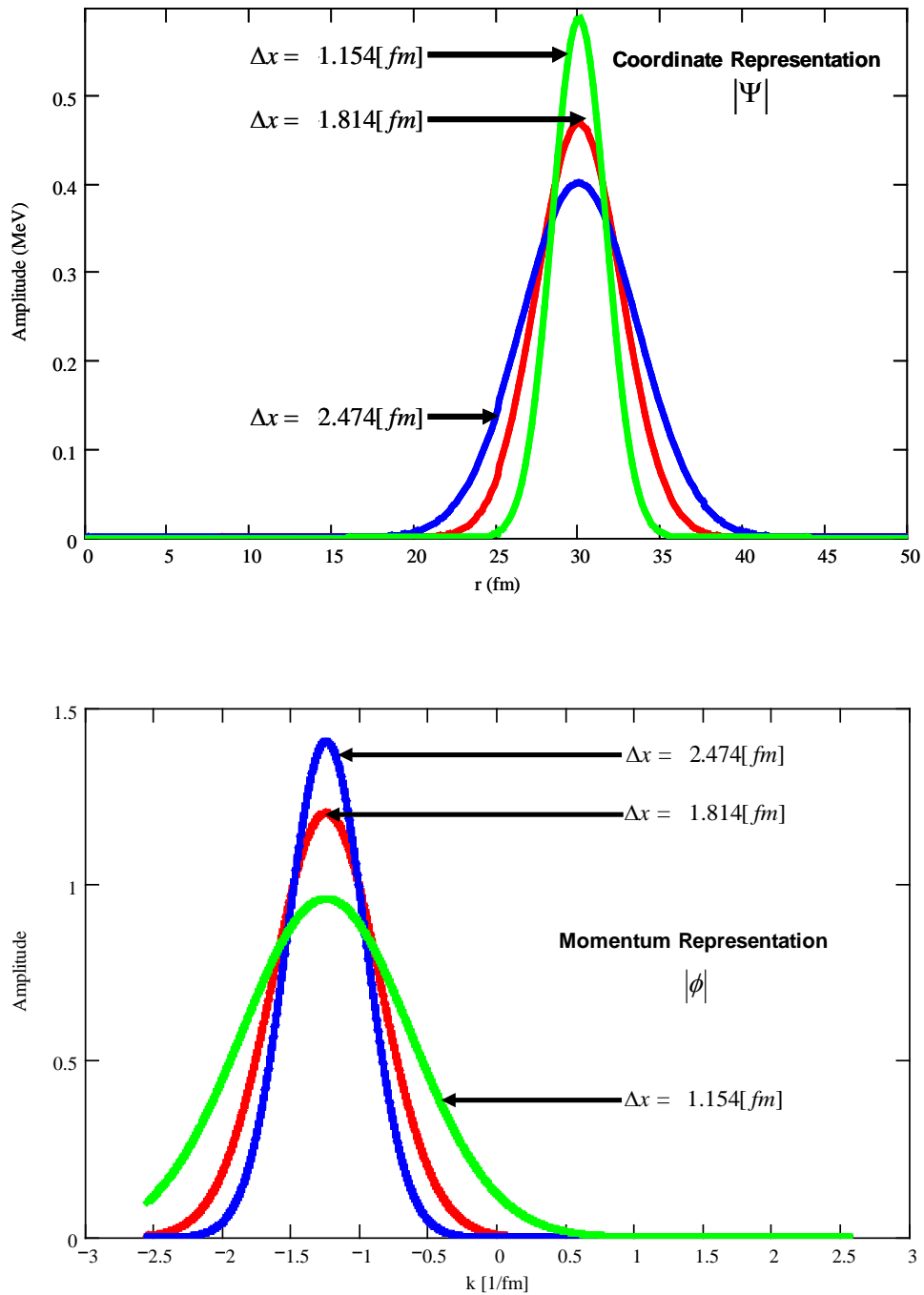


Figure 5.12. The Coordinate Representation (top frame) and Momentum Representation (bottom frame) of the Same Three Wave Packets. A decrease in coordinate space wave packet spread constitutes an increase in the wave packet spread in the momentum space complementary wave packet. Both representations must be monitored to ensure the wave packets fit on the available grid space.

For a Δx of 2.474 fm , the wave-packet amplitude tends to zero at k values of approximately $-2.0 [1/\text{fm}]$ and $-0.5 [1/\text{fm}]$. The effective energy range may be estimated from these k values and the reduced mass, μ , of the interacting pair via,

$$E = \frac{\hbar^2 k^2}{2\mu}. \quad (5.85)$$

So for this particular choice of Δx , an effective energy range between 20 MeV and 330 MeV is obtained. Although this is a perfectly acceptable selection, what is desired is a slightly wider energy range. So, a narrower Δx would be a better choice.

Now, consider Δx of 1.154 fm . Figure 5.12 illustrates two problems with this choice. The first, rather obvious, problem is that the wave-packet does not fit on the selected grid space. The second is a little more subtle. Note that the right side of the wave-packet tends to zero past the point of zero momentum in the positive momentum region. Since this wave-packet contains both positive and negative momentum components, the wave-packet will split. The negative components will probe the potential whereas the positive components will leave the interaction region. In other words, the reflection amplitude of the S-matrix elements will no longer be one and the information necessary to compute the correct phase shift will be lost. Here, the most useful choice for Δx is 1.814 fm as it both fits on the grid space and has an energy range from about 5 MeV to about 420 MeV . The remaining parameters pertaining to this calculation are summarized in Table 5.4.

Table 5.4. 1-D Scattering Parameters

Parameter	Quantity	Units
Mass	0.01201	m_v
x max	1600	fm
k max	2.56	$1/fm$
Coordinate Points	213	
Coordinate Step Size	0.195	fm
τ_{max}	20	τ_v
Temporal Points	218	
Time Step	7.63×10^{-5}	τ_v
<i>Initial Coordinate Reactant Wave-Packet Position ($x1_0$)</i>	30	fm
<i>Initial Coordinate Product Wave-Packet Position ($x2_0$)</i>	30	fm
<i>Initial Reactant Momentum ($k1_0$)</i>	-1.253	$1/fm$
<i>Initial Product Momentum ($k1_0$)</i>	1.253	$1/fm$
Packet Spread (Δx)	1.814	fm

Since no portion of the wave-packet resides within the potential, the requirement to first propagate the wave-packets to the asymptotic limit under the channel asymptotic Hamiltonian and back under the full channel Hamiltonian is eliminated. For this problem, these are our Møller states of equation (4.8).

To calculate S-Matrix elements, a FORTRAN wave-packet propagation code was developed. Snapshots of the reactant wave-packet's time evolution are provided in Figure 5.13- Figure 5.16 with absolute values shown for clarity.

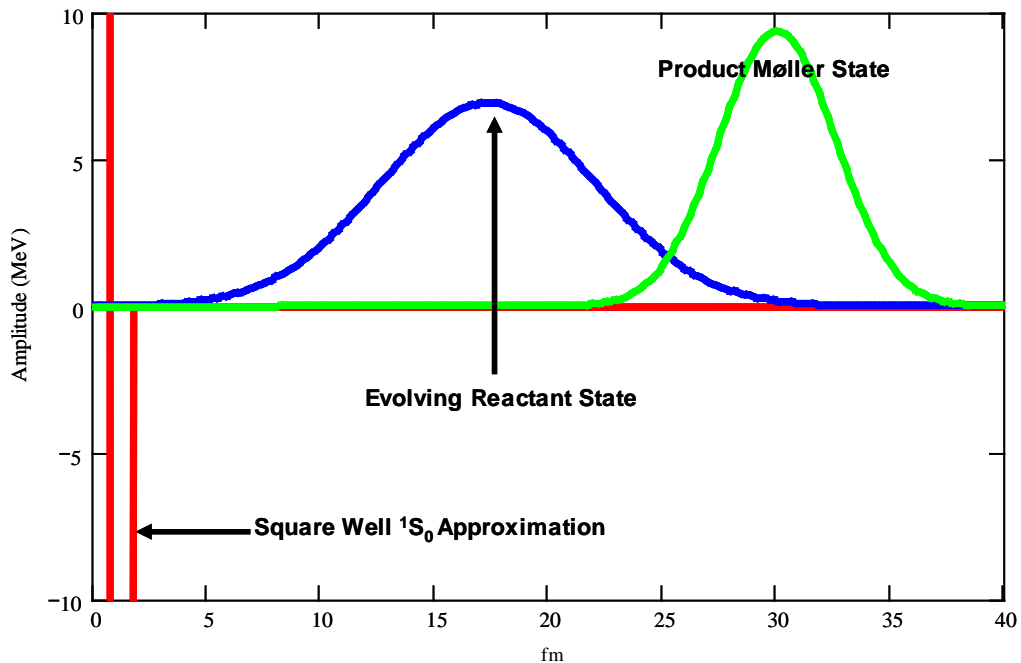


Figure 5.13. Scaled Evolving Wave Packet at $0.122 \tau_v$. The evolving wave packet has left its initial position and has traversed half the distance to square well. Absolute Values are Plotted

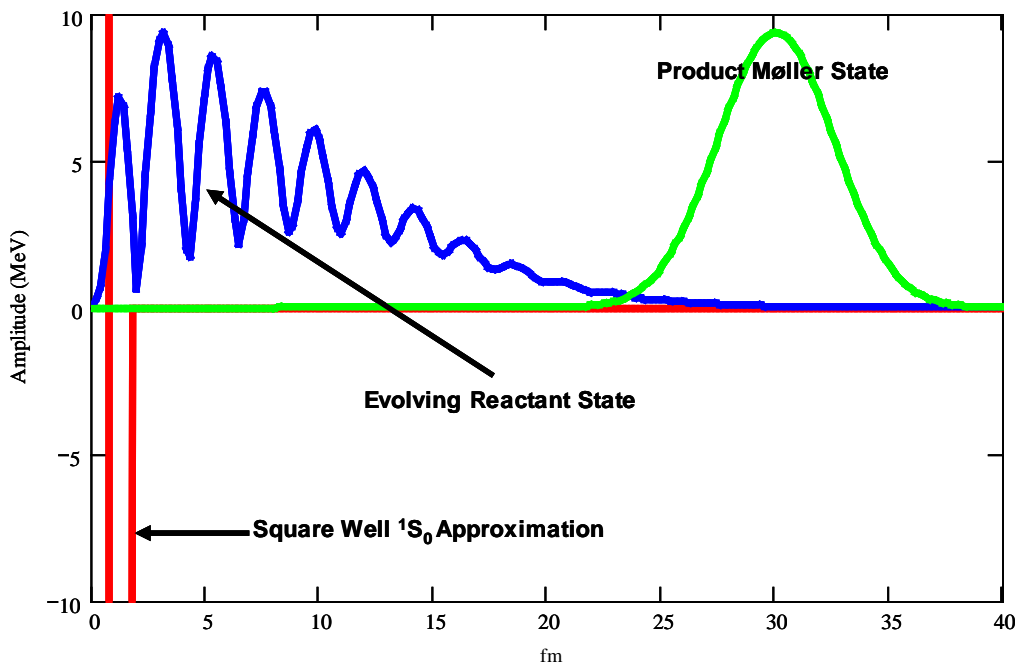


Figure 5.14. Wave Packet Propagation at $0.244 \tau_v$. The evolving wave packet has begun interacting with the square well. No evidence of bifurcation is present.

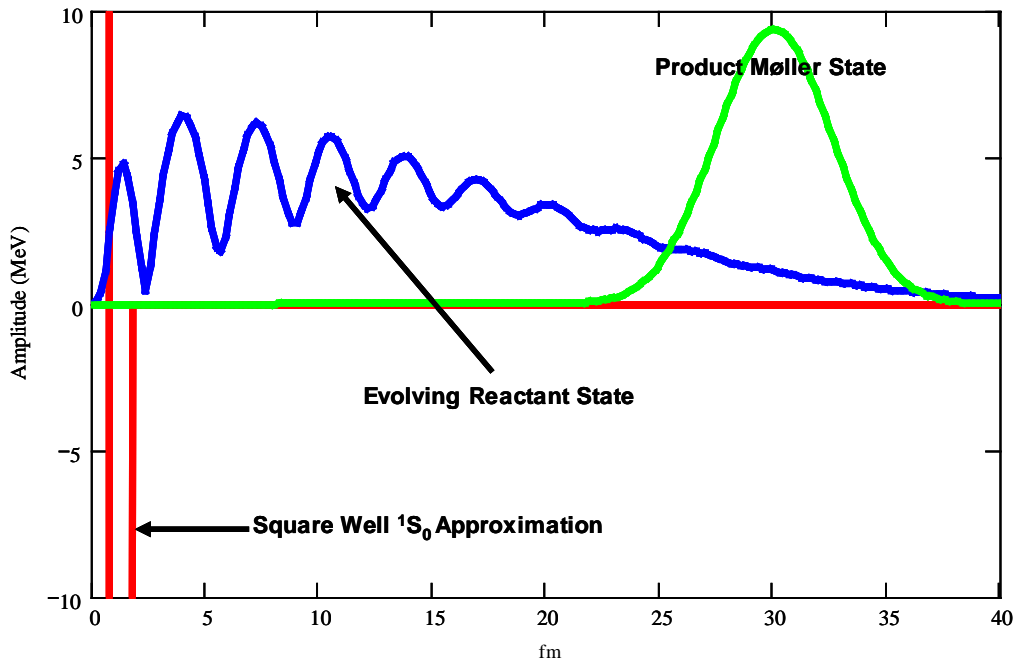


Figure 5.15. Wave Packet Propagation at $0.366 \tau_v$. The higher energy components of the wave packet have left the interaction region and are returning to the initial position so that the correlation with the product wave packet may be computed.

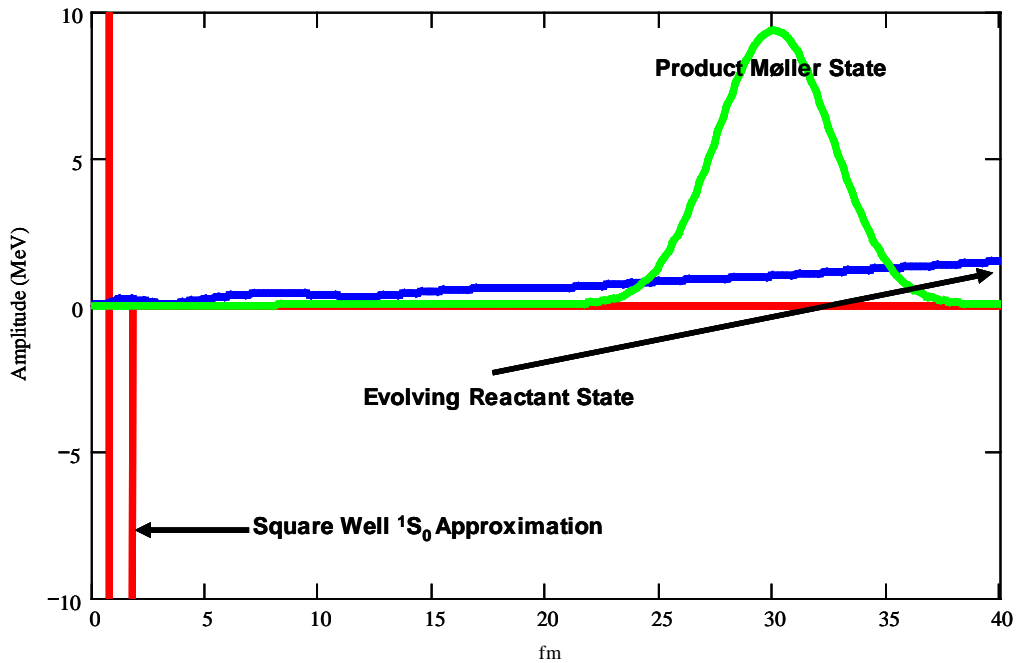


Figure 5.16. Wave Packet Propagation at 0.977. With the exception of the lowest energy components, the wave packet has all but left the interaction region.

In the first frame, the wave-packet peak has advanced under the full Hamiltonian from $t=0$ approximately 13 fm toward the potential. At this point, no useful data has been collected as the wave-packet has not yet entered the interaction region. By the second frame ($0.244 \tau_v$), the higher momentum components of the wave packet have reached the interaction region and collided with the barrier. Here, the total energy within the well area climbs as kinetic energy is exchanged for potential energy. No evidence of bifurcation is apparent. Later at $0.366 \tau_v$, the wave-packet after collision is shown beginning to exit the area having collected information about the potential. At each time step, the correlation function $C(t)$ is determined by taking the scalar product between the evolving wave-packet and the product Møller state. By $0.977 \tau_v$ (Figure 5.16), the calculation is essentially complete as all but the lower momentum components have exited.

From the correlation function $C(t)$ between the evolving reactant state and the stationary product state recorded at each time step, we obtain the correlation function as a function of energy by taking the Fourier Transform

$$\langle \psi_- | A_+(E) \rangle = \int_{-\tau}^{\tau} \text{Exp} \left[\frac{-i\hat{E}t}{\hbar} \right] C(t) dt \quad (5.86)$$

S-matrix elements,

$$S_{-k,+k}(E) = \frac{\hbar |k(E)|}{2\pi\mu\eta_-^*(-k(E))\eta_+(+k(E))} \langle \psi_- | A_+(E) \rangle \quad (5.87)$$

are then computed by expressing both k and the reactant/product initial expansion coefficients $\eta_{\pm}[k]$ in the momentum representation as a function of energy,

$$k(E) = \frac{\sqrt{2\mu E}}{\hbar} \quad (5.88)$$

$$\eta(k(E)) = \left(\frac{2}{\pi} \Delta x^2\right)^{1/4} \exp\left[-(k(E) - k_0)^2 \cdot \Delta x^2 + ik(E)x_0\right] \quad (5.89)$$

The $\eta_{\pm}[k]$ s are determined analytically from the Gaussian wave function which defined our initial states at $t = 0$ (equation(5.82)). Here, k_0 and x_0 refer to the respective initial conditions for each wave-packet from Table 5.4.

The overlap between initial expansion coefficients $\eta_{\pm}[k(E)]$, the wave vector $k_{\mp}(E)$, and the Fourier transform of the correlation function $\langle \psi_{-} | A_{+}(E) \rangle$ are shown in Figure 5.17.

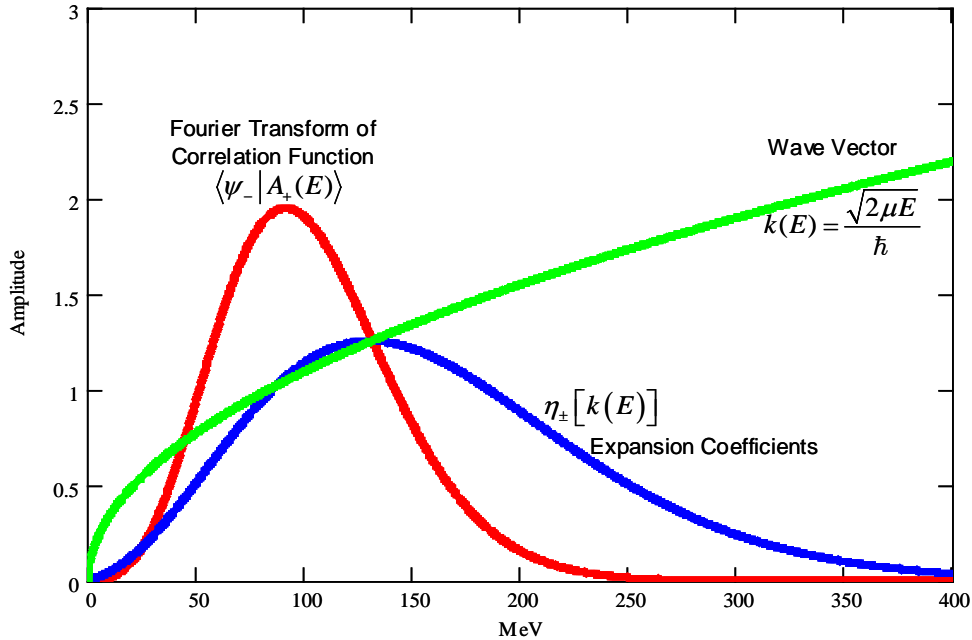


Figure 5.17. Scaled Overlap of equation (5.87) components as a function of Energy. Since the correlation function can rise much faster than the product of the expansion coefficients a division error is possible at low energies. How to deal with low energy calculations is discussed in Section 6.

Clearly, a division error resulting from dividing a larger number by a smaller number exists at low energies since the Fourier Transform of the correlation function can rise much faster than the product of the initial expansion coefficients in the denominator of equation (5.87). Methods for dealing with low energy resolution will be discussed in Chapter 6 where low energy phase shifts are investigated.

An issue may arise during the calculation of the correlation function between the dispersing wave-packet and the periodic nature of the Fourier transform. When the dispersing wave-packet crosses the grid boundary, the transform will cause the exiting wave-packet to reemerge from the opposite boundary and continue propagating across the same grid space. If this occurs before the dot product of the reactant wave-packet's trailing edge and product Møller state is negligible, the leading edge will introduce non-physical anomalies into the correlation calculation. This non-desirable situation can precipitate construction of larger and larger coordinate grid spaces to compensate, which is not computationally advantageous. Fortunately, a proven workaround does exist, the inclusion of an absorbing boundary condition.

An absorbing boundary condition is a useful tool often employed to compensate for this phenomenon. To employ this technique, the interaction potential operator, \hat{V}_I , of the Hamiltonian is augmented by an additional imaginary piece,

$$\hat{V} = \hat{V}_I \pm i\hat{V}_a, \quad (5.90)$$

which attenuates the wave function as it approaches the edge of the grid space. Inclusion of this non-physical condition does not have an adverse effect on the calculation unless the absorbing boundary overlaps the product Møller state. If the absorbing boundary did

overlap the product Møller state, the absorbing boundary would artificially reduce the evolving wave-packet/product Møller state correlation function. For this research, we utilize the same exponential functional form successfully employed by Calfas and Weeks, [39] and later Niday [41] for three body atomic problems,

$$V_a = A \exp \left[\frac{-(x-x_0)^2}{B} \right] \quad (5.91)$$

where the amplitude (A) and width (B) parameters can be tweaked to maximize attenuation and minimize reflection at the boundary. Here, x_0 was set to $x_{\max} = 1600 \text{ fm}$ whereas the values for $A = 3000 \text{ MeV}$ and $B = 27195 \text{ fm}^2$ were determined by trial and error.

5.9.3. Analytic – Numerical Comparison

Given the information from the previous section, determining scattering matrix elements from equation (5.87) is uncomplicated. Figure 5.18 compares the scattering amplitude analytic to the numerical solution whereas Figure 5.19 contrasts the phase shift solutions. The analytic solutions are represented as circles.

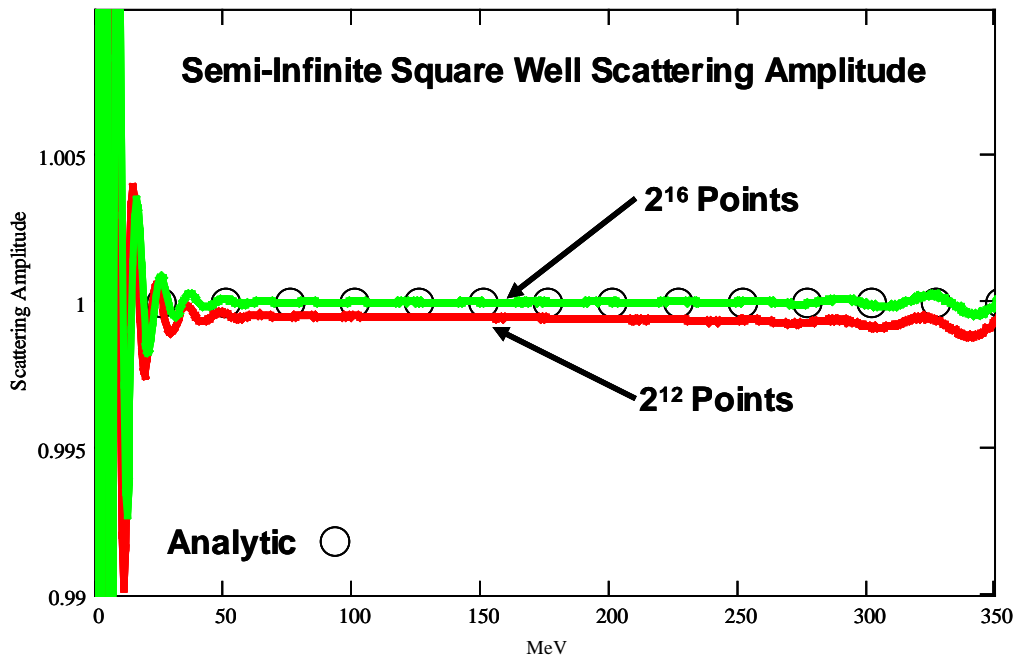


Figure 5.18. Analytic vs. Numerical S-Matrix Amplitude. A scattering amplitude of unity is expected since the entire wave form should be reflected from the potential barrier at an $r \approx 0.5 \text{ fm}$. The apparent ringing low energy is associated with a division error and can be remedied by an appropriate choice of a low energy wave packet. The lower sampling rate failed to converge to one due to a poor choice in coordinate step size.

Intuitively we would expect the scattering amplitude to be one since the entire waveform should be reflected from the potential barrier. The failure of the lower sampling rate to meet this expectation stems from a poor choice of step size. Here the lower sampling rate corresponds to about two samples per fm which implies that the square well appears to have more of a trapezoid shape than that of a square. If we increase the sampling rate by four orders of magnitude, the expected scattering amplitude of one is obtained. Note that both solutions also exhibit a ringing effect at the upper and lower energy limits, which is independent of sampling rate. This ringing is a result of the

division by the product of the expansion coefficients $\eta_{\mp}[k(E)]$ in equation(5.87), which are small.

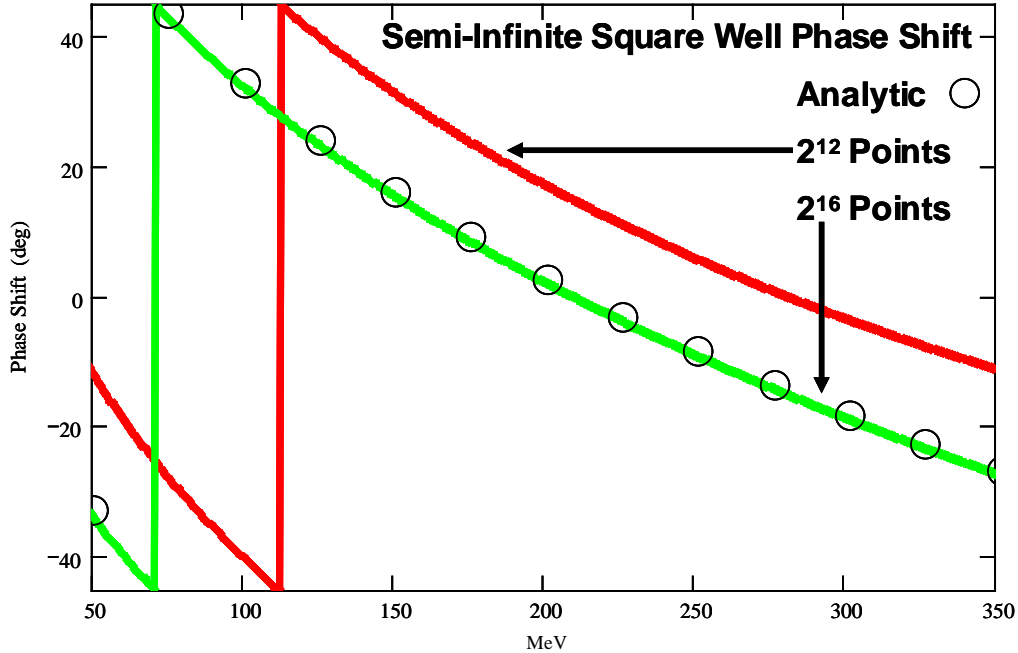


Figure 5.19. Analytic vs. Numerical Phase Shift. The phase shift is more susceptible to a poor choice in coordinate step size than the scattering matrix amplitude. At the lower sampling rate, the square well appears to be more of a trapezoid than a square well and fails to converge to the analytic solution. Since the actual potentials are free of sharp discontinuities, lower sampling rates should be possible when calculations with the AV18 are performed.

Shifting the focus now to Figure 5.19, the asymmetric square well phase shift exhibits a greater sensitivity to the trapezoid appearance of the well than the scattering matrix amplitude. At the low 2^{12} rate, the analytic and calculated differ by about 15 degrees. As the sampling rate is increased to 2^{16} , the phase shift aligns with the analytic solution. These issues should not pose a problem with the actual AV18 potential since all surfaces are smooth and free of sharp discontinuities within the range of the nuclear strong force.

6. Presentation of Results

The results of this research are presented in three main sections. The first examines the 1S_0 potential. The 1S_0 potential is the simplest two-nucleon case where all three nucleon- nucleon combinations are possible (pp, pn, and nn). The lack of a centrifugal component makes it possible to position the wave-packets close to the potential well on a small grid space. As a result, computational time is significantly reduced. Subsequent calculations, however, become more complex as the effect of angular momentum can no longer be ignored. Coordinate grid spaces must be expanded to compensate for the longer range of the centrifugal term $\frac{L(L+1)}{2\mu R^2}$ of V_{eff} . Section 6.2 assesses the computational impact of angular momentum through $J=4$. Finally, a more efficient method for calculating nuclear phase shifts that exploits the innate characteristics of the potential is developed in Section 6.3.

6.1. *The 1S_0 Potential*

For the 1S_0 potentials, there exists one effective potential surface for each possible nucleon combination, one for neutron-neutron, one for neutron-proton, and one for proton-proton. These are shown in Figure 6.1.

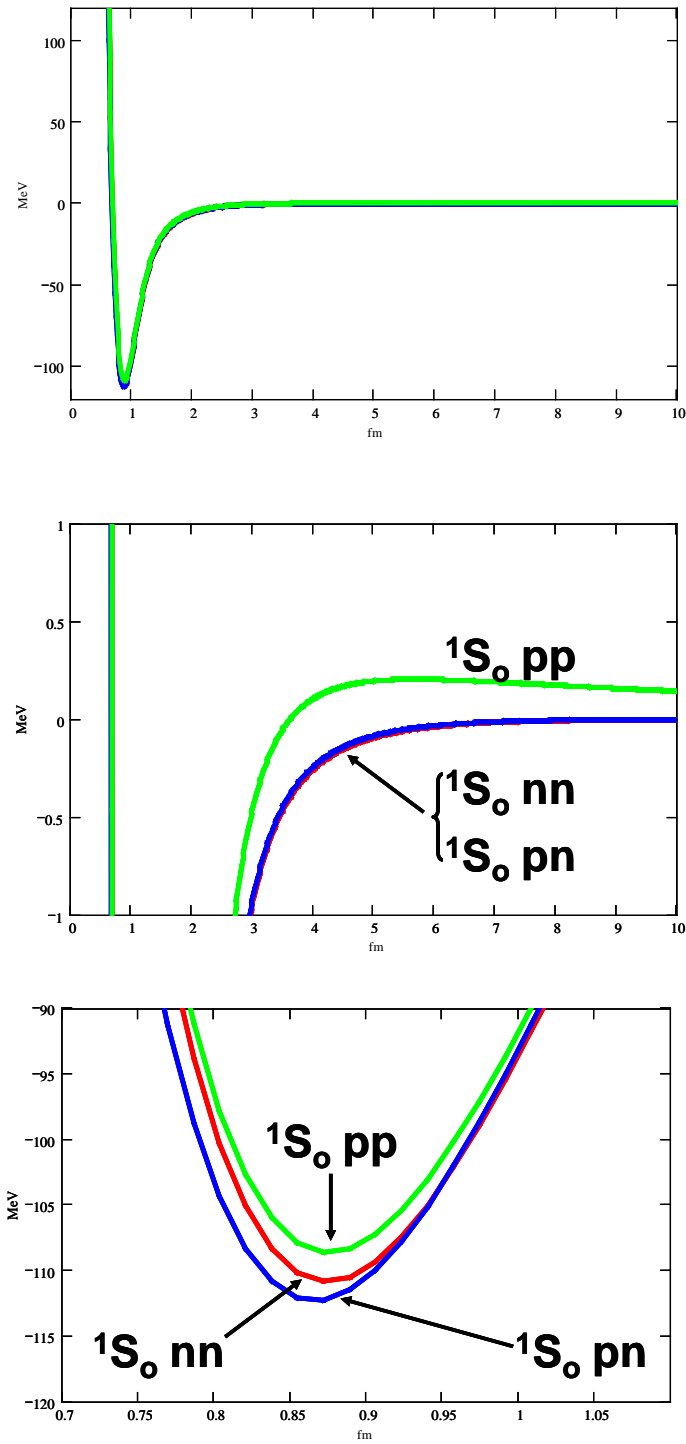


Figure 6.1. The 1S_0 AV18 potentials. The first frame shows the dimensions of the potentials. The second frame highlights the 0.3 MeV Coulombic barrier on approach to the well. The third frame illustrates the slight differences in maximum well depth between the three potentials.

A noticeable surface similarity between the plots is immediately apparent. In fact, the only distinguishing feature between them is the slight increase in the pp potential approaching the nuclear well. The small differences in the last frame of Figure 6.1 are due to the charge dependence of the strong force whereas the slight increase in the middle frame is a consequence of Coulombic repulsion. Despite the surface similarity, some general information about the phase shift's qualitative aspects may be inferred:

1. Secondary wells are not evident so portions of the wave packet cannot become delayed in exiting the interaction region and generate resonant features such as secondary peaks in the amplitude of the scattered wave packet.
2. The phase shifts should be similar since only minor differences exist between the three 1S_0 potentials.
3. All are attractive (negative) therefore, the resulting phase shifts should be primarily positive [77].

As shown, the AV18 potentials are smooth and free of any discontinuities within the interaction region. This is not the case outside the interaction region where only the nn and np potentials tend to zero well before the 140 fm cut-off. Here, the pp potential is still slightly positive at termination due the slow $\frac{1}{r}$ Coulombic tail decay (Figure 6.2).

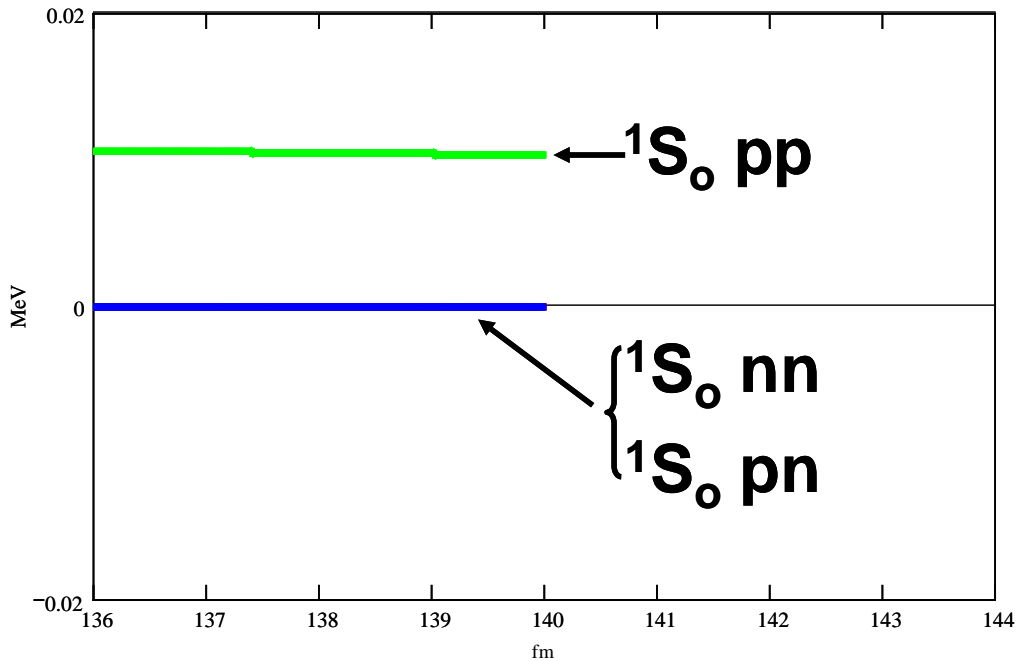


Figure 6.2. The 1S_0 potentials at cut-off. The 0.01 MeV step in the proton-proton potential should have minimal impact on the phase shift calculation.

Although the 1S_0 potential's step at 140 fm has minimal impact on the phase for the 1S_0 potential, we still choose the initial coordinate position of the wave-packets to be well outside the interaction region at 400 fm to minimize any possible low energy interference. Subsection 6.1.1 discusses the initial guess for coordinate/temporal step size. Refinement of parameters and test for convergence of these step sizes are the subject of Subsection 6.1.2. Subsection 6.1.3 describes a methodology for determining an appropriate set of absorbing boundary conditions. Finally, Subsection 6.1.4 presents the results of the CPM for the 1S_0 potential.

6.1.1. Selection of Initial Coordinate and Temporal Step Size

Obviously, the choice of coordinate and temporal grid parameters size can significantly influence the computational cost of this technique. A poor choice may never provide any useful information nor prove to be more advantageous than traditional time-independent methods. In this section, an outline on how to estimate an appropriate step size is presented.

Nyquist's sampling theorem provides a useful prescription for establishing an initial guess for an appropriate coordinate step size. The theorem stipulates that in order to reconstruct an original analog signal digitally, the sampling rate must be twice the highest frequency observed in the original analog waveform. Here, the interesting features of the potential well illustrated in Figure 6.1 only exist over the first few femtometers so at least two samples per fm are required to provide some reasonable phase shift information. Given our initial choice of a 1600 fm coordinate grid and the power of 2 FFT condition,

$$\frac{1600[fm]}{2^{12}} = 0.391[fm] \quad (6.1)$$

is the first possible step size candidate that meets the criterion.

An initial estimate for the temporal step size can just as easily be determined using our nuclear convention form of the energy-time uncertainty relation,

$$\Delta t = \frac{1}{E_{\max}}, \quad (6.2)$$

Here, E_{\max} is the sum of the potential energy given by the depth of the nuclear well (115 MeV) and the kinetic energy computed from the highest value of k contained within the

wave packets (543 MeV). For convenience, we set $E_{\text{max}} = 1000 \text{ MeV}$ which establishes $0.001 \tau_\nu$ as an upper limit for $\Delta\tau$. Given that it takes about $80 \tau_\nu$ for the amplitude of the correlation function between the evolving/product wave-packet to fall below 10^{-5} , we have,

$$0.001 \tau_\nu \geq \frac{80 \tau_\nu}{2^{17}} = 0.0006104 \tau_\nu, \quad (6.3)$$

for the temporal step initial guess. These choices again represent initial guesses and should not be assumed to be optimal. Refinement of these parameters is the subject of the next section.

6.1.2. Parameter Refinement and Convergence Tests

In this section, we seek to ascertain the most appropriate coordinate and temporal step size to achieve suitable results while minimizing computational effort. Beginning with the initial guesses identified in the last subsection, systematic convergence tests were performed using the $^1S_0 pn$ potential. To test for coordinate step size convergence, the time step was held constant while Δr was successively reduced by factors of two until the phase shift converged on a stable phase value. As shown in Figure 6.3, the threshold for coordinate step convergence is obtained at a Δr of 0.195 fm .

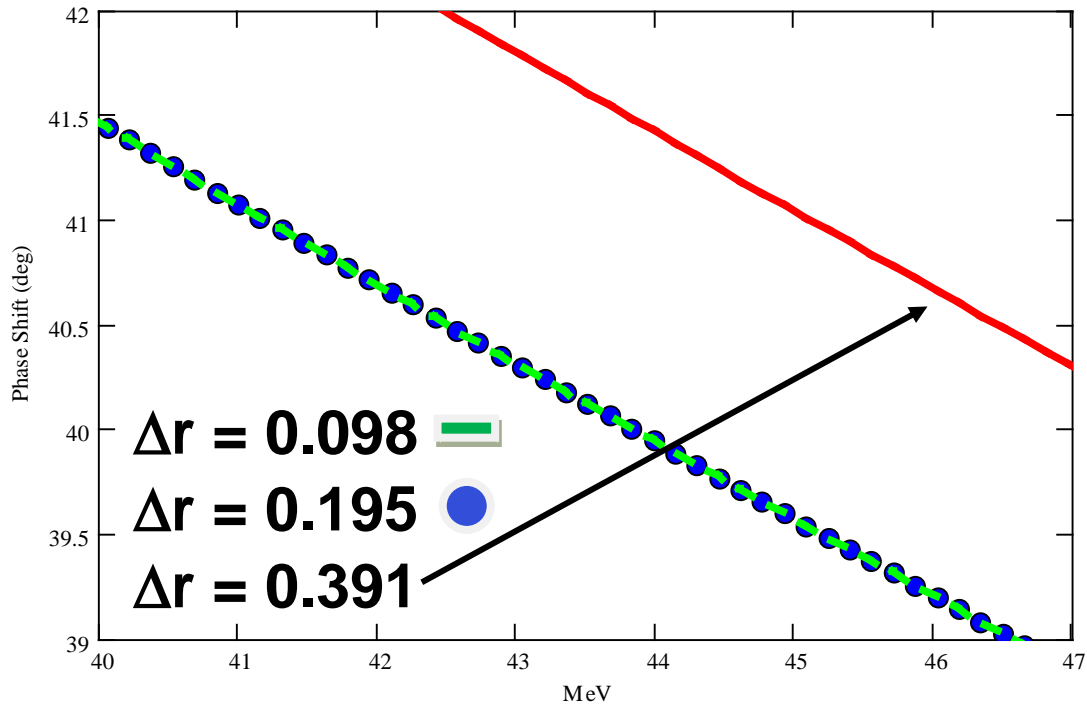


Figure 6.3. Delta r Convergence for Fixed Delta t . A step size smaller 0,195 fm is unnecessary since the phase shift has already converged to a stable value.

Here we have chosen to zoom into a small energy range since small variations in the phase shift would not be readily apparent on the 0-350 MeV scale. This choice for

Δr fixes the maximum momentum supported by the grid space to be $\pm 2.56 \frac{1}{fm}$ since

$\frac{1}{\Delta r} = k_{\max}$. An optimal value for Δt ($0.00031 \tau_v$) was determined similarly by holding

this new Δr constant while reducing Δt by factors of two.

6.1.3. Absorbing Boundary Conditions

Obviously, the amount of time required to perform CPM calculations is a function of grid size; the larger the grid, the more time that is required to complete the calculation. For these and subsequent higher order J calculations, insertion of an appropriate boundary condition is critical as it not only reduces grid size and computation effort but also prevents faster moving wave-packet components from reaching the boundary before the slower components have probed the potential.

Selection of an appropriate boundary hinges on proper selection of the boundary width B and amplitude A parameters of equation 4.59,

$$V_a = A \exp \left[\frac{-(x-x_0)^2}{B} \right]. \quad (6.4)$$

An appropriate selection was made by computing the correlation function between the reflected portion of an evolving wave-packet incident on the boundary and negative momentum product state. A negative momentum product state refers to a wave-packet with the same exact parameters as the initial reactant state save one, the sign of the initial momentum. The dissipation of a propagating wave-packet by an absorbing boundary is shown in Figure 6.4 .

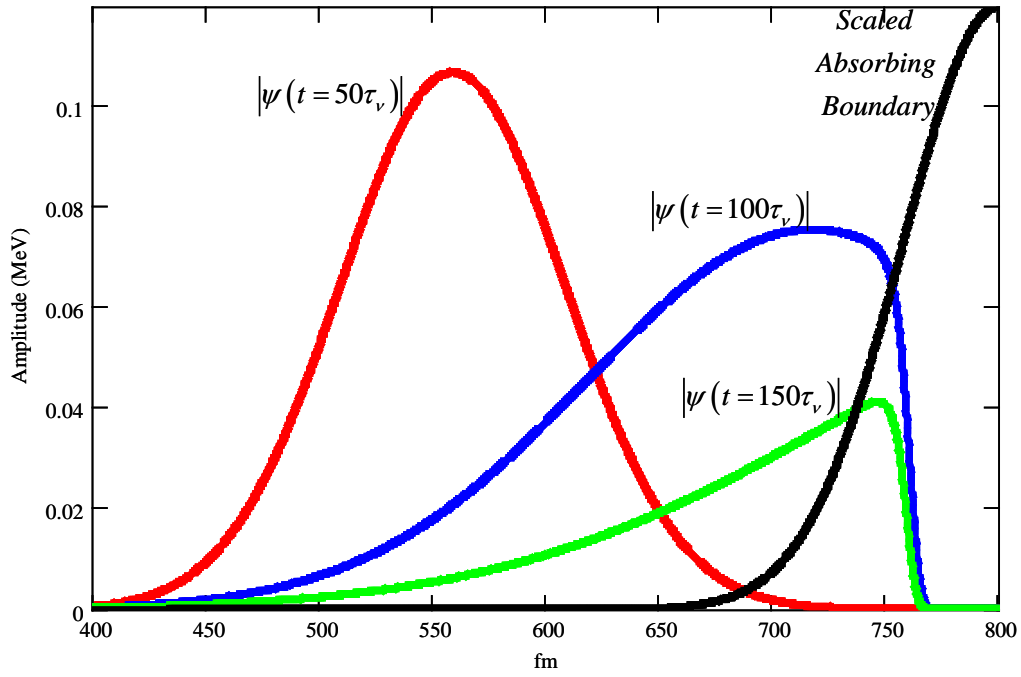


Figure 6.4. Dissipation of an Evolving Wave-Packet by an Absorbing Boundary. The choice of an appropriate absorbing barrier quickly dissipates the propagating wave packet. An absorbing boundary improves computational efficiency by reducing the coordinate grid space necessary to perform a time dependent scattering calculations.

By $150 \tau_v$, most of the incident wave packet has been dissipated. The absorption of the boundary was maximized by varying the parameters by trial and error until the correlation function between the wave packet reflected off the barrier and the negative momentum product state was minimized. Using this approach, an amplitude, A , of 3000 MeV and a width, B , of 329.063 fm were found to be acceptable. All 1S_0 CPM parameters are summarized in Table 6.1.

Table 6.1. Initial Parameters used for nuclear CPM calculations

Parameter	Quantity	Units
x_{\max}	1600	<i>fm</i>
k_{\max}	2.56	<i>1/fm</i>
Neutron-Proton Reduced Mass, μ_{pn}	0.01205660	m_v
Neutron- Neutron Reduced Mass, μ_{nn}	0.01206491	m_v
Proton -Proton Reduced Mass, μ_{pp}	0.01204830	m_v
Coordinate Points	2^{13}	
Coordinate Step	0.195	<i>fm</i>
Time	80	τ_v
Temporal Points	2^{18}	
Time Step	0.000305	τ_v
Initial Reactant Coordinate, $x1_0$	400	<i>fm</i>
Initial Product Coordinate, $x2_0$	400	<i>fm</i>
Initial Reactant Momentum, $k1_0$	-1.253	<i>1/fm</i>
Initial Product Momentum, $k2_0$	1.253	<i>1/fm</i>
Packet Spread, Δx	1.814	<i>fm</i>
Barrier Amplitude (A)	3000	<i>MeV</i>
Barrier Width (B)	329.063	<i>fm</i>

6.1.4. The 1S_0 Phase Shifts

The absorbing boundaries and wave-packets were configured based upon the Table 6.1 parameters for propagating on the three 1S_0 potentials. For each case, a correlation function, S-matrix, and phase shift were computed for comparison to the ANL published phase shift data. The CPM/ANL 1S_0 phase shift comparisons are shown in Figure 6.5 through Figure 6.7. ANL's data was only available at the discrete energies of 1, 5, 10, 25, 50, 100, 150, 200, 250, 300, and 350 *MeV*.

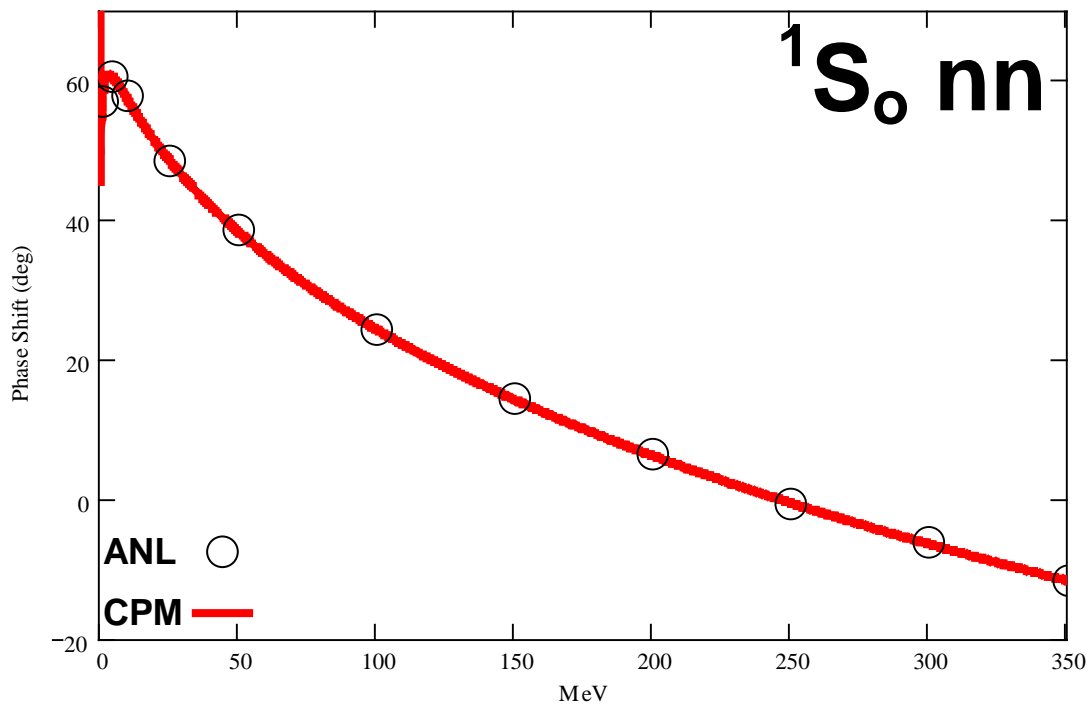


Figure 6.5. 1S_0 CPM vs. ANL neutron-neutron phase shift.

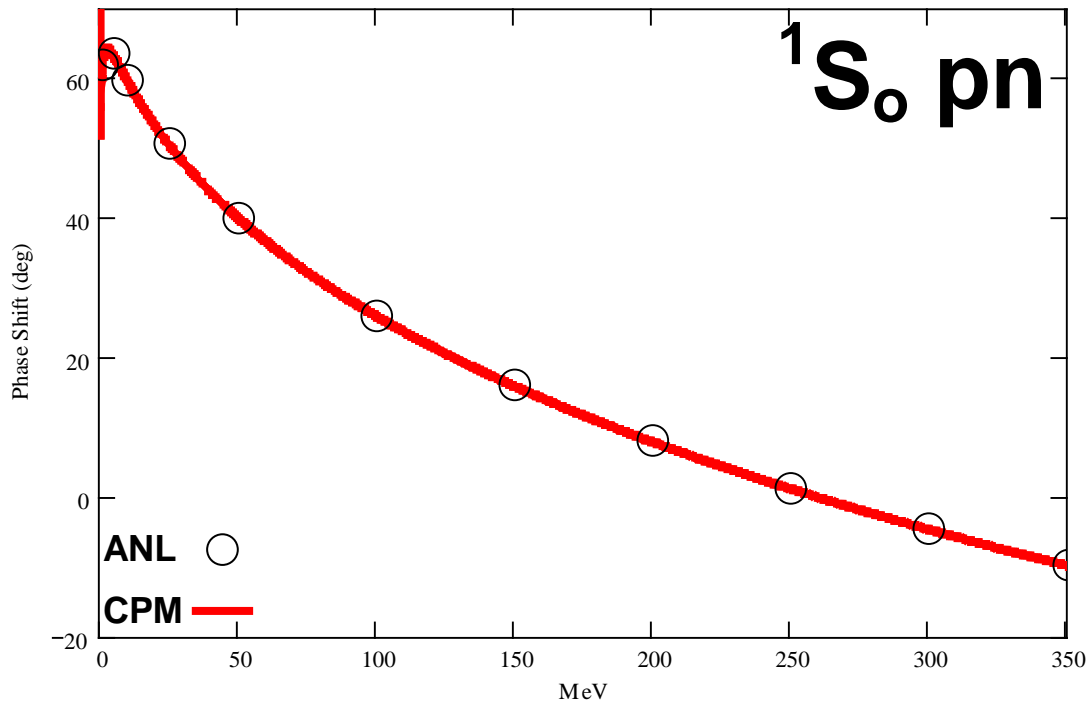


Figure 6.6. 1S_0 CPM vs. ANL proton-neutron phase shift

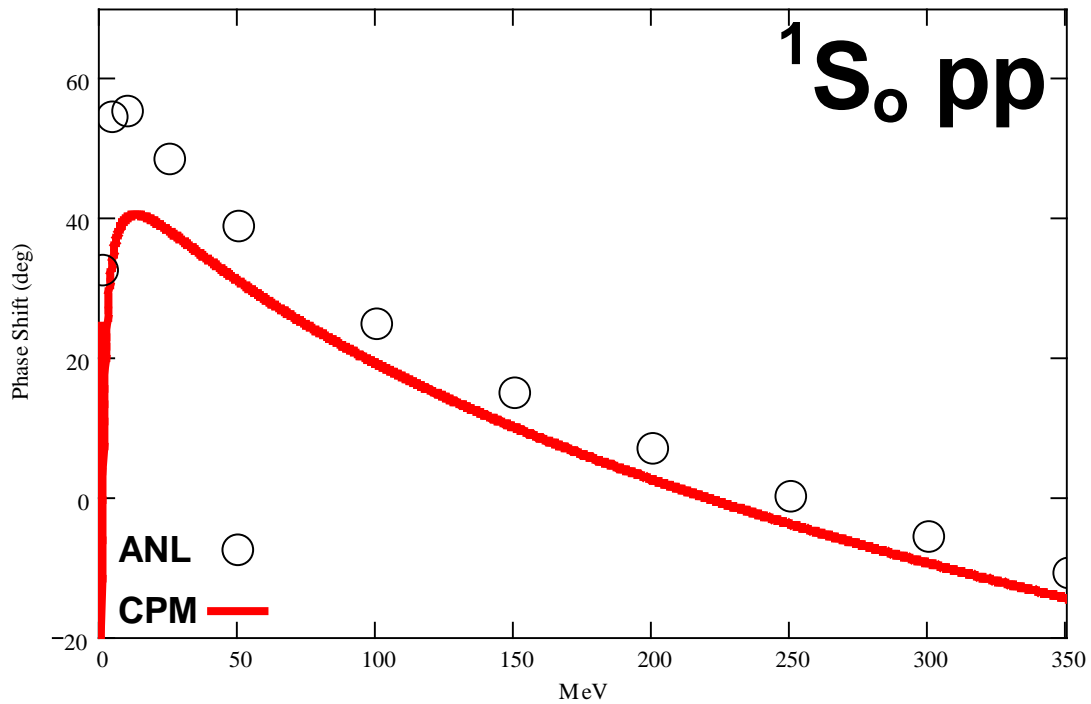


Figure 6.7. 1S_0 CPM vs. ANL proton-proton phase shift without analytic correction

All of these plots are smooth, free from resonant features, and exhibit a positive slope that is indicative of an attractive potential. Here, the neutron-neutron and neutron-proton phase shifts achieve extremely good agreement with ANL's published results, whereas the proton-proton case does not due to the long-range Coulombic tail. Application of the Coulombic correction term from section 5.6.4 is discussed in the next subsection.

6.1.5. The 1S_0 pp Phase Shift Coulombic Correction

As we saw in the last section, $^1S_0 pp$ phase shift did not agree well with the published ANL results. Here, we apply the Coulombic correction developed in Section 5.6 to obtain a $^1S_0 pp$ solution similar to ANL. Agreement with ANL may be obtained by correct application of the Coulombic

$$\sigma_L = \arg \Gamma(1 + i\gamma + L), \quad (6.5)$$

and the cut-off correction,

$$\gamma \ln(2kp), \quad (6.6)$$

where,

$$\gamma = \frac{\mu e^2}{4\pi\epsilon_0 \hbar k}, \quad k = \sqrt{\frac{2\mu E}{\hbar^2}}. \quad (6.7)$$

Here, μ is the pp reduced mass, E is Energy, \hbar is Plank's constant, p is the coordinate grid Coulombic cutoff point of 140 fm , ϵ_0 is the permittivity of free space and e is the electron charge magnitude (Table 6.2). Note that only the Coulombic term depends on the angular momentum L whereas both the Coulombic and the cutoff correction terms depend on the momentum, $\hbar k$. It is apparent from the plot of these two terms (Figure 6.8) that the cut-off correction has little impact on the solution and that the Coulombic term dominates. Given our calculated 1S_0 pp phase shift δ_L , a solution that more closely aligns with ANL's data may be obtained by using equation (5.60),

$$v_L = \delta_L - \sigma_L + \gamma \ln(2kp) \quad (6.8)$$

The corrected CPM solution is also shown in Figure 6.8.

Table 6.2. 1S_0 Coulombic and Cut-off Correction Parameters

Parameter	Quantity	Units
Angular Momentum, L	0	
Electron Charge Magnitude, e	1.602×10^{-19}	C
Permittivity of Free Space, ϵ_0	8.854×10^{-27}	$[\text{farad}/\text{fm}]$
Coulombic Cut-off Point, p	140	fm
Proton -Proton Reduced Mass, μ_{pp}	0.01204830	m_v

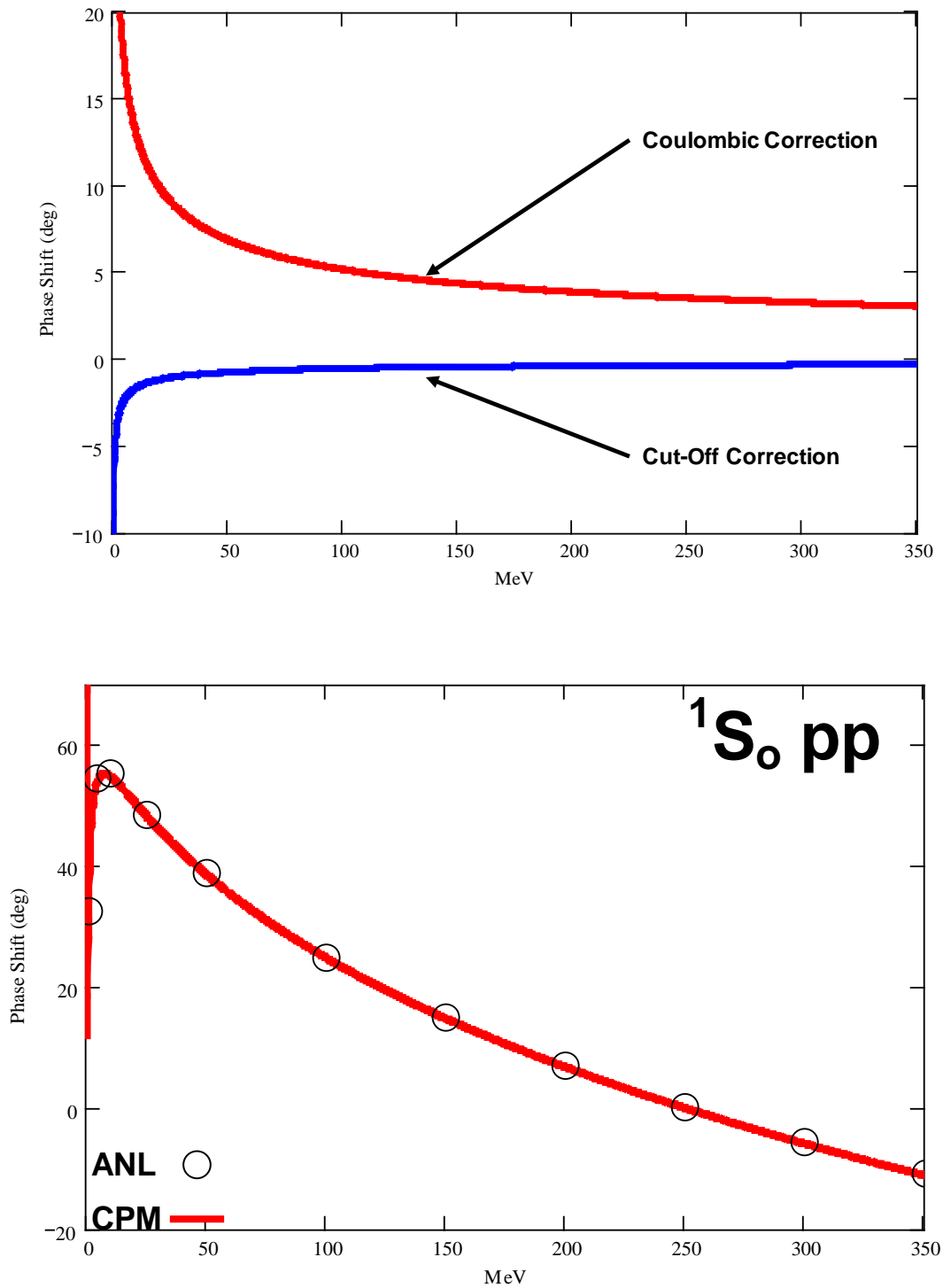


Figure 6.8. The Coulombic and Cut-off Corrections (upper diagram) to the 1S_0 pp Phase Shift (lower diagram). The cutoff correction is small with respect to the magnitude of the Coulombic correction. When these corrections are applied, the 1S_0 CPM result aligns with the published results from ANL.

6.2. Wave-Packets and the Asymptotic Limit

We now look at the non 2x2 isospin triplet for each value of total momentum, J , through $J = 3$. In the previous section, the angular momentum, L , was zero and had no impact on the calculation. However, this is not the case for both the remaining 1x1 and 2x2 isospin triplets. As L increases, so does the centrifugal barrier contribution to the potential (Figure 6.9).

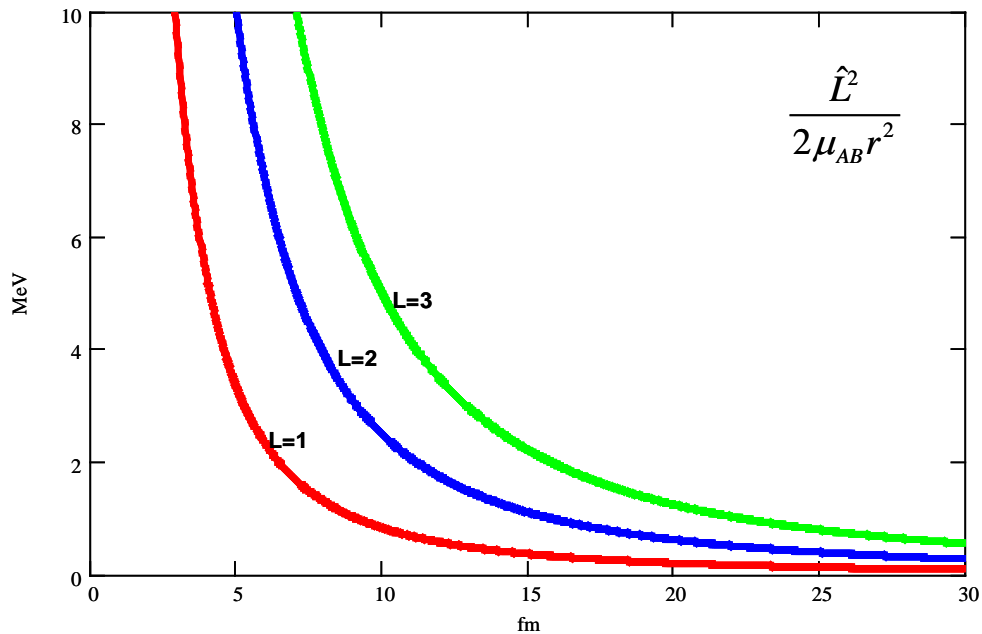


Figure 6.9. Centrifugal Barrier Potentials for $L=1-3$. As the centrifugal barrier increases, the nuclear potential represents only a minor perturbation to the barrier. Phase shifts for $L \geq 2$ are expected to be small.

In fact for $L \geq 2$, the short range nuclear well represents only a minor perturbation to the barrier potential.

In the previous 1S_0 phase calculations, the wave-packets could be placed relatively close to the interaction region at 400 fm . For that problem, the wave packets could be

considered in the asymptotic limit since the AV18 potential terminated at 140 fm and the centrifugal barrier provided no contribution (See Figure 6.2). Here however $L \neq 0$, so a choice for the initial position of the wave packets must be made further away from the origin. Ideally, a point will be chosen close enough to the interaction region to minimize computational effort but still far enough away from the area to minimize the barrier potentials impact on the correlation function. As an initial guess, points are chosen where each potential falls to roughly $1 \times 10^{-4} \text{ MeV}$. For the 3P_1 , this occurs at a distance of 800 fm (Figure 6.10).

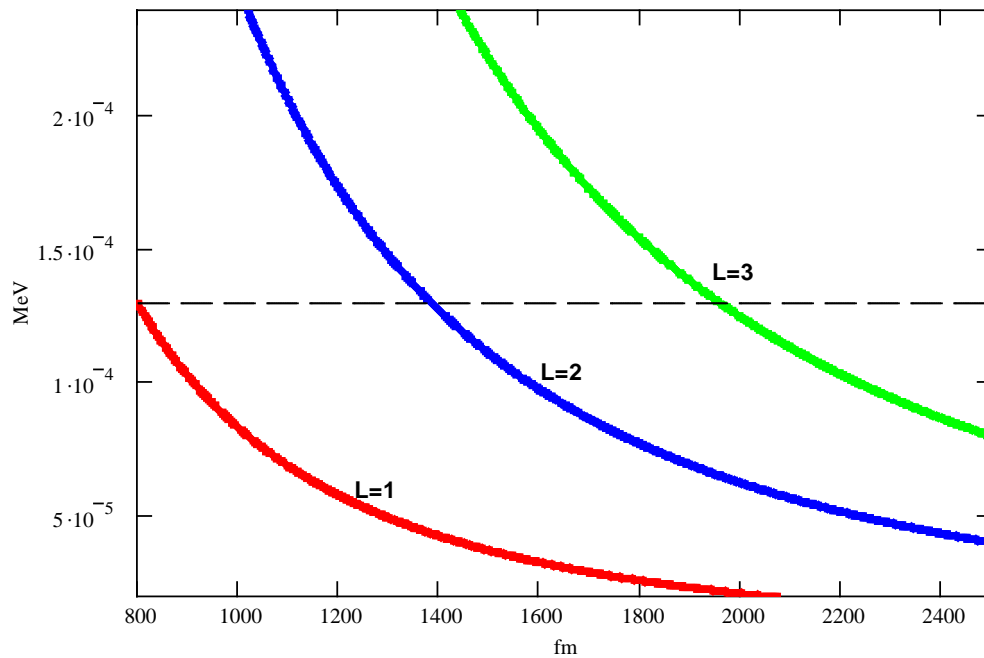


Figure 6.10. Decay of the Barrier Potential at Higher Values of r . The asymptotic limit was initially assumed to be where the barrier potential fell below $1 \times 10^{-4} \text{ MeV}$. Møller states were established to begin wave packet propagation based on this assumption at 800 fm , 1600 fm , and 3200 fm for $L = 1, 2,$ and 3 respectively.

For each higher order L calculation, the initial positions were doubled such that the 1D_2 and 3F_3 cases started at 1600 fm and 3200 fm respectively. To accommodate these changes, the coordinate grid size and number sampling points were increased by factors of two to maintain the 0.195 fm coordinate step size. The same principle was applied to the number of time steps and τ_{\max} . The values for Δx , k , and packet spread were the same as those previously given by Table 6.1. The results of the pn CPM calculations are presented in the next three figures.

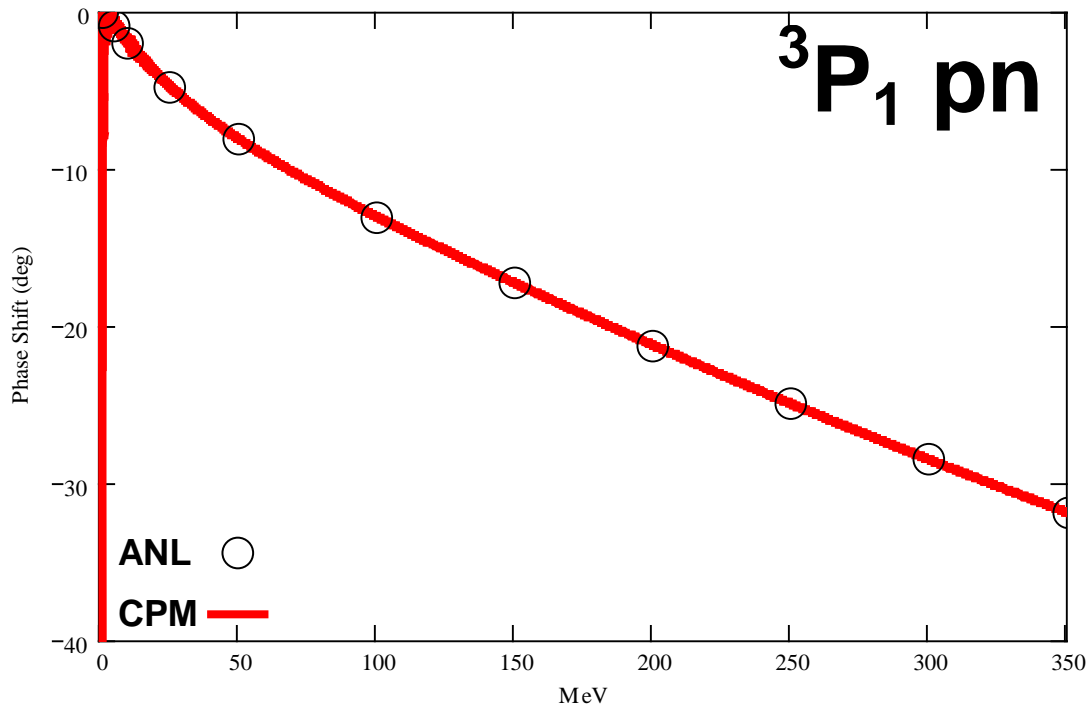


Figure 6.11. ${}^3P_1\text{ pn}$ Phase Shift. Calculated from Wave Packets Initially Placed at 800 fm .

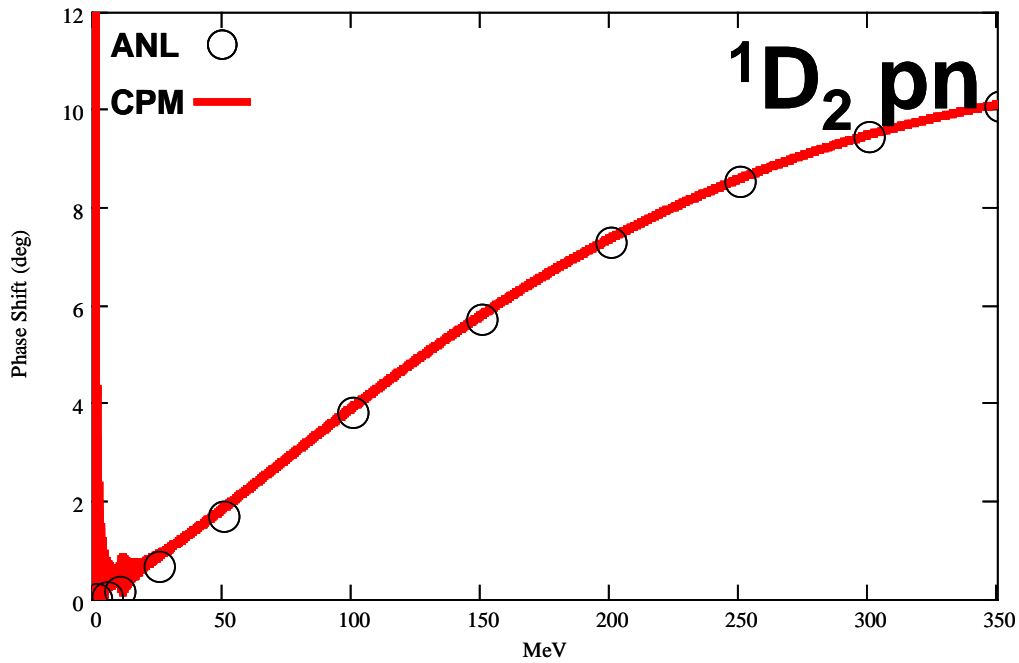


Figure 6.12. 1D_2 pn Phase Shift Calculated from Wave Packets Initially Placed at 1600 *fm*.

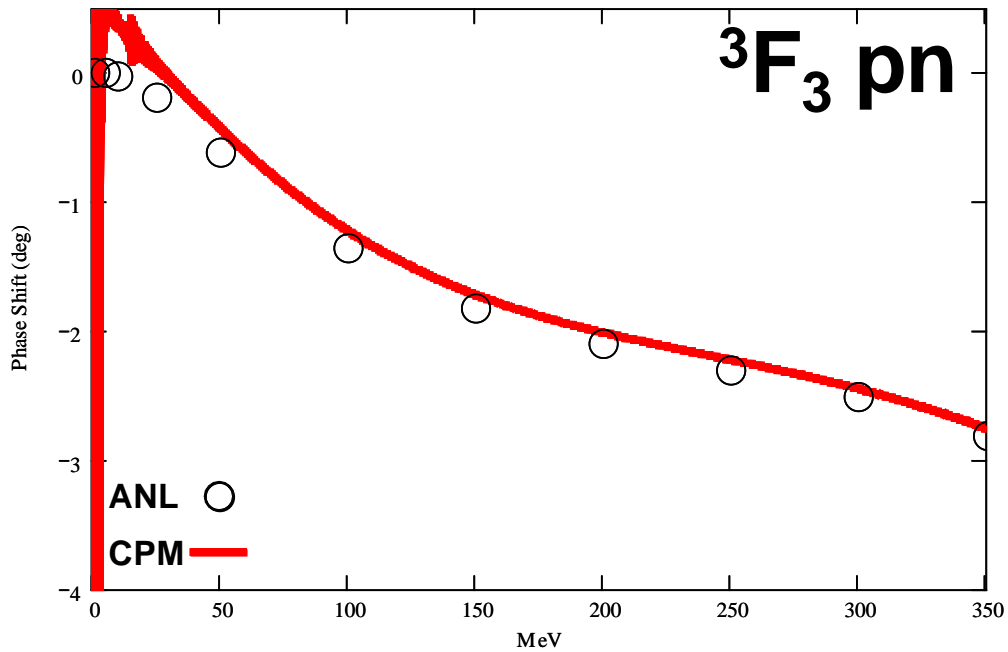


Figure 6.13. 3F_3 pn Phase Shift Calculated from Wave Packets Initially Placed at 3200 *fm*, The low energy noise in this plot and the previous two plots results from a poor choice of wave packet. The disagreement with the ANL, which increases as a function of L , is a result of a bad asymptotic limit assumption.

Although these solutions track well with ANL's published results, two deficiencies are readily apparent. First, there is a high degree of noise in the low energy regime (below 50 MeV), which suggests an inappropriate wave-packet choice was made to resolve this specific energy range adequately. Our original wave packet amplitude was small at low MeV energies. How to increase resolution at low MeV energies is discussed in Section 6.3. The other more noteworthy deficiency is that the error increases with each increase with L . This suggests a poor choice was made for the asymptotic assumption. In an attempt to correct this problem, the initial start positions and grid sizes were doubled yet again. The 3F_3 phase shifts from this trial were still not satisfactory. Crude calculations showed (See Figure 6.14) that for the 3F_3 an initial position of 12,800 fm, a coordinate grid of 2^{17} points, and temporal grid of 2^{23} points would be more suitable.

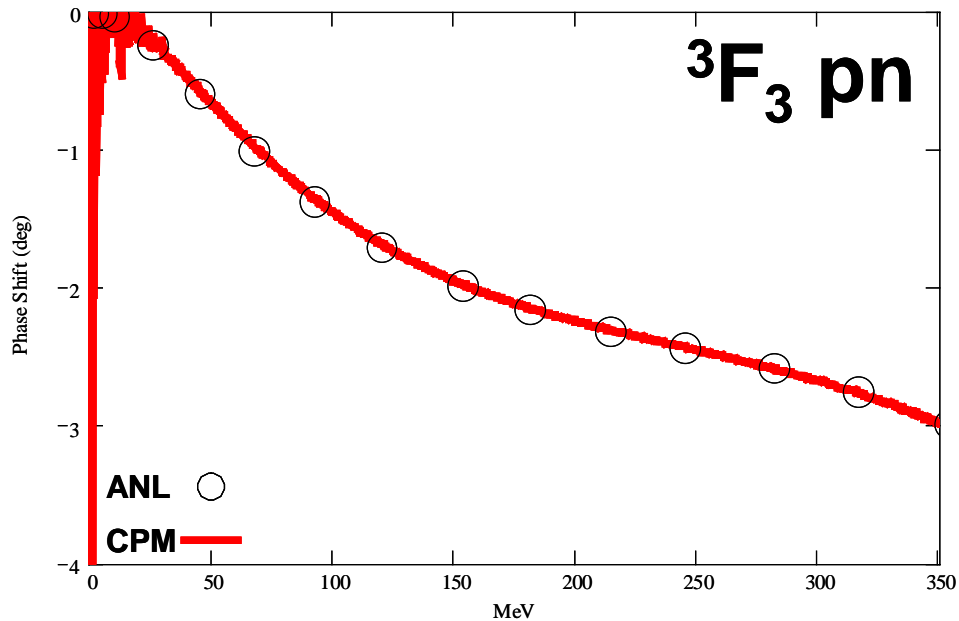


Figure 6.14. Crude 3F_3 Phase Shift Calculated from Wave Packets Initially Placed at 12,800 fm. The results of this crude calculation indicate that placing the wave packets at 12,800 fm from the nuclear well would be a good asymptotic limit approximation.

Projections for both MSRC and Desktop processing based on previous optimized run times indicated these grid sizes would require a minimum 14-15 days per calculation for the 3F_3 and high L cases independent of platform (Table 5.2). Parallelization provides little or no additional benefit as the CPM is a serial algorithm.

Table 6.3. Projected MSRC and PC Run-Times

Coord/Time Points	MSRC-HPC11 RunTime (Days)	P4 2400 Desktop RunTime (Days)
17,17	0.22	0.24
17,18	0.44	0.47
17,19	0.88	0.94
17,20	1.75	1.89
17,21	3.50	3.78
17,22	7.00	7.56
17,23	14.0	15.11
17,24	28.0	30.22

Dispersion further compounds the problem. As we move farther from the interaction region, the lower energy wave-packet components require more time to probe the potential and return to the initial position; making the computational cost of this technique become less attractive. The next section presents an alternative methodology for handling these two issues.

6.3. *An Intermediate State Calculation*

As we saw in the last section, the computational cost of placing the wave-packet in the asymptotic limit can be extremely high. The following alternative approach leverages the specific problem characteristics to our benefit. This section is divided into

two subsections. The first deals with the 1x1 matrix elements of V_{eff} and the second (Section 6.3.2) deals with the 2x2 elements matrix elements of V_{eff} .

6.3.1. The Single Element Case

To minimize dispersion and accelerate subsequent calculation of the correlation function, it would be useful to place the wave-packets as close as possible to the interaction region. A useful choice would be to center the wave packets at 400 fm as we did in Section 6.1 since it is well outside the AV18 pp cutoff point and far enough away from the absorbing boundaries for them to pose any problems. In order to start the wave-packet calculations in closer proximity to the well, we return to the definition of the Møller operator

$$\hat{\Omega}_{\pm}^{\gamma} = \lim_{t \rightarrow \mp\infty} \text{Exp} \left[\frac{i\hat{H}t}{\hbar} \right] \text{Exp} \left[\frac{-i\hat{H}_0^{\gamma}t}{\hbar} \right]. \quad (6.9)$$

Previous calculations assumed that the propagation began in the asymptotic limit solely under the full Hamiltonian, H . Since acceptable results were not obtained under this assumption, the full form must be employed.

If we recall that the first operator, H_0 , contains only kinetic energy information, we can use equation (5.82) to analytically determine the reactant (product) wave packet's form at some position where the centripetal barrier is negligible. Here, τ was increased until the wave packet peaks were well outside our asymptotic estimate of $12,800\text{ fm}$ determined in section 5.2. (Figure 6.15) These intermediate states were then propagated back to $\tau = 0$ under the full Hamiltonian, H , using the propagation algorithm. This process established new Møller states for the phase shift calculations.

Since it requires considerable time to propagate the wave-packets back from $-\tau(\tau)$, it would be useful to know if the time step could be increased given that over this region the potential remains negligible. So, comparisons were made between a wave packet determined analytically at $235 \tau_v$ and a wave packet propagated to that same point using the propagation algorithm using $\Delta\tau$'s of $0.00022 \tau_v$, $0.00045 \tau_v$, $0.00090 \tau_v$, and $0.0018 \tau_v$. Absolute error tests indicated the time step could be increased by a factor of 2^3 without significant waveform degradation.

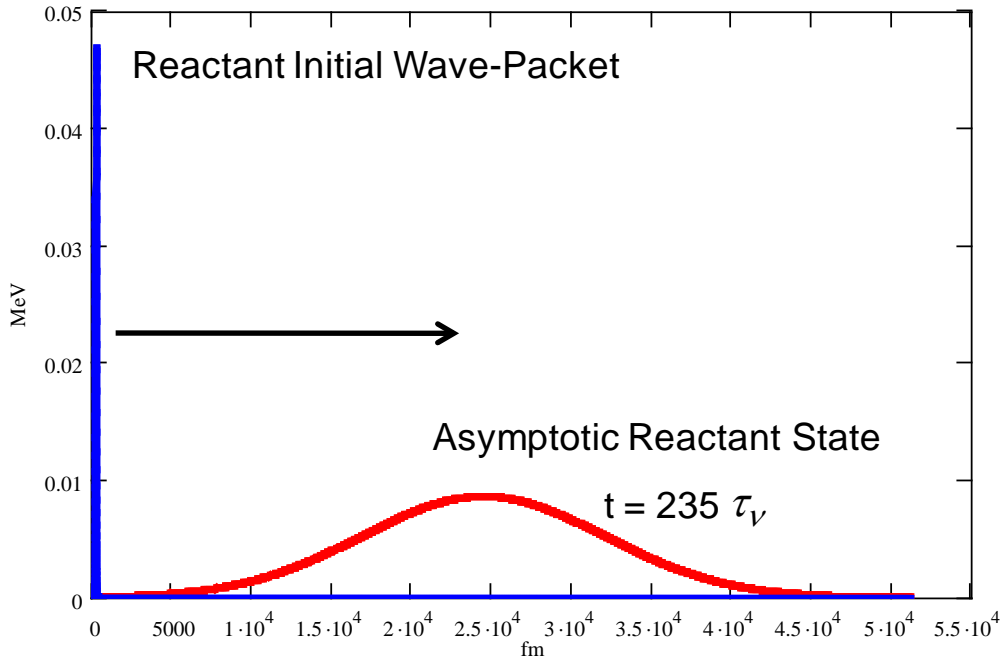


Figure 6.15. Absolute Value of Dispersed Initial Reactant Wave-Packet. The dispersed wave packet was calculated using the analytic free space propagator equation (5.82). The peak of the wave packet was centered at twice the distance indicated by the crude calculation shown in Figure 6.14 to ensure minimal barrier interference. This dispersed wave packet was then propagated back to the initial position to integrate barrier information into the Møller state for scattering matrix calculations.

There is an inherent simplicity to this approach. Consider the kinetic energy tumbling term,

$$\frac{L(L+1)}{2\mu_{AB}R^2}. \quad (6.10)$$

Notice that the only difference between potentials outside the interaction region for a given choice of wave-packet is due to the reduced mass, μ , and angular momentum, L . This implies that if the reactant and product Møller states differ only by the sign of k_0 , the intermediate Møller state need only be calculated once for a specific L and μ combination. In other words, these Møller states can be stored and used repeatedly. This capability facilitates rapid calculation of improved phase shifts as both our understanding of the strong force and our models that describe this understanding improve.

The usefulness of this approach is apparent if we consider the calculation of the neutron-proton $L=3$ phase shifts, 3F2, 1F3, 3F3 and 3F4. From Table 6.3, it would require at least 28 days of computational time to calculate each phase shift on a grid the size shown in Figure 6.15 (112 days total). However if the Møller state is pre-calculated as described in the preceding paragraphs, the same four calculations can be performed in less than 12 hours. This is a 99% reduction in computer runtime. Subsequent neutron-proton $L=3$ phase shifts can be obtained from these intermediate Møller states in a matter of minutes. This capability provides the nuclear community with a powerful new tool to calculate detailed phase shift information rapidly as new improved nuclear models become available. For these and all remaining phase calculations, three wave-packets were employed to reduce the distortion prevalent below 50 MeV in the Section 5.2 outputs (Figure 6.16 and Figure 6.17)

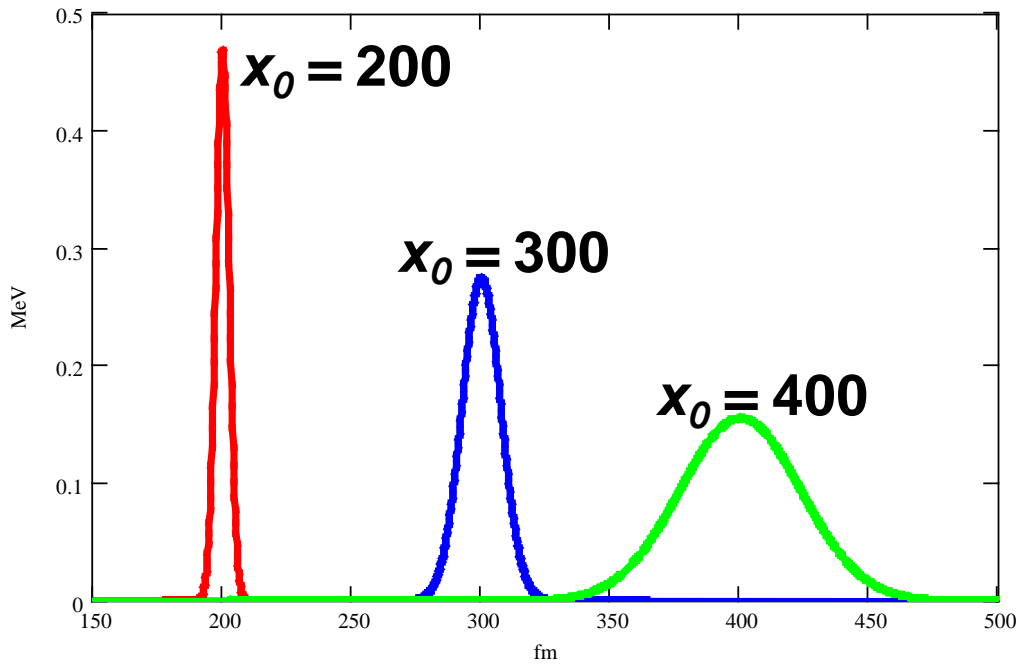


Figure 6.16. Initial Positions of the Three Wave-Packets

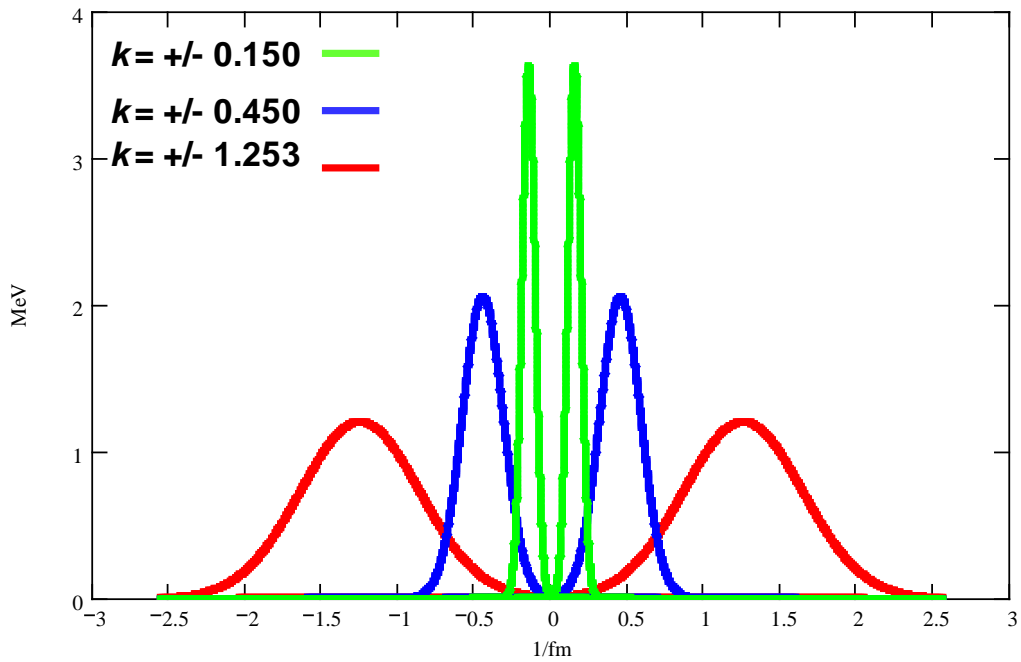


Figure 6.17. Initial Momentum Values of the Three Wave-Packets

To achieve low energy resolution, the momentum wave packet must be narrow in k space and close to zero as shown in Figure 6.17. However the narrower in k space we make the wave packet the broader the coordinate wave packet becomes (Figure 6.16). This necessitates initial coordinate wave packet positions farther from the interaction region. The coordinate initial peak positions used here are centered at 200 fm , 300 fm , and 400 fm which correspond to k space peaks centered ± 1.253 [$1/fm$], ± 0.450 [$1/fm$], and ± 0.150 [$1/fm$] respectively. The parameters used to calculate the Møller states from these wave packets are given in Table 6.4.

Table 6.4. Parameters used to calculate the Møller states for each wave-packet

Broad Energy Wave Packet		
x_{\max}	51200	fm
Time	235	τ_v
Coordinate/Temporal Points	$2^{18}, 2^{17}$	
Coordinate Packet Peak	200	fm
Momentum Packet Peak	-1.253	$1/fm$
Packet Spread	1.814	fm
Mid Energy Wave Packet		
x_{\max}	102400	fm
Time	1320	τ_v
Coordinate/Temporal Points	$2^{19}, 2^{17}$	
Coordinate Packet Peak	300	fm
Momentum Packet Peak	-0.450	$1/fm$
Packet Spread	5.277	fm
Low Energy Wave Packet		
x_{\max}	102400	fm
Time	3950	τ_v
Coordinate/Temporal Points	$2^{19}, 2^{15}$	
Coordinate Packet Peak	400	fm
Momentum Packet Peak	-0.150	$1/fm$
Packet Spread	16.491	fm

For each wave-packet, an intermediate state was calculated using equation (5.82) under the assumption that a dispersed peak location of at least 25,000 fm from the interaction region would be an acceptable asymptotic limit approximation (Figure 6.18).

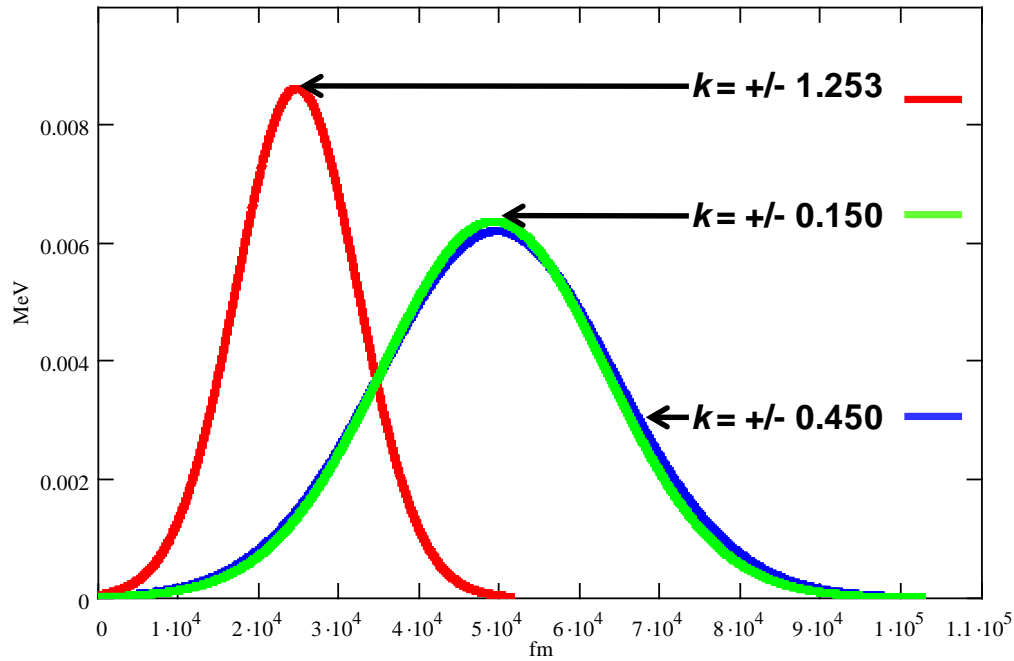


Figure 6.18. Absolute Value of the Three Wave Functions in the Intermediate Reactant States in the Asymptotic Limit. The peak positions of the lower energy wave packets were doubled to further reduce the possibility of barrier interference.

As an extra precaution, the intermediate peak positions of the low energy wave packets were doubled to further reduce the possibility of barrier interference. These asymptotic states were then propagated back toward the interaction region under their respective full Hamiltonians until $\tau = 0$ using our propagation algorithm; reconstituting our non-dispersed wave packet with the desired centripetal barrier information. Phase shifts were then calculated with the three wave-packets as before but with different propagation times since lower k wave packets are slower and require more time to interact with the

potential and return to their initial positions. The results of these calculations were then spliced together to present a complete phase shift picture. The parameters used to calculate the phase shifts using these Møller states are provided in Table 6.5. On the next series of pages, the 3P_1 , 1D_2 , and 3F_3 pn and pp phase shifts are shown. From this series of plots, it is apparent that very good agreement exists between the ANL values and our CPM technique down to a few MeV . Additional phase shifts combinations are included in Appendix 1.

Table 6.5. Parameters Used to Calculate the Phase Shifts from Three Møller States.

Broad Energy Wave Packet		
x_{\max}	1600	fm
Time	80	τ_v
Coordinate/Temporal Points	$2^{13}, 2^{18}$	
Coordinate Packet Peak	200	fm
Momentum Packet Peak	$-/+ 1.253$	$1/fm$
Packet Spread	1.814	fm
Mid Energy Wave Packet		
x_{\max}	1600	fm
Time	160	τ_v
Coordinate/Temporal Points	$2^{13}, 2^{19}$	
Coordinate Packet Peak	300	fm
Momentum Packet Peak	$-/+ 0.450$	$1/fm$
Packet Spread	5.277	fm
Low Energy Wave Packet		
x_{\max}	1600	fm
Time	320	τ_v
Coordinate/Temporal Points	$2^{13}, 2^{20}$	
Coordinate Packet Peak	400	fm
Momentum Packet Peak	$-/+ 0.150$	$1/fm$
Packet Spread	16.491	fm

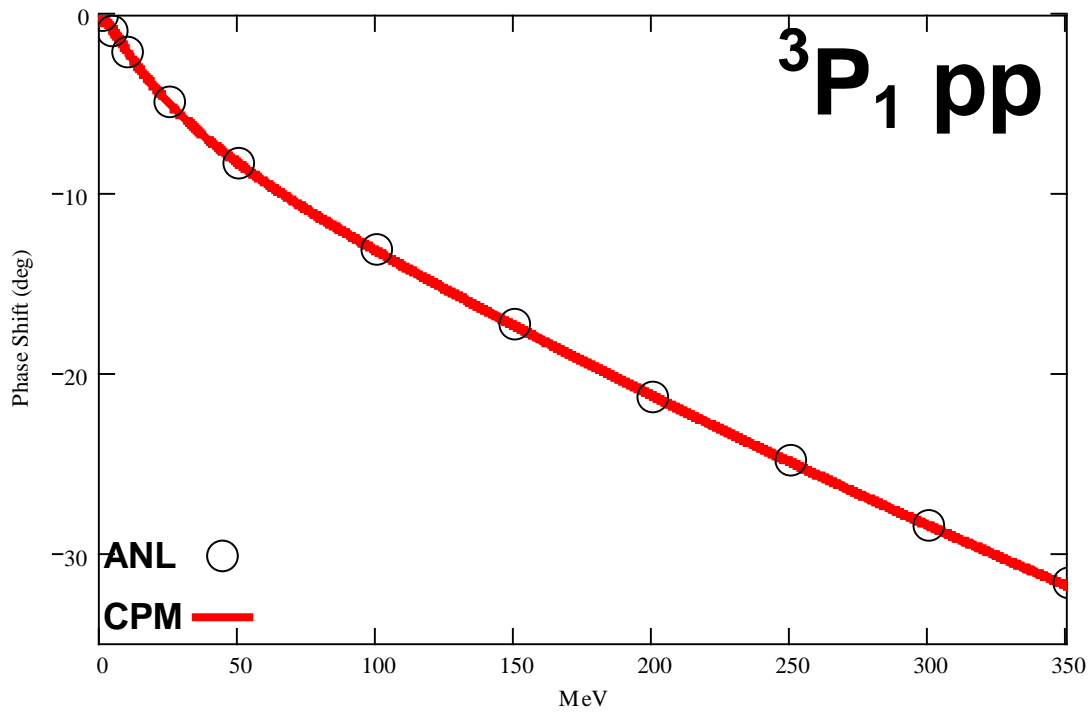
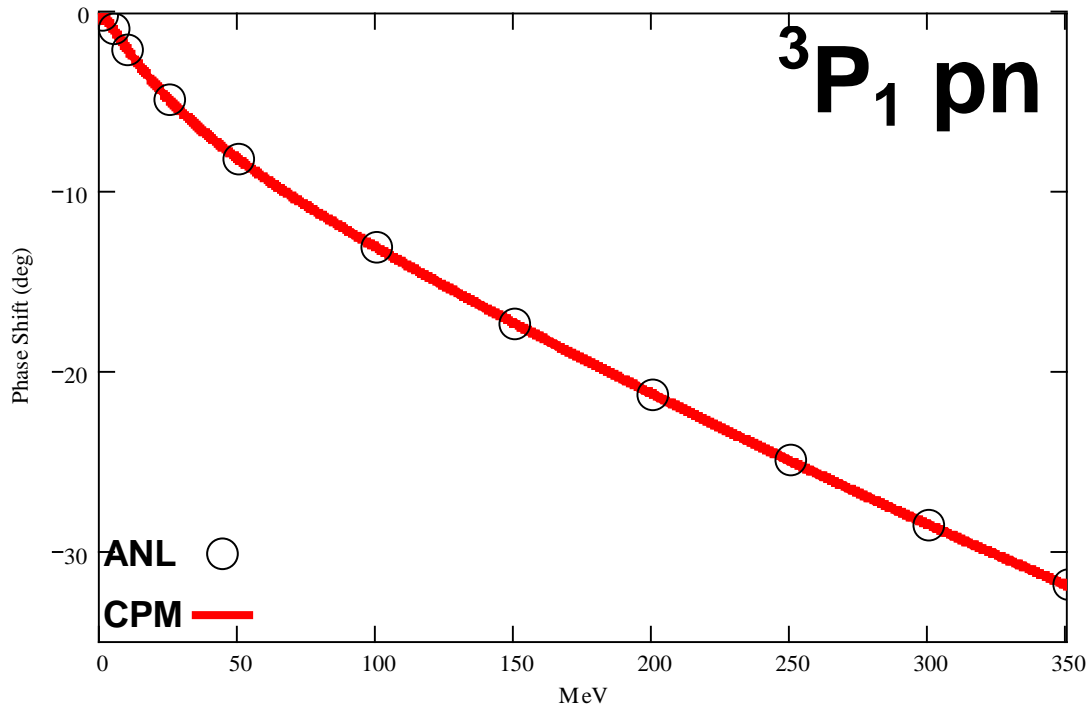


Figure 6.19. Composite CPM Calculation for the 3P_1 pn and the 3P_1 pp Phase Shift.

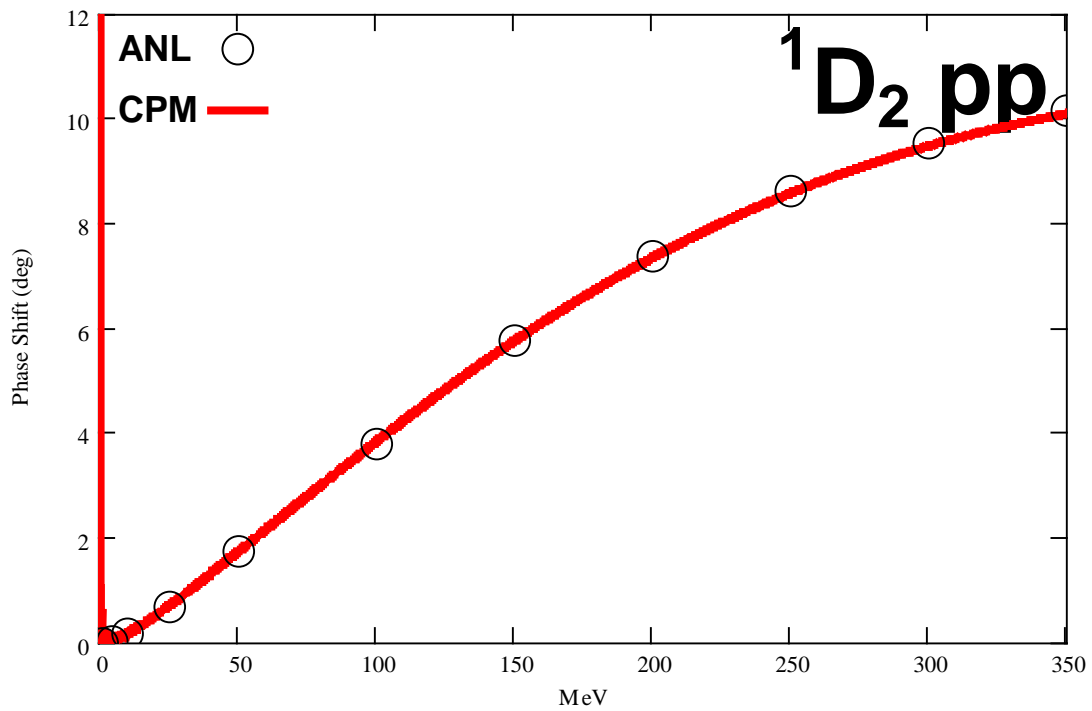
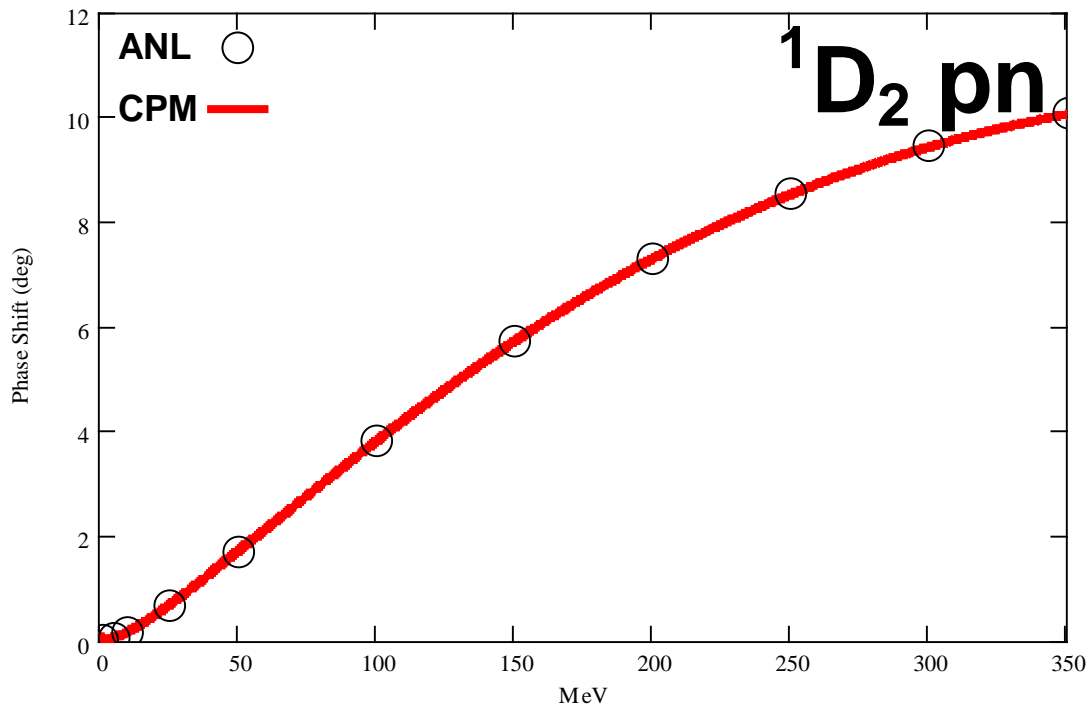


Figure 6.20. Composite CPM Calculation for the 1D_2 pn and the 1D_2 pp Phase Shift

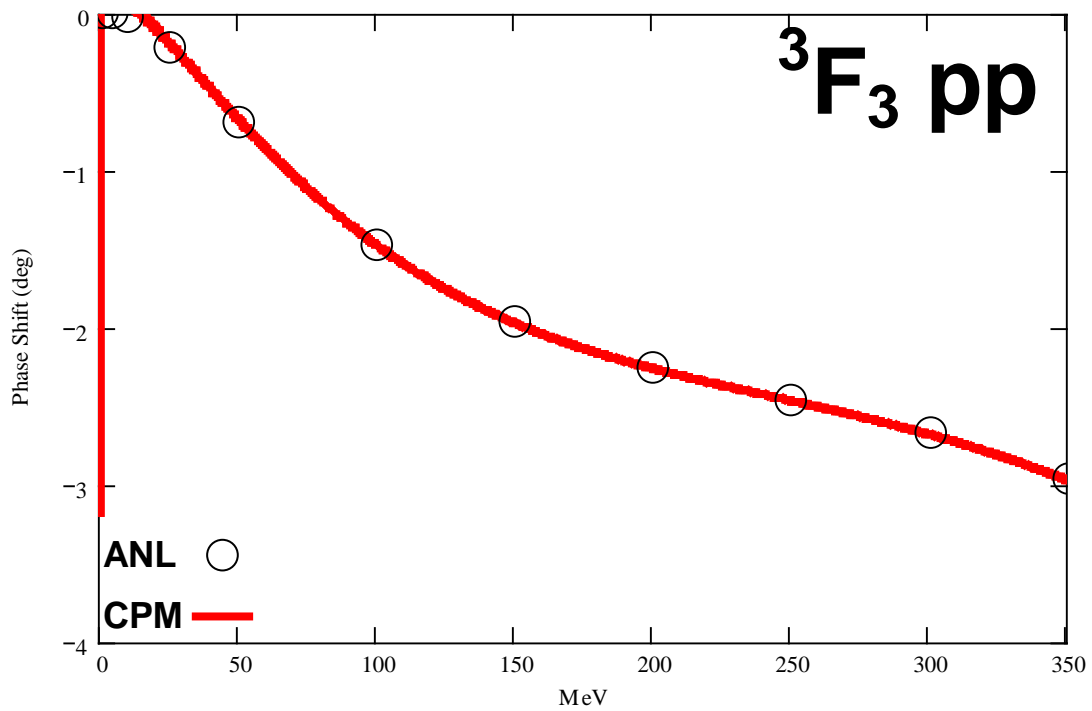
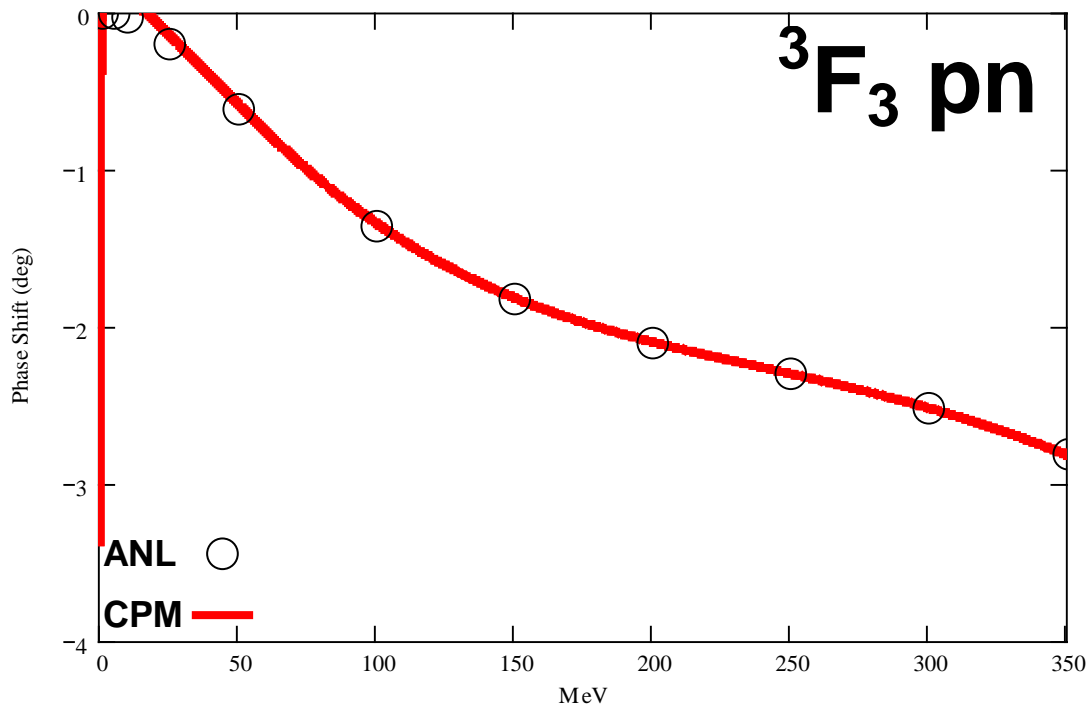


Figure 6.21. Composite CPM Calculation for the 3F_3 pn and the 3F_3 pp Phase Shift

6.3.2. The 2x2 calculation

The first 2x2 block of V_{eff} (3S_1 and 3D_1) represents our most difficult application of the CPM thus far. S-Matrix element calculations for the 2x2 involve propagation on two coupled surfaces and subsequent computation of four-correlation functions. Since the potential in the $|L, S, J, T\rangle$ basis is not diagonal, it is more efficient to transform to a diagonal basis to simplify exponentiation. However, the kinetic energy matrix is undiagonalized as a consequence of this transformation. Therefore, propagation requires two extra steps to transform between representations to the basis where the respective matrix is diagonal before operating on the wave vector. These unitary transformations were identified by U and U^\dagger back in equation (5.29).

Although the same three initial wave-packets from the last section will be used for this calculation, to help illustrate the process here we only discuss the wave packet starting at 200 *fm*. A sequence of four frames (Figure 6.22-Figure 6.25) from the multi-surface propagation is provided to guide the discussion. In the first frame, the reactant wave-packet is started on the lower 3S_1 surface and two identical product wave-packets are positioned at the same location to determine the scattering probability to each channel. The lower product state measures the reflected amplitude and phase in the 3S_1 channel and the upper wave-packet measures the magnitude and phase that is transferred to the coupled channel. By the third frame, the incident wave-packet has entered the interaction region of the potential and has become mixed, as amplitude is apparent of the upper surface. Both waveforms have started leaving the interaction region by the fourth frame. The propagation is allowed to continue until the correlation function between the

incident and product wave-packets on both channels drops to the order of 10^{-5} , completing the first part of the calculation. The same computation is then computed again except the wave-packet is started on the upper 3D_1 surface to complete the 2×2 block (not shown).

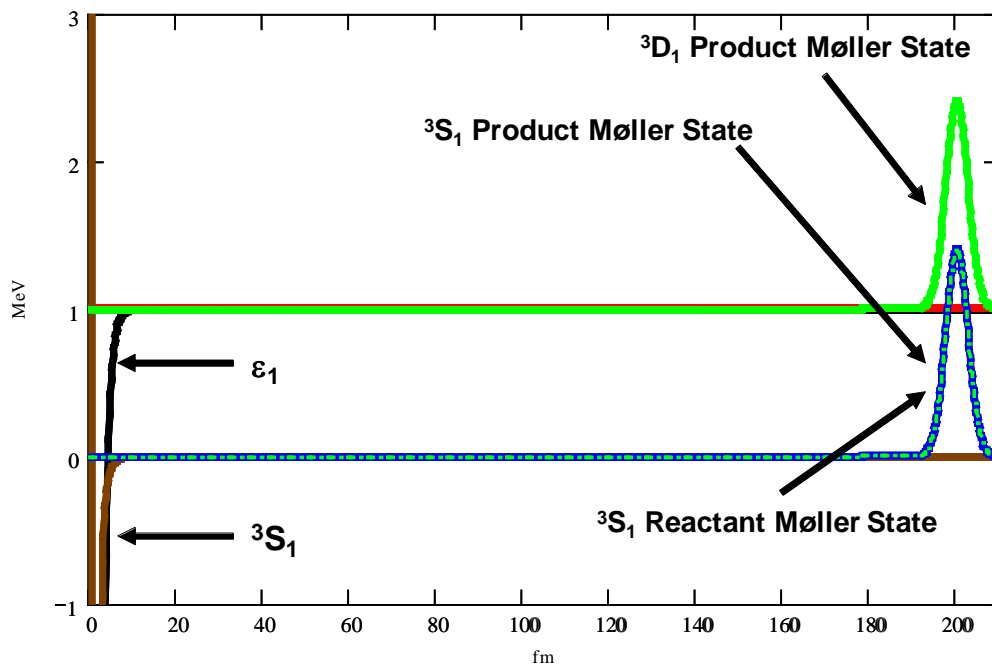


Figure 6.22. Initial 2×2 Wave-Packet Positions (Scaled).. The reactant wave packet is superimposed over the product wave packet on the 3S_1 channel. In this diagram, the 3D_1 surface is not shown and the first off diagonal coupling surface ϵ_1 from Figure 5.2 is artificially displaced for clarity along with the 3D_1 product Møller state. Absolute values of the wave packet are plotted.

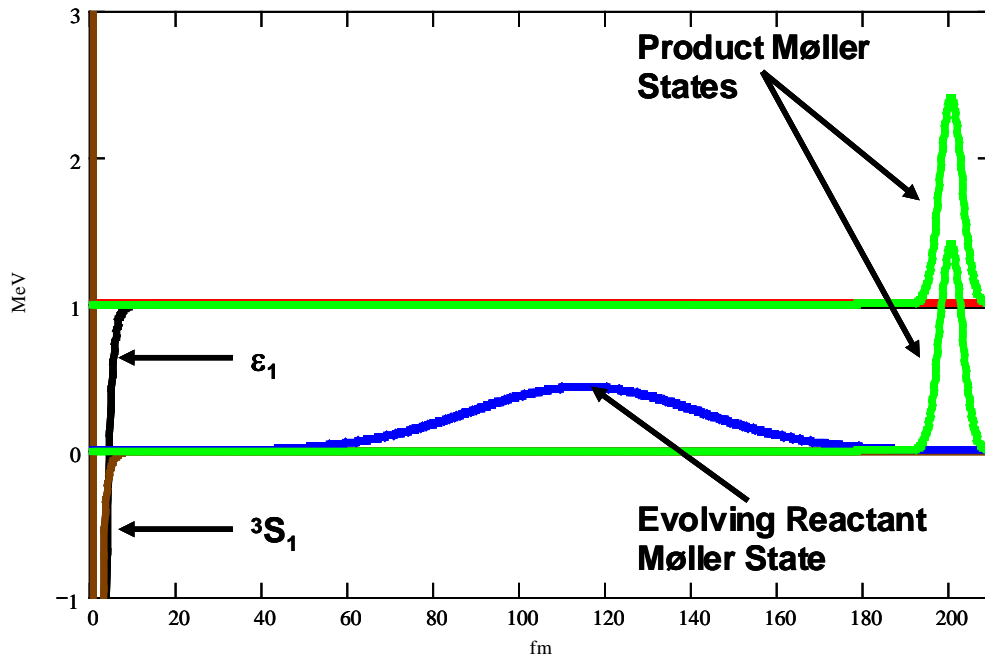


Figure 6.23. Evolving Packet Converges on Potential (Scaled)

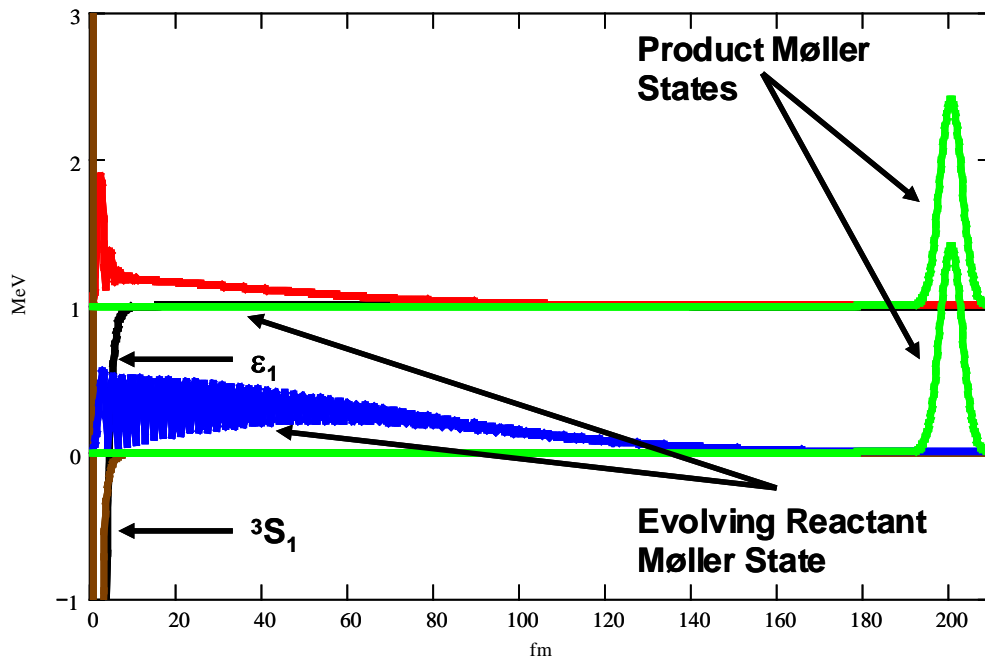


Figure 6.24. Reactant Packet Couples to Mixing Channel (Scaled)

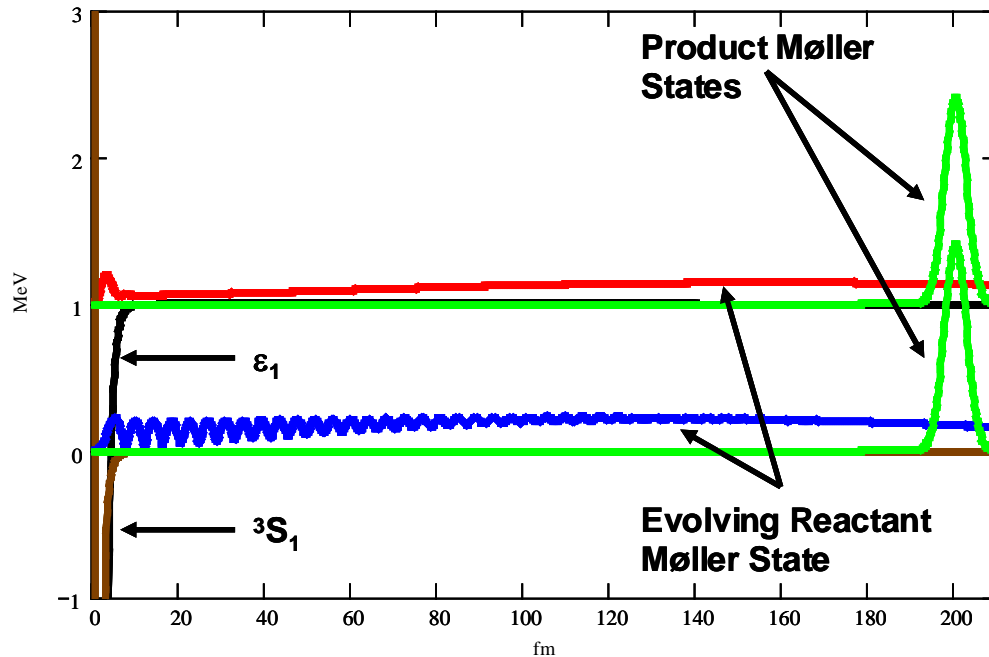


Figure 6.25. Mixed Packets Leave Interaction Region On Both Channels (Scaled). The lower energy components of the wave packet have yet to leave the interaction region.

The phase outputs obtained from this 2x2 calculation are highlighted Figure 6.26 and Figure 6.27. Again, good agreement exists between the CPM and the data provided by ANL. The only slight abnormality is in the low energy region of the 3D_1 which is on the order of a tenth of a degree and considered to be negligible. Additional computation can reduce this error further but was deemed not necessary since it has already been shown that enhanced low energy results can be obtained with the selection of an appropriate wave packet. Here, L has even parity ($L=0$ or 2) and S is symmetric ($S=1$). So, the wave function is symmetric and the pp and nn phase shifts do not need to be computed. However, in the next 2x2 block, 3P_2 and 3F_2 , all three will need to be determined since L and S are anti-symmetric.

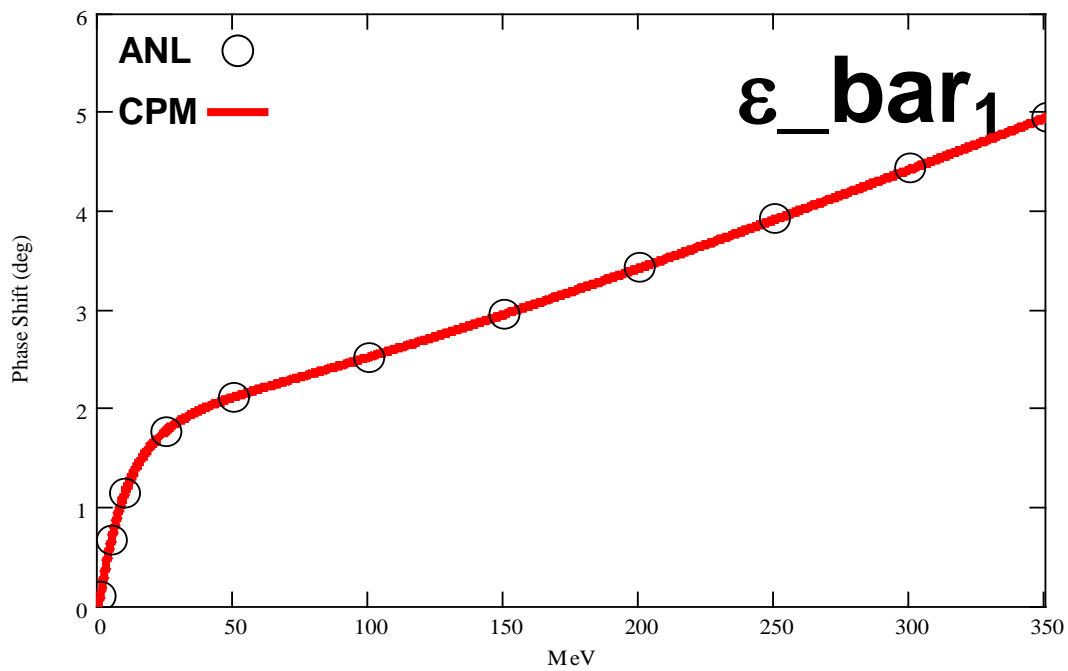
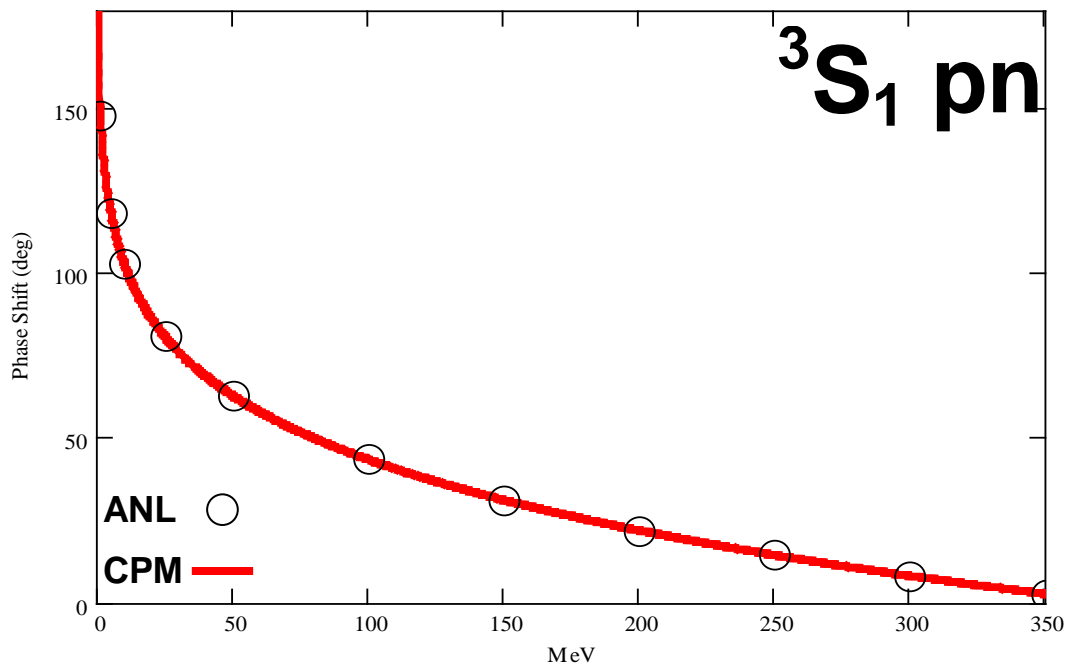


Figure 6.26. Composite CPM Calculation for the 3S_1 pn (top frame) and the $\bar{\epsilon}_1$ pn (bottom frame) Phase Shifts. The $\bar{\epsilon}_1$ pn phase shift is associated with the off diagonal component of the first 2x2 block in the potential matrix given in Figure 5.2

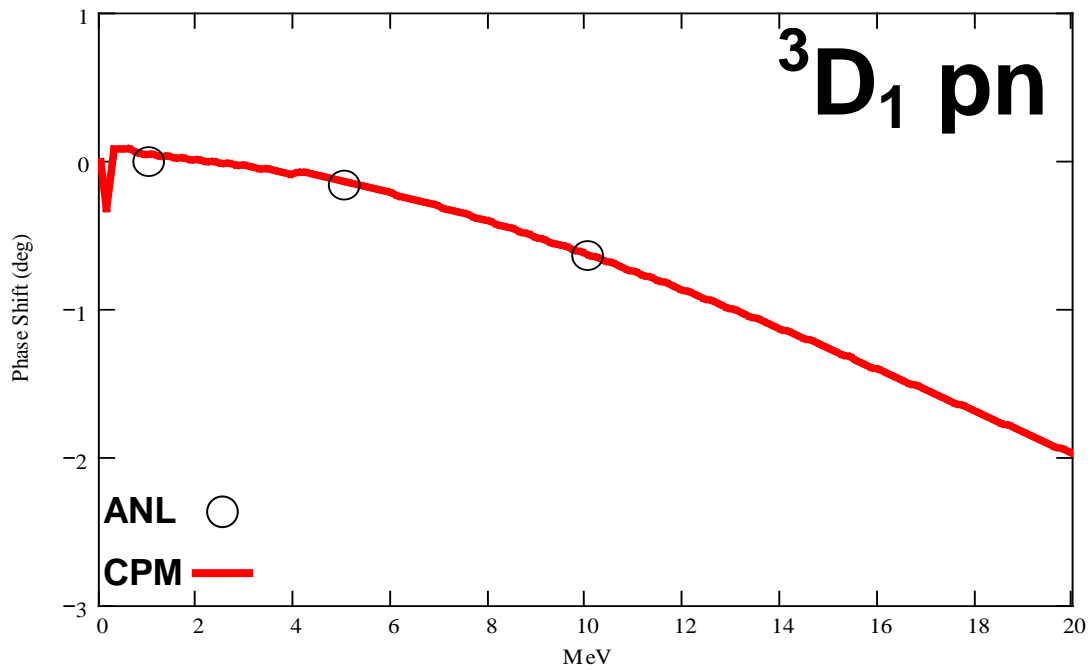
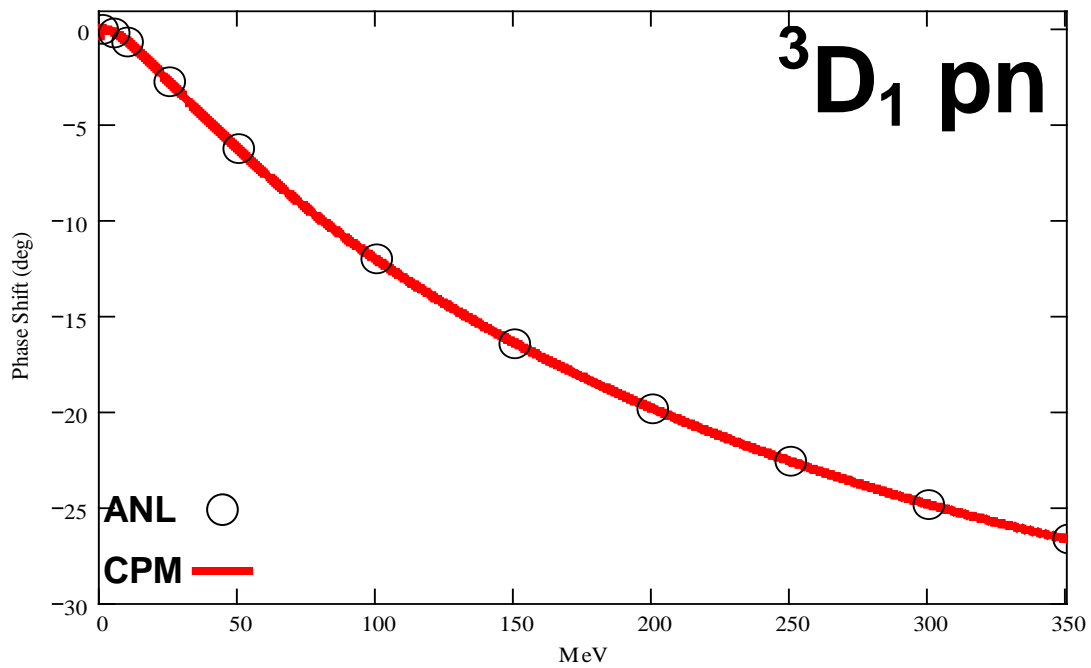


Figure 6.27. Composite CPM Calculation for 3D_1 pn phase shift (top frame). As the lower frame illustrates, the three wave packets chosen to perform these calculations provide good agreement with the published results down to about 1 MeV.

For the 3P_2 and 3F_2 2x2 block, phase shifts were computed for the isospin triplet. These are shown in Figure 6.28 through Figure 6.31. Of the three possible combinations only the pn and pp are given here, the remaining nn phase shifts are included in the Appendices.

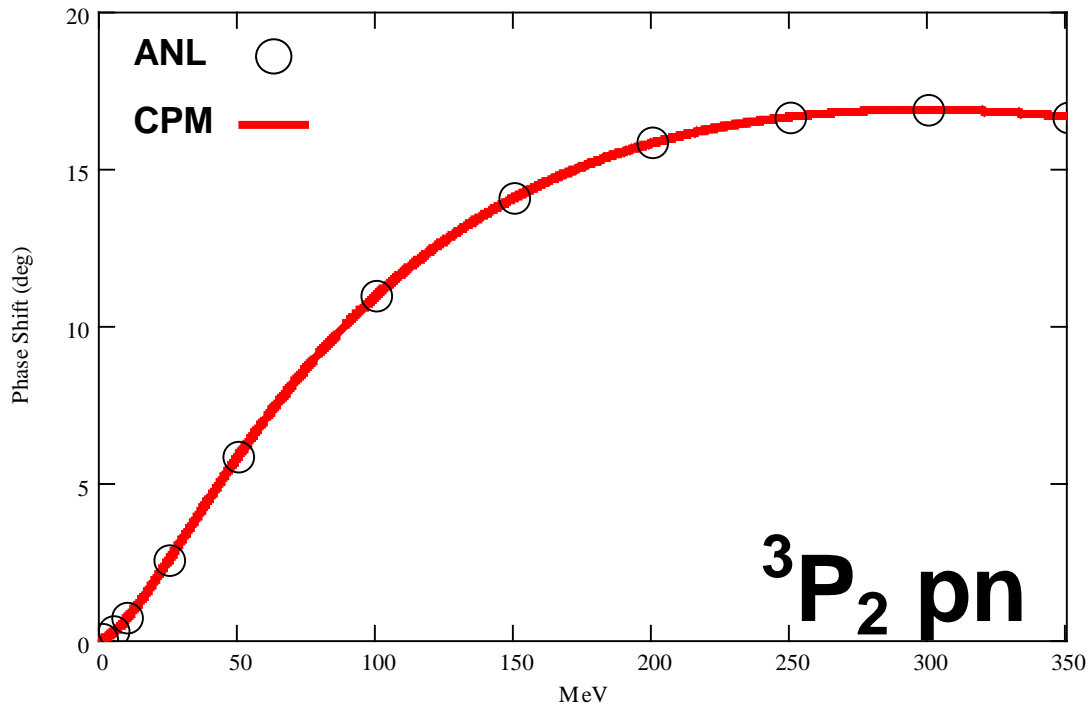


Figure 6.28. Composite CPM Calculation for the 3P_2 pn Phase Shift .

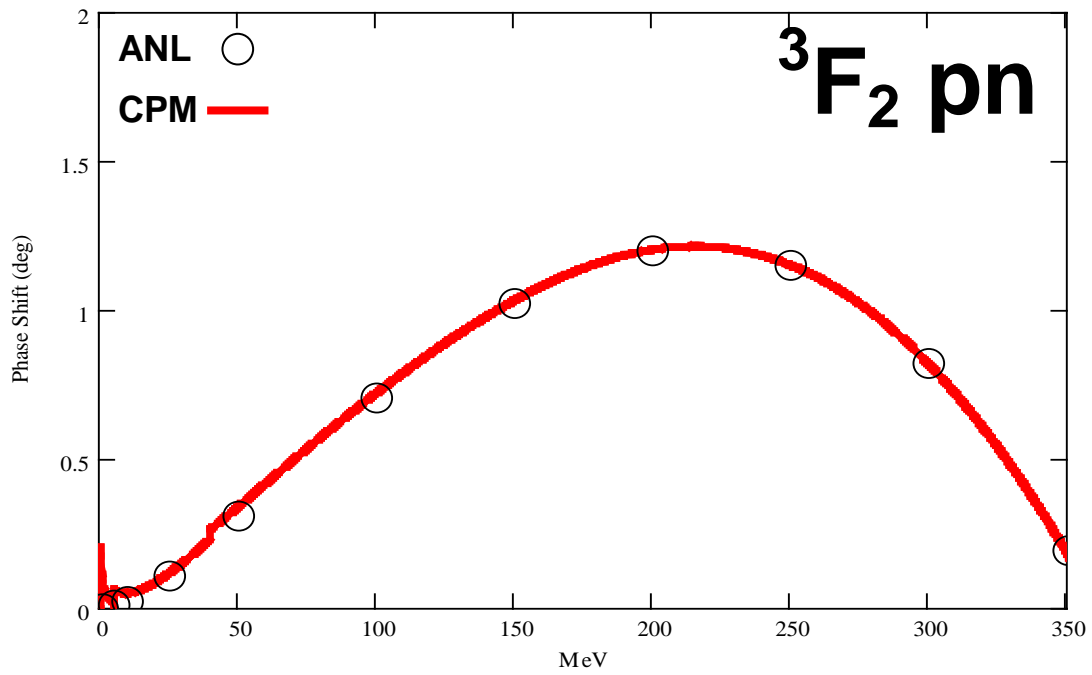
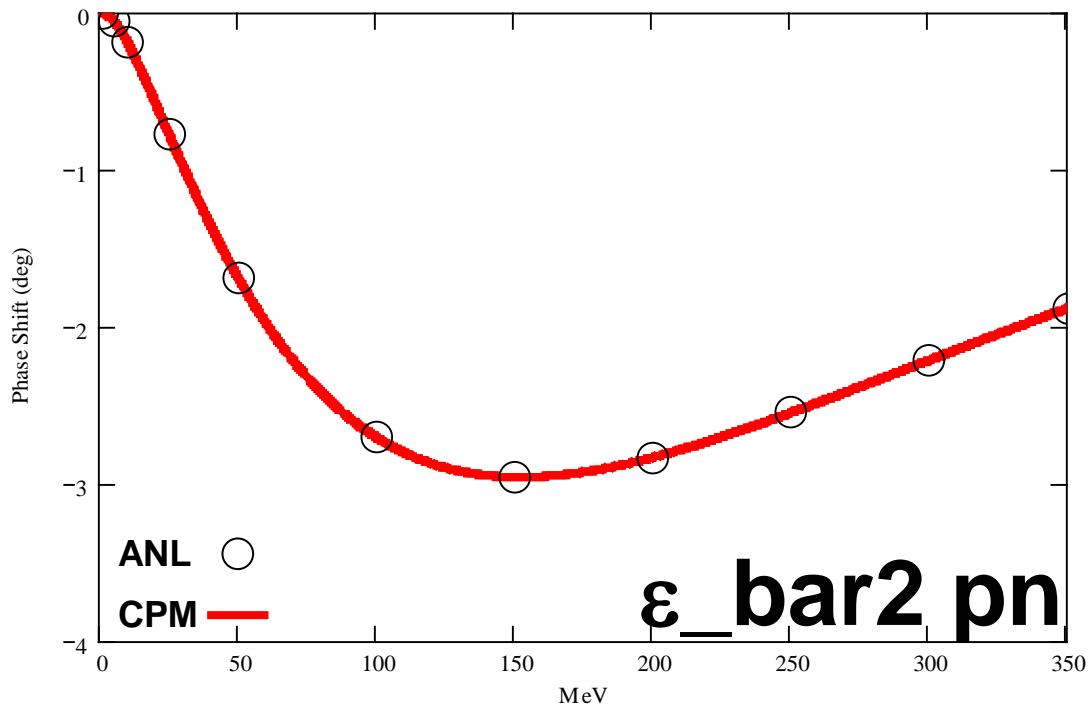


Figure 6.29. Composite CPM Calculation for the $\bar{\epsilon}_2$ pn Phase Shift (upper frame) and the 3F_2 pn Phase Shift (lower frame).. The slight difference in phase at about 40 MeV is a splicing artifact .

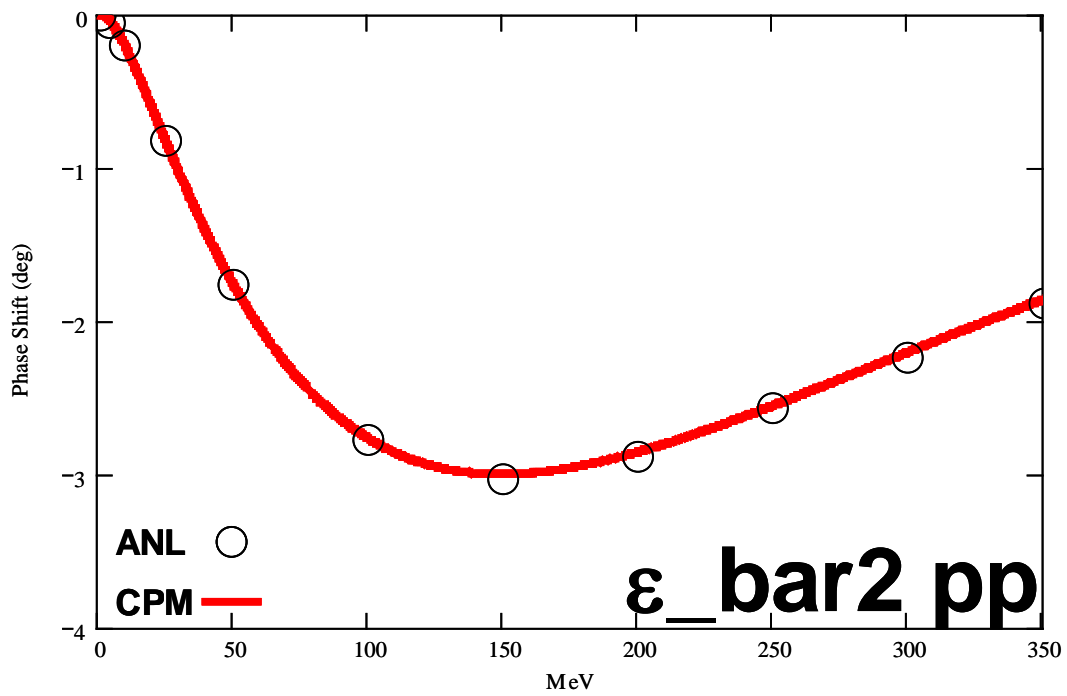
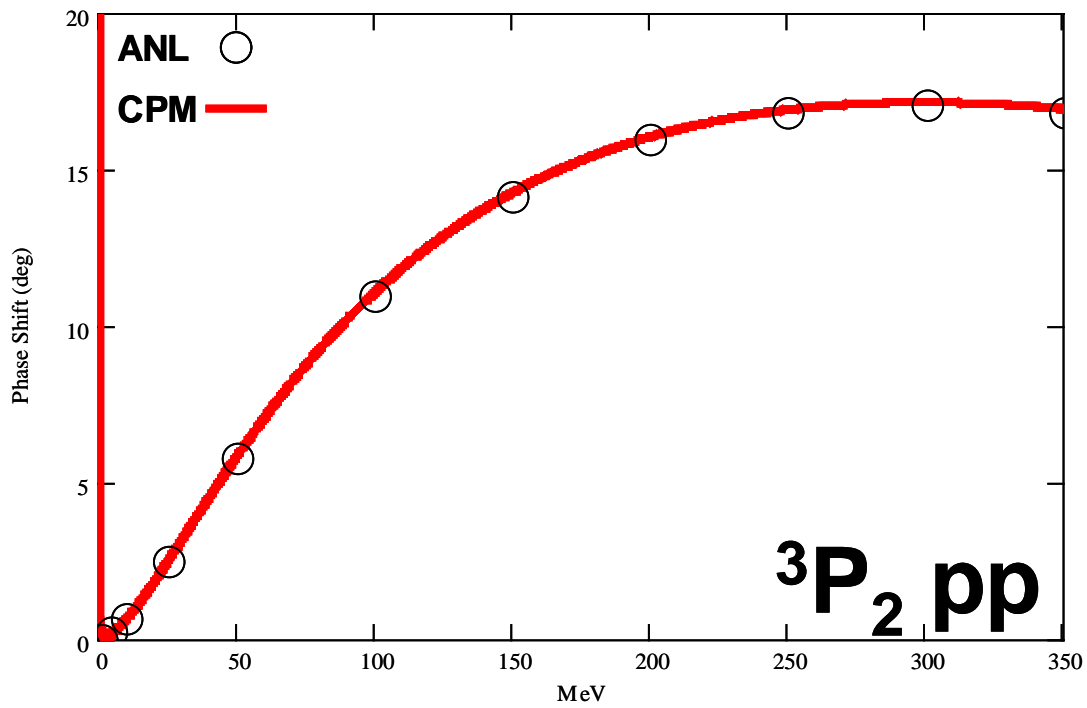


Figure 6.30. Composite CPM Calculation for the 3P_2 pp Phase Shift (upper frame) and the $\bar{\epsilon}_2$ pp Phase Shift (lower frame).

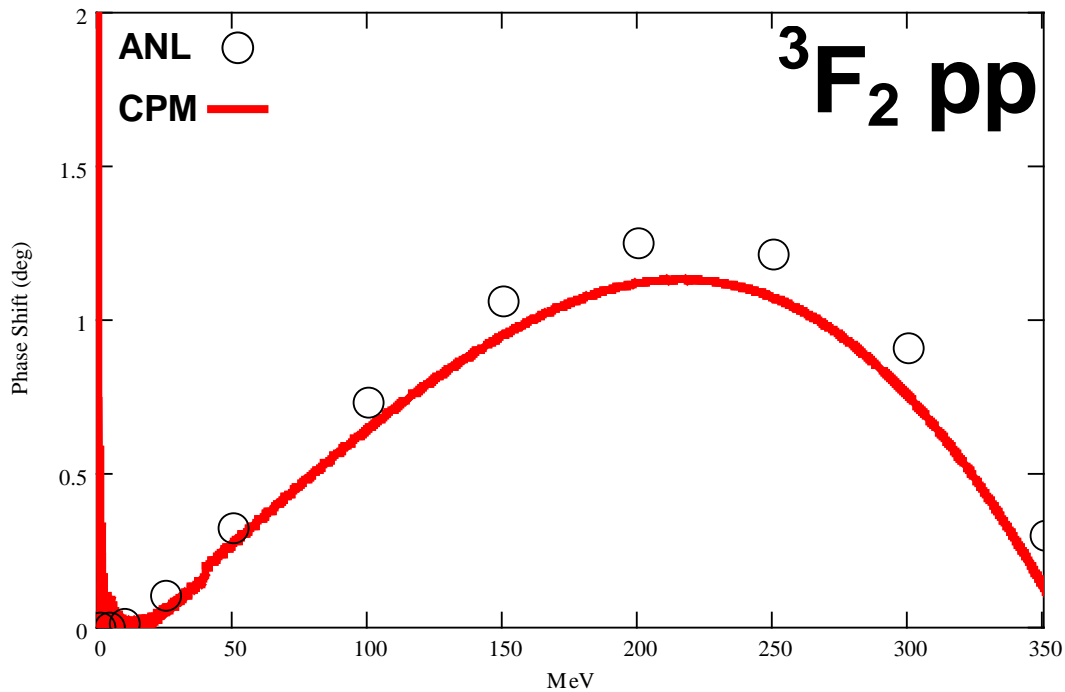


Figure 6.31. Composite CPM Calculation for the 3F_2 pp Phase Shift. The deviation from the published results stems from how the Coulombic correction is applied to the CPM results. Higher L calculations of either 1×1 pp or 2×2 pn phase shifts do not exhibit this deviation

Here, there is again good agreement with the published results for the 3P_2 , $\epsilon_{\bar{2}}$, and 3F_2 pn phase shifts. There is only a small (tenth of a degree) step around 40 MeV in the 3F_2 pn phase shift which is merely a splicing artifact. The same step is evident in the 3P_2 pn phase shift when placed on the same scale. What immediately stands out about the complementary 2×2 pp phase shifts is the deviation of our 3F_2 phase shift from the published results (Figure 6.31). This same error is present in the 3P_2 pp phase shift, it is just not as apparent because the scale of the plot is an order of magnitude larger. Since the error is not apparent in the 3P_2 , $\epsilon_{\bar{2}}$, and 3F_2 pn shifts or 1×1 pp phase shifts of higher order L (Figure 6.21), the source of the error must be associated with how we

applied the Coulombic correction to the 3P_2 , $\varepsilon_{\text{bar}_2}$, and 3F_2 2×2 pp block. Stapp [18] has a possible explanation.

The Coulombic correction developed in Section 5.6.4 corresponds to what Stapp [18] calls a “pure” state calculation or a 1×1 pp matrix element of V_{eff} . In the 2×2 pp calculation, the evolving wave packets enter the interaction region and are mixed yielding s-matrix elements and phase shifts that are linear combinations of P and F. These final P and F states are no longer “pure.” Ideally, we could determine the unitary matrix which would diagonalize the 3P_2 , $\varepsilon_{\text{bar}_2}$, and 3F_2 pp 2×2 block and use the transformation to compute a mixed basis Coulombic correction. Here we choose however to follow Stapp’s advice. In his 1957 paper, he states that the “pure” Coulombic correction may be applied directly to the “bar” phase shifts without introducing a significant amount of error. The tenth of a degree phase difference between the published results and our 3F_2 pp CPM solution is not significant and as Figure 6.32 illustrates well within the range of 3F_2 results obtained from other models [23-25, 32].

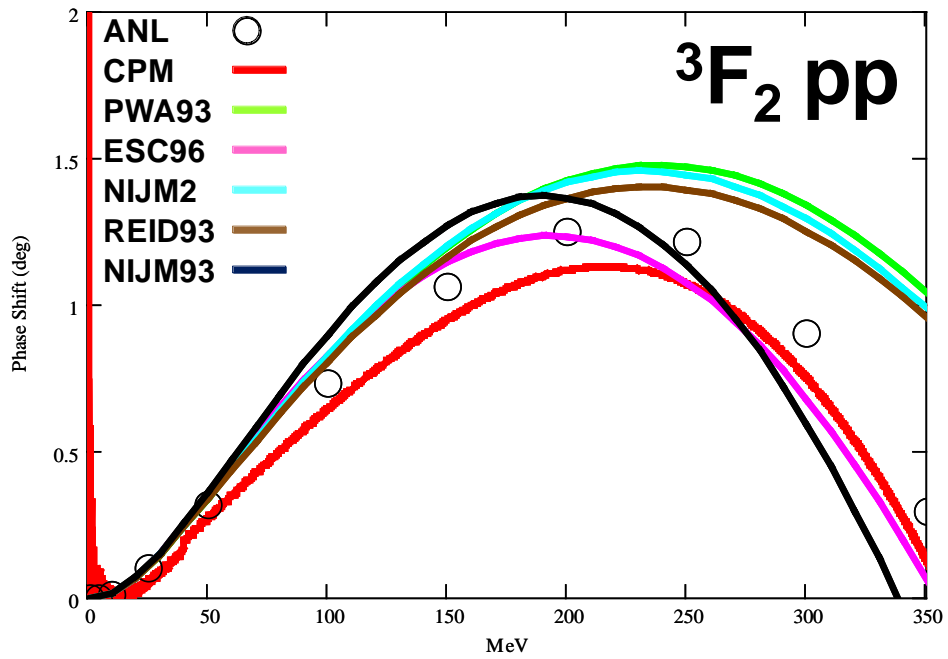


Figure 6.32. Comparison of the Calculated CPM 3F_2 Phase Shift to Published Results from Other Time-Independent Calculations. The tenth of a degree difference between the CPM result and the ANL results is not significant when compared to the differences between the AV18 results and the other models results.

6.3.3. The Cross Section

Nuclear calculations rely heavily on the determination of accurate cross sections to ascertain the probability of reaction between nuclides. The phase shifts calculated in the previous section lend themselves readily to the determination of the nn , pn , and pp cross-sections. Cross sections may be calculated by taking a weighted sum of the triplet and singlet phase shifts for a specified value of angular momentum L given by [7, 78],

$$\sigma = 4\pi \left(\frac{3}{4} a_{\text{triplet}}^2 + \frac{1}{4} a_{\text{singlet}}^2 \right). \quad (6.11)$$

with,

$$\begin{aligned} a_{\text{singlet}}^2 &= \frac{1}{k^2} \sum_{L=0}^{\infty} (2L+1) \sin^2 \delta_L \\ a_{\text{triplet}}^2 &= \frac{1}{k^2} \sum_{J=0}^{\infty} \frac{1}{3} (2J+1) \left(\sin^2 \delta_{L=J-1} + \sin^2 \delta_{L=J} + \sin^2 \delta_{L=J+1} \right) \end{aligned} \quad (6.12)$$

where k is the wave vector. In these calculations, partial waves above $L = 2$ were not considered in the summation since $\sin^2(\text{angle} \leq 1 \text{ degree})$ is very small and does not contribute significantly to the total cross section. The calculated pn , pp , and nn total cross sections in units of barn ($1 \text{ barn} = 10^{-24} \text{ m}^2$) are presented in Figure 6.33 and Figure 6.34 respectively.

It was our original intention to compare these cross sections to the Evaluated Nuclear Data Files (ENDF) posted on the Los Alamos National Lab website. Although there was ample pn cross section data on the website, complementary pp and nn data was not available. Attempts were also made to locate pp and nn total cross sections in the literature without success. After an extensive search, we were only able to obtain

differential cross section data in our 0-400 *MeV* energy range. Nonetheless, we can still make a couple of qualitative assessments about these plots. One, the total cross section was determined correctly from the phase shifts otherwise; the *pn* phase shift in Figure 6.33 would not have such a tight correlation with the published ENDF files. Two, the *pp* total cross section (Figure 6.34) is the total cross section due to short-range forces alone. This is not what would be observed in the laboratory as the long range Coulomb force between the protons would combine with the nuclear potential and produce a different result. Indeed, Blatt [7] mentions that below 10 *MeV*, the only partial wave appreciably changed by the nuclear well is 1S_0 phase shift. All other partial waves with $L > 0$ would be scattered by the Coulomb force long before the particles could become close enough to experience nuclear effects.

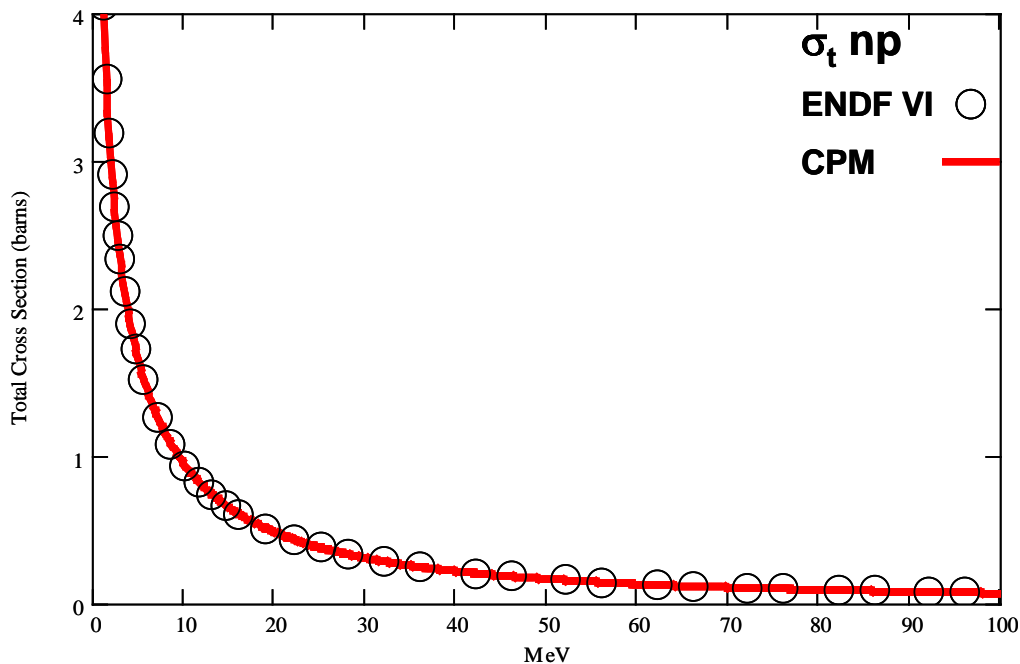


Figure 6.33. Total *np* Scattering Cross Section Compared to the LANL ENDF Data.

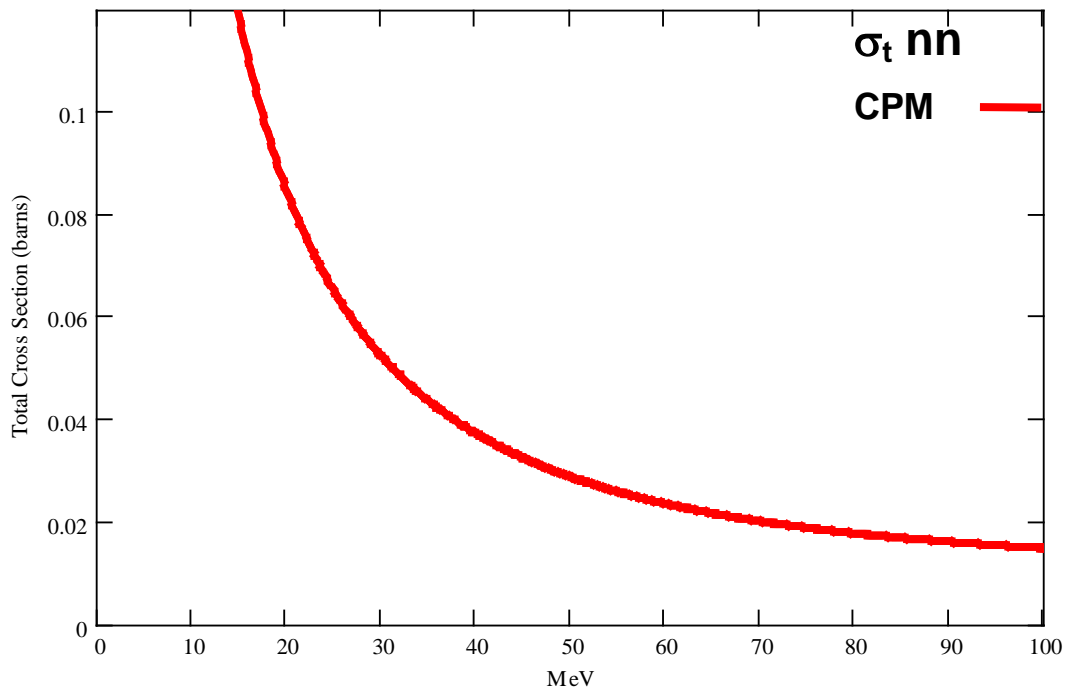
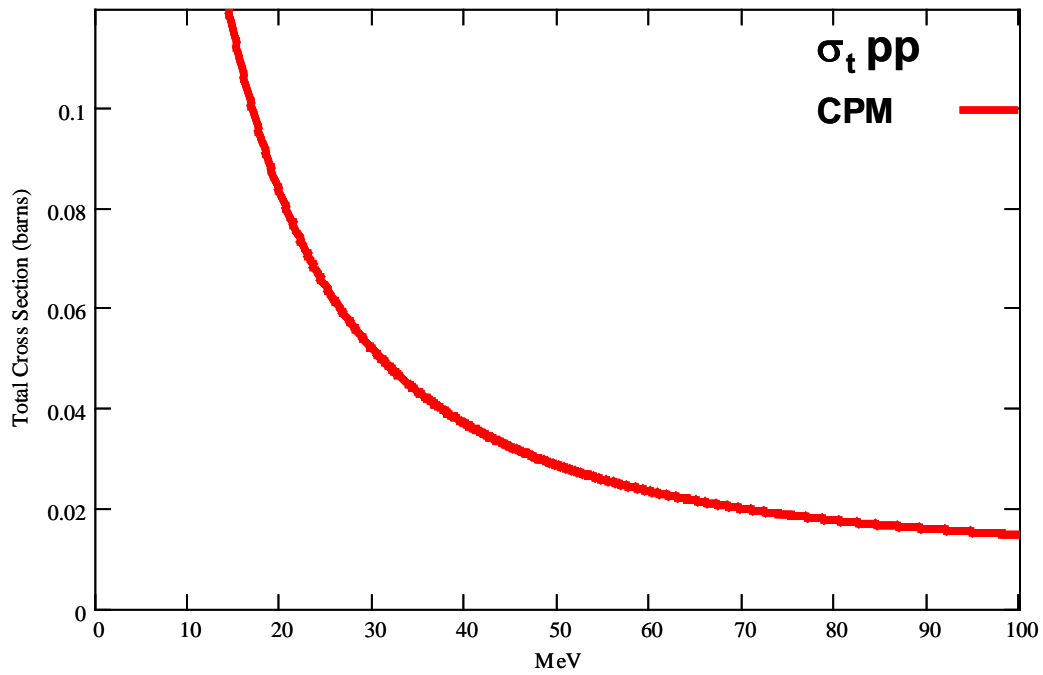


Figure 6.34. Total pp Scattering Cross Section (top frame) and the Total nn Scattering Cross Section (bottom frame). It is important to remember that the pp cross section presented here is the total cross section due to short range forces alone. No published results could be located for comparison

7. Conclusion and Recommendations for Future Work

This research effort is the first to demonstrate complete determination of nuclear scattering matrix elements for proton-proton, neutron-proton, and neutron-neutron scattering events utilizing the time-dependent CPM technique. Wave-packet interaction with a potential in this technique is analogous to a laboratory experiment and provides intuitive insight into scattering dynamics. This is a distinct advantage over the current time-independent scattering methods used by the nuclear community, which retain no additional collision data.

This work was also the first to demonstrate how Møller states can be leveraged to rapidly calculate high-energy resolution scattering matrix elements and phase shifts for an entire block of angular momentum, J . This provides an ancillary utility. Since the nuclear potential has such a short range, these same Møller states can be stored as reused to compute improved phase shifts as higher precision nuclear models become available with minimal computational effort.

The CPM determines the entire phase shift for a range of energies, whereas time-independent techniques typically obtain a range of phase values for a specified energy. Thus depending on the desired information, CPM may be more advantageous. CPM may also be advantageous as the problems become more complex since computational cost of this matrix multiplication technique scales as N^2 or better versus the time-independent approaches which scale as N^3 [50]. This section details the conclusions and outlines the recommendations for future research initiatives.

When we initially set up our channel packet calculations, we attempted to place the Møller states within few thousand femtometers of the nuclear well and calculate the nuclear scattering matrix elements under the assumption that the centripetal barrier's amplitude was small enough as to not interfere with the calculation. This was an incorrect assumption. Each increase in angular momentum corresponded to a significant increase in wave-packet start position. From test calculations for $L = 3$ and 4 , it was shown that the computational cost of positioning the wave-packets in a good asymptotic limit approximation was not practical. As many as 14-15 days would be required for each phase shift calculation for $L \geq 3$ to achieve suitable convergence to the published data.

In an alternative approach, an analytic equation was used to obtain an intermediate state in a suitable asymptotic limit approximation. Then, the time dependent algorithm was used to incorporate information about the centripetal barrier into each wave packet as the wave packets were propagated back to their original positions close to the nuclear well. It was shown that not only could these Møller states be created at a time step 2^3 greater than utilized in the original approach but that these Møller states need only be calculated once for each nucleon-nucleon and angular momentum pairing. This shift in approach resulted in a dramatic 25-50 fold increase in computation efficiency and reproduced published results from ANL with added energy resolution.

The work presented in this dissertation provides a foundation for future time-dependent nuclear scattering calculations. There are two primary proposals for future work. One centers on application of this technique to a three nucleon scattering problem.

The other focuses on the development of an analytic technique for propagating a wave-packet on the centrifugal barrier. These two research initiatives are discussed below.

7.1. *The Three-Body Problem*

The three-body problem is the next logical extension of this research. Here, there are three interacting partners that require nine coordinates to completely describe the motion. Fortunately, nature helps limit the sheer number of possible scattering partners to two since the deuteron is the only two-nucleon system to exhibit binding. For that reason, an incident proton and an incident neutron on a deuteron target are the only two possible three-body combinations. Here, as in the two-body problem, the coordinate system, Hamiltonian, and basis must be determined before any three-body CPM calculations can be performed.

Although the choice could be made to perform this calculation in the Space-Fixed Center of Mass frame as we did in the two nucleon scattering problem, a more suitable coordinate system for the three-nucleon problem is the body fixed coordinate system. In this coordinate system, the motion of the center of mass is eliminated by selecting Jacobi coordinates to describe the interaction. These are shown in Figure 7.1 .

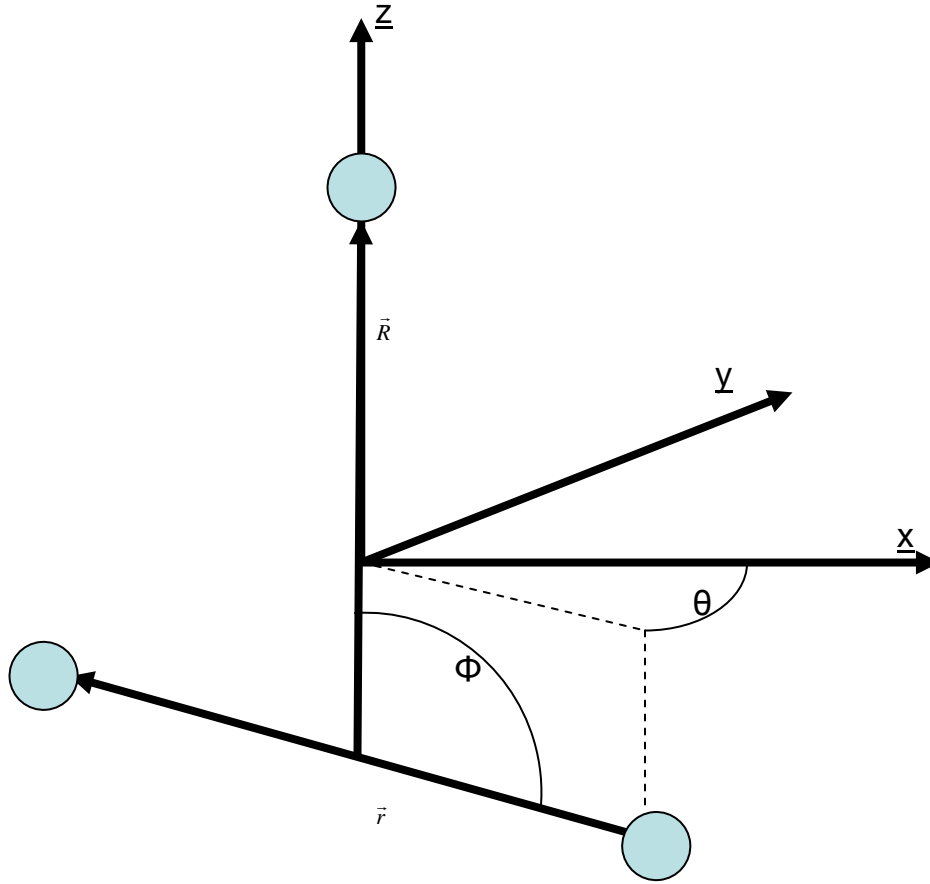


Figure 7.1. Jacobi Coordinates. The Jacobi coordinate system is a useful choice for performing three-body time-dependent scattering calculations.

Here, \vec{R} is aligned along the body fixed z-axis and represents the separation between the deuteron and the incident particle, \vec{r} is the distance between the deuteron constituents, ϕ is the azimuthal angle between the \vec{R} and \vec{r} , and θ is orientation of the di-nucleon about body z axis.

The Full Hamiltonian well suited for three-body problem is,

$$\hat{H} = \frac{\hat{P}_R^2}{2\mu_{A,BC}} + \frac{\hat{L}^2}{2\mu_{A,BC}R^2} + \frac{\hat{j}^2}{2\mu_{BC}r^2} + \hat{V}_{Interaction} = \frac{\hat{P}_R^2}{2\mu_{A,BC}} + \hat{V}_{eff}. \quad (7.1)$$

where L^2 refers to the tumbling of the composite system around the center of mass and J^2 refers to the rotation of the di-nucleon. These terms are incorporated into the potential creating an effective potential of the form,

$$V_{eff} = \sum v_{ij} + \sum v_{ijk} + \frac{\hat{L}^2}{2\mu_{A,BC}R^2} + \frac{\hat{j}^2}{2\mu_{BC}r^2} \quad (7.2)$$

where the AV18 model represented here as v_{ij} is augmented by a three body correction, v_{ijk} . Neither the AV18 Model, nor any of the other NN models, serves as a suitable description of the three-body potential by themselves since all fail to adequately describe the coupling between three interacting partners. Bound state energies of the Tritium atom in the AV18 are underestimated by around by 1 *MeV* compared to the measured value of 8.48 *MeV* [8]. As shown in Figure 7.2, the agreement between the AV18 binding prediction (blue bars) and observation (green bars) continues to deteriorate rapidly with increasing N [80]. To compensate for the underbinding in heavier nuclei, ANL and the University of Illinois at Urbana have developed a new three-body correction designated as the IL2. The IL2 (red bars in Figure 7.2) has been shown to be able closely approximate observed binding energies of heavier nuclei through $A=12$. At this time, however, distributable code for the IL2 is not available so applying the CPM technique to the three-body problem will require development of an AFIT IL2 FORTRAN code [79]

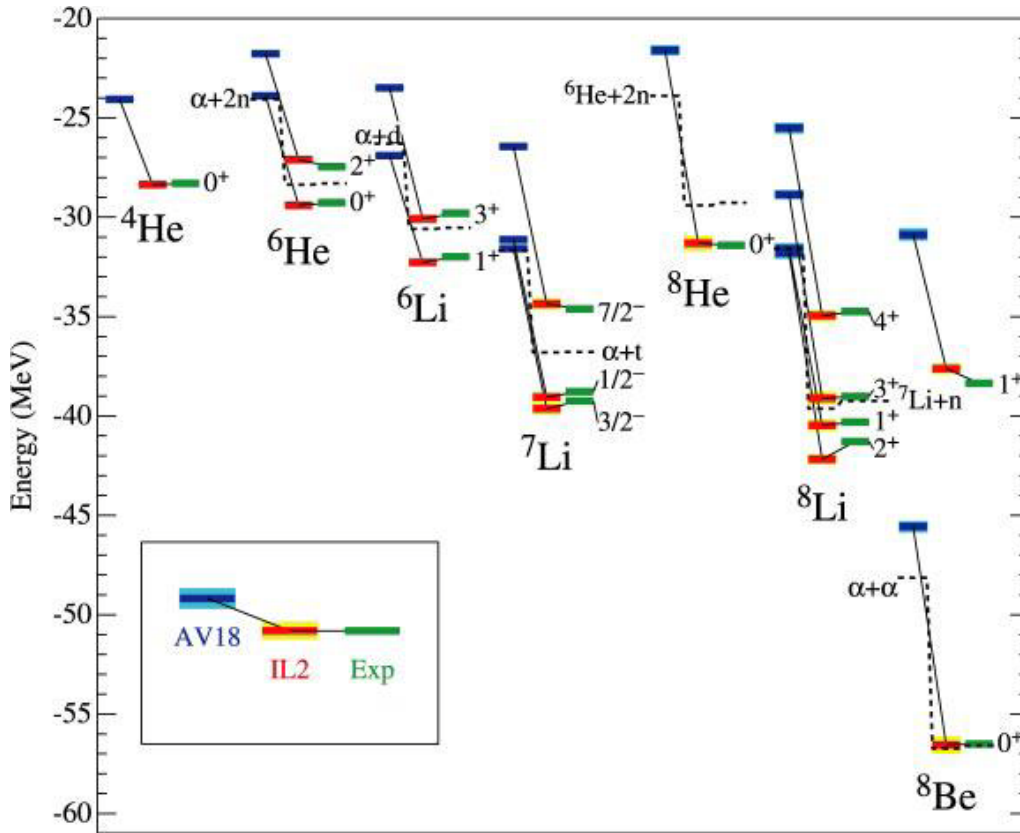


Figure 7.2. AV18, AV18/IL2, and Experimental Binding Energy. [8, 80] Note the improvement in the binding energy when the IL2 correction is applied to the AV18. The IL2 correction to the AV18 has been able to reproduce the binding energies of nuclei containing up to twelve nucleons.

A well-suited basis set in which to represent the Hamiltonian is always important. Since the core of the three-body potential is the AV18, we expect that the basis set would resemble the basis set utilized in the two-body analysis,

$$|\psi\rangle = |J L S s_1 s_2 s_2 T \tau_1 \tau_2 \tau_2 R \rangle_1 \quad (7.3)$$

and that the same spin (isospin) coupling encountered in Chapter 5.4 should help reduce the basis set to the more manageable form,

$$|\psi\rangle = |J L S T R r\rangle \quad (7.4)$$

Here, it is recommended that the research be broken into at least two separate projects. The first should focus on developing a working IL2 code and calculating phase shifts for the elastic problem below 2.42 MeV . The second project should focus on the inelastic scattering problem above 2.42 MeV . For this second problem, the CPM technique will need to be extended for a change of channel from $A + (BC)$ to $A+B+C$ before inelastic phase shifts can be computed. Both projects will be challenging.

7.2. *Analytic Determination of the Møller State*

Back in Section 6.3, we used equation (5.82) to analytically determine an intermediate state in a suitable asymptotic limit approximation then used the time dependent algorithm to propagate the wave packets back to their original positions to establish Møller states. This approach incorporated centripetal barrier information into each wave packet prior to computing scattering matrix elements and reduced the amount of time required compute scattering matrix elements 99%. Although we were able to make huge gains in computational efficiency, it still took almost twelve hours to compute the initial Møller states for the scattering matrix calculations.

An even more efficient and useful approach would be to develop an analytic solution to the time-dependent radial form of Schrödinger's equation,

$$i\hbar \frac{\partial \psi}{\partial t} = \left[-\frac{\hbar^2}{2\mu r} \frac{\partial^2}{\partial r^2} r + \frac{L \cdot (L+1) \hbar^2}{2\mu r^2} + V(r) \right] \psi \quad (7.5)$$

where the potential $V(r)$ is set to zero. This equation has the inhomogeneous PDE form

$$u_t = k u_{xx} + f(x, t) \quad (7.6)$$

and can be expressed in terms of a Green's function, K [81]

$$\psi(r, t) = \int K(r', r, t) \psi(r', 0) dr' \quad (7.7)$$

which relates the initial condition, $\psi(r', 0)$, to some final state at some later time, $\psi(r, t)$.

Andrews [44] has shown the solution to this Green's function kernel for the repulsive $\frac{1}{r^2}$ potential as,

$$K(r, r', t) = i^{-(\nu+1)} \left(\frac{\mu}{\hbar} \right) \frac{\sqrt{r r'}}{t} \exp \left[\frac{i\mu}{2\hbar t} (r^2 + r'^2) \right] J_\nu \left(\frac{r r' \mu}{\hbar t} \right) \quad (7.8)$$

where μ denotes the reduced mass, J_ν denotes Bessel functions of the first kind, and the orbital momentum dependence is contained within dimensionless parameter ν ,

$$\nu = \sqrt{\left(\frac{1}{4} + L \cdot (L+1) \right)} \quad (7.9)$$

Since solutions to ν are in $n + \frac{1}{2}$ powers of angular momentum, the Bessel functions can be expanded in terms of cosines and sines [76]

$$J_{\frac{1}{2}}(x) = \sqrt{\frac{2}{\pi x}} \sin(x) \quad (7.10)$$

$$J_{\frac{3}{2}}(x) = \sqrt{\frac{2}{\pi x}} \left[\frac{\sin(x)}{x} - \cos(x) \right] \quad (7.11)$$

$$J_{\frac{5}{2}}(x) = \sqrt{\frac{2}{\pi x}} \left\{ \left(\frac{3}{x^2} - 1 \right) \sin(x) - \frac{3}{x^2} \cos(x) \right\} \quad (7.12)$$

Given the above information, a test calculation was performed using the broad energy wave packet parameters given in Table 6.4 and a trapezoid integration algorithm.

Although similar results were obtained to those obtained via our CPM calculations, an

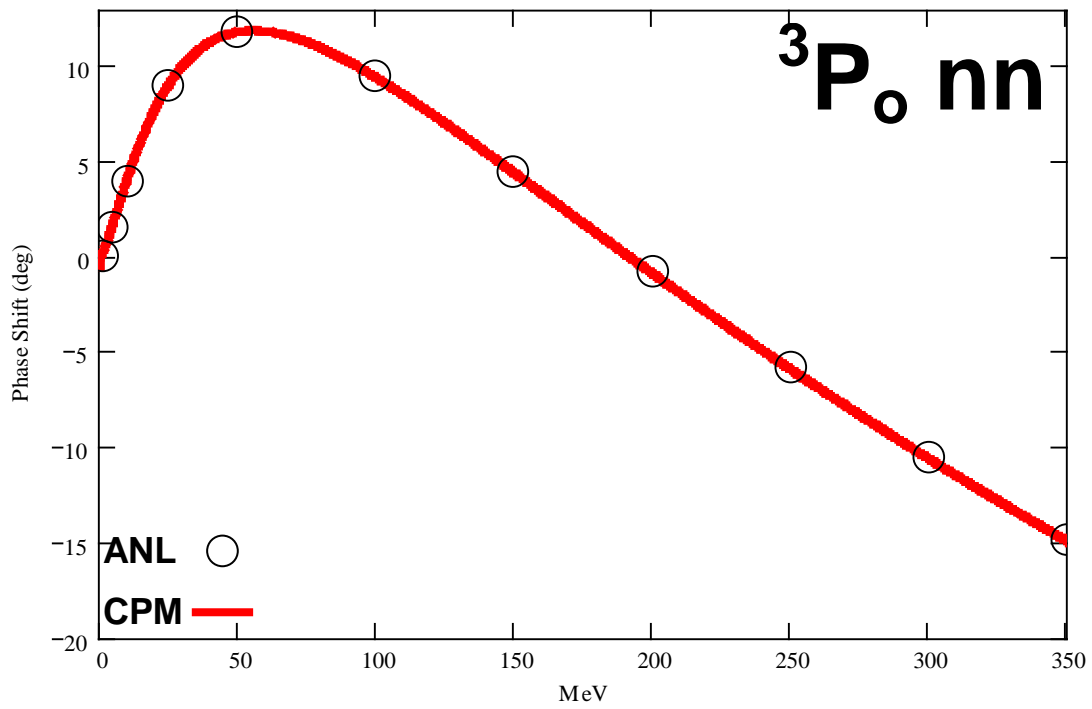
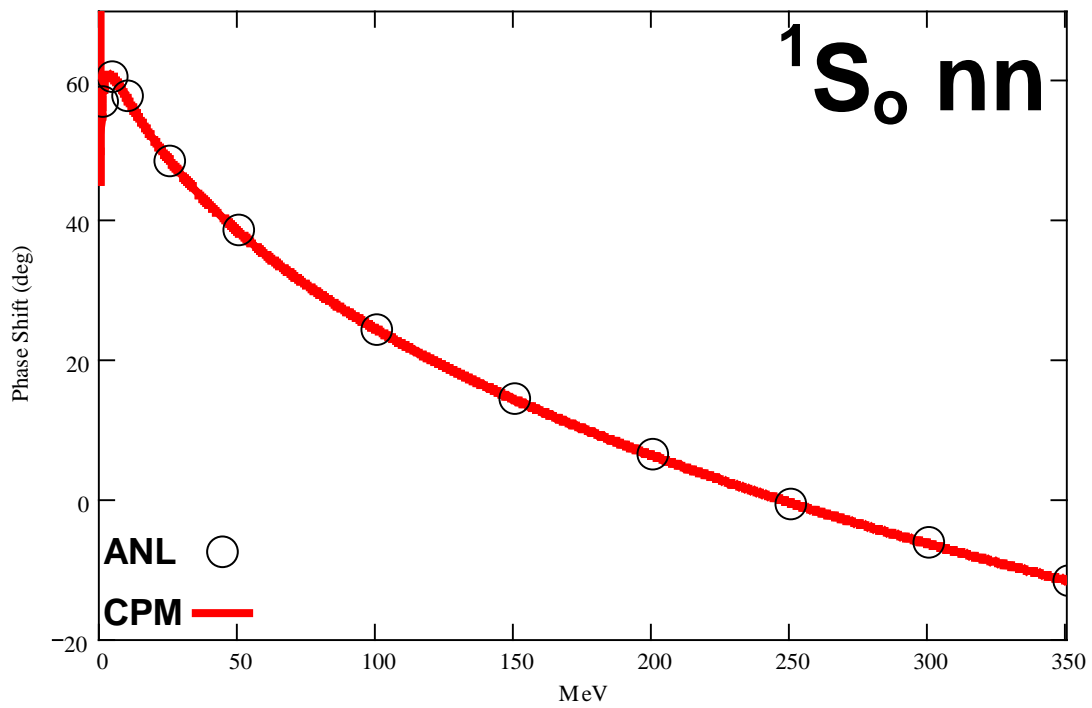
additional 12 hours was required to complete the calculation. Andrew's Green's function solution may be a good starting point for subsequent research.

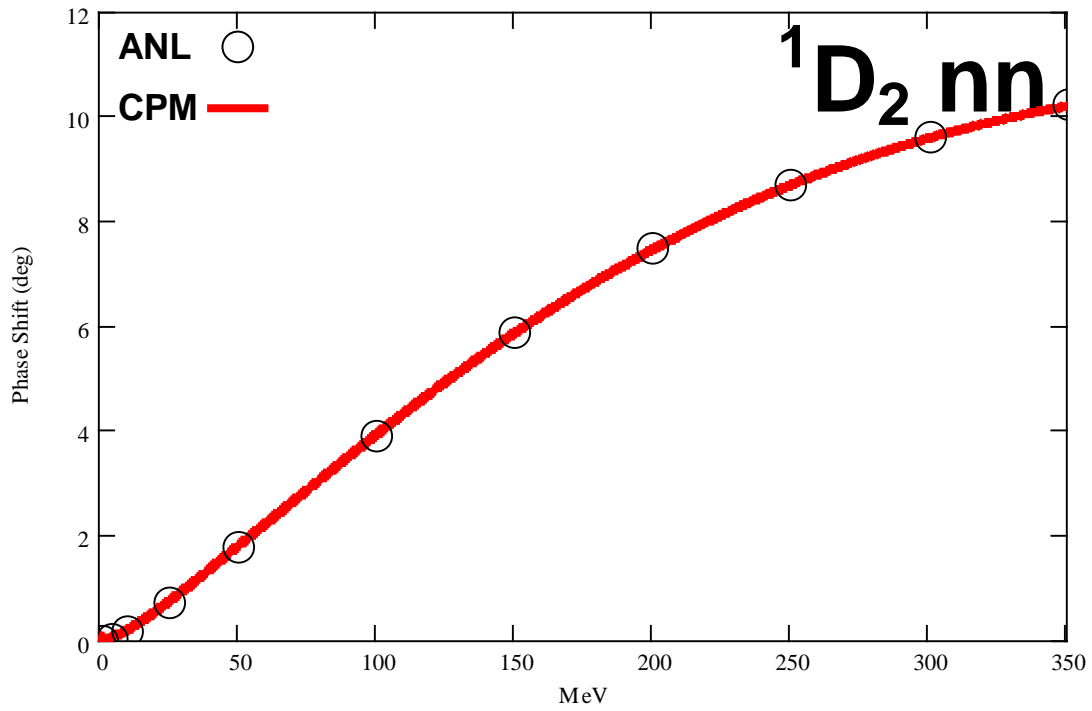
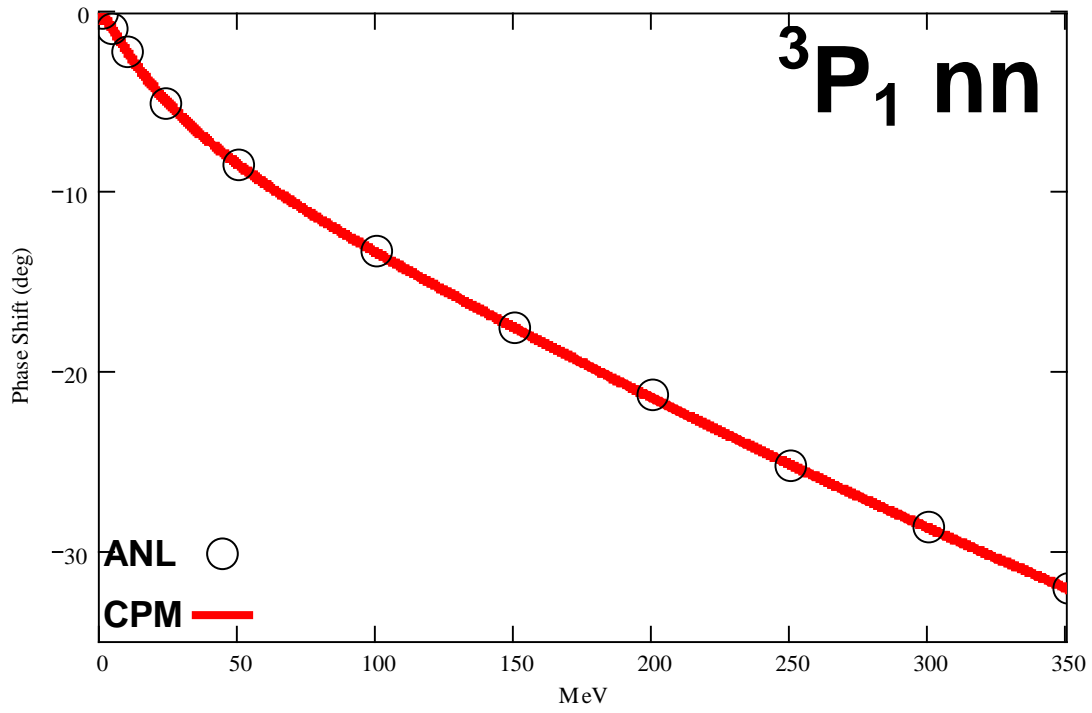
Appendix

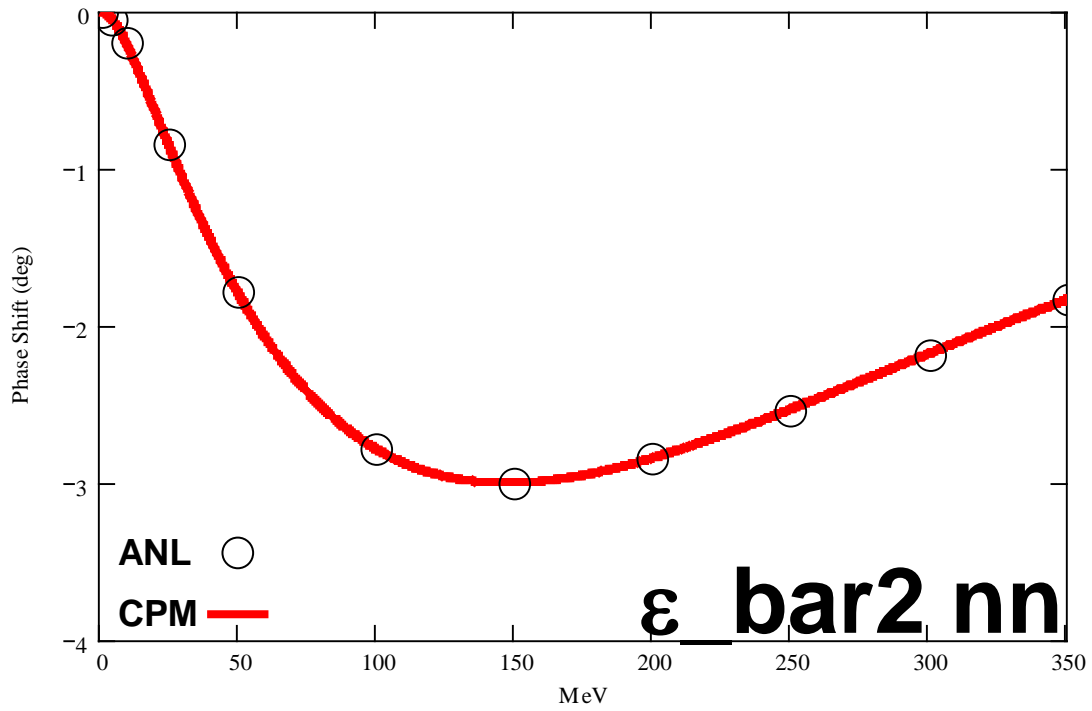
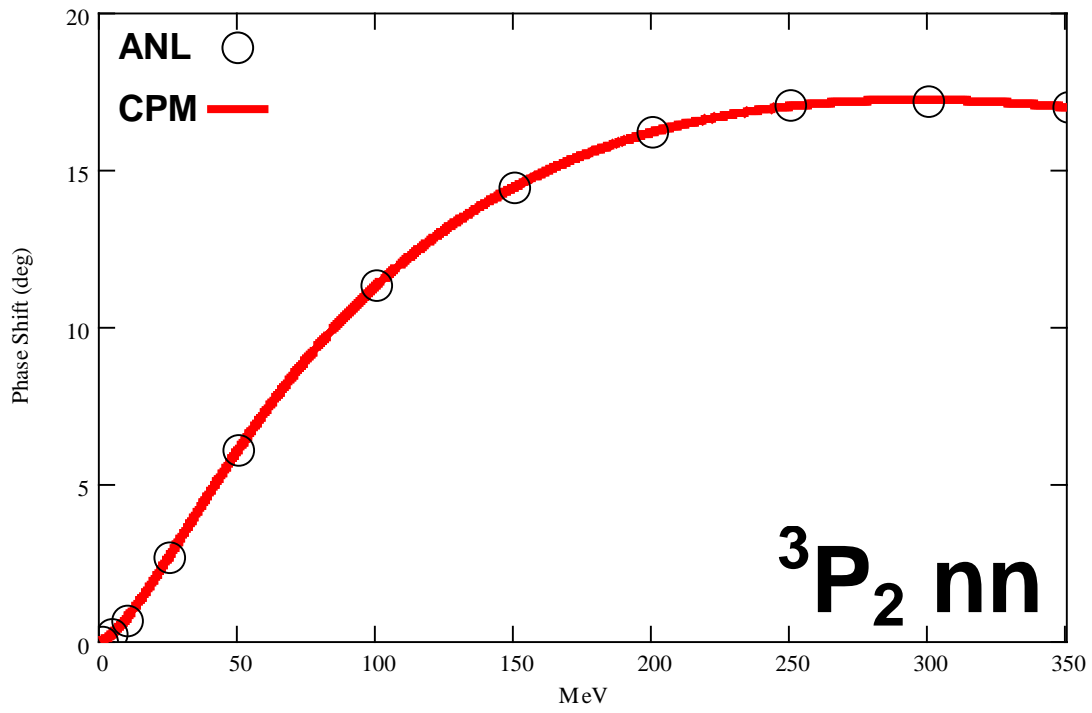
NN PHASE SHIFTS

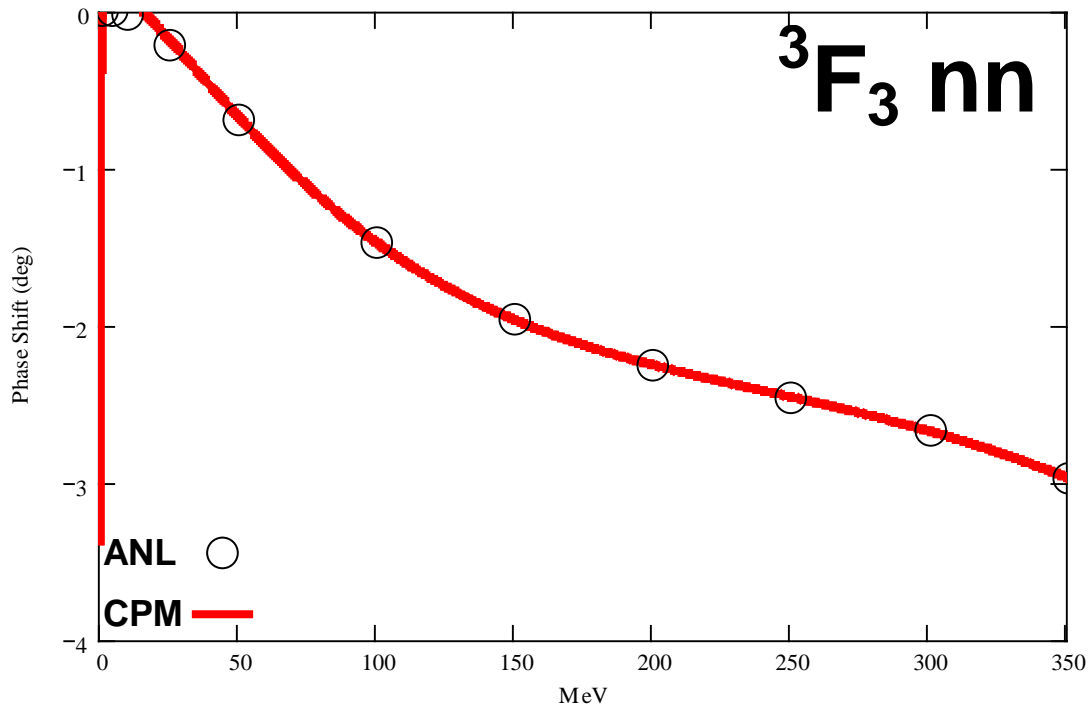
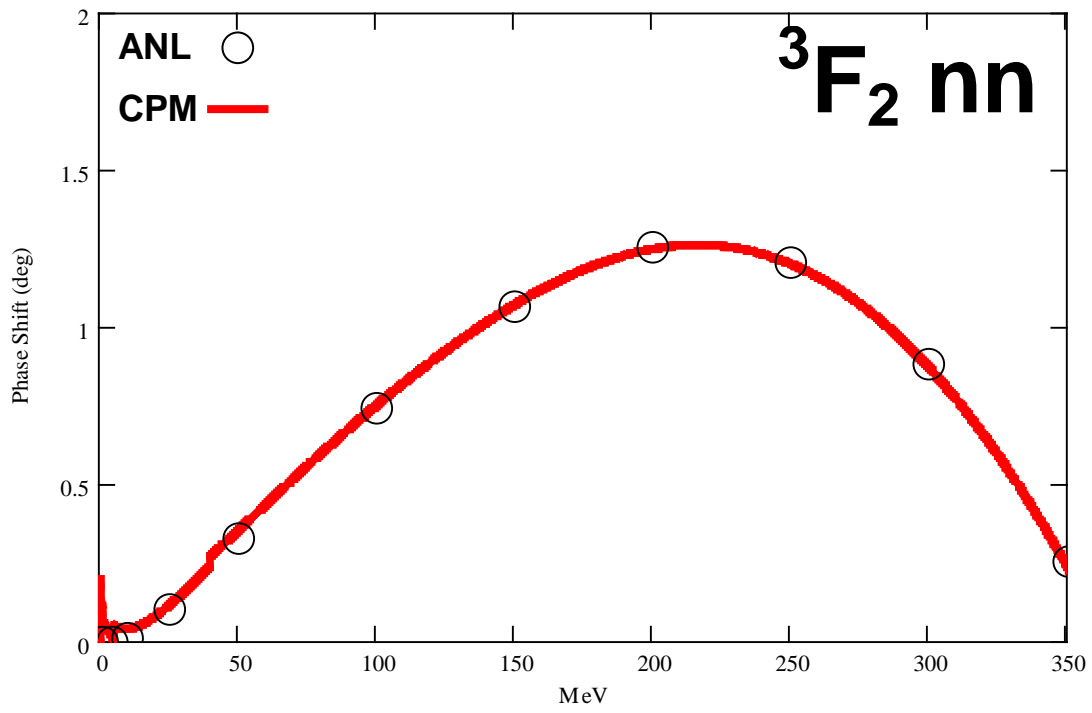
FOR $J = 0 - 5$

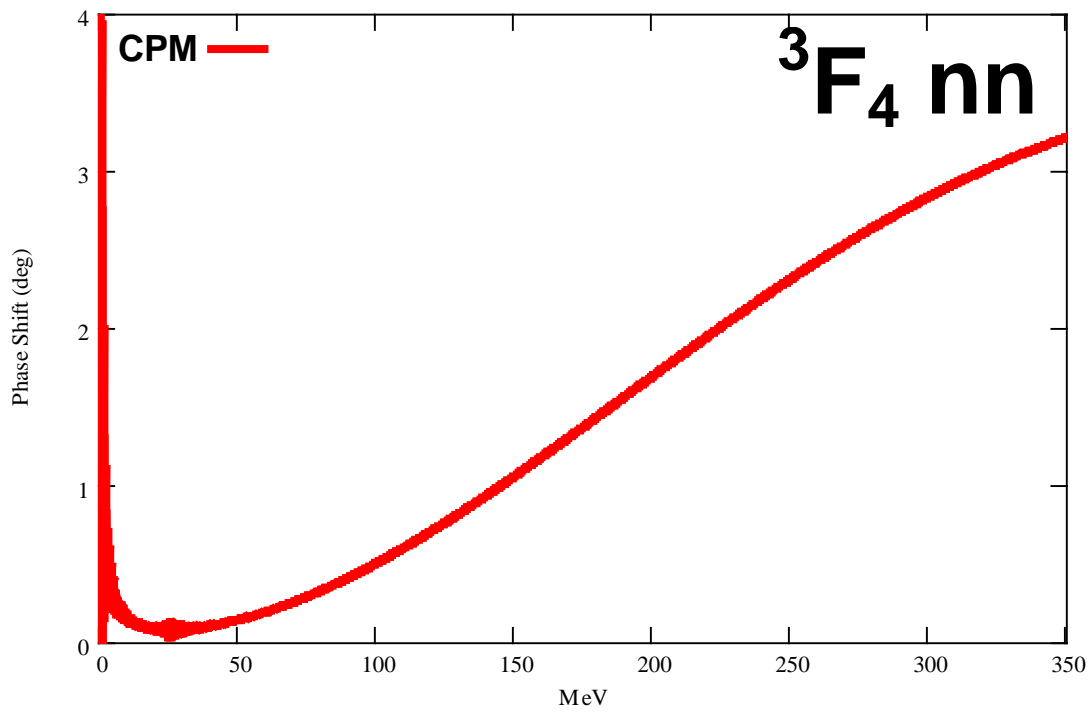
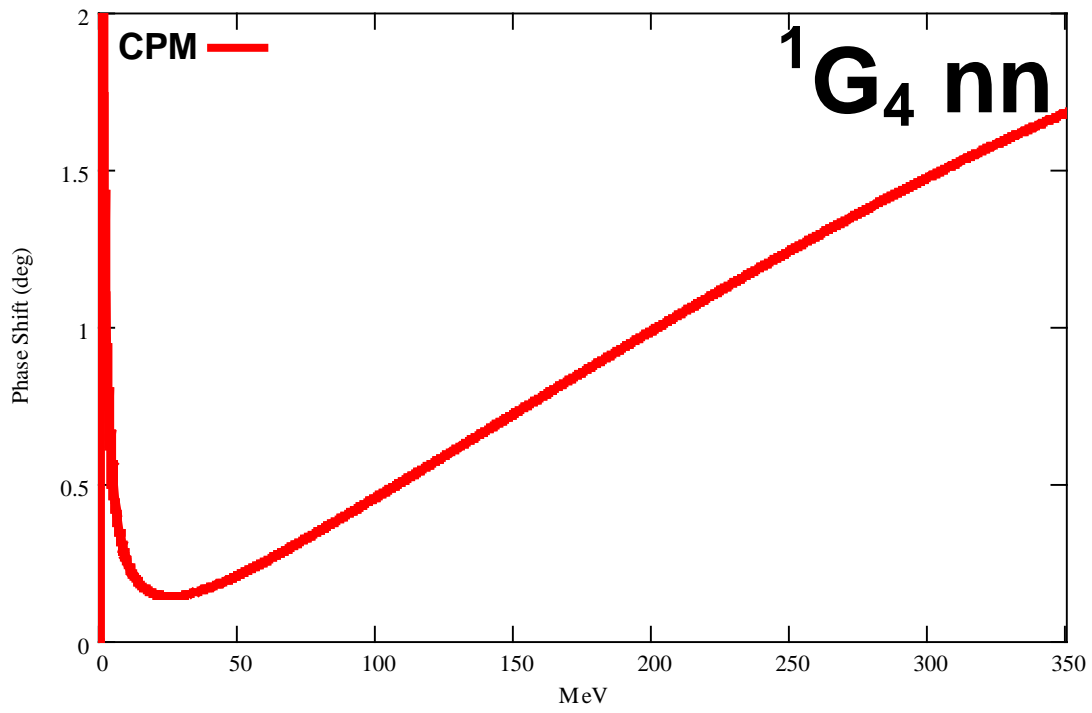
Data from Nijmegen (PWA) experimental data used when ANL data not available

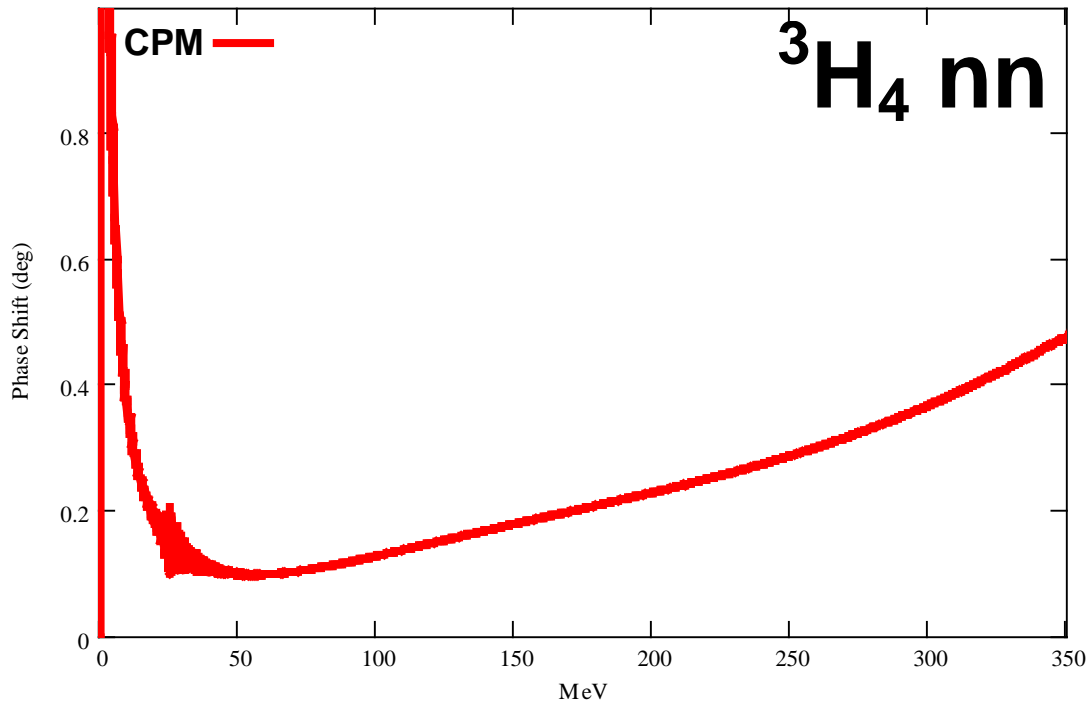
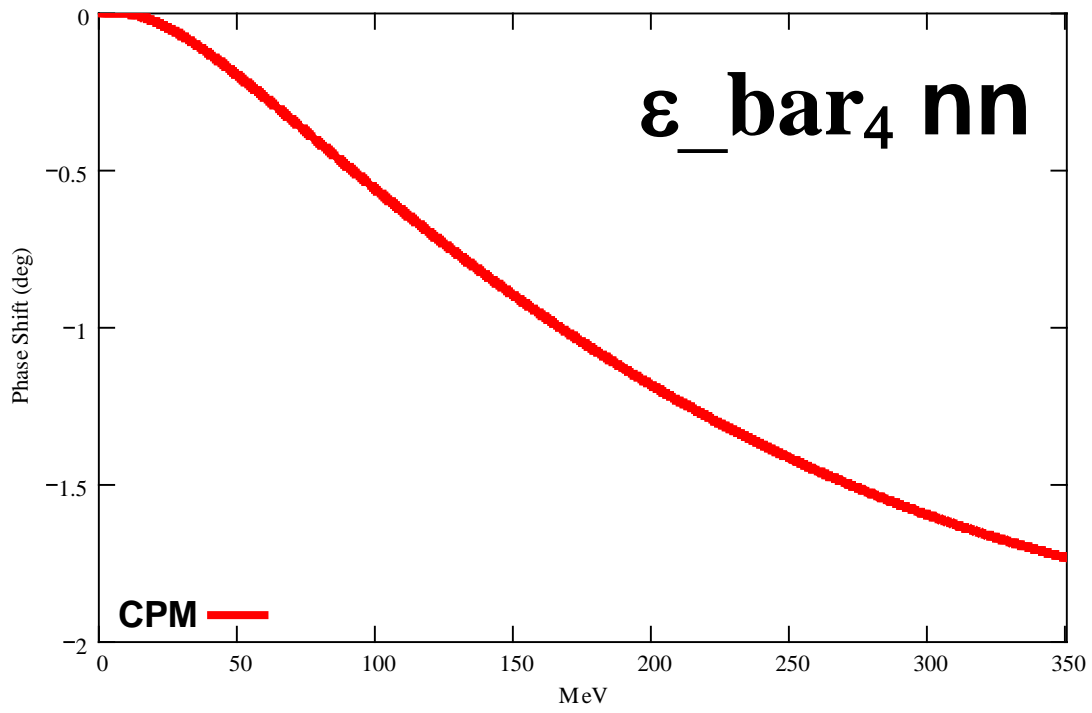


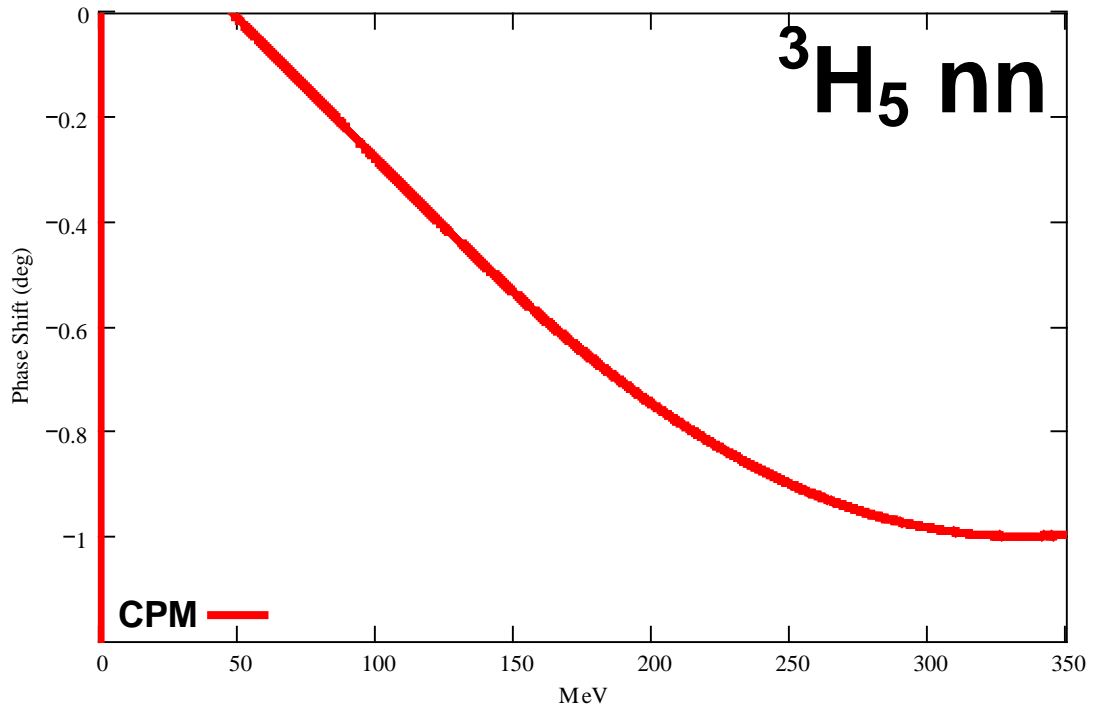








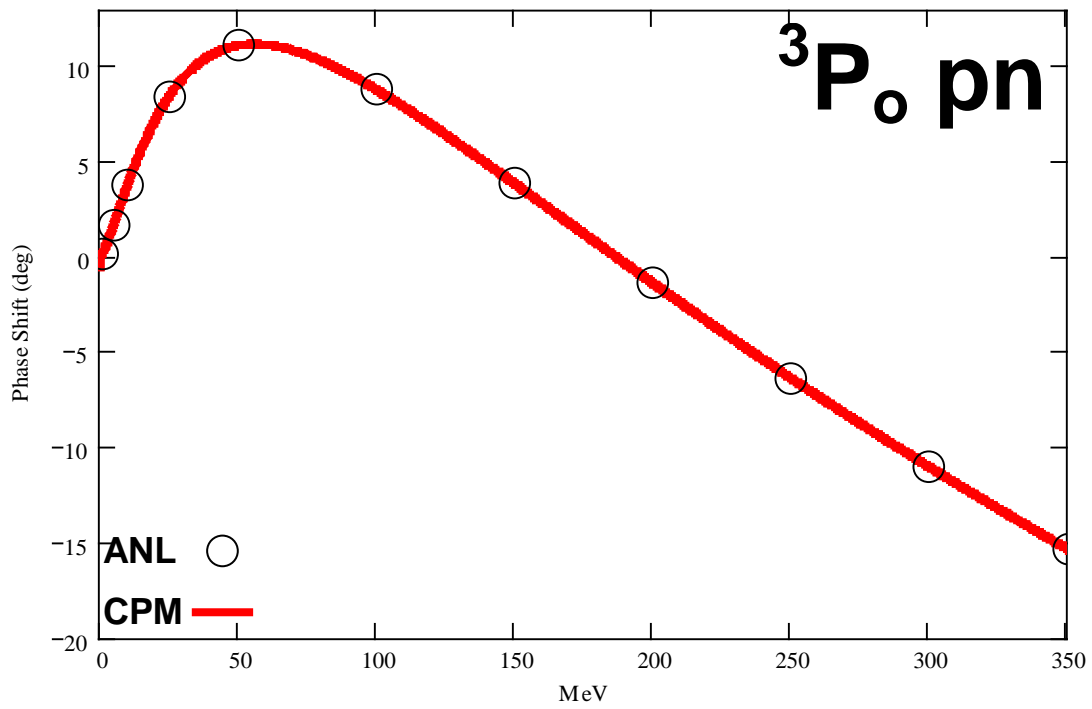
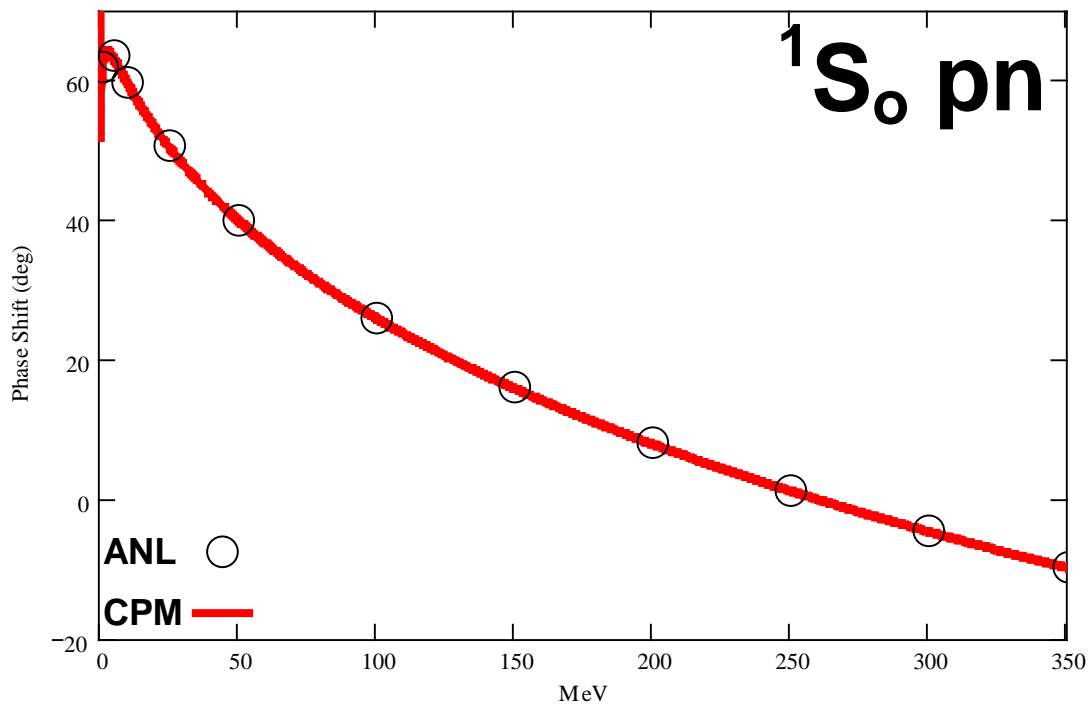


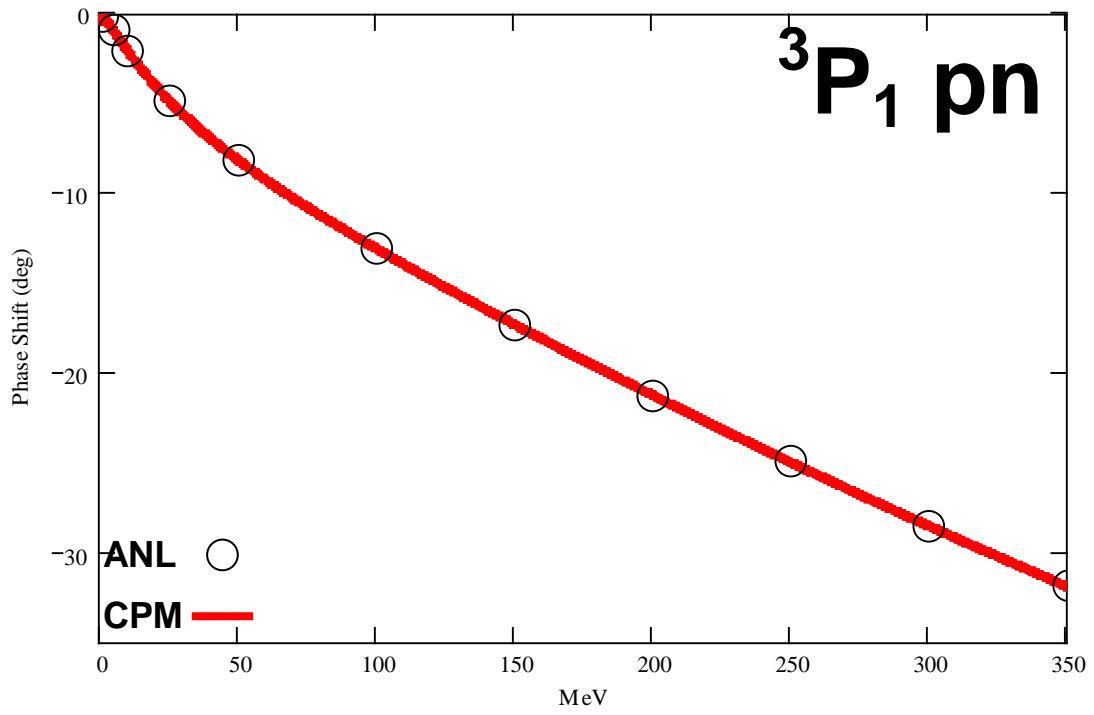
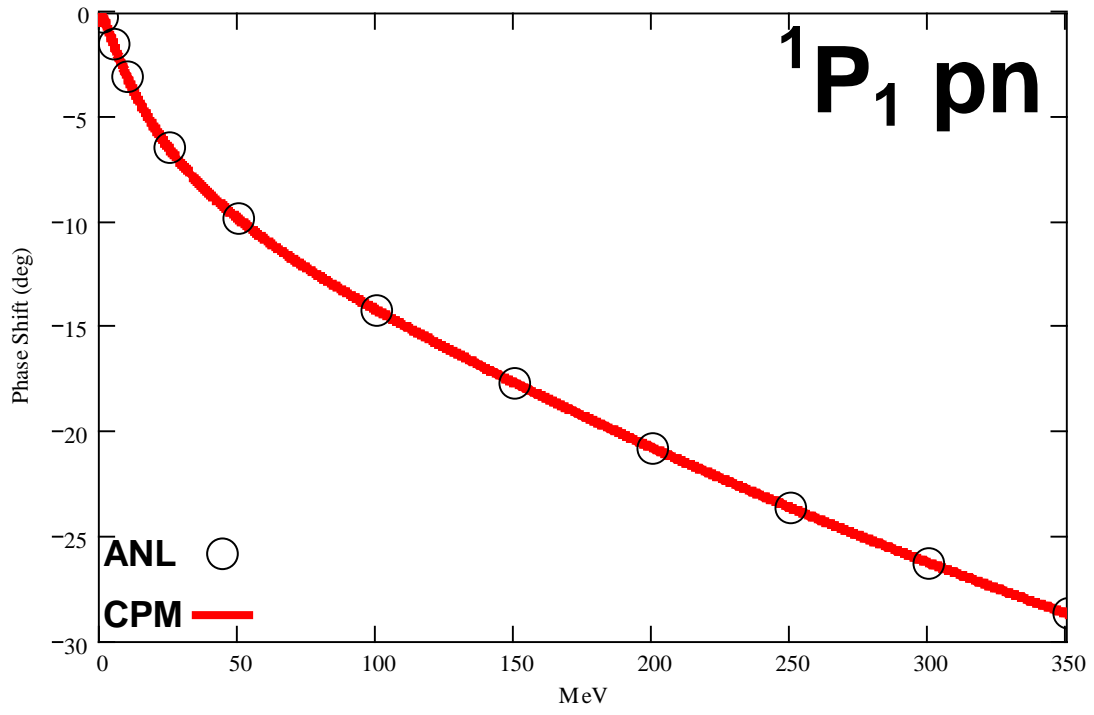


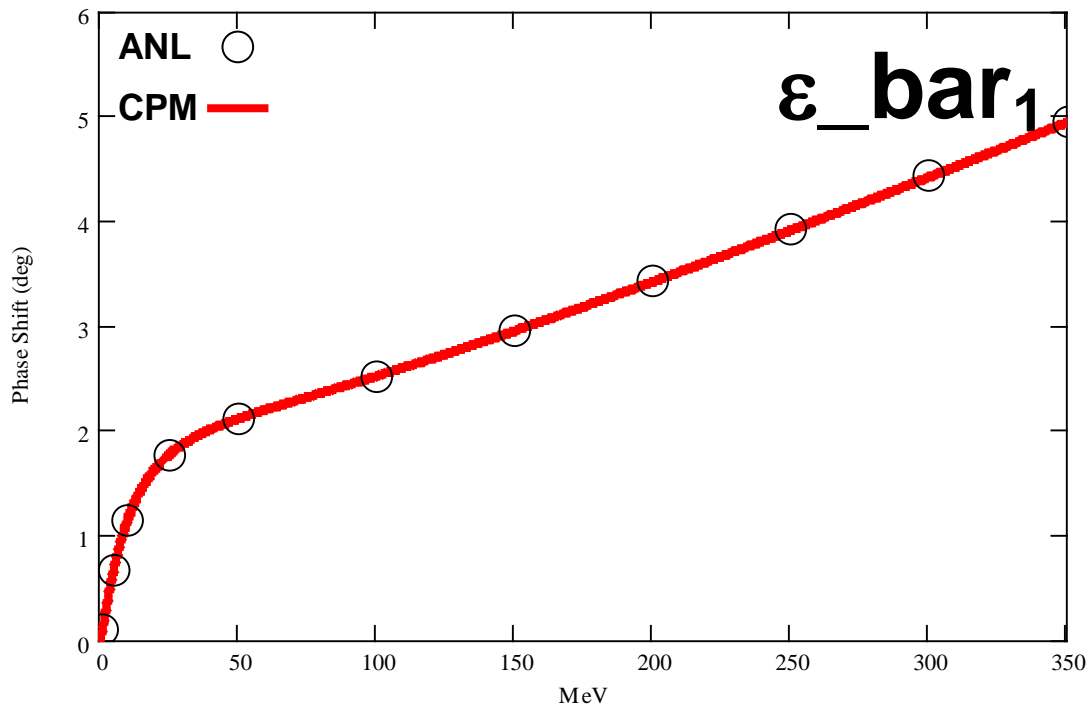
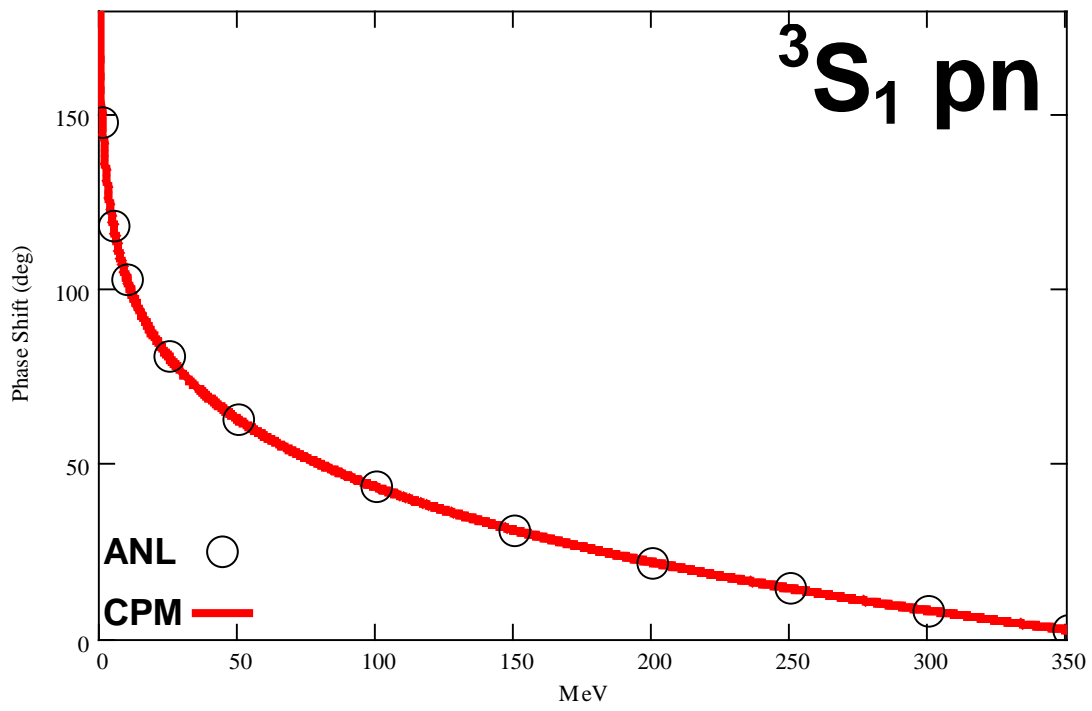
NP PHASE SHIFTS

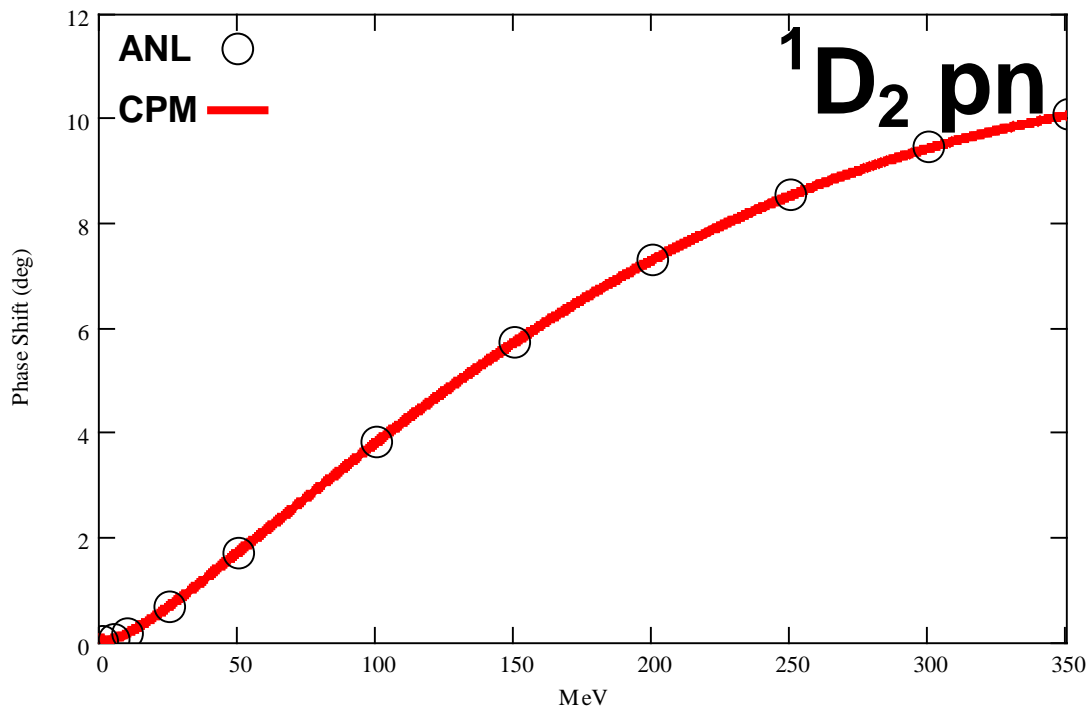
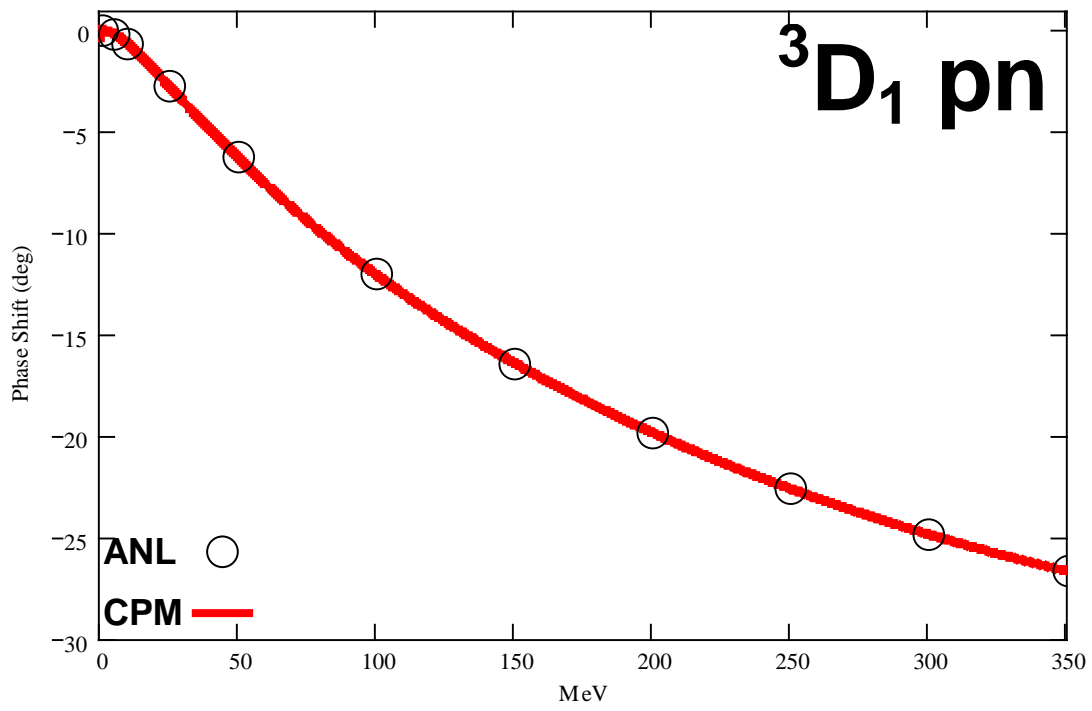
FOR $J = 0 - 5$

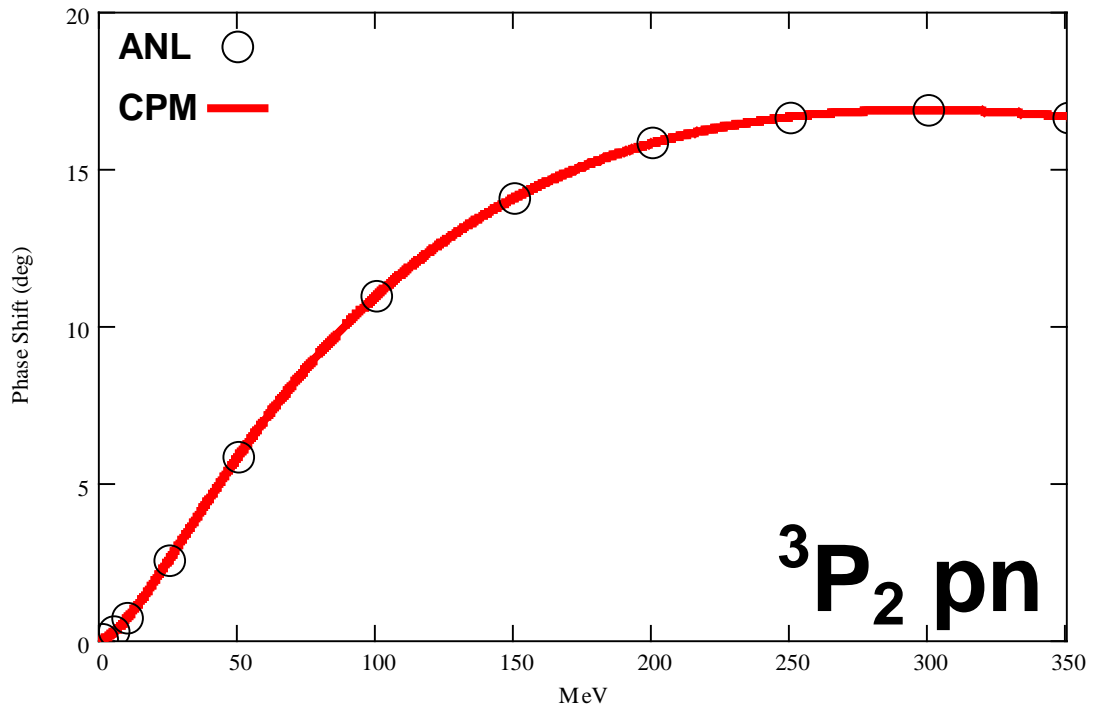
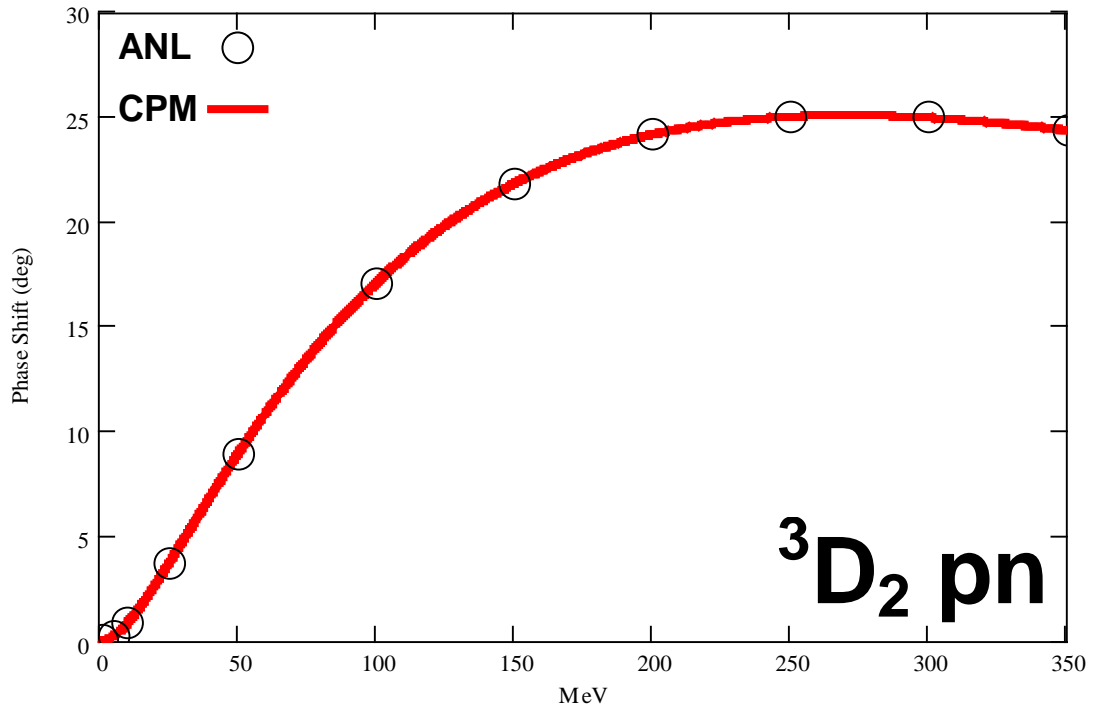
Data Compared To Results Provided From ANL

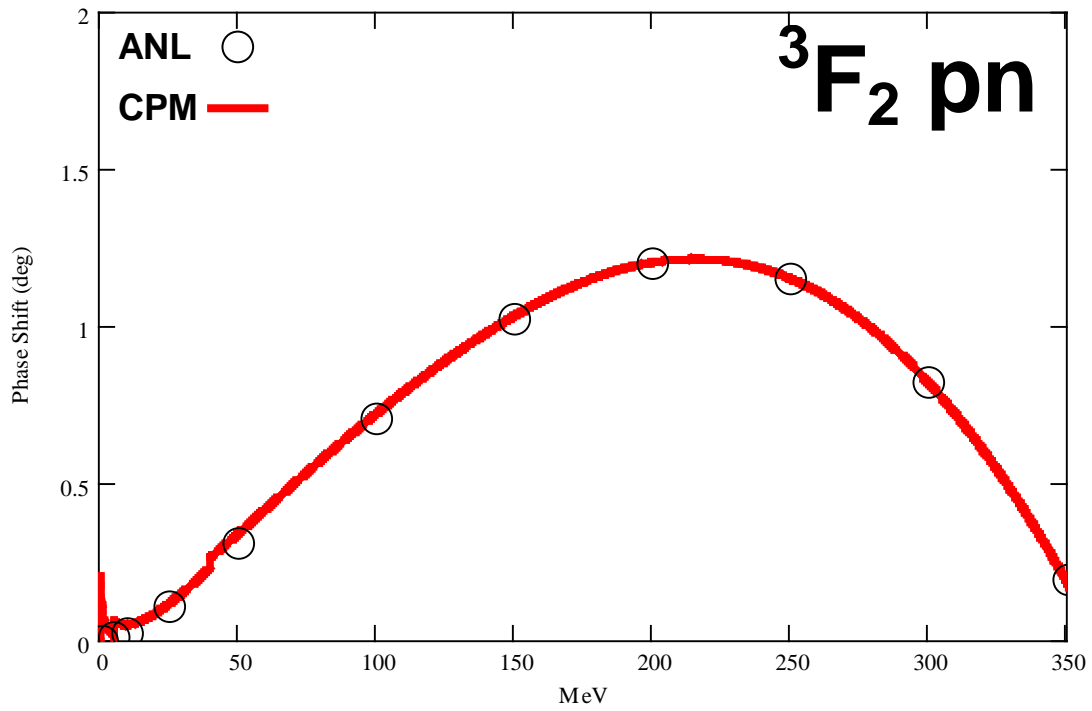
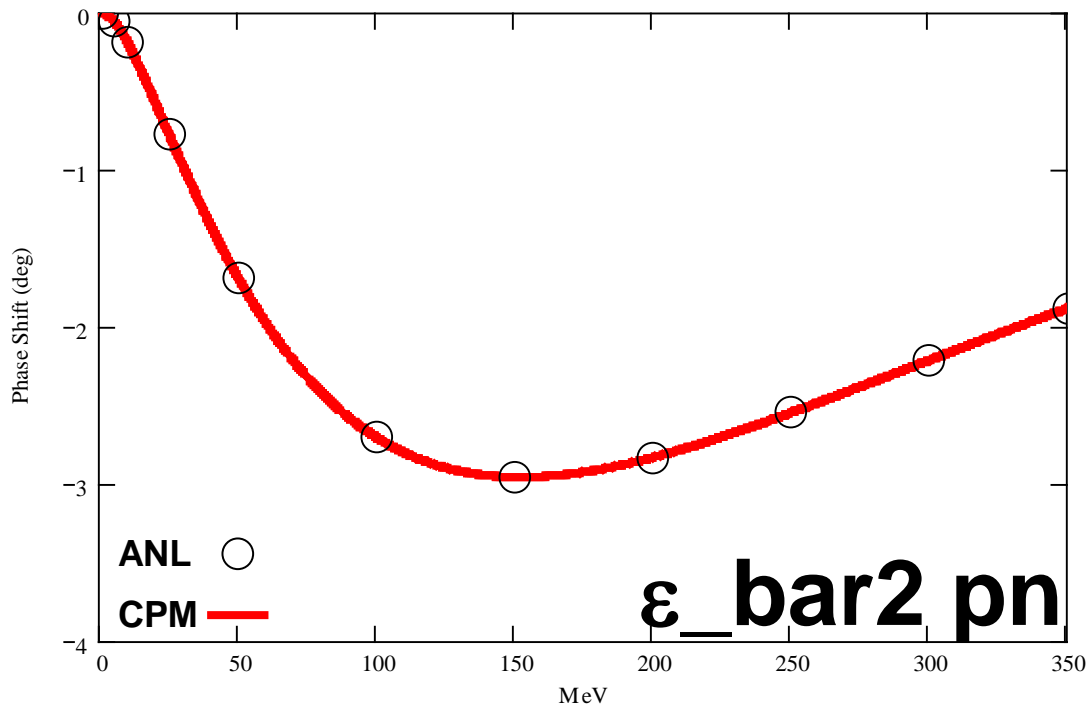


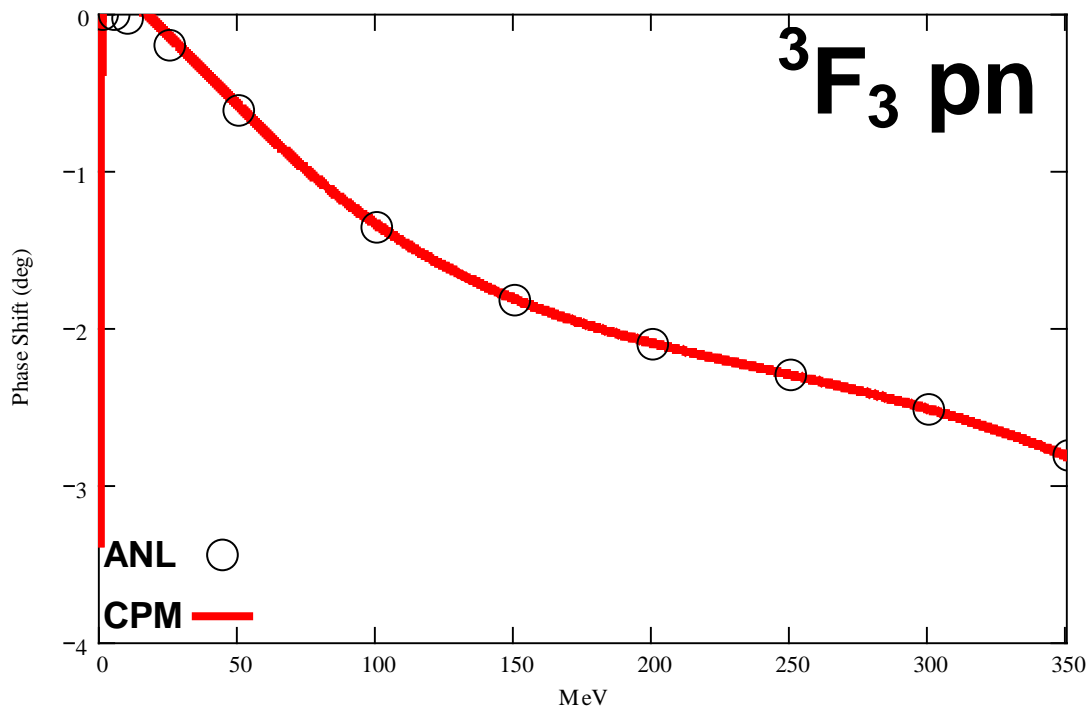
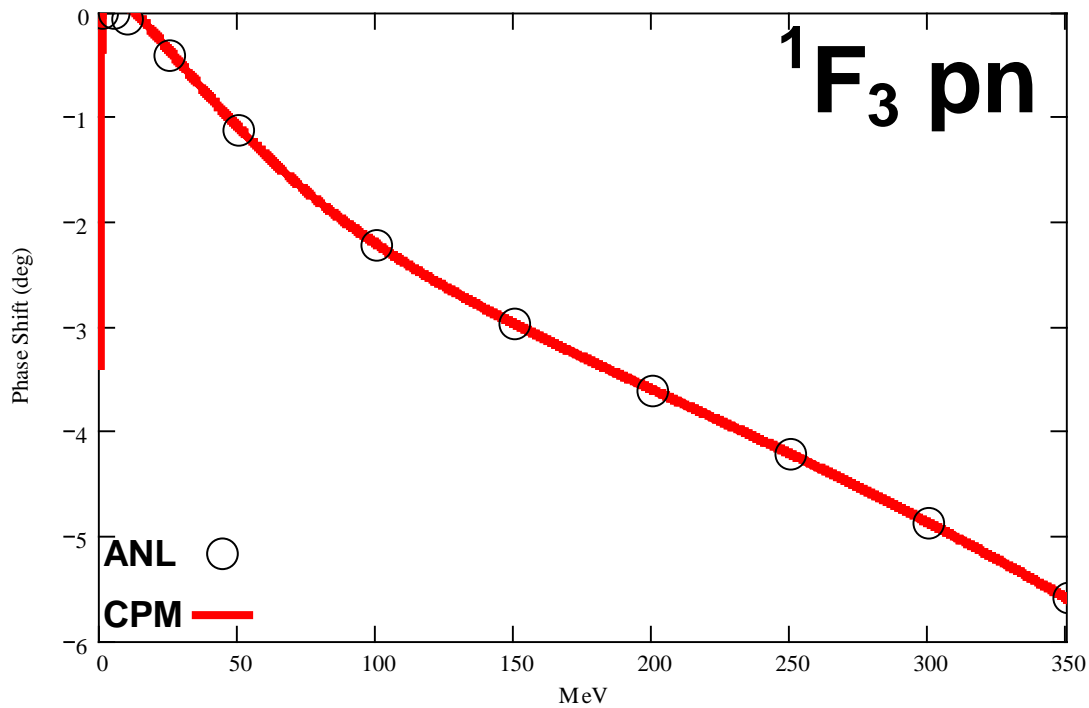


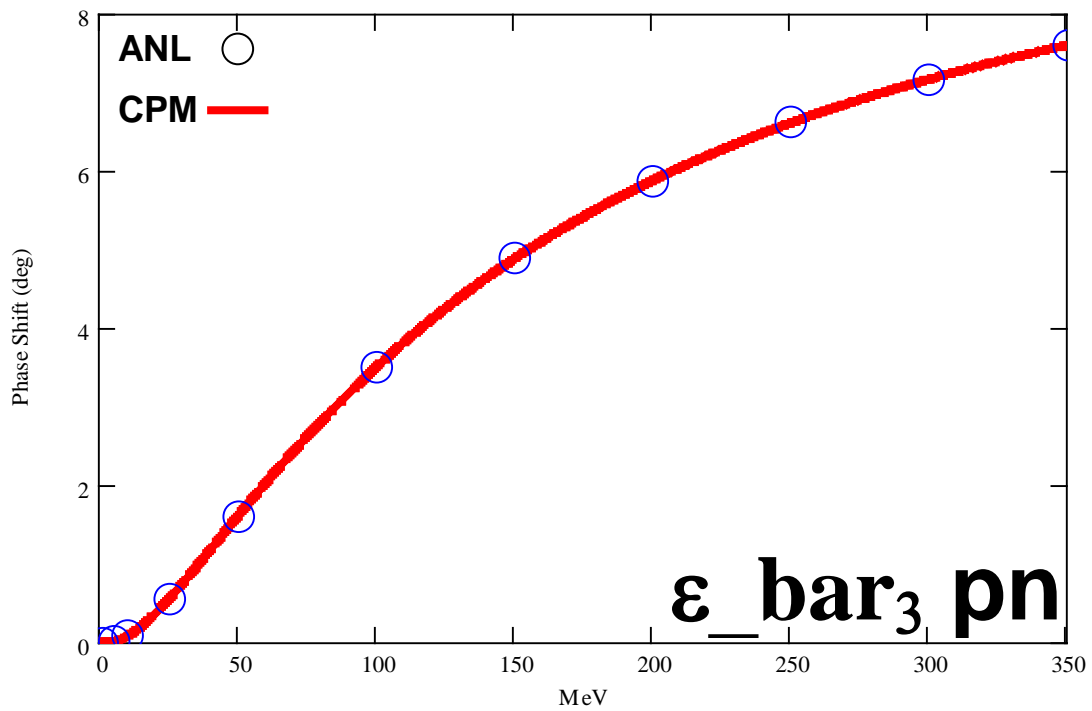
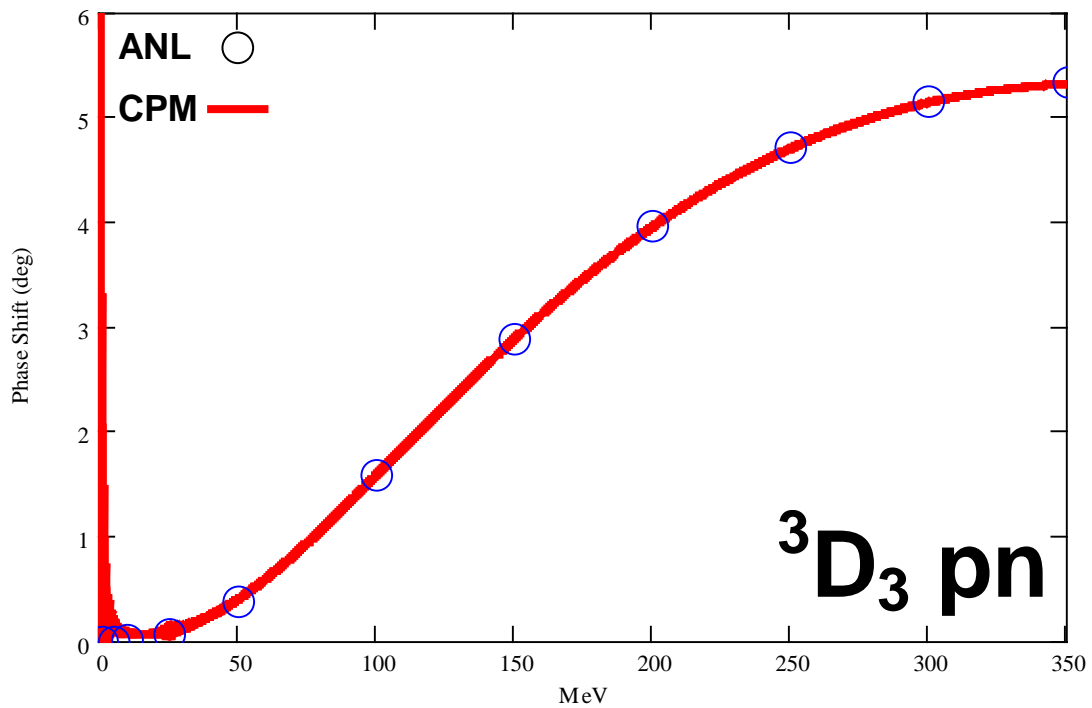


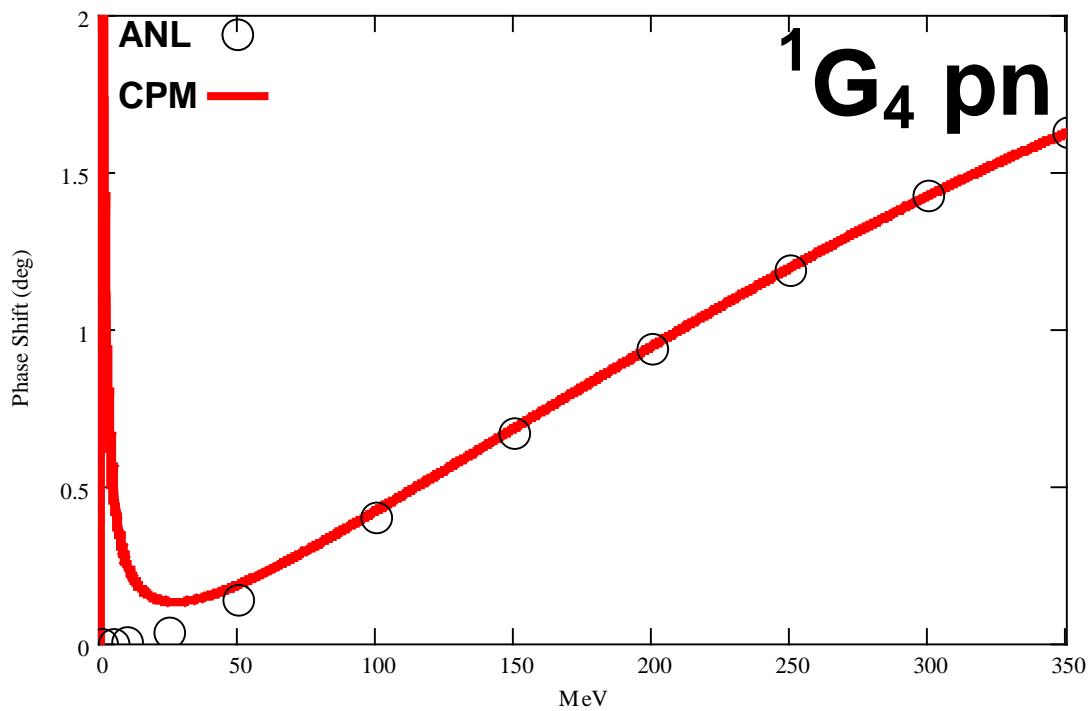
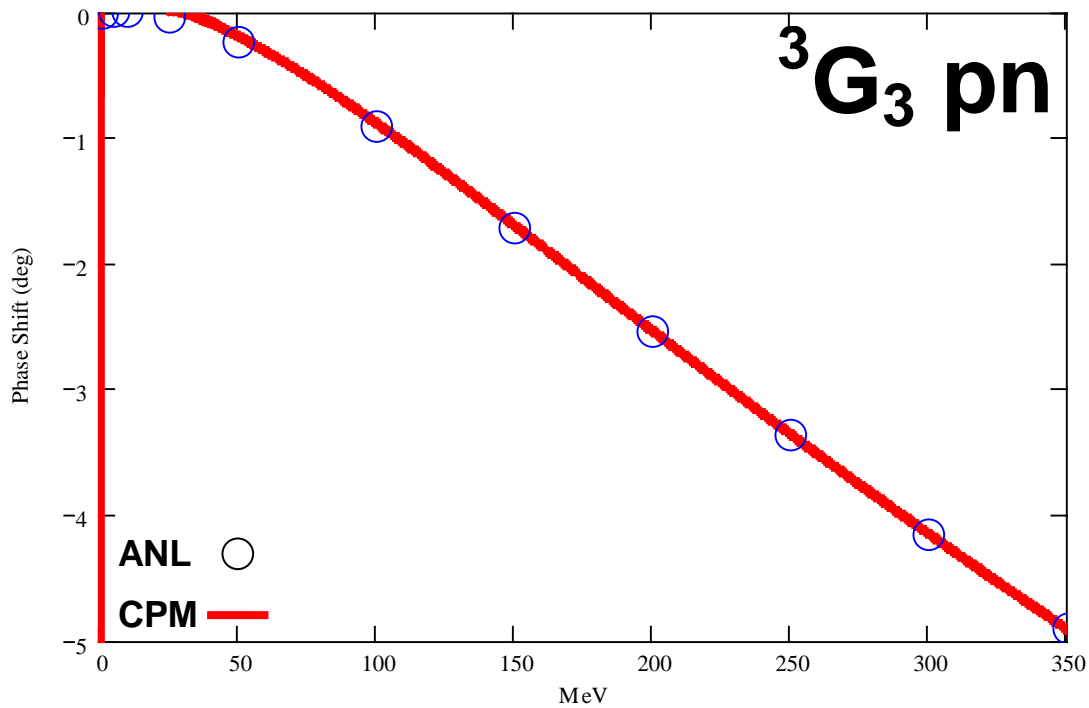


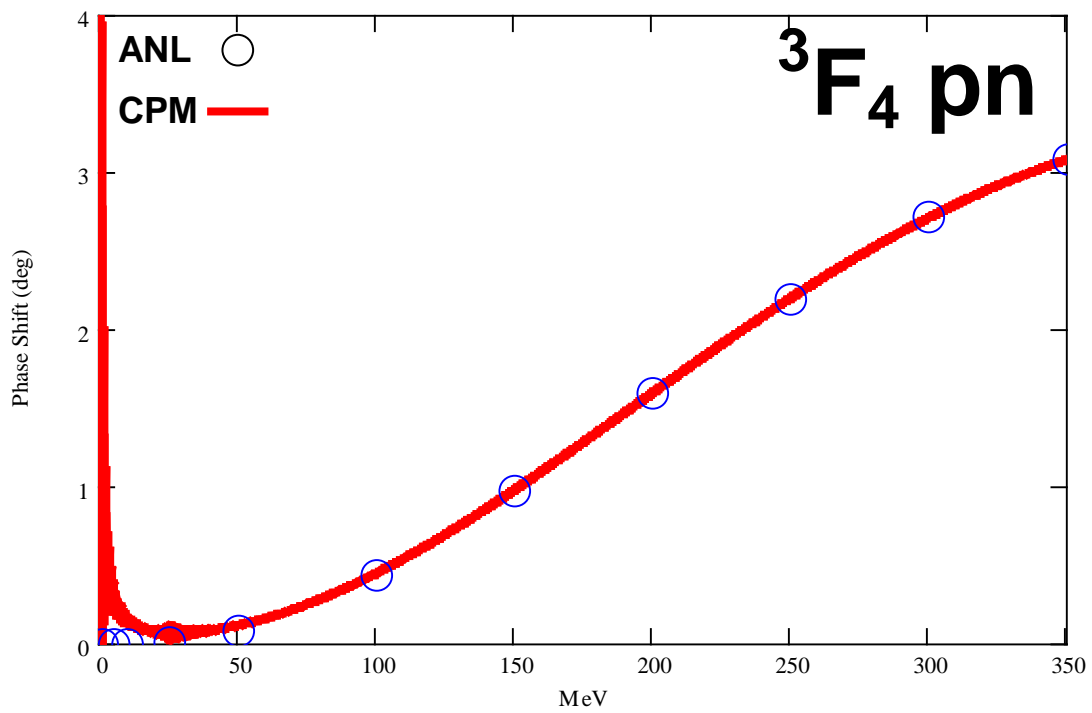
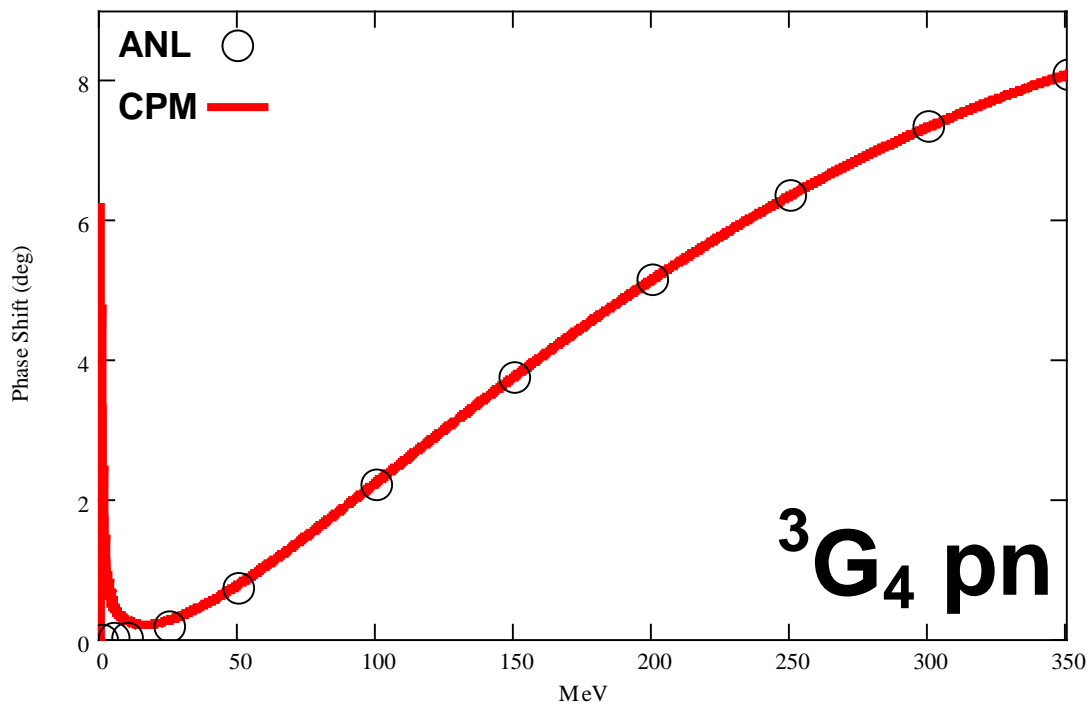


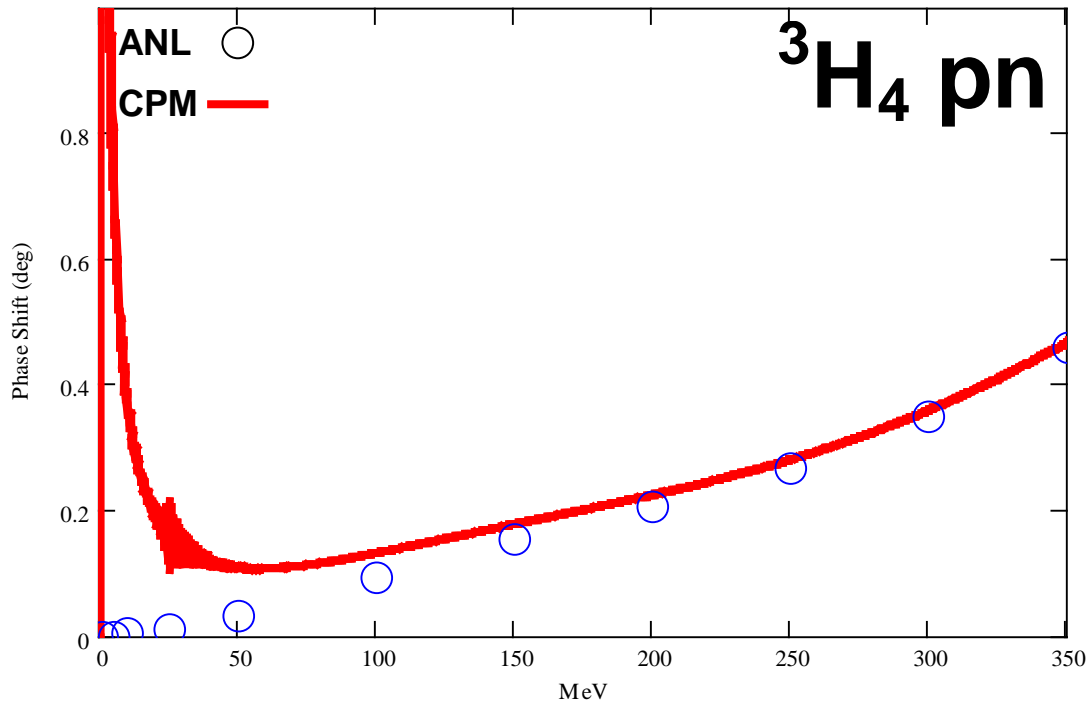
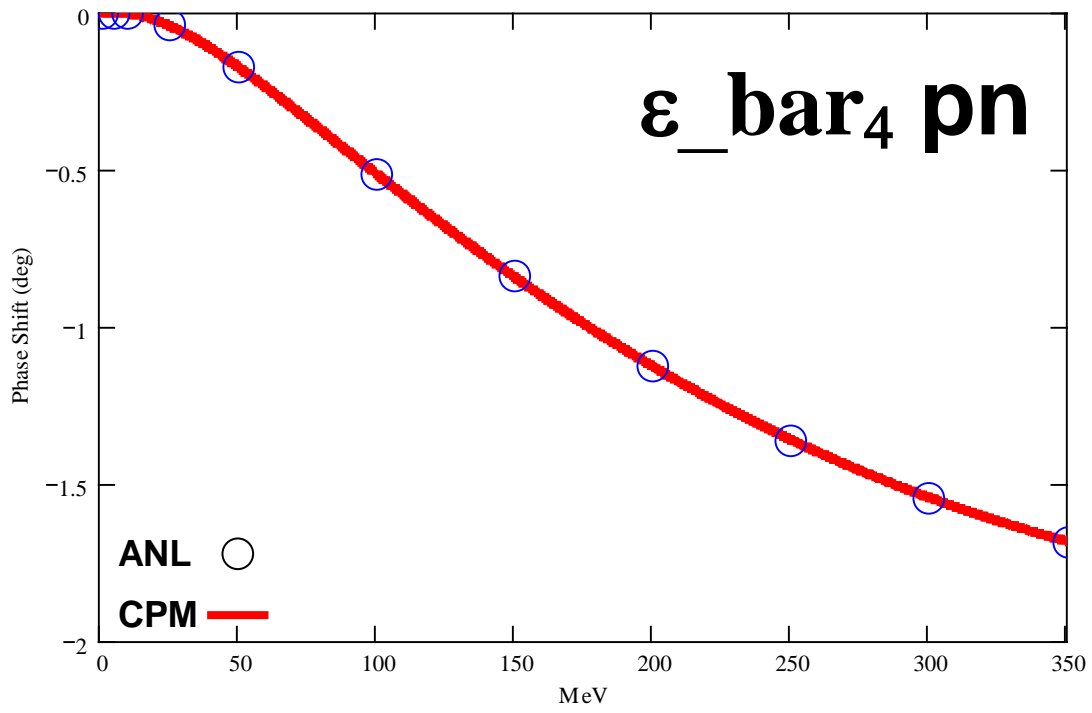


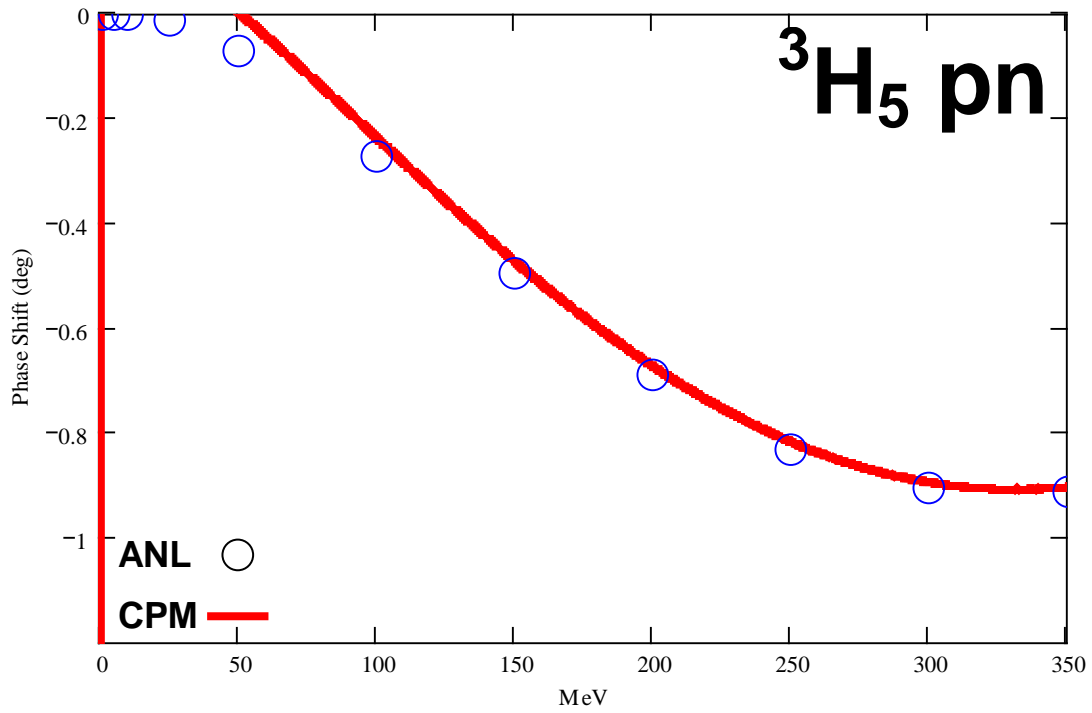
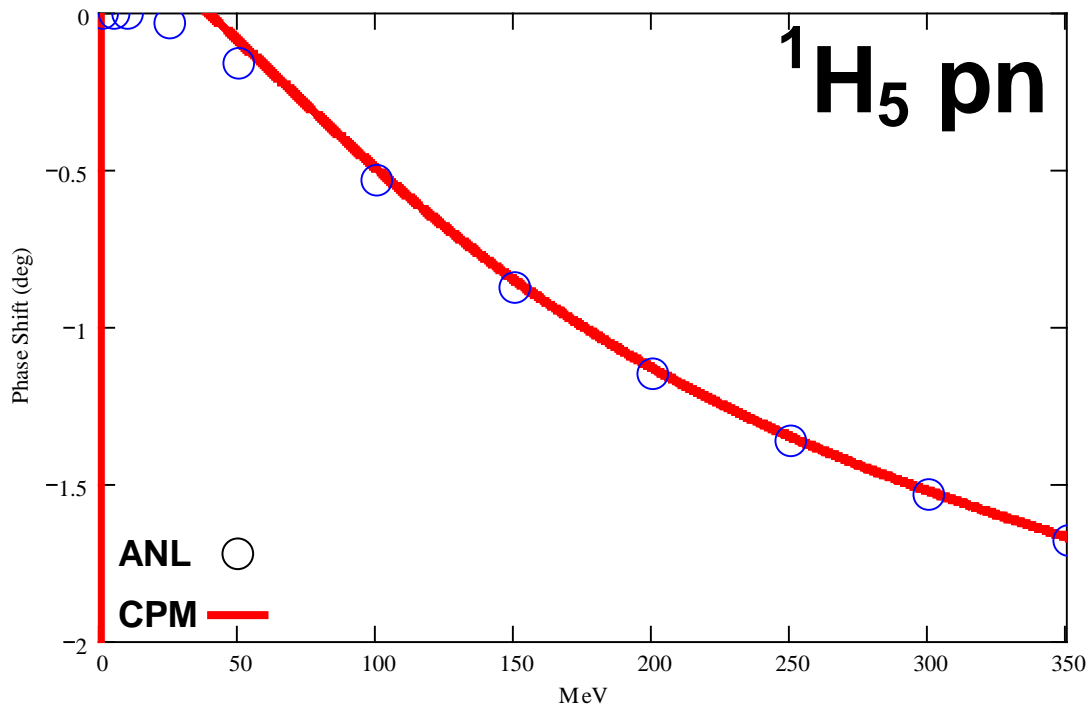








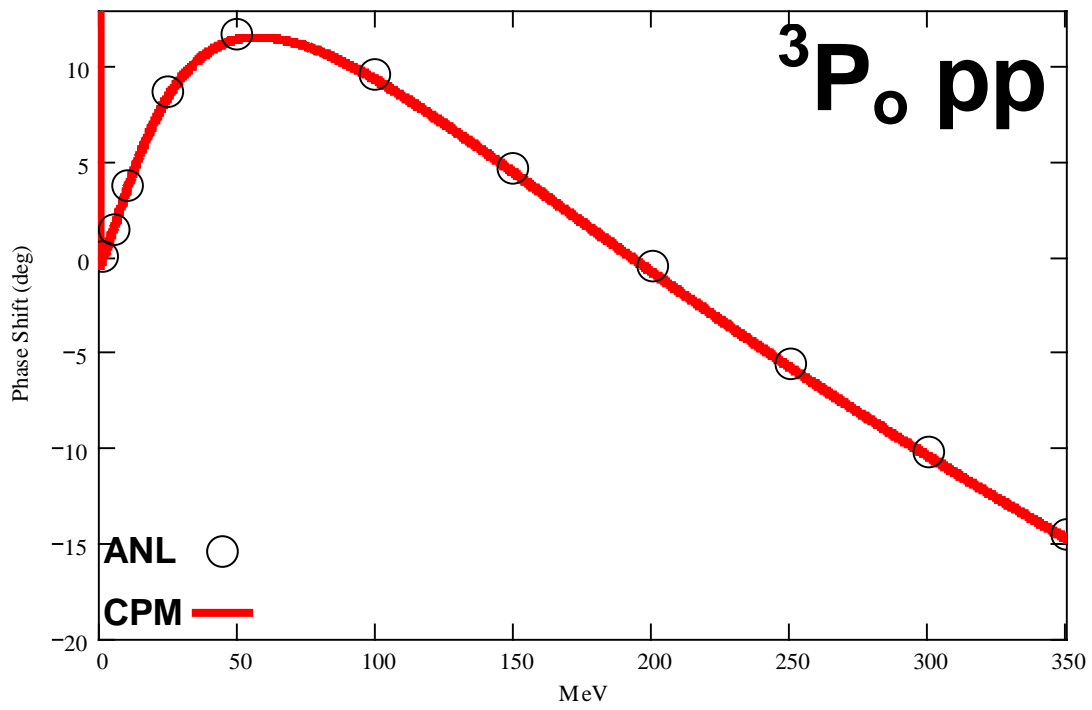
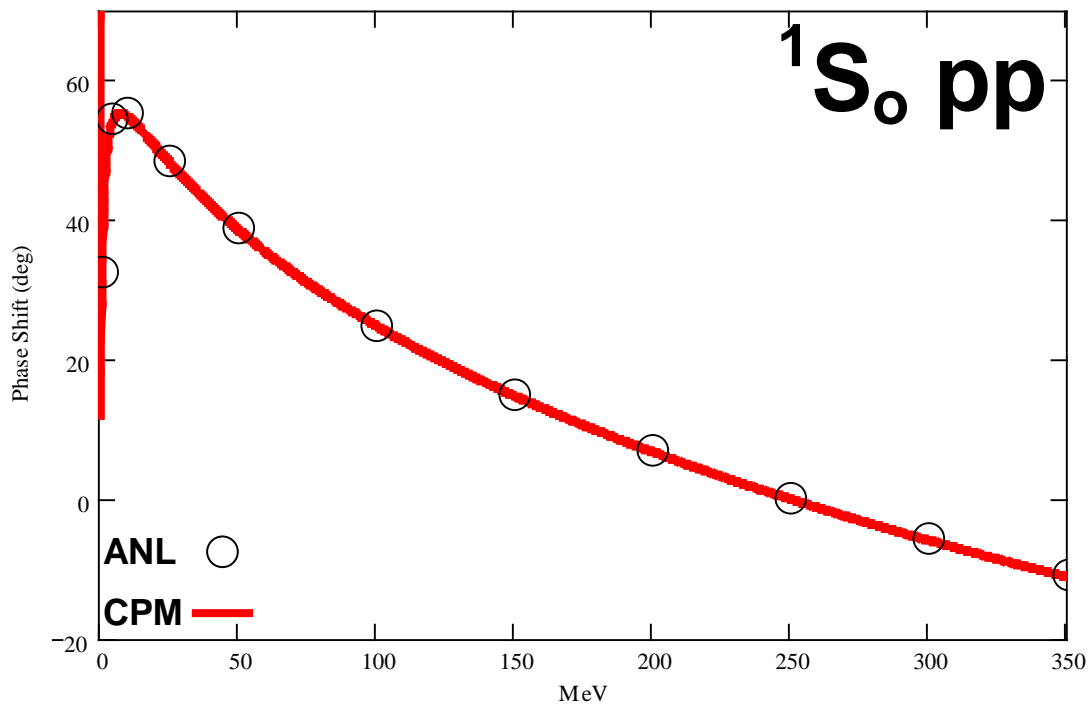


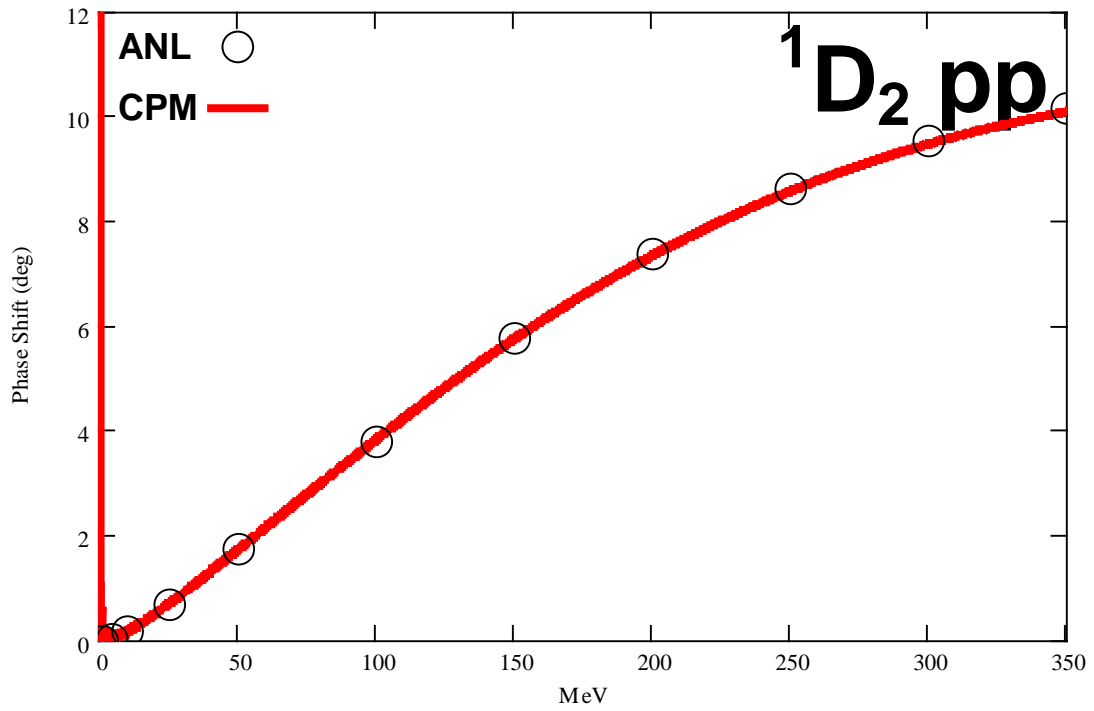
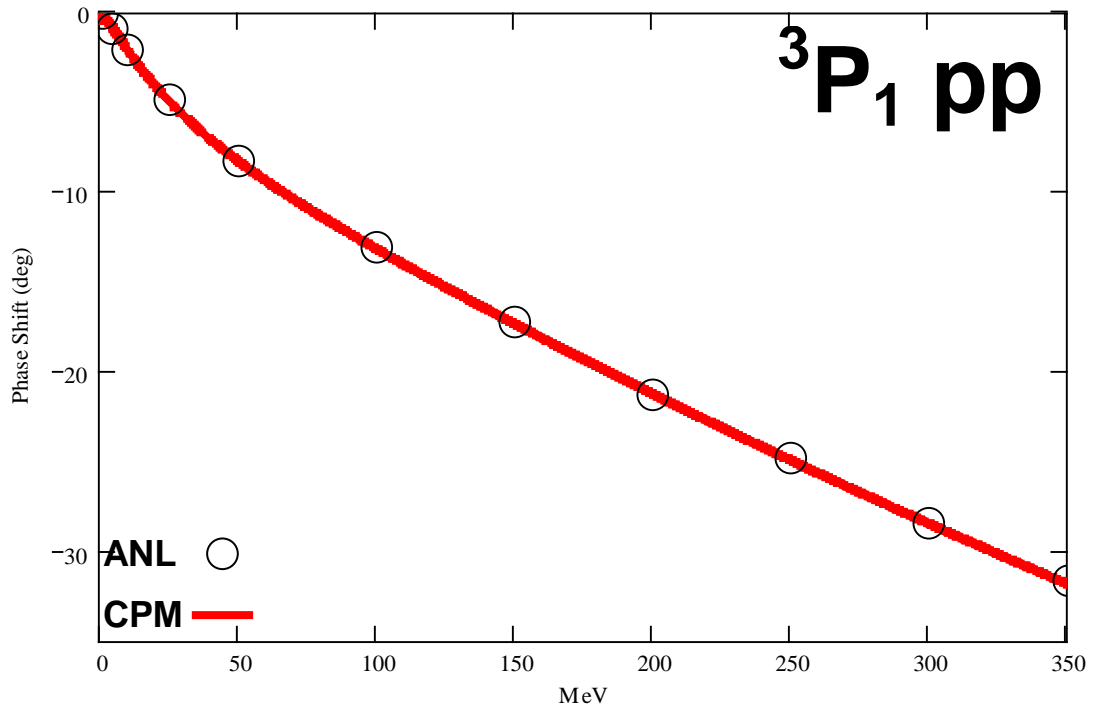


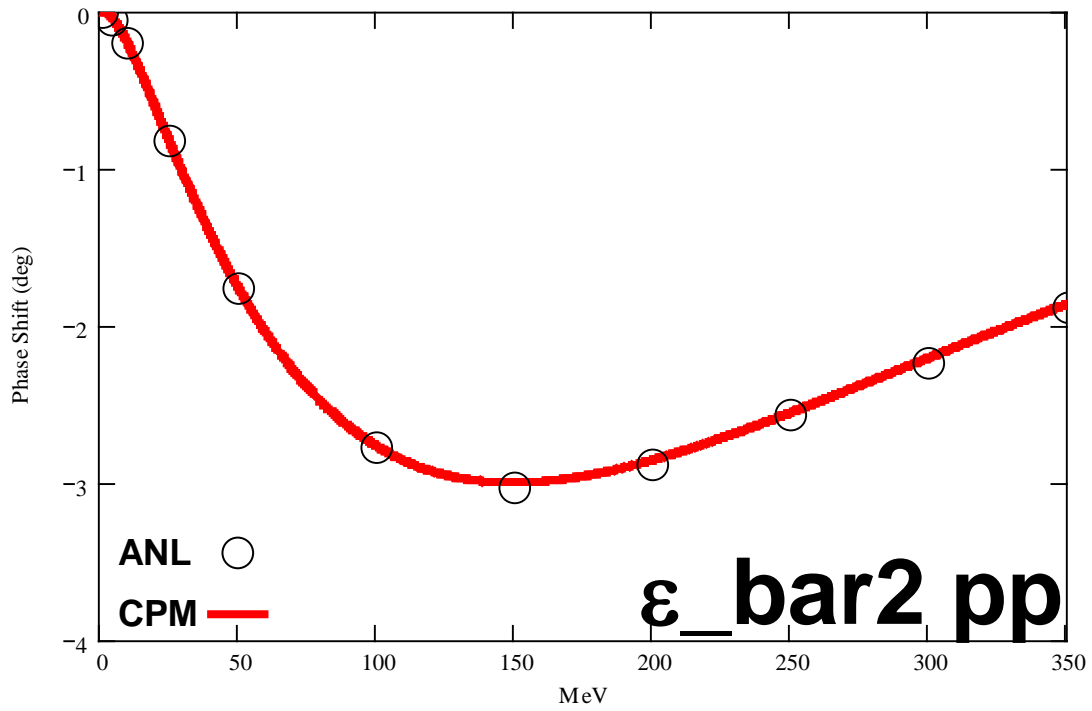
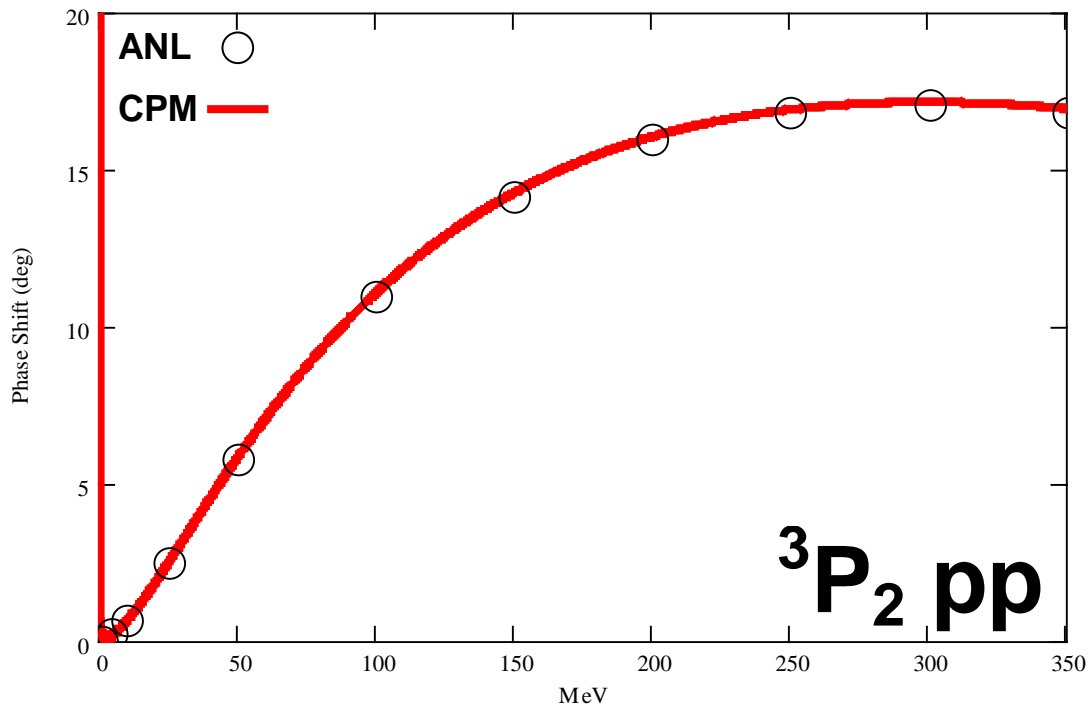
PP PHASE SHIFTS

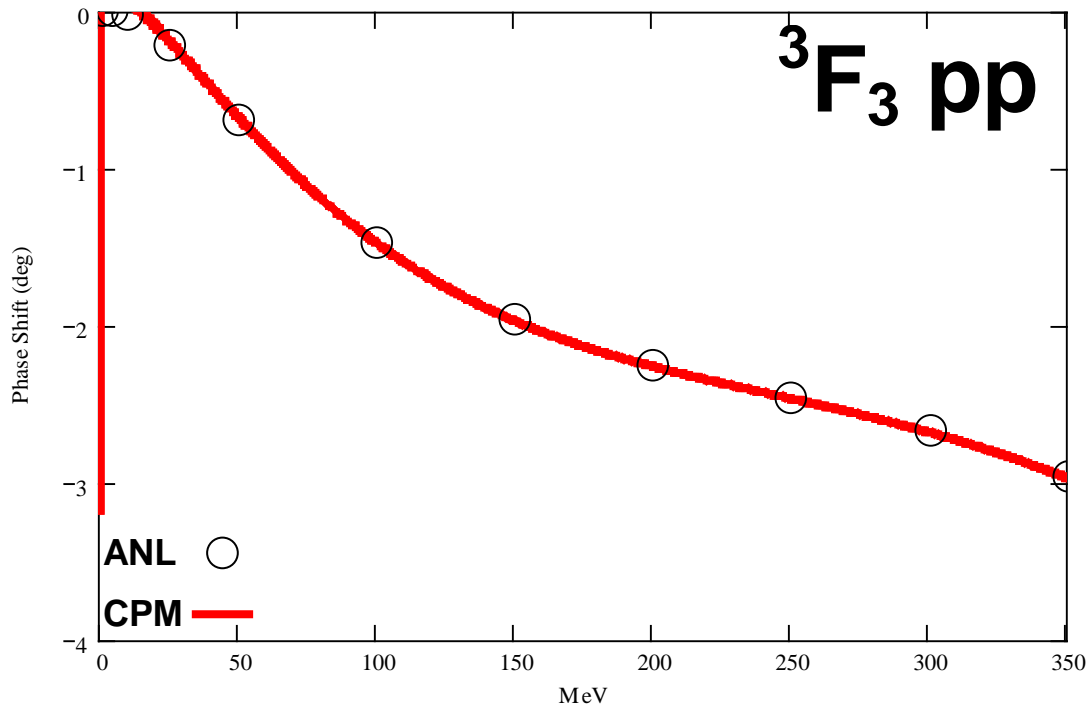
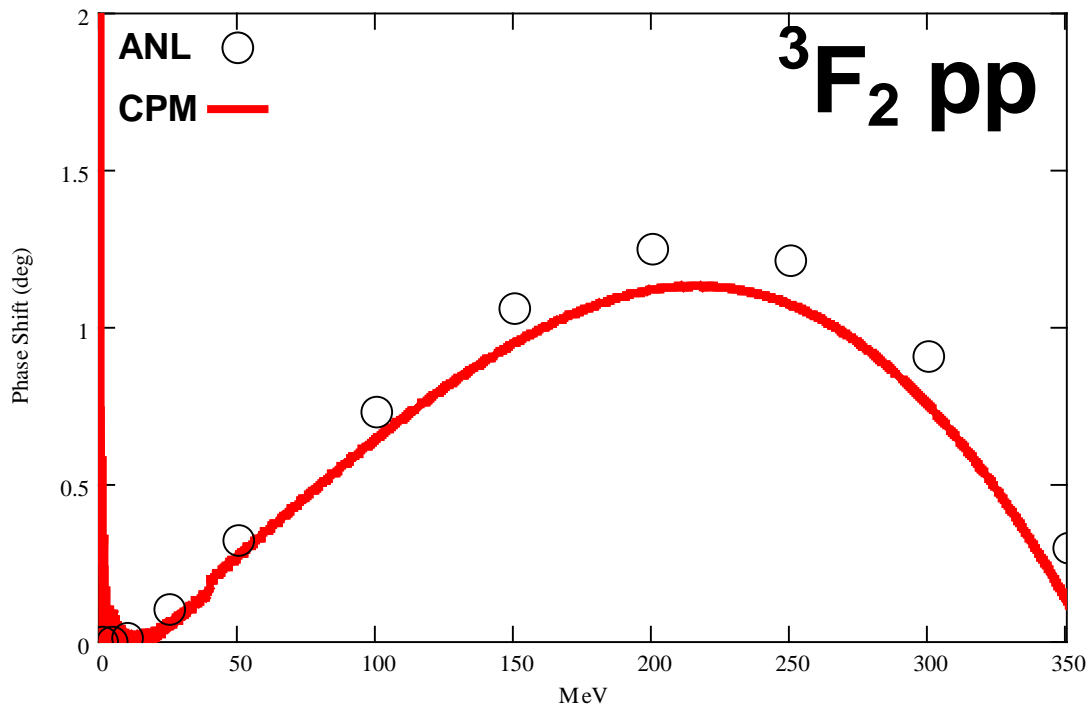
FOR $J = 0 - 5$

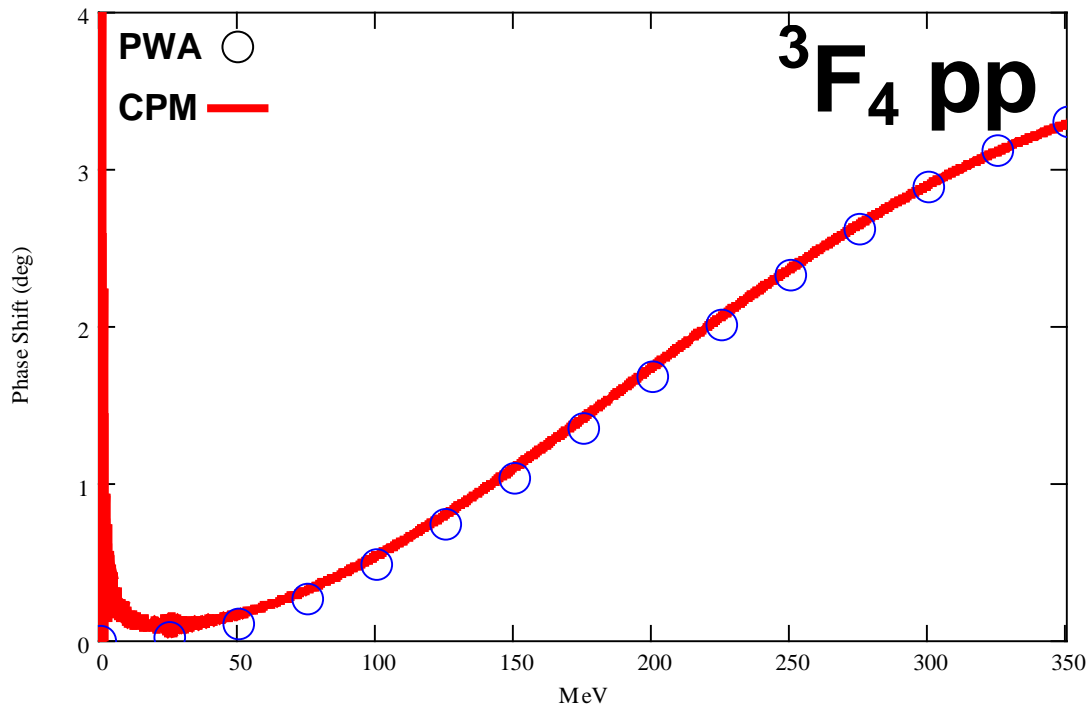
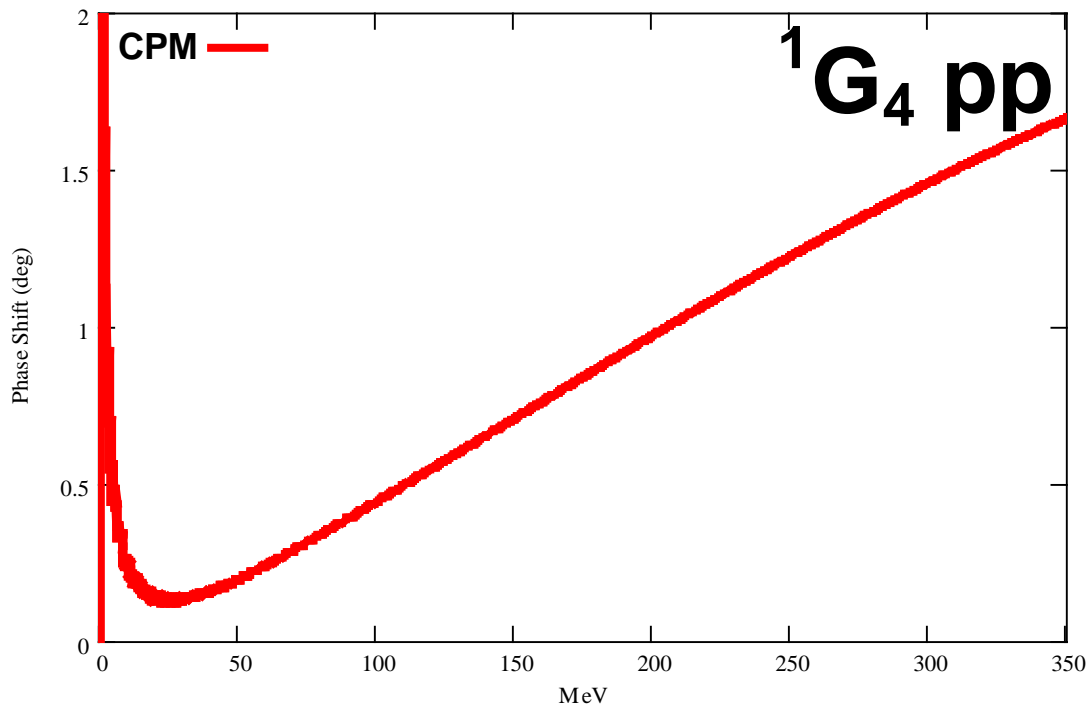
Data from Nijmegen (PWA) experimental data used when ANL data not available

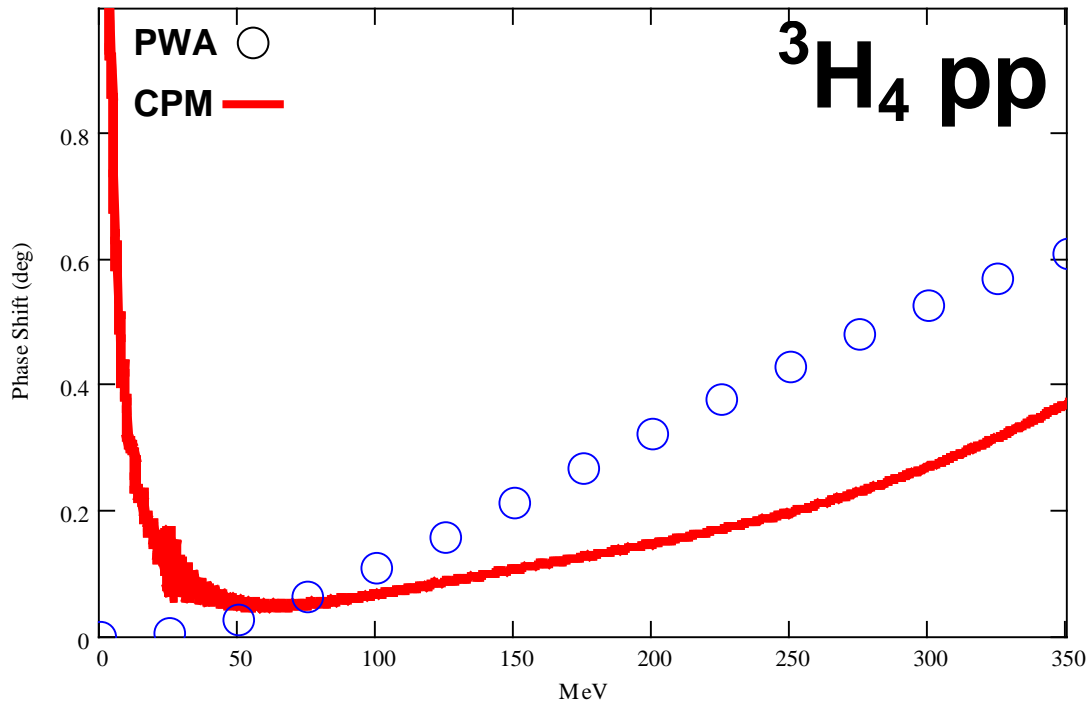
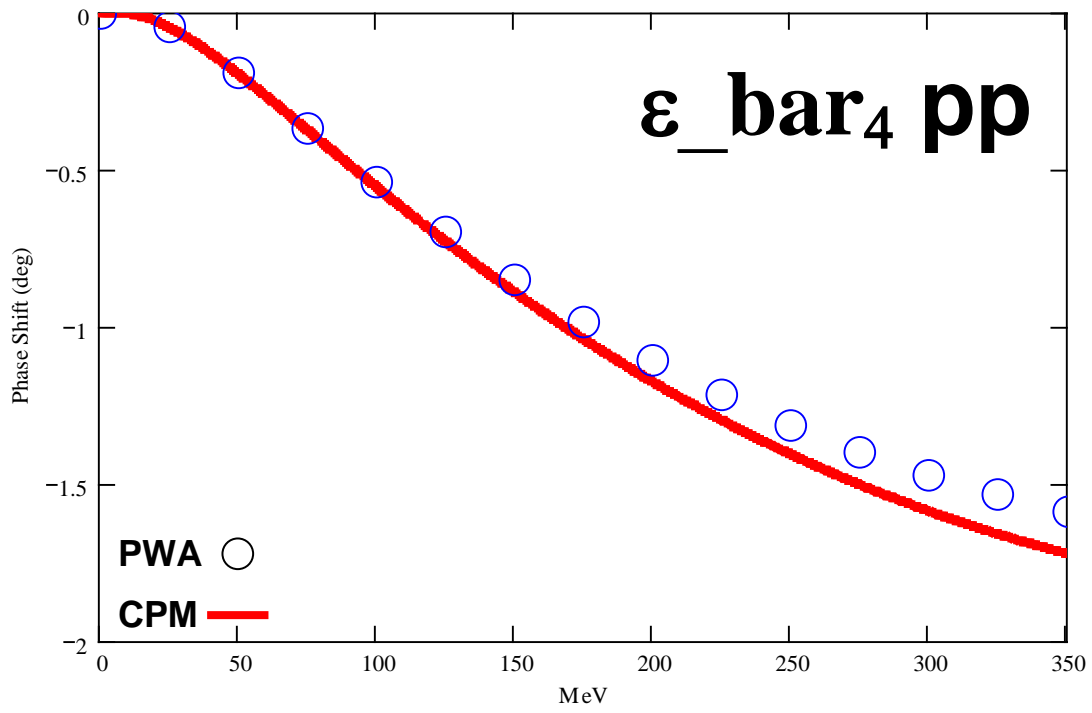


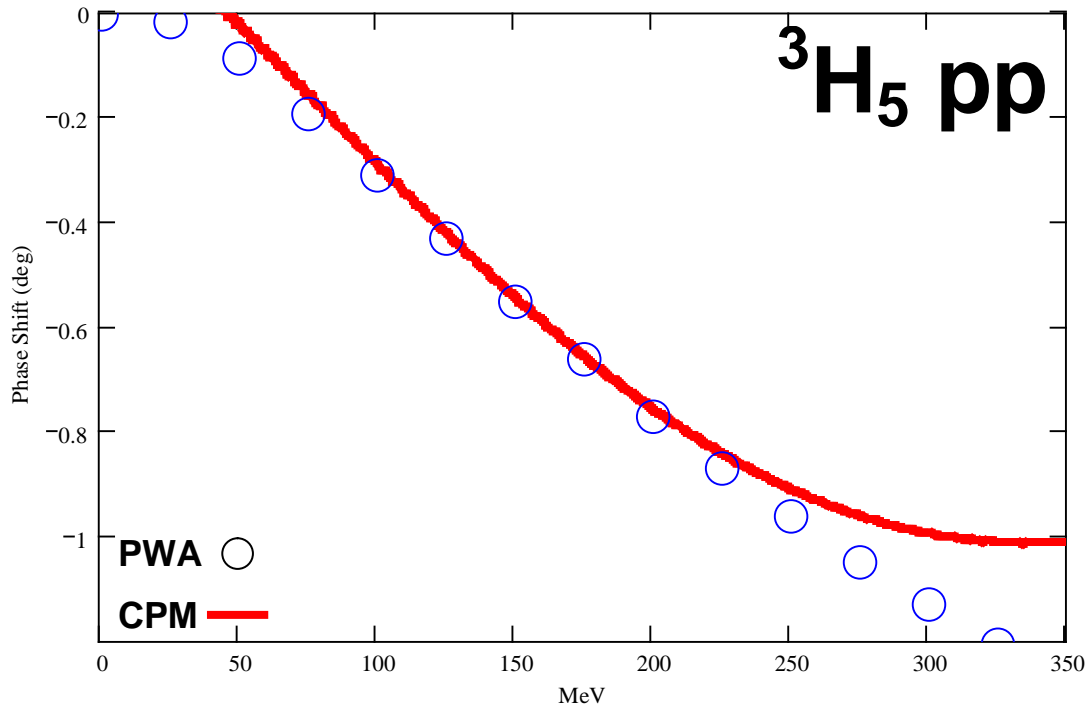












Bibliography

1. Bethe, Hans A., "What Holds the Nucleus Together?" *Scientific American*, V189, 58-63 (1953)
2. Machleidt, R. and I. Slaus. "Topical Review: The Nucleon-Nucleon Interaction," *Journal of Physics G*, 27: R69-R108 (2001)
3. Machleidt, R. "The Theory of Nuclear Forces: Is the Never-Ending Story Coming to an End?," *Nuclear Physics A*, 790: 17c-23c (2007)
4. Wiringa, R.B., V.G.J.Stoks, and R. Schiavilla. "Accurate Nucleon-Nucleon Potential with Charge-Independent Breaking," *Physical Review C*, V51,N1:38-51 (January 1995)
5. Wiringa, R.B., R.A. Smith, and T.L. Ainsworth. "Nucleon-Nucleon Potentials With and Without $\Delta(1232)$ Degrees of Freedom," *Physical Review C*, V29,N4:1207-1221 (April 1984)
6. Schiavilla, R., R.B Wiringa., V.G.J.Stoks, W. Glöckle, H. Kamada, A. Nogga, J. Carlson, R. Machleidt, V.R. Pandharipande, and A. Kievsky, "Weak Capture Of Protons by Protons," *Physical Review C*, V58,N2:1263-1277 (August 1998)
7. Blatt, John M. and V. F. Weisskopf. *Theoretical Nuclear Physics*. New York: Dover Publications, Inc., 1991. pp. 48-190
8. Pieper, Steven C. V.R. Pandharipande, R.B Wiringa, and J Carlson. "Realistic Models of Pion-Exchange Three Nucleon Reactions," *Physical Review C*, V64:1-21 (2001)
9. Eisenberg, Judah M. and W. Greiner. *Microscopic Theory of the Nucleus (Nuclear Theory Volume 3)*. Elsevier Pub Co, 1976. pp. 13-90.
10. Bethe, H.A. "The Meson Theory of Nuclear Forces, General Theory I," *Physical Review*, V57:260-272 (Feb 1940)
11. Bethe, H.A. "The Meson Theory of Nuclear Forces, General Theory II, Theory of the Deuteron" *Physical Review C*, V57:390-413 (Mar 1940)
12. Holz, J. and W. Glöckle. "Nucleon-Nucleon Scattering in a Time-Dependent Treatment," *Physical Review C*, V37N4:1386-1402 (April 1988)
13. Phillips, R.J.N. "The Two-Nucleon Interaction," *Reports Progress Physics*, 22:562-634 (1959)

14. J.M. Blatt and L.C. Biedenharn, "Neutron-proton scattering with spin-orbit coupling (I), General expressions," *Physical Review*, 86, 399 (1952)
15. Pieper, Steven C., K.Varga, and R.B. Wiringa. "Quantum Monte Carlo calculations of A=9,10 nuclei," *Physical Review C*, V66, 2002.
16. Frank, W. M., D. J. Land, and R. M. Spector. "Singular Potentials" *Reviews of Modern Physics*, V43 N1, 1971.
17. Schweiger W, W Plessas, L. P. Kok and H. van Haeringen. "Coulomb Plus Separable Potential in Coupled Channel," *Physical Review C*, V28 N3, 1983.
18. H.P. Stapp, T.J. Ypsilantis, and N. Metropolis. "Phase-shift analysis of 310 MeV proton-proton scattering experiments," *Physical Review*,. 105, 302 (1957).
19. Wiringa, R. B. and S. Pieper. "Evolution of Nuclear Spectra with Nuclear Forces," *Physical Review Letters*, V89, N18, 2002.
20. Carlson, J., V.R. Pandharipande, and R.B. Wiringa. "Three-Nucleon Interaction in 3- and 4- and ∞ -Body Systems." *Nuclear Physics A*, 401, 59-85, 1983.
21. Pandharipande, V.R. "Nuclear Forces and Nuclear Structure," *Nuclear Physics A*, V738:66-72 (2004)
22. Pieper, Steven C. and R.B Wiringa. "Quantum Monte Carlo Calculations of Light Nuclei," *Annual Review of Particle Science*, V51:53-90 (2001)
23. V.G.J. Stoks, R.A.M. Klomp, M.C.M. Rentmeester, and J.J. de Swart. "Partial Wave Analysis of All Nucleon-Nucleon Scattering Data Below 350 MeV," *Physical Review C* 48 (1993), 792
24. Th.A. Rijken and V.G.J. Stoks. "Soft Two-Meson-Exchange Nucleon-Nucleon Potentials. I. One and Two Pair Diagrams," *Physical Review C*, 54 (1996), 2851.
25. Th.A. Rijken and V.G.J. Stoks. "Soft Two-Meson-Exchange Nucleon-Nucleon Potentials. II. One and Two Pair Diagrams," *Physical Review C*, 54 (1996), 2869
26. Yukawa, H. "On the Interaction of Elementary Particles I," *Proceedings of the Physics-Math Society Japan*, 17 (1935), 48-57.
27. J.R. Bergervoet, P.C. van Campen, Klomp, R., de Kok, J., Rijken, T.A., Stoks, V.G. J., and J.J. de Swart. "Phase Shift Analysis of all proton-proton scattering data below $T_{\text{Lab}}=350\text{MeV}$," *Physical Review C*, V41, 1435-1451 (1990)
28. Roy, R.R.and B.P. Nigam. *Nuclear Physics: Theory and Experiment*. New York: John Wiley and Sons, 1967. pp. 46-140, 563-583.

29. Preston, M.A. and R.K. Bhaduri. *Structure of the Nucleus*. Massachusetts: Addison Wesley, 1982. pp. 3-53, 158-166.
30. Wong, Samuel S. M. *Introductory Nuclear Physics*. New York: John Wiley and Sons, 1998. pp. 21-102, 409-434.
31. Hans, H. S. *Nuclear Physics: Experimental and Theoretical*. New Delhi: New Age, 2001. pp. 175-189
32. Pashinin, V V.G.J. Stoks, R.A.M. Klomp, C.P.F. Terheggen, and J.J. de Swart. "Construction of high-quality NN potential models," *Physical Review C*, **49**, 2950 (1994).
33. Machleidt, R. "High Precision, Charge Dependent Bonn Nucleon-Nucleon Model" *Physical Review C*, V63, 1-32 (2001)
34. Kröger, H. "Time Dependent Methods in Scattering Theory," *Physics Reports*, V210 45-109, 1992.
35. Eisenbud, Leonard. "Time Dependent Formulation of the Collision Problem in Quantum Mechanics," *Journal of the Franklin Institute*, 261, 409-420 (1956)
36. Weeks, David E. and David J. Tannor. "A time-dependent formulation of the scattering matrix using Møller operators," *Chemical Physics Letters*, 207: 301-308 (May 1993)
37. Tannor, David J. and David E. Weeks. "Wave packet correlation function formulation of scattering theory: The quantum analog of classical S-matrix theory," *The Journal of Chemical Physics*, 98: 3884-3893 (March 1993)
38. Weeks, David E. and David J. Tannor. "A time-dependent formulation of the scattering matrix form the collinear reaction $H + H_2(u) \rightarrow H_2(u') + H$," *Chemical Physics Letters*, 224: 451-458 (July 1994)
39. Calfas, R.S. and David E. Weeks. "A new application of absorbing boundary conditions for computing collinear quantum reactive scattering matrix elements," *Chemical Physics Letters*, 263: 292-296 (December 1996)
40. Weeks, David E. and Roy S. Calfas, Air Force Technical Report, in press.
41. Niday, Thomas A. "Inelastic Scattering Matrix Elements for the Collision $B(^2P_{1/2}) + H_2(j) \rightarrow B(^2P_{3/2}) + H_2(j')$," Air Force Institute of Technology (AU), Wright-Patterson AFB OH, 1999. Thesis AFIT/GAP/ENP/99M 06
42. Leforestier, C., R. H. Bisseling, C. Cerjan, M.D. Feit, R. Friesner, A. Guldberg, A. Hammerisch, G. Jolicard, W. Karrlein, H.D. Meyer, N. Lipkin, O. Roncero and R.

- Kosloff. "A Comparison of Different Propagation Schemes for the Time Dependent Schrödinger Equation," *The Journal of Computational Physics*, 94: 59-80 (1991)
43. Auerbach, N, J Huffner, A.K. Kerman, and C.M. Shaken. "A Theory of Analog Resonances," *Review Modern Physics*, V44, 48 (1972)
 44. Andrews, Mark. "Total Time Derivatives in Quantum Mechanics," *American Journal of Physics*, V71 (4), 2003.
 45. Althorpe, S. C. and D. C. Clary. "Quantum Scattering Calculations on Chemical Reactions," *Annual Review of Physical Chemistry*, 54, 493-529, 2003.
 46. Jolicard, G. "Effective Hamiltonian Theory and Molecular Dynamics," *Annual Review of Physical Chemistry*, V46, 83-108, 1995.
 47. Bowman, J. M. and G. Schatz. "Theoretical Studies of Polyatomic Bimolecular Reaction Dynamics," *Annual Review of Physical Chemistry*, V46, 169-195, 1995.
 48. Jackson, B. "Time-Dependent Wave-Packet Approach to Quantum Reactive Scattering," *Annual Review of Physical Chemistry*, V46, 251-274, 1995.
 49. Tannor, David J. *Introduction to Quantum Mechanics: A Time Dependent Perspective*. California: University Science, 2007. pp. 559-600.
 50. Kosloff, Ronnie. "Time Dependent Quantum-Mechanical Methods for Molecular Dynamics," *Journal of Chemical Physics*. V92, 2087-2100, 1988
 51. Taylor, J.R. *Scattering Theory: The Quantum Theory of Nonrelativistic Collisions*. New York: Krieger, 1987. pp. 7-36, 180-185, 259-270.
 52. Calfas, Roy S. *Reactive Quantum Scattering in Two Dimensions*. Air Force Institute of Technology (AU), Wright-Patterson AFB OH, 1997. Dissertation AFIT/DSP/ENP/97 02
 53. Krane, Kenneth S. *Introductory Nuclear Physics*. New York: John Wiley and Sons, Inc., 1988. pp. 80-160.
 54. Turner, James E. *Atoms, Radiation, and Radiation Protection*. New York: John Wiley and Sons, 1995
 55. Shultis, J. Kenneth and Richard E. Faw. *Fundamentals of Nuclear Science and Engineering*. Florida, CRC Press, 2002. pp. 27-35.
 56. Bridgman, Charles J. *Introduction to Nuclear Weapons Effects*. Defense Threat Reduction Agency, 2001

57. Wilson, Edmund. *An Introduction to Particle Accelerators*. New York: Oxford, 2001
58. Lechanoine-LeLuc, C and F. Lehar. "Nucleon-Nucleon Elastic Scattering and Total Cross Sections," *Reviews of Modern Physics*, V65, No.1 (1993)
59. Eisberg, R. and R. Resnick. *Quantum Physics of Atoms, Molecules, Solids, Nuclei, and Particles*. New York: John Wiley and Sons, 1985. pp. 289-296, 667-707.
60. Frizsch, H. *Quarks: The Stuff of Matter*. New York: Basic, 1983
61. Eisenbud, L. and E.P. Wigner. "Invariant Forms of Interaction between Nuclear Particles," *Proceedings of National Academy of Sciences*, 27 (1941), 281-289
62. Grenier, W. and J.A. Maruhn. *Nuclear Models*. New York: Springer-Verlag, 1996.
63. Krohn, V.E. and G.R.Ringo. "Measurement of the Electron-Neutron Interaction by the Asymmetrical Scattering of Thermal Neutrons by Noble Gases," *Physical Review*. V148, Number 4, 1303-1311, 1966
64. Koonin, Stephen E. *Computational Physics*. California, Benjamin Cummings: 1986. pp. 55-105.
65. Glöckle, W. *The Quantum Mechanical Few-Body Problem*. New York, Springer-Verlag, 1983. pp. 40-76.
66. Townsend, John S. *A Modern Approach to Quantum Mechanics*. New York: McGraw Hill, 1992. pp. 120-146.
67. Mathews, P.M. and K. Venkatesan. *A Textbook of Quantum Mechanics*. New Delhi: McGraw-Hill, 1976. pp. 237-257.
68. Edmonds, A.R. *Angular Momentum in Quantum Mechanics*. New Jersey: Princeton University Press, 1957. pp. 122-132.
69. Griffiths, David J. *Introduction to Quantum Mechanics*. New Jersey: Prentice Hall, 1982. pp. 323-325, 352-373.
70. Marion, Jerry B. and Stephen T. Thornton. *Classical Dynamics of Particles and Systems*. California: Thomson, 2004. pp. 345-350.
71. Farina, J. E. G. *Quantum Theory of Scattering Processes*. New York, Pergamon, 1973. pp. 29-45.
72. Messiah, Albert. *Quantum Mechanics*. New York, John Wiley and Sons, 1970. pp. 303-432.

73. Mott, N. and H. Massey. *The Theory of Atomic Collisions, 3rd Edition*. London: Oxford, 1965. pp. 53-68.
74. Devanathan, Varadarajan. *Quantum Mechanics*. Middlesex: Alpha Science, 2005. pp. 221-224.
75. Levine, Raphael D. *Molecular Reaction Dynamics*. New York: Cambridge, 2005. pp. 49-51.
76. Abramowitz, M., and I. Stegun. *Handbook of Mathematical Functions with Formulas, Graphs, and Mathematical Tables*. New York, Dover, 1964
77. Hulthén, L. and M. Sugawara. *Handbuch der Physik*, 39, 1957.
78. Cohen-Tannoudji, C., B. Diu., and F. Laloë. *Quantum Mechanics (2 Volumes)*. New York: John Wiley and Sons, 1977. pp. 903-964.
79. Private Communication with R. B. Wiringa
80. Pieper, Steven C. "Quantum Monte Carlo Calculations of Light Nuclei," *Nuclear Physics A*, V751:516-532 (2005)
81. Merzbacher, Eugene. *Quantum Mechanics*. New York: John Wiley and Sons, Inc., 1997. pp. 35-53, 139-191, 215-251.
82. Hamming, R.W. *Numerical Methods for Scientists and Engineers*. New York: Dover Publications, Inc., 1973. pp. 382-387, 503-563.
83. Burden, Richard L. and J. Douglas Faires. *Numerical Analysis*. Pacific Grove: Brooks/Cole Publishing Company, 1997. pp. 188-201, 249-342.
84. Kameyama, H., M. Kamimura., Y. Fukushima. "Coupled-Rearrangement-Channel Gaussian-Basis Variational Method for Tri-Nucleon States," *Physical Review C*, V40,N2:974-987 (August 1989)
85. Taylor, J.R. *An Introduction to Error Analysis*. Mill Valley, Ca: University Science Books, 1982. pp. 45-79.
86. Valderrama, M Pavon and E.Ruis Arrioloa, "Low Energy NN Scattering at Next-to-Next-to-Next-to-Next-to-leading order for partial waves with $j \leq 5$," *Physical Review C*, 72, 2005
87. Stoks, V.G. J. and J.J. de Swart. "Comparison of Potential Models with PP Scattering Data Below 350 MeV," *Physical Review C*, V47, 761-767 (1993)
88. Sitenko, A and V Tartakoovskii, *Theory of Nucleus, Nuclear Structure and Interaction*, Boston, Kluwer, 1997. pp. 1-89.

89. Rodberg, Leonard S. and R. M. Thaler. *Introduction to the Quantum Theory of Scattering*, New York, Academic Press, 1967. pp. 63-73
90. Austen, G.J.M. and J.J. de Swart. "Improved Coulomb potential", *Physical Review Letters*, **50**, 2039 (1983).
91. J.R. Bergervoet, P.C. van Campen, W.A. van der Sanden, and J.J. de Swart. "Phase shift analysis of 0-30 MeV pp scattering data," *Physical Review C*, **38**, 15 (1988).
92. Suslov, V.M. and B. Vlahovic., "Generalization of the Numerov method for solution of Nd breakup problem in configuration space", *Physical Review C*, V69, 2004
93. Burcham, W. E. *Elements of Nuclear Physics*, New York, Longman, 1979.
94. Breit, G. and R.D. Haracz. *Nucleon-Nucleon Scattering, High Energy Physics Volume I*. New York, Academic Press, 1967.
95. MacGregor, M. H., M. J. Moravcsik, and H.P. Stapp. "Nucleon-Nucleon Scattering Experiments and their Phenomenological Analysis," *Annual Review of Nuclear Science*, V10, 1960.
96. Glöckle, W. H. Witala, D. Hüber, H. Kamada, and J. Golak. "The Three Nucleon Continuum: Achievements, Challenges, and Applications," *Physics Reports*, 274, 107-285, 1996.
97. Carlson J. and R. Schiavilla. "Structure and Dynamics of Few Nucleon Systems," *Reviews of Modern Physics*., V70 N3, 1998.
98. Faddeev, L. D. *Sov. Phys. JETP*, 12, 1014, 1961.
99. Chen, Z. M., W. Tornow, and A. Kievsky. "Extension of the Proton-Deuteron Phase-Shift Analysis to $E_p=22.7$ MeV and 4P_j Phase Shifts," *Few Body Systems*, V35, 15-31, 2004
100. Tornow, W., A. Kievsky., and H. Witala. "Improved Proton-Deuteron Phase-Shift Analysis Above the Deuteron Breakup Threshold and the Three-Nucleon Analyzing-Power Puzzle," *Few Body Systems*, V32, 53-81, 2002
101. Hüber, D., W. Glöckle., J. Golak., H. Witala., H. Kamada., A. Kievsky., S. Rosati., and M. Viviani. "Realistic Phase Shift and Mixing Parameters for Elastic neutron-deuteron scattering: Comparison of Momentum Space and Configuration Space Methods," *Physical Review C*, V51, Number 3, 1100-1107, 1995

102. Kievsky, A., M. Viviani ., S. Rosati., D. Hüber., W. Glöckle., H. Kamada., H. Witala., and J. Golak. “Benchmark Calculations for Polarization Observables in Three-Nucleon Scattering,” *Physical Review C*, V58, Number 6, 3085-3092, 1998
103. Breit, G. “Relativistic Corrections for High-Energy p-p Scattering,” *Physical Review*, 99, 1581 (1955).
104. Fujita, J. and H. Miyazawa. “Pion Theory of Three-Body Forces,” *Progress of Theoretical Physics*, V17:360-365 (1957)
105. Feit M.D., J.A. Fleck, Jr., and A. Steiger. “Solution of the Schrödinger equation by a spectral method,” *Journal of Computational Physics*, **47**, 412 (1982)
106. Loveland, Walter D., David J. Morrissey, and Glenn T. Seaborg *Modern Nuclear Chemistry*. New Jersey: John Wiley and Sons, 2006

Vita

Major Brian S. Davis graduated from Ware Shoals High School in Ware Shoals, South Carolina in 1987. After having served in the United States Air Force as a Photo-Sensor Maintenance Specialist at RAF Bentwaters, UK, Major Davis entered undergraduate study at Clemson University where he majored in Physics and graduated in 1996. He enrolled in the graduate physics program in 1999 and was awarded a Master of Science in Physics from Wright State University in 2002. Major Davis was commissioned through AFROTC Detachment 770 at Clemson University in 1996.

His first officer assignment in 1996 was at Holloman AFB where he performed the duties of Propulsion and Munitions Flight Commander. After a three-year tour, he worked as a bio-acoustic research physicist assigned to the Human Effectiveness Directorate, Air Force Research Laboratory, Wright-Patterson AFB Ohio. In 2002, he entered the Nuclear Physics program of the Department of Engineering Physics, Graduate School of Engineering Management, Air Force Institute of Technology. From 2006 to present, he has served as Sciences Support Division Deputy, Materials Directorate, Air Force Technical Application Center at Patrick AFB.

REPORT DOCUMENTATION PAGE

Form Approved
OMB No. 074-0188

The public reporting burden for this collection of information is estimated to average 1 hour per response, including the time for reviewing instructions, searching existing data sources, gathering and maintaining the data needed, and completing and reviewing the collection of information. Send comments regarding this burden estimate or any other aspect of the collection of information, including suggestions for reducing this burden to Department of Defense, Washington Headquarters Services, Directorate for Information Operations and Reports (0704-0188), 1215 Jefferson Davis Highway, Suite 1204, Arlington, VA 22202-4302. Respondents should be aware that notwithstanding any other provision of law, no person shall be subject to a penalty for failing to comply with a collection of information if it does not display a currently valid OMB control number.

PLEASE DO NOT RETURN YOUR FORM TO THE ABOVE ADDRESS.

1. REPORT DATE (DD-MM-YYYY) 25-03-2010		2. REPORT TYPE Doctoral Dissertation		3. DATES COVERED (From - To) Sep 2002 - Mar 2010		
4. TITLE AND SUBTITLE Time Dependent Channel Packet Calculation of Two Nucleon Scattering Matrix Elements				5a. CONTRACT NUMBER		
				5b. GRANT NUMBER		
				5c. PROGRAM ELEMENT NUMBER		
6. AUTHOR(S) Davis, Brian S., Major, USAF				5d. PROJECT NUMBER		
				5e. TASK NUMBER		
				5f. WORK UNIT NUMBER		
7. PERFORMING ORGANIZATION NAMES(S) AND ADDRESS(S) Air Force Institute of Technology Graduate School of Engineering and Management (AFIT/EN) 2950 Hobson Way WPAFB OH 45433-7765				8. PERFORMING ORGANIZATION REPORT NUMBER AFIT/DS/ENP/10-M03		
9. SPONSORING/MONITORING AGENCY NAME(S) AND ADDRESS(ES) Dr. Charles Brennan Air Force Technical Applications Center 1030 South Highway A1A Patrick AFB, Fl 32925				10. SPONSOR/MONITOR'S ACRONYM(S)		
				11. SPONSOR/MONITOR'S REPORT NUMBER(S)		
12. DISTRIBUTION/AVAILABILITY STATEMENT APPROVED FOR PUBLIC RELEASE; DISTRIBUTION UNLIMITED.						
13. SUPPLEMENTARY NOTES						
14. ABSTRACT A new approach to calculating nucleon-nucleon scattering matrix elements using a proven atomic time-dependent wave packet technique is investigated. Wave packets containing centripetal barrier information are prepared in close proximity to nuclear well. This is accomplished by first using an analytic equation to determine the wave packets in a suitable intermediate asymptotic state where the centripetal barrier is negligible. Then, the split operator technique is used to propagate the wave packets back to their original positions under the full Hamiltonian. Here, one wave packet is held stationary while the other is allowed to evolve and explore the nuclear well. Scattering matrix elements are computed from the correlation function between the stationary wave packet and the evolving wave-packet after it has interacted with the nuclear potential. Determination of nucleon-nucleon phase shifts follows directly from computation of the scattering matrix elements. This technique is ideally suited for determining nuclear scattering matrix elements and phase shifts as it provides a high degree of energy resolution with lower computational effort than traditional time independent methods. These advantages will lead to a greater understanding of reactions involving nucleons with other elementary particles.						
15. SUBJECT TERMS Nucleon-Nucleon, Scattering Matrix, Time Dependent , Phase Shift, Wave Packet, Split Operator						
16. SECURITY CLASSIFICATION OF:			17. LIMITATION OF ABSTRACT	18. NUMBER OF PAGES	19a. NAME OF RESPONSIBLE PERSON	
REPORT U	ABSTRACT U	c. THIS PAGE U	UU	206	Dr. David E Weeks, AFIT/ENP	
					19b. TELEPHONE NUMBER (Include area code) (937) 255-3636, ext 4561; e-mail: david.weeks@afit.edu	

Standard Form 298 (Rev: 8-98)

Prescribed by ANSI Std. Z39-18